Satellite Observations Of C_2H_2 And C_2H_6 In The Upper Troposphere

Thesis submitted for the degree of
Doctor of Philosophy
at the University of Leicester

by

Robert John Parker
Earth Observation Science Group
Departments of Physics and Chemistry
University of Leicester

March 2010

Declaration

I hearby declare that no part of this thesis has been previously submitted to this or any other University as part of the requirement for a higher degree. The work described herein was conducted by the undersigned except for contributions from colleagues as acknowledged in the text.

Robert John Parker
March 9, 2010

Satellite Observations Of C_2H_2 And C_2H_6 In The Upper Troposphere

Robert John Parker

ABSTRACT

In this thesis, the potential for the observation of acetylene (C_2H_2) and ethane (C_2H_6) from the Michelson Interferometer for Passive Atmospheric Sounding (MIPAS) infrared limb emission spectra is assessed. C_2H_2 is primarily produced from biomass and biofuel burning with C_2H_6 also emitted during natural gas production. The ability to successfully observe such species at high spatial and temporal resolutions allows a detailed study of their sources and transport to be conducted, an area of uncertainty in global tropospheric chemistry.

A fast detection algorithm for both C_2H_2 and C_2H_6 in the upper troposphere/lower stratosphere (UTLS) was developed (Chapter 4), capable of performing a "first look" at MIPAS data. Monthly C_2H_2 detection results for 2003 were analysed and shown to be well-correlated to retrieval results. This allowed African and Asian biomass burning transport, the relative influence of biomass burning to natural gas sources and the Asian monsoon anticyclone formation to be investigated.

An optimal estimation retrieval was developed for both gases and successfully applied for August 2003 (Chapter 5). This enabled the vertical structure of the distributions to be examined in the context of deep convection as well as the chemical isolation of the Asian monsoon anticyclone and biomass burning export.

Of particular note were the results that C_2H_2 was clearly isolated within the anticyclone and the observation of uplift via deep convection of C_2H_2 over South-East Asia (Chapter 6). Evidence for the penetration of C_2H_2 from the troposphere into the stratosphere above the anticyclone is also presented.

Ratios of the gas concentrations were examined (Chapter 6). The C_2H_2/CO ratio provides information on the photochemical evolution of the biomass burning plumes. The C_2H_2/C_2H_6 ratio suggests differentiation of biomass burning and fossil fuel production sources. C_2H_6 enhancements observed over Mexico are attributed to the processing of natural gas.

PUBLICATIONS

Journal Articles

Hamilton, J. F., Allen, G., Watson, N. M., Lee, J. D., Saxton, J. E., Lewis, A. C., Vaughan, G., Bower, K. N., Flynn, M. J., Crosier, J., Carver, G. D., Harris, N. R. P., Parker, R. J., Remedios, J. J., Richards, N. A. D., Observations of an atmospheric chemical equator and its implications for the tropical warm pool region, *J. Geophys. Res.*, 113, 2008

Illingworth, S. M. and Remedios, J. J. and Parker, R. J., Intercomparison of integrated IASI and AATSR calibrated radiances at 11 and 12 μm, *Atmospheric Chemistry and Physics*, 9, 18, 6677-6683, 2009

Conference Proceedings And Reports

Robert Parker, John Remedios, David Moore, Vijay Kanawade, and Manasvi Panchal, Global Observations Of C_2H_2 as an indicator for biomass burning from MIPAS L1B Spectra, *Proceedings of the ESA Atmospheric Science Conference, Barcelona*, September 2009

John Remedios, David Moore, Robert Parker, Vijay Kanawade, and Manasvi Panchal, MIPAS Observations of Organic compounds in the Upper Troposphere, *Proceedings of the ESA Atmospheric Science Conference, Barcelona*, September 2009

David P. Moore, John J. Remedios, Nigel A. D. Richards, Martyn Chipperfield, Robert Parker and Steve Arnold, Assessing acetone and PAN measurements in the UTLS from the MIPAS-E instrument, *Proceedings of the ESA Atmospheric Science Conference, Barcelona*, September 2009

Remedios, J.J., Parker, R. J., Panchal, M., Leigh, R.J., and Corlett, G., Signatures of Atmospheric and surface Climate variables through Analyses of Infra-Red spectra (SATSCAN-IR), *Proceedings of the First EPS/Metop RAO Workshop, ESA-ESRIN, Frascati, Rome*, May 2006

Remedios, J., Moore, D., Sembhi, H., Parker, R., Kanawade, V. and Panchal, M., Infra-red Sensing for the Retrieval of Tropospheric Composition from Space, A contribution to ACCENT-TROPOSAT-2, Task Group 1: Infra-red, *ACCENT-TROPOSAT-2 Final Report: The Remote Sensing of Tropospheric Constituents from Space*, John Burrows and Peter Borrel editors, 2008

Remedios, J., Parker, R., Moore, D., Kanawade, V. and Panchal, M., Infra-red Sensing for the Retrieval of Tropospheric Composition from Space, A contribution to ACCENT-TROPOSAT-2, Task Group 1: Infra-red, *ACCENT-TROPOSAT-2 Activities 2006-7: The Remote Sensing of Tropospheric Constituents from Space*, John Burrows and Peter Borrel editors, 2007

ACKNOWLEDGEMENTS

The time spent undertaking the work for this PhD has comprised the majority of my life for the past four years and I would just like to take this opportunity to offer my thanks to everyone involved for their help and support.

Firstly acknowledgement must go to my supervisor, Prof. John Remedios, for not only giving me the opportunity to take up this PhD and become a part of the Earth Observation Science Group but for his continued help and guidance over the past four years without which I would not have had a chance to reach the stage I am now at. Thanks must also go to Dr. David Moore who at times almost felt like an extra supervisor with the huge amount of time and effort spent helping not only myself but my colleagues on a daily basis, often whether he had time to or not! In addition, all of the post-docs, especially Harj, Lizzie and Roland have always been a huge source of help and advice whenever it was needed. Thanks also to Prof. Paul Monks for his help and advice as well as Dr. Kevin Smith and Gary Williams at RAL without whom I wouldn't have been able to obtain any ethane spectra.

I would also like to thank all of my other colleagues in EOS, especially my fellow PhD students Alan, Austin, Dee, Manasvi, Sam, Vijay and Xiuping for keeping our office an enjoyable (although sometimes loud!) place to work over the past few years and without whom I certainly wouldn't have had as enjoyable a PhD experience.

Above all I would like to thank my family, my parents Robin and Carole and my fiancée Vicki for all of their love and support without which I would never have got this far.

Contents

List of Figures

List of Tables

LIST OF ABBREVIATIONS

AATSR	Along Track Scanning Radiometer
ACE	Atmospheric Chemistry Experiment
DOFS	Degrees of Freedom of Signal
ECMWF	European Centre for Medium Range Weather Forecasts
Envisat	ENVironment SATellite
ESA	European Space Agency
FOV	Field of View
FTIR	Fourier Transform Infrared Spectrometer
GEISA	Gestion et Etude des Informations Spectroscopiques Atmosphriques
HITRAN	HIgh-resolution TRANsmission molecular absorption database
HYSPLIT	Hybrid Single Particle Lagrangian Integrated Trajectory Model
IFOV	Instantaneous Field of View
ILS	Instrument Line Shape
MLS	Microwave Limb Sounder
MIPAS	Michelson Interferometer for Passive Atmospheric Sounding
MOPITT	Measurement Of Pollution In The Troposphere
MORSE	MIPAS Orbital Retrieval using Sequential Estimation
MSF	Molecular Spectroscopy Facility
NASA	National Aeronautics and Space Administration
NCEP	National Centers for Environmental Prediction
NESR	Noise Equivalent Spectral Radiance
NOAA	National Oceanic and Atmospheric Administration
OLR	Out-going Longwave Radiation
ORM	Optimised Retrieval Module
ppbv	Parts per billion by volume
pptv	Parts per trillion by volume
RAL	Rutherford Appleton Laboratories
RFM	Reference Forward MODEL
UTLS	Upper Troposphere - Lower Stratosphere
VMR	Volume Mixing Ratio

Chapter 1

Introduction And Background

The Earth's atmosphere extends from the surface to over 100 km and consists primarily of nitrogen (78%), oxygen (21%) and argon (0.9%). The remaining 0.1% is composed of a variety of trace gases including carbon dioxide, ozone, water vapour, methane. Although only constituting a small fraction of the atmosphere, it is these trace species which play such an important role in the atmosphere and drive the study of atmospheric composition.

The structure of the atmosphere is outlined in Figure 1.1 which shows the various layers of the atmosphere. The study of atmospheric composition is primarily related to the tropospheric and stratospheric layers.

The troposphere is the lowest layer of the atmosphere and it is the layer in which the majority of the Earth's "weather" occurs. It contains virtually all of the atmosphere's water vapour and aerosols and over three-quarters of the total atmospheric mass. As seen in Figure 1.1, the troposphere is defined by a decrease in temperature with height caused by the absorption of incoming solar radiation by the surface and the subsequent re-emission in the infrared. This mechanism leads to the heating of the atmosphere from the surface and along with the fact that as the air becomes less dense with altitude it can expand and cool, is responsible for the temperature structure in the troposphere.

A temperature inversion at the tropopause marks the boundary between the troposphere and the stratosphere. This region acts as a "lid" to convection from below, causing a separation between the troposphere and stratosphere with the majority of the convective processes confined to the lower level of the atmosphere. The height of the tropopause varies with both latitude and season but can be located anywhere from as high as 15 km in the tropics where there is significant heating and convection to as low as 8 km at the poles.

Above the tropopause, ultraviolet solar radiation is absorbed by stratospheric ozone, both protecting the surface from harmful UV radiation and producing the warming effect with height seen in the stratosphere up to the stratopause at approximately 50 km.

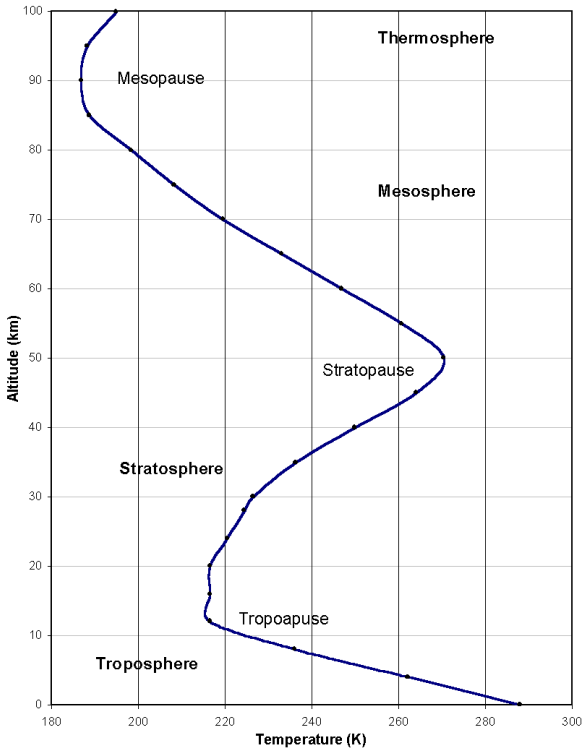

FIGURE 1.1. The temperature structure of the atmosphere (US Standard Atmosphere, 1976). Figure taken from www.atmosp.physics.utoronto.ca.

1.1 The Remote Sensing Of Atmospheric Composition

Prior to the development of satellites for the purpose of earth observation, measurements regarding the composition of the atmosphere were related to either ground-based or in situ aircraft/balloon-based measurements. This meant that data was confined to only examining the variability on a local or regional scale and normally only for a short period of time.

In contrast, since the advent of satellite remote sensing of the Earth's atmosphere, we are now capable of examining atmospheric composition on a global scale with datasets extending over a long period of time.

Currently two of the most prominent Earth Observation platforms in Low-Earth Orbit (LEO) are the European Space Agency's (ESA) ENVIronmental SATtellite (ENVISAT) (see Section 3.1), which hosts a variety of instruments capable of monitoring the Earth's land, ocean and atmosphere systems, and the NASA A-train constellation of satellites.

Challenges relating to the retrieval of atmospheric concentrations from satellite

signal are outlined in Chapter 2 where Retrieval Theory is discussed in more detail.

1.2 Tropospheric Chemistry And Organic Compounds

The photolysis of ozone O_3 by UV radiation is the primary source of OH radicals in the troposphere. First identified by Crutzen [1974], this involves the photolysis of O_3 to electronically excited $O(^1D)$, which then reacts with water vapour. It is these OH-radicals that provide the mechanism for the removal of pollutants and greenhouse gases such as carbon monoxide and methane from the lower troposphere.

In addition to the above, due to its nature as a powerful oxidant, O_3 itself is hazardous to plants and animals with high levels of tropospheric ozone being harmful.

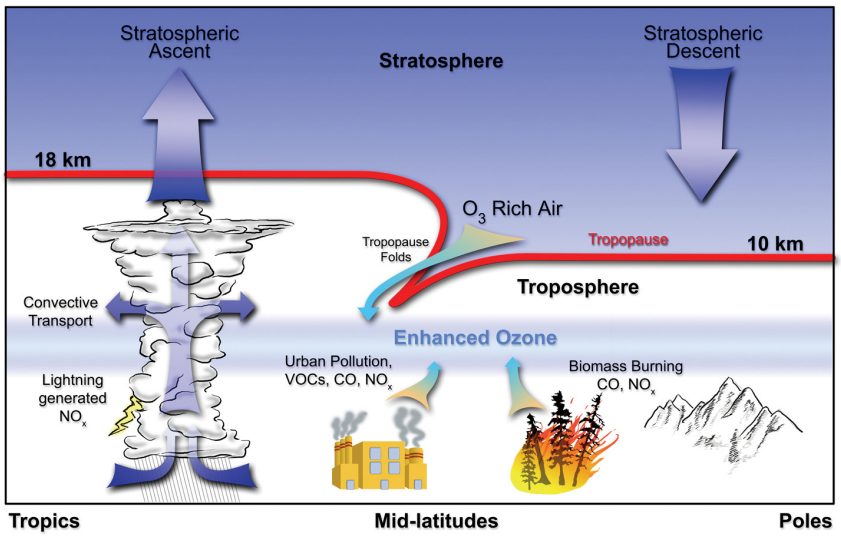

FIGURE 1.2. Biomass burning and industrial activity produce carbon monoxide (CO) and volatile organic compounds (VOCs) which are oxidised to form ozone. Figure taken from http://earthobservatory.nasa.gov.

There are two primary sources of tropospheric ozone. Either ozone is transported down from the stratosphere or it is created in-situ through the photolysis of nitrogen dioxide (NO_2) into nitric oxide (NO) and O, the latter which then reacts with O_2 to form O_3. For these reactions to be effective at producing tropospheric O_3, another oxidant is needed to oxidise NO back to NO_2 without the consumption of O_3. In all but the most pristine parts of the troposphere, NO forms NO_2 by radical chemistry involving HO_2 (Eqn. 1.3).

This reaction process is summarised below:

$$NO_2 + hv \longrightarrow NO + O \tag{1.1}$$
$$O + O_2 \longrightarrow O_3 \tag{1.2}$$

$$HO_2 + NO \longrightarrow OH + NO_2 \tag{1.3}$$

$$OH + CO \longrightarrow H + CO_2 \tag{1.4}$$
$$H + O_2 \longrightarrow HO_2 \tag{1.5}$$

Carbon monoxide plays a large role in the atmosphere. Not only is it harmful to humans [US-EPA, 1995], it is also significantly involved with the distribution of the OH radical. OH plays a major role in atmospheric chemistry and as in many areas the removal of OH is controlled by CO it becomes extremely important. CO controls the OH levels and hence the oxidising capacity of the atmosphere [Bloss et al., 2005].

In Equation 1.4 the reaction between CO and OH produces a hydrogen atom which in the atmosphere immediately reacts with O_2, to give HO_2. A similar situation occurs for hydrocarbons. Taking methane (CH_4) as an example hydrocarbon, the following reaction process may occur [Wayne and Wayne, 1996]:

$$OH + CH_4 \longrightarrow CH_3 + H_2O \tag{1.6}$$
$$CH_3 + O_2 + M \longrightarrow CH_3O_2 + M \tag{1.7}$$
$$CH_3O_2 + NO \longrightarrow CH_3O + NO_2 \tag{1.8}$$
$$CH_3O + O_2 \longrightarrow HCHO + HO_2 \tag{1.9}$$
$$HO_2 + NO \longrightarrow OH + NO_2 \tag{1.10}$$

$$NO_2 + hv \longrightarrow NO + O\,^3P \tag{1.11}$$

$$O\,^3P + O_2 \longrightarrow O_3 \tag{1.12}$$

Both CH_3O_2 and HO_2 peroxy radicals are created as a result of the reactions and are able to oxidise the NO to NO_2 which in turn leads again to the production of more O_3 as in Equations 1.1 - 1.3. The above demonstrates how organic compounds play a key role in the chemistry of ozone and hence in tropospheric chemistry in general.

Figure 1.3 details the reactions which take place and lead to both the removal of CO and the oxidation of NO to NO_2 by the HO_2 peroxy radical.

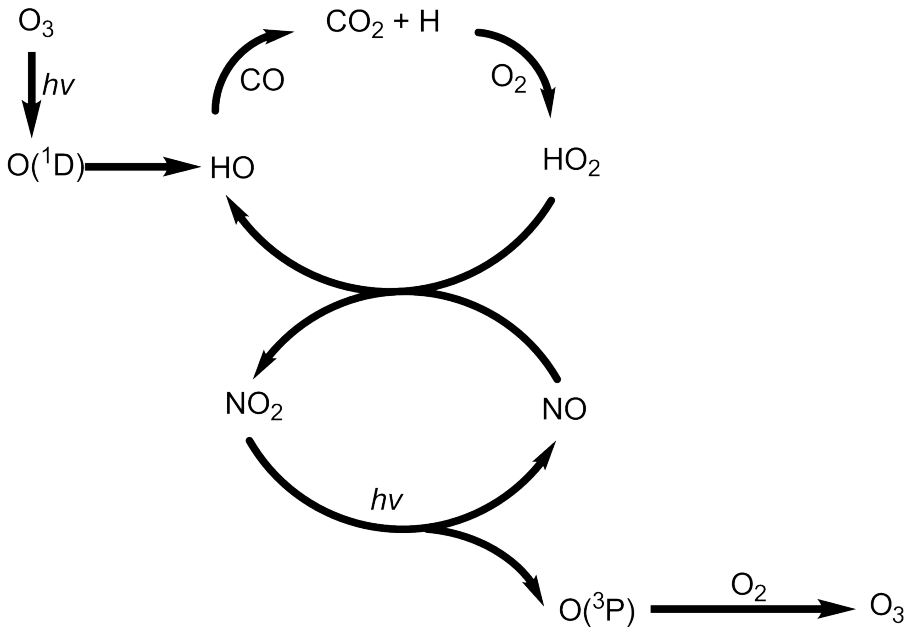

FIGURE 1.3. Tropospheric chemistry reactions involving CO and OH leading to the production of O_3. The peroxy radical (HO_2) oxidises NO_2 to NO, producing O which goes on to form O_3.

One of the major sources of CO is oxidation of CH_4 via formaldehyde, with 30-60% of tropospheric CO levels estimated to come from the oxidation of either methane or non-methane hydrocarbons (NMHC) [Poisson et al., 2000]. The other major sources of CO are related to the incomplete combustion from either biomass or fossil fuel burning.

As discussed above, the major CO sink is the reaction between CO and OH which accounts for approximately 80% of CO removal [Poisson et al., 2000] with the remaining sinks being due to uptake by soils and stratospheric transport.

1.3 Biomass Burning

Biomass burning is the burning of vegetation, whether living and dead. This burning is capable of releasing large quantities of gases into the atmosphere. Due to this, biomass burning is considered a major source for the injection of trace gases into the atmosphere. Whilst a large proportion of this burning is in the tropics, as much as 80%, there is a significant amount in boreal regions (45°N - 70°N) such as Alaska and Siberia [Koppmann et al., 2005].

There are many impacts of biomass burning which include the release of:

- Greenhouse gases such as carbon dioxide and methane which lead to global warming
- Chemically active gases such as carbon monoxide and hydrocarbons. These lead to the photochemical production of tropospheric ozone and acid precipitation
- Methyl bromide which can lead to the photochemical destruction of stratospheric ozone
- Atmospheric aerosols which can have severe impacts on the global climate

Major sources of biomass burning include deforestation, savanna fires, wood fuel and crop residue burning.

Savanna or agricultural burning accounts for approximately two-thirds of biomass burning with about 15% relating to biofuel and tropical forests. Approximately 40% of all biomass burning occurs in Africa, particularly on the savanna where human-induced fires account for up to 30% of all tropical biomass burning. In addition to Africa, a further 25% of the world's biomass burning is located in South America with the rest in areas such as Siberia, Alaska, South-East Asia and Australia [Koppmann et al., 2005].

With regards to the seasonality of biomass burning, in the Northern Hemisphere biomass burning is at a maximum between February and April whilst in the Southern Hemisphere it peaks between August and October. Figure 1.4 is taken from Duncan et al. [2003] and shows the seasonality of biomass burning as identified by average biomass burning emission rate. This data was produced by considering both ATSR/AVHRR observed fire counts along with emission inventories to estimate the average emission rates.

As opposed to open biomass burning such as savanna or forest fires, the contribution from domestic fuel burning is still poorly understood but it is believed that approximately 15% of the worlds energy requirements are met by the burning of biofuel [Hall, 1991] with some sources estimating this to be as high as 25%. This figure can be understood due to the fact that almost three-quarters of the world's population use wood as their main source or energy, be it for cooking or heating. This is even more the case for Africa where almost 90% of the energy used in homes comes from wood or charcoal burning which accounts for 60% of the total energy consumption. As the population in Africa and other third world countries continues to increase, so too does the amount of biofuel burning.

1.4 C_2H_2 And C_2H_6 Sources And Sinks

1.4.1 C_2H_2

Biomass burning and combustion were thought to be the major sources of acetylene (C_2H_2) [Hegg et al., 1990; Blake et al., 1996; Whitby and Altwicker, 1978]. However,

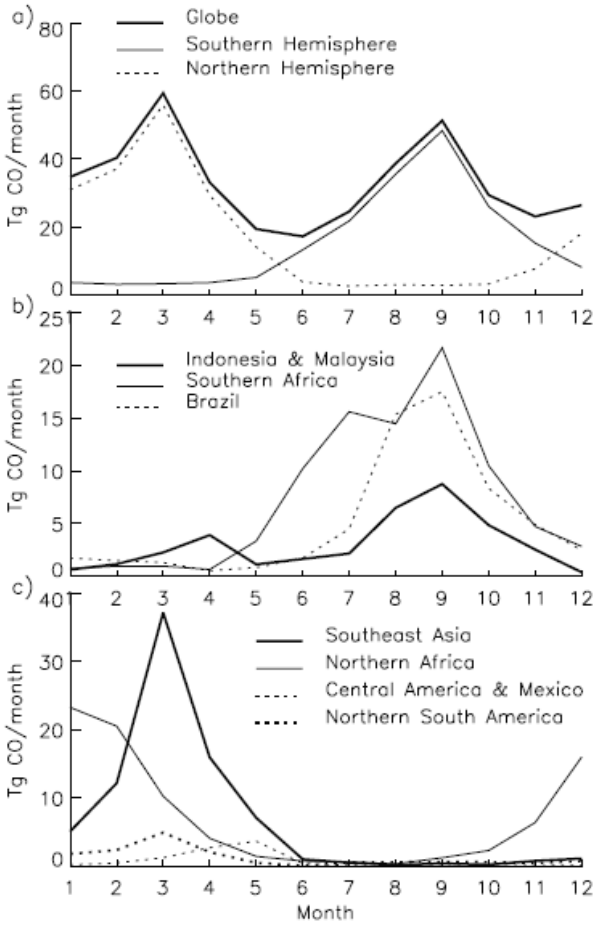

FIGURE 1.4. Average biomass burning emission rate (Tg CO / month) for the a) globe, Northern Hemisphere, and Southern Hemisphere, b) Indonesia and Malaysia, Brazil, and southern Africa, and c) Southeast Asia, northern Africa, Central America and Mexico, and northern South America. Figure taken from Duncan et al. [2003].

recent work also suggests that biofuel emissions may contribute as the dominant source of C_2H_2 with [Xiao et al., 2007] estimating that as much as half of the global C_2H_2 source is due to biofuel (3.3 Tg yr^{-1}) with the remainder being due to fossil fuel (1.7 Tg yr^{-1}) and biomass burning (1.6 Tg yr^{-1}). Streets et al. [2003] estimated from their emission study that 45% of the C_2H_2 emissions in Asia were due to biofuel (Fig. 1.6).

It should be noted that Streets et al. [2003] make a clear distinction between what they term open biomass burning (i.e. forest fires) and the combustion of biofuels (wood, crop residue, dung, etc) in domestic cooking and heating. The importance of biofuel as a C_2H_2 source has also been identified in Africa, where Bertschi et al. [2003] state that in their study of Zambia, the emission of C_2H_2 due to biofuel was significantly greater than that due to savanna biomass burning.

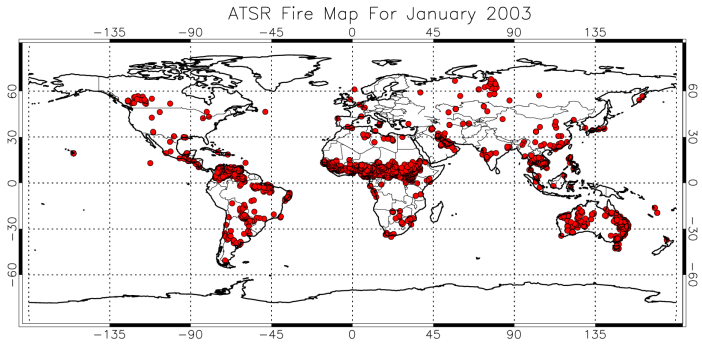

(a) January 2003

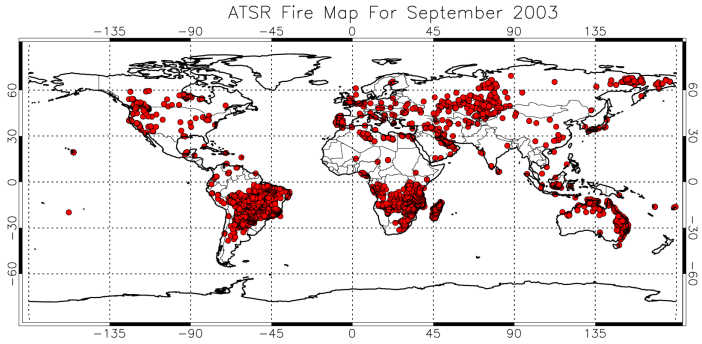

(b) September 2003

FIGURE 1.5. AATSR Fire Maps for January and September 2003 showing the distribution of fires for these periods.

As it is estimated that Asia accounts for around 70% of global biofuel emissions [Streets et al., 2003] as well as being a significant source for biomass burning and industrial emissions, it follows that Asia is the major source of C_2H_2 emissions. Africa is also an important source of C_2H_2 emissions, whether through biomass burning, fossil fuel or biofuel emissions.

Whilst C_2H_2 has been observed from both satellite [Rinsland et al., 2005] and aircraft measurements [Smyth et al., 1996; Talbot et al., 2003], there is still considerable uncertainty as to the distribution of not only C_2H_2 but non-methane hydrocarbons (NMVOCs) in general due to the poor understanding of the emissions from the large number of varying sources [Streets et al., 2003].

In addition to the interest in C_2H_2 as a tracer for the transport of biomass/biofuel burning, C_2H_2 plays an important role in the formation of glyoxal (CHOCHO) and has implications for the production of secondary organic aerosol (SOA) as discussed recently by Volkamer et al. [2008]. For this reason, the ability to accurately retrieve global distributions of C_2H_2 may also prove important for future air quality and climate simulations.

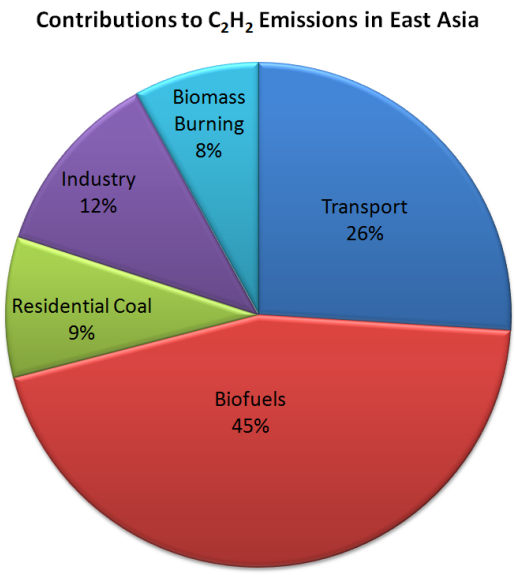

FIGURE 1.6. Contributions to the C_2H_2 emissions in East Asia. Adapted from Streets et al. 2003.

1.4.2 C_2H_6

Typical ethane (C_2H_6) mixing ratios in the troposphere range from below one part per billion up to a few parts per billion. This is approximately three orders of magnitude less than those of methane but ethane is still the second most abundant organic trace gas in the background troposphere. The importance of ethane to tropospheric chemistry lies in the fact that it is both a reactive species and is capable of forming more complex intermediates such as acetic acid, acetaldehyde and PAN [Xiao et al., 2008].

Due to its considerable atmospheric lifetime which can exceed several months [Xiao et al., 2008], it is also possible to use ethane to study atmospheric transport and source distributions. As for C_2H_2, the reaction with OH acts as the major sink of C_2H_6.

The tropospheric distribution and budget of ethane has been studied in various works, including Rudolph [1995]. Here, longitudinally and altitudinally averaged seasonal and latitudinal profiles of the ethane mixing ratio were produced. It was found that the seasonal cycle of ethane reaches a maximum in the winter period for both hemispheres and a minima during the summer period. This seasonality was attributed to the seasonality of both the OH-radical concentrations and the biomass burning which were thought to have a significant effect.

The global emission of ethane into the troposphere due to biomass burning can be calculated from the emission ratios of ethane compared to other biomass burning products such as carbon monoxide or carbon dioxide. The ratio of ethane

to carbon dioxide emissions are estimated to be between 0.04% and 0.18% with an average value of 0.09% [Rudolph, 1995]. Based on carbon dioxide emissions related to biomass burning of 1600-4100 Tg C/yr [Crutzen and Andreae, 1990], the ratios lead to an ethane source strength between 3-10 Tg yr^{-1} with an average estimate of 6.4 Tg yr^{-1}. Using the ratios for ethane to carbon monoxide, Rudolph [1995] found a similar estimate for the ethane source strength of 2.4-12 Tg yr^{-1} with an average of 6.8 Tg yr^{-1}. Note however, the large range of uncertainty in estimated sources.

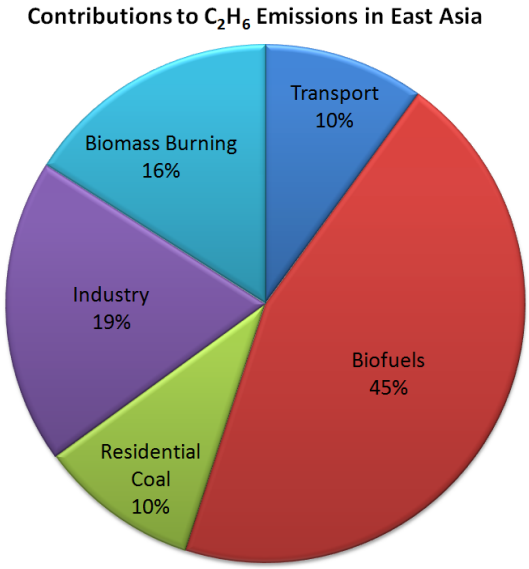

FIGURE 1.7. Contributions to the C_2H_6 emissions in East Asia. Adapted from Streets et al. 2003.

As was the case for C_2H_2, there is considerable uncertainty in the contribution of biofuel to the ethane emissions but Streets et al. [2003] suggest that for East Asia, the contribution from domestic biofuel burning may be as high as 45% with just 16% relating to biomass burning for this region.

Whilst one of the most significant sources of ethane, biomass burning is not the major ethane source. Xiao et al. [2008] estimate that as much as 60% of the global ethane budget may be related to the production of fossil fuels. Other sources not considered by Streets et al. [2003] include ocean and biogenic emissions.

Hydrocarbon emission from the ocean has been studied in detail [Ratte et al., 1995]. Although there is considerable uncertainty in these estimates, it is thought that the ocean only provides a minor contribution to the ethane budget of the atmosphere. Current estimates by Plass-Dulmer et al. [1995] place the figure at between 0.2 Tg yr^{-1} and 0.5 Tg yr^{-1}.

Biogenic emissions include those from soils, vegetation and wetlands. Through a similar process as described above, using the ratio of ethane to methane emissions

and taking an estimate of 195 Tg yr^{-1} from Lelieveld and Crutzen [1993] for wetland emissions of methane an estimate of 0.001-0.02 Tg yr^{-1} can be derived. This suggests that the contribution to atmospheric ethane from wetlands is negligible.

The ability to quantify the effect of soil emissions on the ethane budget is limited by a lack of data but it has been suggested by Hahn et al. [1992] and Rudolph [1995] that soil emissions may be of a comparable magnitude to the total NMHC emissions from certain crops in the United States, meaning that they may prove a significant contribution to the ethane budget. Likewise, there are similar difficulties in estimating the effect of vegetation emissions on the ethane budget, despite attempts to quantify this effect [Hahn et al., 1992].

The last process which may have a significant effect on the ethane budget is the escape of natural gases. The methane loss from natural gases due to anthropogenic activities such as oil drilling is estimated by Lelieveld and Crutzen [1993] to be 80 Tg yr^{-1} 45 Tg yr^{-1}. In addition to this, a further 35 Tg yr^{-1} of fossil methane is estimated to be emitted due to coal mining. This leads to an estimation for the global ethane emission of 2.6 Tg yr^{-1} to 11 Tg yr^{-1} with an average value of 6 Tg yr^{-1}.

During the course of this thesis, work undertaken by Xiao et al. [2008] has examined the global budget of ethane through the use of a chemical transport model (the GEOS-CHEM CTM) and has produced an estimate for the global emissions of ethane of 13 Tg $yr^{-1}$with 8 Tg yr^{-1} being attributed to fossil fuel production, 2.6 Tg yr^{-1} from biofuel combustion and just 2.4 Tg yr^{-1} from biomass burning with over 80% of the emissions occurring in the Northern Hemisphere.

The above demonstrates that whilst biomass and biofuel burning are large sources of ethane emissions, natural gas production may also prove to be significant but with a much greater uncertainty and fossil fuel production should be taken into account when interpreting the C_2H_6 distributions. Figure 1.8 shows the natural gas production by country and agrees with the statement that the majority occurs in the Northern Hemisphere.

Focusing on North and Central America in particular, Figure 1.9 shows the sedimentary basins and major oil and gas fields in North America. Particularly large "supergiants" are situated both on the Mexican coast as well as in Texas. It may be expected that the C_2H_6 signatures from these facilities might be observed in MIPAS data assuming that the necessary convective mechanisms were in place to uplift the C_2H_6 to sufficient altitudes. This will be explored more in Chapter 6.

1.5 The Asian Monsoon

The influence of the Asian monsoon on the distribution of atmospheric trace gases is one of the key issues investigated in this thesis. At its peak in the Northern Hemisphere summer season, the Asian summer monsoon extends from the Middle East region to South-East Asia and can act as a significant barrier to zonal transport.

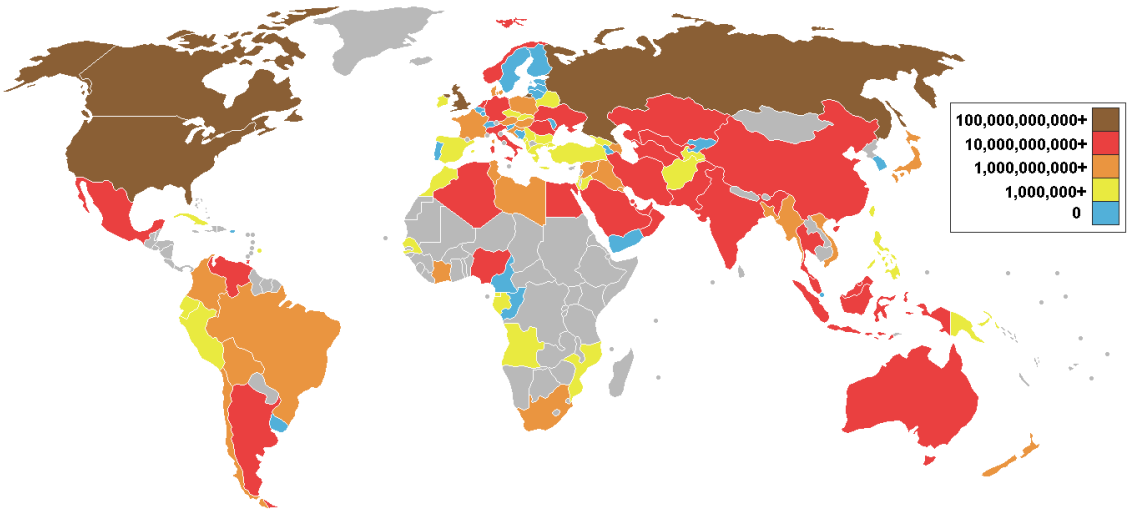

FIGURE 1.8. Map of natural gas production in cubic metres per year from CIA World Factbook figures assessed in 30 March 2006.

During April, weak convection is present over India related to the subsiding air along the equator and the weather over Northern India becomes hot and dry. Typically this leads to mean temperatures in Delhi increasing from 23°C in March to 33°C in May. This heating over the northern Indian subcontinent causes the hot air to rise, leading to low pressures over the region. This in turn causes the colder air over the India Ocean to be drawn into a low pressure system, where its movement is limited by the Himalayas. As this air rises and cools, it leads to the precipitation associated with the monsoon.

As we continue into July, the monsoon anticyclone expands to cover large regions of South and South-East Asia with a strong easterly jet at 150 mb extending westwards over Saudi Arabia and Africa.

The deep convection located over India and South-East Asia which drives the anticyclone can also quickly transport trace gases from the surface where they become isolated within the anticyclone circulation in the upper troposphere - lower stratosphere (UTLS).

There have been several studies utilising model, aircraft and satellite remote sensing data to examine the effects of the Asian Monsoon anticyclone and the resulting transportation, convection and isolation. The following sections will briefly describe some of this work.

1.5.1 Ozone Maximum (Li et al, 2001)

Previous work concerning atmospheric composition in the Middle East region has identified an ozone maximum [Li et al., 2001] in simulated model data which is

FIGURE 1.9. Sedimentary basins and major oil and gas fields of North America. Source Encyclopedia Britannica

consistent with commercial aircraft measurements in the region. When discussing the source of this maximum, Li et al. [2001] note the large contribution from upper tropospheric production related to the large-scale subsidence over the region.

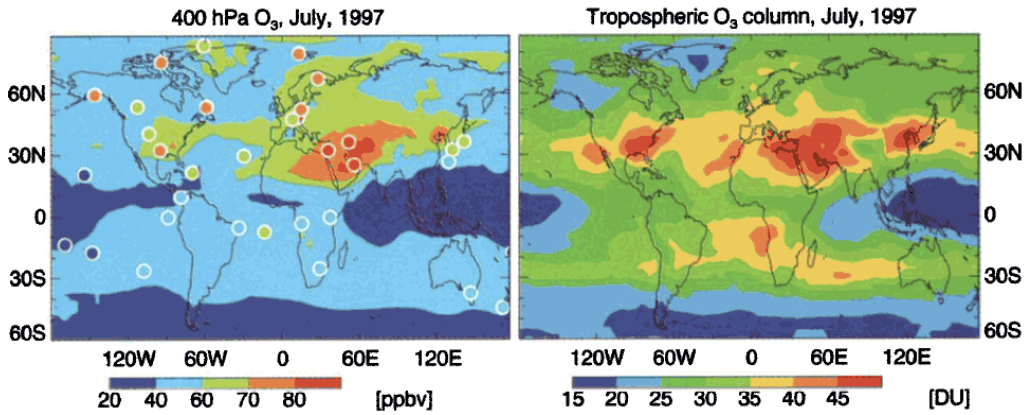

FIGURE 1.10. GEOS-Chem simulated monthly mean O_3 for 400 hpa level (left) and tropospheric column (right) showing the O_3 maximum located over the Middle East. Figure taken from Li et al. [2001].

In terms of anthropogenic contributions, Li et al. [2001] deduce that the anticyclonic circulation funnels northern mid-latitude pollution from Europe and North

America transported in the westerly subtropical jet as well as pollution from eastern Asia transported by the easterly jet.

1.5.2 Mountain Venting - Kar et al. [2006]

In addition to the O_3 enhancements discussed above, a CO maximum in this region has been observed from satellite data [Kar et al., 2006] and is believed to be due to the effect of mountain venting by thermal winds caused by strong daytime differential heating, allowing fast transport from the surface into the troposphere.

Kar et al. [2006] observed enhanced CO over the Zagros mountains in Iran from MOPITT satellite data. This enhancement was seen to follow the local topography (Fig. 1.11) and it was concluded that the phenomenon was due to mountain venting of the boundary layer air by thermal winds related to the strong daytime differential heating.

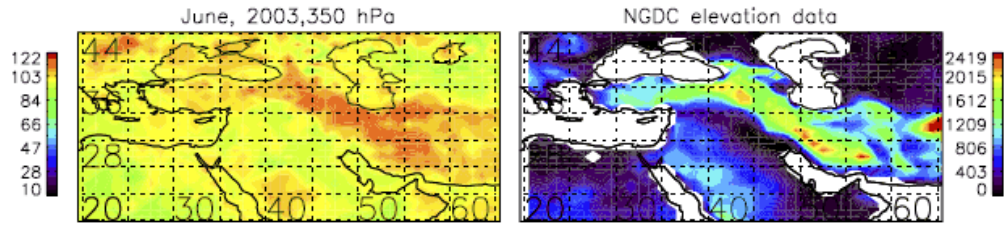

FIGURE 1.11. MOPITT CO for June 2003 at 350 hpa (left) and NGDC elevation data (right) showing the apparent signature of mountain venting in the CO distribution. Figure taken from Kar et al. [2006].

Care must be taken as there has been no such mountain venting signature observed from other satellite measurements such as MLS. Despite this, if correct these observations are the first identification of mountain venting from satellite data and may have important implications for the pollution scenarios both locally as well as over the entire monsoon anticyclone region. Henne et al. [2004] have previously performed model studies showing the potential importance of mountain venting on European pollution export.

1.5.3 Monsoon Chemical Isolation - Park et al. [2008]

During the course of this thesis, following on from previous work examining the monsoon anticyclone with data from the Aura Microwave Limb Sounder (MLS) [Park et al., 2007], Park et al. [2008] have used data from the Atmospheric Chemistry Experiment Fourier Transform Spectrometer (ACE-FTS) instrument [Bernath et al., 2005] to examine the chemical isolation inside the monsoon anticyclone.

Due to the high signal-to-noise ratio (SNR) obtained from the solar occultation technique as well as its high spectral resolution, ACE-FTS can measure a wide variety of compounds. CO, HCN, C_2H_6, C_2H_2, CH_3CL and OCS profiles were all examined. The data was separated between those profiles deemed to be within the monsoon anticyclone and those outside of its influence. Significant enhancements were observed for the profiles within the anticyclone, typically around 15 km (Fig. 1.13)

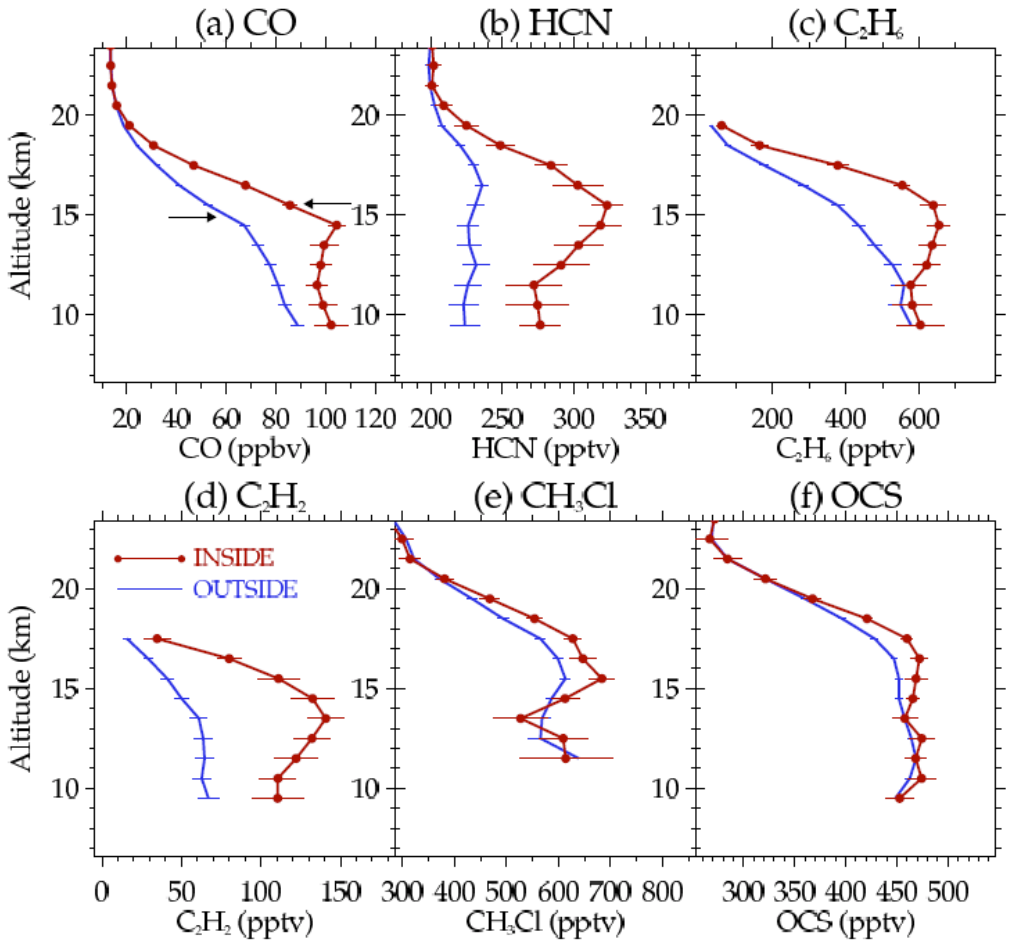

FIGURE 1.12. Average profiles of a variety of tropospheric tracers measured by ACE (CO, HCN, C_2H_6, C_2H_2, CH_3CL and OCS) inside (red) and outside (blue) the monsoon anticyclone. Figure taken from Park et al. [2008].

A strong correlation is observed between the CO and C_2H_2 with a distinct difference in the slope inside and outside of the anticyclone. This ratio of C_2H_2/CO suggests that the anticyclone contains relatively younger air than that outside of the anticyclone.

This use of a C_2H_2/CO ratio is discussed in more detail in Section 1.7 and is

utilised to examine the relative photochemical age of air from the C_2H_2 retrievals performed in this thesis (Section 6.1).

Although as discussed above, ACE provides an extremely high SNR ideal for the retrieval of these compounds, one issue with the solar occultation technique is the limited number of profiles that can be measured in a day. In addition to this, the majority of occultations occur at high latitudes, resulting in poor coverage over the tropics. In order to account for this and obtain adequate spatial coverage, it was necessary for Park et al. [2008] to take all data from June until August for three years of ACE data (2004-2006). Even then, data over the anticyclone region was limited to approximately 30 measurements which is not ideal when attempting to examine the monsoon activity at a high spatial and temporal resolution.

The work in this thesis addresses some of these issues. Although the Michelson Interferometer for Passive Atmospheric Sounding (MIPAS) does not have as high SNR as ACE and hence retrievals can prove considerably more difficult, the increase in both spatial and temporal resolution is vital for examining the effects relating to the anticyclone.

1.5.4 Air Pollution Crossroads Over The Mediterranean - Lelieveld et al. [2002]

In addition to the use of satellite data, aircraft and ground-based measurements have been performed relating to the monsoon anticyclone.

Lelieveld et al. [2002] examine the Mediterranean region as part of the Mediterranean Intensive Oxidant Study (MINOS) in summer 2001.

It was found that the Mediterranean region acts as a "crossroads" for global air pollution with Asian and North American pollution from the west and further Asian pollution from the east due to the Asian monsoon anticyclone.

The observed Asian pollution was found to contain enhanced C_2H_2, PAN, CH_3CN and CH_3Cl indicating a strong contribution from Asian biomass and biofuel burning. This pollution was transported over Africa and then northwards towards the Mediterranean by the anticyclone. This pollution was also found to reach the lower stratosphere, leading to further stratospheric pollution at high latitudes.

This work has not only identified the significant role of the Asian monsoon anticyclone in transporting Asian pollution to the Mediterranean region but also the role of the anticyclone in stratospheric pollution.

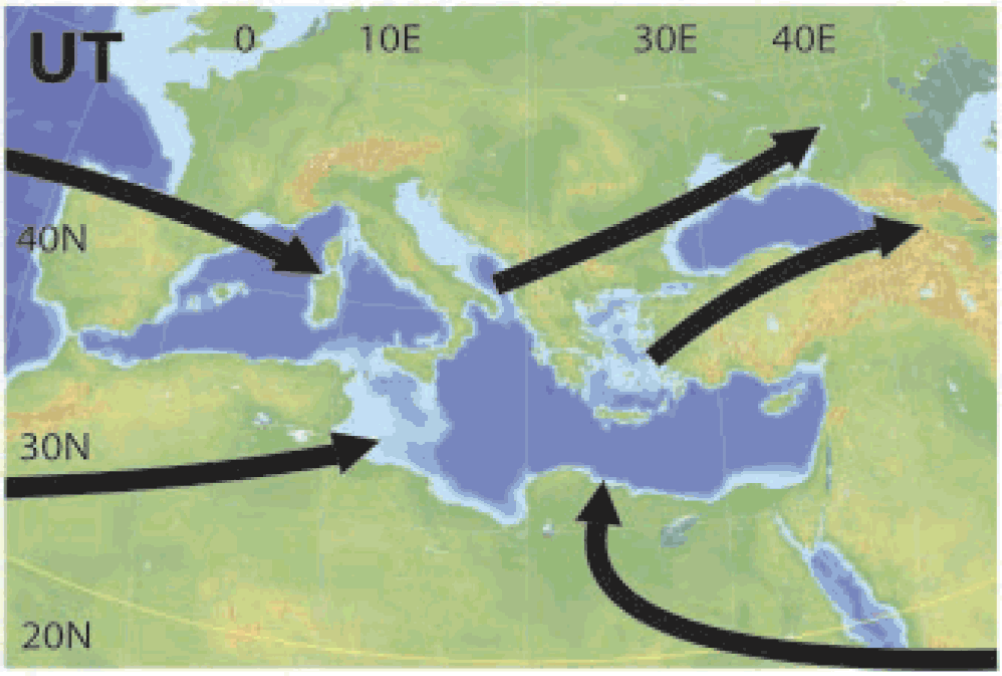

FIGURE 1.13. Schematic of air mass trajectories in the upper troposphere over the Mediterranean during the MINOS campaign. Figure taken from Lelieveld et al. [2002].

1.6 Using Molecular Pairs (C_2H_2/CO) As Indication Of Photochemical Age Of Air/Transport

The distribution of trace gases in the atmosphere is generally affected by three processes. These are production/emission, transportation and loss. As light hydrocarbons such as C_2H_2 and C_2H_6 can have similar source and loss mechanisms (i.e. OH) but with a variety of atmospheric lifetimes they prove ideal for sampling transport processes over a variety of different timescales. When the concentrations of such species are ratioed, this negates some of the dependence on transport and sources and instead allows the chemical loss rates to be examined.

One example of this is the ratio of C_2H_2/CO. Due to the fact that C_2H_2 and CO have common sources relating to combustion and that both are removed by reaction with the OH radical, they are often found to remain highly correlated in the atmosphere and therefore the combination makes an ideal "photochemical clock" to time transport processes as described by Parrish [1992]; McKeen and Liu [1993]; Smyth et al. [1996].

As described in Smyth et al. [1996], in the simple case where the photochemical processing with the OH radical is the only effect acting to change the hydrocarbon's concentration, the timescale of the reaction can be expressed as

$$\Delta t = \frac{ln(C_0/C_t)}{k_c[OH]} \tag{1.13}$$

with C_0 and C_t the concentration of the species at an initial time (0) and a later time (t) and k_c is the reaction rate coefficient of the species with OH. Smyth et al. [1996] further extends this concept in an attempt to remove the dilution of pure air effects due to transport by using a combination of species with similar sources (in this case biomass/biofuel burning) and sinks (e.g. reaction with OH). Using the above example of C_2H_2 and CO, Equation 1.13 now becomes

$$\Delta t = \frac{ln((C_2H_2/CO)_0/(C_2H_2/CO)_t)}{(k_{C_2H_2} - k_{CO})[OH]} \tag{1.14}$$

Unfortunately rather than the simple dilution with pure air, in reality the air mass will undergo dilution involving air with non-zero amounts of the species considered and hence Equation 1.14 is no longer strictly valid but the ratio of C_2H_2/CO will still provide qualitative information on the atmospheric processing the airmass has undergone.

The above has discussed how the VMR of C_2H_2 is strongly correlated to CO [Wang et al., 2004] and the ratio of the two can be used as a robust tracer for the age of the air mass since it last encountered a combustion source [Xiao et al., 2007] due to the relatively long life-times involved and the fact that the correlation remains strong over this period. In favourable cases, this allows the relative age of

biomass plumes to be estimated as well as the amount of photochemical processing they have undergone [Xiao et al., 2007; Smyth et al., 1996, 1999].

Note that some care must be taken when utilising C_2H_6, as it differs from most other hydrocarbons in that its primary source is natural gas production rather than combustion [Xiao et al., 2008] although it is still emitted from biomass burning and may prove useful as both a biomass burning tracer as well as an indicator for fossil fuel production.

1.7 Summary

This chapter has detailed some of the areas to be explored through the work in this thesis. Biomass burning observations from satellite data, in particular the distribution of C_2H_2 and C_2H_6 and the effect of the Asian monsoon anticyclone are areas in which further work is required as there is a considerable lack of knowledge of the regional and global upper-tropospheric distributions of these hydrocarbons.

The work in this thesis aims to first and foremost show that it is possible to identify enhancements of these key hydrocarbons from MIPAS satellite observations with a higher temporal and spatial resolution than has previously been possible. In order to achieve this, in addition to the use of an optimal estimation retrieval scheme, the development of a fast detection algorithm allows the seasonality in the distributions to be examined.

A particular focus is placed on the effects of the Asian monsoon on the distribution and transport of these species and the resulting chemical isolation over Asia and the Middle East.

The successful retrieval of C_2H_2 and C_2H_6 will allow the use of ratioing against CO to determine the relative photochemical age of air which will aid in the understanding of the large-scale transport of biomass burning species as well as the natural gas production emissions of C_2H_6.

This remainder of this thesis is structured as follows:

- Chapter 2 - Basic theory relating to radiative transfer and spectroscopy is outlined. Comparisons between the spectroscopic data available for C_2H_6 from the two main spectroscopic databases are shown as well as the results of preliminary spectroscopic measurements of C_2H_6 performed as part of this thesis. The retrieval theory to be used later in this thesis is also introduced.

- Chapter 3 - The Michelson Interferometer for Passive Atmospheric Sounding (MIPAS) instrument is introduced in detail with particular focus on data processing and performance of the instrument. Here the different retrieval schemes are discussed and an argument is made for the use of the MIPAS Orbital Retrieval using Sequential Estimation (MORSE) retrieval scheme.

- Chapter 4 - The development of a fast detection algorithm is described along with global distributions for both C_2H_2 and C_2H_6. The formation of the Asian monsoon anticyclone is discussed in detail.

- Chapter 5 - The quality of the retrieval results are discussed in detail and then compared to the results of the detection algorithm, both globally and over regions of interest.

- Chapter 6 - C_2H_2 and C_2H_6 retrievals are compared to CO data from the MOPITT instrument in order to show that the species remain correlated through various dynamical processes and hence qualitative photochemical age of air information can be obtained. The vertical distribution of C_2H_2 is examined in more detail by both zonal and meridional plots taken across the various regions of interest. In addition, the C_2H_2/C_2H_6 ratio is used to differentiate between sources of biomass burning and fossil fuel production.

- Chapter 7 - Conclusions from the current work are presented as well as suggestions for future work.

Chapter 2

Spectroscopy And Radiative Transfer Relating To C_2H_2 And C_2H_6

2.1 Thermal Infrared Radiative Transfer In the Atmosphere

The remote sensing of characteristics of the Earth's atmosphere such as temperature profiles or trace gas concentrations is achieved through the measurement of emitted, reflected, transmitted and scattered radiation. In the case of this thesis, the thermal infrared region of the spectrum is utilised. Therefore an understanding of the processes relating to the thermal infrared radiative transfer of the atmosphere is vital when employing remote sensing instruments to obtain information about the trace gas concentrations in the atmosphere.

In the infra-red, the fundamental Planck Function:

$$B_v(T)dv = \frac{2h\nu^3}{c^2(exp(h\nu/kT) - 1)} \tag{2.1}$$

describes the emitted source radiation distribution of a black body as a function of frequency at a given temperature T, typically the temperature of the Earth.

A remote sensing instrument will not only measure all the radiation passing through the atmosphere within its field of view but also radiation emitted along the viewing path by atmospheric molecules, or scattered by clouds and aerosols. This can be viewed most easily for the thermal infrared, considering radiative transfer in the nadir direction. The true atmosphere is composed of continuous vertical profiles of gas, not just one layer, i.e. the atmosphere is separated into a number of layers, each of which absorb and re-emit radiation. The atmosphere can therefore be considered as a series of layers. The radiative transfer through each of these

atmospheric layers can be defined by the Schwarzschild Equation in LTE (Eq. 2.2), which (when neglecting scattering) takes the form:

$$dI_\nu = -k_\nu I_\nu dz + k_\nu B(\nu, T)\rho dz \tag{2.2}$$

where I_ν is the intensity of radiation at frequency ν, k_ν is the absorption coefficient, ρ is the density of the medium as a function of the distance travelled z and B_ν is the Planck Function (Eq. 2.1).

In the nadir case, the observed intensity at some frequency at a particular height, z, is then obtained by integrating (Eq. 2.2) over the complete vertical path travelled by the radiation through the atmosphere.

$$I_\nu = \varepsilon_s B(\nu, T_s)\tau(\nu) + \int B(\nu, T_z)(d\tau(\nu, \rho, T_z)/dz)dz \tag{2.3}$$

Here the first term is the emission from the surface attenuated by the transmission from the Earth to space. The second term weights the Planck Function (Eq. 2.1.3) at each layer by the transmission at that layer and determines the contribution of that layer to the total measurement. Therefore the dependence on the transmission of each layer is determined by the $\int B(\nu, T_z)(d\tau(\nu, \rho, T_z)/dz)dz$ term in Equation 2.3 [Stephen, 1994]. This function $d\tau(\nu, \rho, T_z)/dz$ is known as the weighting function. The weighting function defines the contribution to the intensity measurement due to emission from a layer centred on a specific altitude.

The equation derived so far is appropriate for a nadir sounder such as the Measurement Of Pollution In The Troposphere (MOPITT) instrument. The shape of the weighting function is determined by the decrease in absorbing gas with height and the increase in transmission due to the path decreasing when approaching the satellite altitude. These two factors combine to give bell-shaped weighting functions for nadir thermal emission sounding as shown in Figure 2.1.

The width of the weighting function indciates the vertical resolution of the retrieval. Typically for nadir sounding instruments the vertical resolution is between 5 km and 15 km. Higher resolutions are achieved for a few gases such as water vapour and ozone.

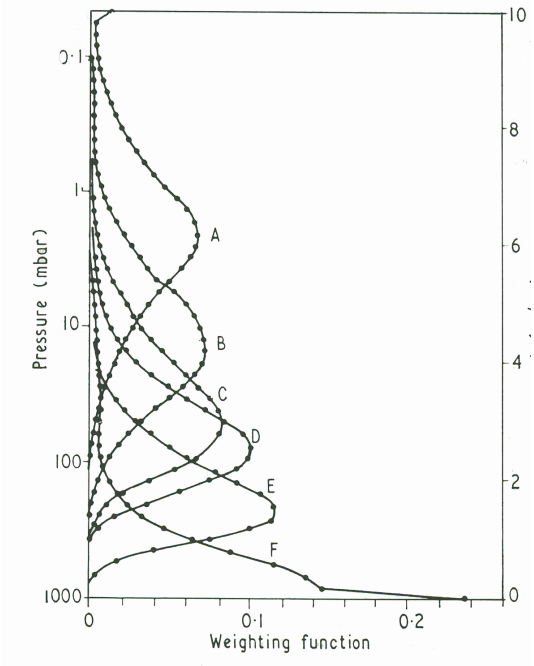

(a) Nadir

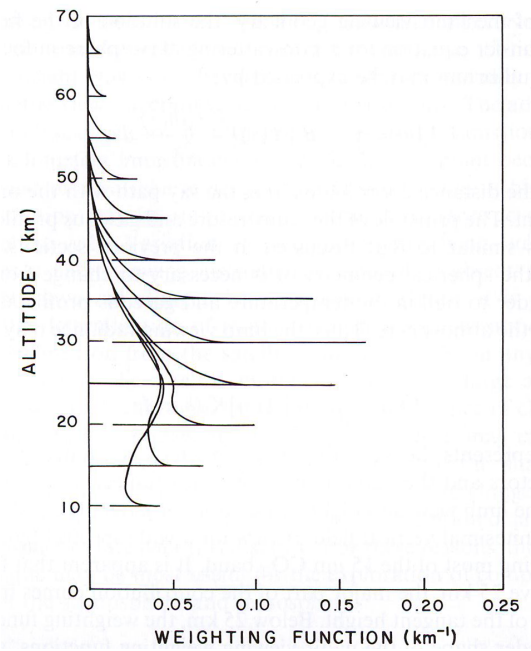

(b) Limb

FIGURE 2.1. Examples of a nadir-sounding and limb-sounding weighting functions. Figures taken from Houghton et al. [1984].

2.1.1 Limb Sounding

The above description is useful because measurements made via both limb-viewing and nadir-viewing instruments are used in this thesis. However, this thesis primarily relates to the MIPAS instrument which observes the atmosphere with a limb-viewing geometry (see Chapter 3).

For a limb sounding instrument, such as MIPAS, the measured intensity (expressed as the integral of the emission along a path) is defined by the tangent height of the measurement.

The Schwarzschild Equation for limb sounders is altered significantly from Equation 2.2. For thermal emission the first term disappears or refers to an external source such as the sun and leaves only the second term relating to the emission from each layer [Liou, 1980]. Therefore the equation becomes

$$I_\nu = \int B(\nu, T_x)(d\tau(\nu, \rho, T_x)/dx)zdx \tag{2.4}$$

where the distance is no longer the altitude, z, but the distance along the limb path, x.

As noted above, this means that in contrast to the nadir measurements, the majority of the observed signal for limb measurements comes from the tangent height. There is little or no influence from the layers below the field-of-view of the lowest tangent altitude or from the surface.

The resulting differences in weighting function lead to several distinct advantages for limb sounding over nadir sounding of emission. These include sharper weighting functions, peaking at the tangent altitudes leading to relatively high vertical resolution (typically 1 to 5 km), negligible surface influence on the measurements in the absence of cloud scattering and a considerably increased path length resulting in far more emissions along the path.

2.2 Spectroscopy

In the Schwarzschild Equation (Eq. 2.2), the term k_ν, relates to the interaction of the molecules with radiation. When a transition occurs between molecular energy levels, the resulting emission or absorption of a photon can be observed via the spectral lines produced.

In the infrared region of the spectrum, these lines are primarily produced by vibrational and rotational transitions within a molecule. It is these transitions which are typical of molecules in the atmosphere and which it is possible to observe through the use of spectroscopic instruments such as MIPAS.

These transitions are governed by the equation $\Delta E = h\nu$ where the difference in energy between levels is related to the frequency. For vibrational transitions this

energy difference is of comparable size to the energy of infrared radiation whereas the energy difference for rotational transitions is much smaller.

In reality, these two processes occur simultaneously and result in infrared bands at the frequency of the vibrational transition containing rotational fine structure.

2.2.1 Rotational Transitions Of Molecules

All molecules contain three mutually perpendicular axes through their centre of gravity and it is the inertia around these axes that defines the molecular rotation of the molecule. The inertias around axes A,B and C are labelled I_A, I_B and I_C respectively with the axes defined such that $I_A \leq I_B \leq I_C$. Molecules are then categorised by the relationship of these values relative to each other.

- Linear molecules; have one moment of inertia equal to zero with the other two equal ($I_A = 0, I_B = I_C$), e.g. CO_2, C_2H_2.
- Symmetric top; e.g. C_2H_6, are sometimes also called rotor molecules, these have two equal moments of inertia with the other different but non-zero. Depending on which two moments of inertia are equal, this category is subdivided into the prolate symmetric top ($I_A \leq I_B = I_C$) and oblate symmetric top ($I_A = I_B \leq I_C$).
- Spherical top; have all three moments of inertia equal ($I_A = I_B = I_C$); e.g. CH_4.
- Asymmetric top; these have all three moments of inertia finite and different from each other ($I_A \neq I_B \neq I_C$). The majority of molecules belong to this class.

For purely rotational transitions, the energies are typically in the microwave region of the spectrum. These energies can in principle be calculated theoretically from the Schrödinger equation and the quantum number selection rules.

2.2.2 Vibrational Transitions Of Molecules

The number of fundamental vibrations of a molecule is determined by the number of degrees of freedom the molecule has and is therefore related to the number of atoms in the molecule.

A molecule containing N atoms has 3N degrees of freedom in total. Three of these are required to describe the translational motions of the molecule and if the molecule is non-linear an additional three are required to describe the rotational motion. If the molecule is linear, the rotational motion can be described by just two degrees of freedom, rather than three.

After these motions have been accounted for, the remaining degrees of freedom are all due to the vibrational motions. Therefore for non-linear molecules there are 3N-6 degrees of freedom associated with vibrational transitions whilst for linear molecules there are 3N-5.

2.2.3 Vibrational-Rotational Bands

As the energy for rotation to occur is much less than that for vibration, whenever there is a vibrational transition there will be an accompanying simultaneous rotational transition. For each vibrational transition, several rotational transitions can occur from different populated levels. As the separation between rotational energy levels is much smaller than that of the vibrational levels, the rotational transitions are grouped closely together, forming a vibration-rotation band [Brown, 1998].

The selection rules which govern the transitions lead to three types of transitions being allowed. These three types of resulting vibrational-rotational bands are generally termed P, Q and R branches. The C_2H_2 spectra contains a strong Q-branch between 604 cm^{-1} and 870 cm^{-1} as discussed in Section 2.3.1.

2.2.4 Line Intensities

In Section 2.1, the absorption coefficient $k(\widetilde{\nu})$ was introduced. The line intensity, S, of a spectral line is defined as

$$S = \int k(\widetilde{\nu}) d\widetilde{\nu} \tag{2.5}$$

integrated over the spectral line and depends on the number of molecules capable of making the transition and the absorption coefficient relating to the transition.

This can be derived using the Einstein coefficient for induced absorption and stimulated emission and will depend on the population of the states between which the transition takes place (governed by the Boltzmann distribution) and the transition probability. For a vibration-rotation line for a transition from some state i to a state j, the line intensity for a single molecule is given by

$$S_{line} = \frac{8\pi^3 \tilde{\nu}_{ji}}{4\pi\varepsilon_0 3hcQ} exp\left(\frac{-E_i}{kT}\right)\left(1 - exp\left(\frac{-hc\tilde{\nu}_{ji}}{kT}\right)\right) S_{ij} \tag{2.6}$$

where Q is the partition function, E_i is the energy of the lower state and S_ij is the line strength, which is defined as the square of the transition moment relative to an axis fixed in space.

2.2.5 Line Widths And Broadening

The spectral lines in the atmosphere are broadened due to a number of factors and there are several distinct types of broadening to consider in the Earth's atmosphere. Doppler and collisional broadening, as well as natural, all affect the intensity and width of a spectral line. The natural broadening due to the Heisenberg Uncertainty Principle is generally negligible and it is the collisional and Doppler broadening that must be considered when examining the spectral lines of atmospheric molecules.

The shape factor is defined as

$$\int_{-\infty}^{\infty} f(\nu - \nu_0) d\nu = 1 \tag{2.7}$$

and represents the relative absorption at a frequency displaced by $\nu - \nu_0$ from the centre of the line.

The equation for Doppler broadening is given by

$$f_D(\nu - \nu_0) = (\pi \alpha_D)^{-\frac{1}{2}} exp\left(\frac{-(\nu - \nu_0)^2}{{\alpha_D}^2}\right) \tag{2.8}$$

where α_D is related to the molecular mass and root mean square speed of the molecule being considered.

Doppler broadening is the result of a shift in the frequency of the emitted radiation due to the random motion of the molecules. In the troposphere, whilst Doppler broadening may have an effect, it is the collisional broadening that dominates.

Collisional broadening, also referred to as pressure broadening, is due to the collision between molecules and the subsequent transition between energy levels that results in a broadening of the spectral lines. Collisional broadening is described by the Lorentz line shape, given below

$$f_L(\nu - \nu_0) = \frac{\alpha_L/\pi}{(\nu - \nu_0)^2 + {\alpha_L}^2} \tag{2.9}$$

Where α_L relates to the mean time between collisions and is referred to as the Lorentz half-width.

2.2.6 The Voigt Lineshape

In reality, atmospheric spectral lines are affected by both Doppler and Lorentz broadening. The effect of Lorentz broadening dominates at lower altitudes, whilst Doppler broadening has a greater effect at higher altitudes where the Lorentz pressure broadening is reduced due to the decrease in pressure. For the case of mid-infrared spectra, the effects of both Lorentz and Doppler broadening become equal

around 30 km and hence in order to accurately simulate atmospheric spectra, both effects must be considered [Liou, 1992].

This combination of both the lineshape mechanisms is described by the Voigt lineshape, providing a convolution of the Doppler and Lorentz lineshapes:

$$k(\tilde{\nu}) = \frac{S}{\alpha_D\sqrt{\pi}}\frac{y}{\pi}\int_{-\infty}^{\infty}\frac{e^{-t^2}dt}{y^2+(x-t^2)} \tag{2.10}$$

where $k(\tilde{\nu})$ is the absorption coefficient at wavenumber $\tilde{\nu}$. S is the line intensity with a line centre at ν_0 and t is the duration of the emission. x and y are defined by the following:

$$x = \frac{\alpha_L}{\alpha_D} \tag{2.11}$$

$$y = \frac{(\nu-\nu_0)}{\alpha_D} \tag{2.12}$$

with α_D and α_L the Doppler and Lorentz half-widths respectively.

2.3 Spectroscopy Of C_2H_2 And C_2H_6

2.3.1 C_2H_2

C_2H_2 is a linear tetratomic molecule comprising of two carbon atoms and two hydrogen atoms. The C_2H_2 spectra contains features in the infrared region at 13.6 μm, 7.5 μm, 5 μm and 3 μm.

A strong Q-branch exists between 604 cm^{-1} and 870 cm^{-1} (13.6 μm region) relating to the ν_5 (cis-bending mode) fundamental band mode as well as additionally to five hot bands in the region [Jacquemart et al., 2003]. The 7.5 μm spectral region (between 1248 cm^{-1} and 1415 cm^{-1}) contains features associated with the $2\nu_5$ mode whilst the $3\nu_5$ mode leads to the band observed between 1810 cm^{-1} and 2255 cm^{-1}. The 3 μm spectral region related to the $5\nu_5$ mode (between 3204 cm^{-1} and 3359 cm^{-1}) also contains the two strong ν_3 (antisymmetric stretch) and ν_2 (C-C stretch) cold bands, as well as numerous hot bands although these are not within the spectral range of the MIPAS instrument.

The spectroscopic uncertainty in C_2H_2 is discussed in Jacquemart et al. [2003]. Line intensities are estimated to be accurate to approximately 5%. Although Jacquemart et al. [2003] do point to the usefulness of new measurements to confirm these errors, attention in this thesis has concentrated on the assessment of the C_2H_6 spectroscopy for which there is much greater uncertainty [Vander Auwera et al., 2007].

A microwindow is a small region of the spectra containing the relevant spectral signatures. For the work in this thesis it is the C_2H_2 microwindow between 776.0 cm^{-1} and 776.15 cm^{-1} which is used. Although the line in this window is not the strongest in the region, there are no contaminating species as there are for the stronger lines [Rinsland et al., 1998]. Further details relating to the selection of this microwindow are given in Section 4.1.1.

2.3.2 C_2H_6

C_2H_6 is of interest to spectroscopists as it is a prototype molecule for methyl rotation about a single bond [Vander Auwera et al., 2007] and can help in the understanding of these large-amplitude internal rotations.

The two strong ethane features observable in the infrared are the strong Q-branches of the ν_5 band (C-H stretch) at 2985.4 cm^{-1} and the ν_9 band (C-C bend) at 821.3 cm^{-1} [Vander Auwera et al., 2007]. It is this 12 μm ν_9 band which is used in this thesis as the spectral range of MIPAS does not include the 3 μm ν_5. It is however possible to observe this band with the ACE instrument where retrievals have already been successfully performed [Rinsland et al., 2005, 2007].

Cooper and Moazzen-Ahmadi [2006] have performed a global fit analysis of the ν_9 band and comment on how any analysis of the vibrational bands of ethane is complicated by the presence of hindered internal rotation. Significant state mixing is observed related to the high density of states associated with the low frequency of the torsional motion. Additionally, various resonant interactions occur between the lowest four vibrational states. These factors lead to the difficulty in characterising the spectroscopic parameters of C_2H_6 and may account for the discrepancies between previous measurements. An assessment of the C_2H_6 spectroscopic errors is more complicated and is discussed in the next section.

2.4 Spectral Databases

Molecular parameters such as line position, intensity, air-broadened and self-broadened half-widths are stored in databases and are available to the scientific community. There are two primary sources that are of use when considering atmospheric spectroscopy, namely the HITRAN and GEISA databases.

2.4.1 HITRAN And GEISA Databases

The HITRAN (HIgh-resolution TRANsmission molecular absorption) database is an international compilation of spectroscopic parameters. During this thesis, an updated version of the HITRAN data was released. HITRAN2004 [Rothman et al., 2005] contains the line-by-line parameters for 39 molecules (Table 2.1). In addition, infrared cross-sections are included for a number of species.

HITRAN ID	Molecule	10	NO_2	20	H_2CO	30	SF_6
1	H_2O	11	NH_3	21	HOCl	31	H_2S
2	CO_2	12	HNO_3	22	N_2	32	HCOOH
3	O_3	13	OH	23	HCN	33	HO_2
4	N_2O	14	HF	24	CH_3Cl	34	O
5	CO	15	HCl	25	H_2O_2	35	$ClONO_2$
6	CH_4	16	HBr	26	C_2H_2	36	NO^+
7	O_2	17	HI	27	C_2H_6	37	HOBr
8	NO	18	ClO	28	PH_3	38	C_2H_4
9	SO_2	19	OCS	29	COF_2	39	CH_3OH

Table 2.1. Table showing all of the molecules with line parameters present in the latest version of the HITRAN database.

The GEISA (Gestion et Etude des Informations Spectroscopiques Atmosphériques) database [Jacquinet-Husson et al., 2005] is similar to the HITRAN database, containing the line transition parameters for 42 molecules in its most recent update. Whilst traditionally HITRAN has been primarily orientated towards terrestrial applications, GEISA was primarily orientated towards planetary atmospheres. GEISA in the form of the GEISA/IASI database is now involved with assessing measurements capabilities of the Infrared Atmospheric Sounding Interferometer (IASI) instrument.

It is important to note that much of the data contained in these databases are not based on experimental measurements but are derived through calculation and hence may include significant errors. Furthermore, where the data are based on laboratory measurements there are often discrepancies between results.

For the purposes of the work in this thesis, the quality of the spectroscopic parameters for both C_2H_2 and C_2H_6 are important. These spectroscopic parameters from HITRAN are one of the key inputs into the forward model (see Section 2.5) and are vital in order to accurately simulate the atmospheric spectra. The influence of the spectroscopic errors to the final retrieval error budget will be discussed in Chapter 5.

2.4.2 Comparing HITRAN (Original And Updated) And GEISA Ethane Spectra

The current knowledge of ethane spectral parameters is not ideal, with large discrepancies between the HITRAN2004 and GEISA spectral databases. Figure 2.2 shows the line intensity taken from each of the databases for the 822.0 cm^{-1} to 823.0 cm^{-1} spectral region. Whilst the maximum intensity for ethane in this region in the HITRAN2004 database is $3.42E^{-21}$ $cm^{-1}/(molecule \cdot cm^{-2})$, the maximum for the GEISA database is just $8.68E^{-22}$ $cm^{-1}/(molecule \cdot cm^{-2})$, less than a quarter of the HITRAN2004 value.

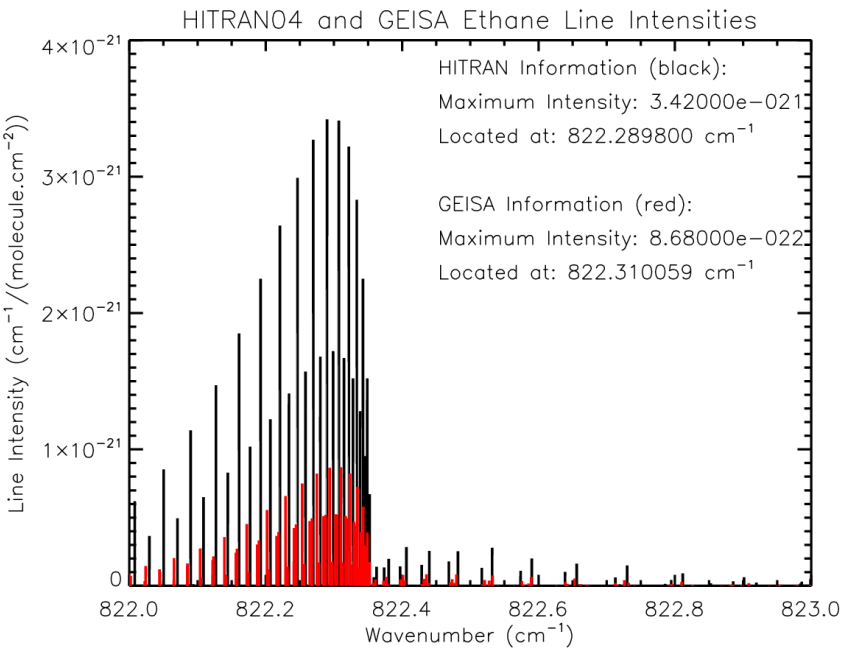

FIGURE 2.2. The intensity and position of the C_2H_6 lines in the 822.0 cm^{-1} to 823.0 cm^{-1} spectral range from both the HITRAN2004 (black) and GEISA (red) spectral databases.

It is not only the magnitude of the intensity which differs but the position of the spectral lines as well. Figure 2.3 is a logarithmic plot of the intensity which helps to highlight the difference in the position of the lines.

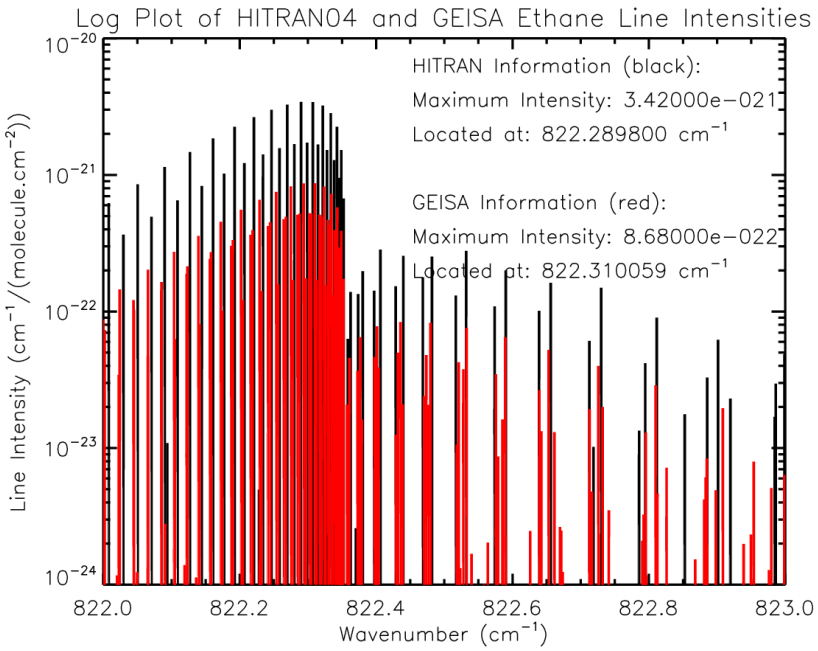

FIGURE 2.3. A logarithmic plot of the intensity and position of the C_2H_6 lines in the 822.0 cm^{-1} to 823.0 cm^{-1} spectral range from both the HITRAN2004 (black) and GEISA (red) spectral databases.

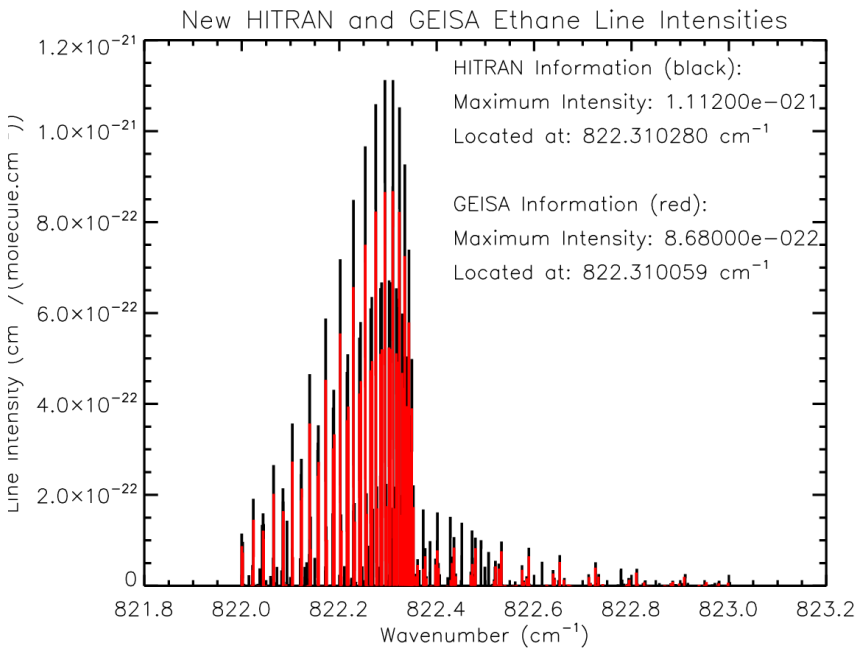

FIGURE 2.4. The intensity and position of the C_2H_6 lines in the 822.0 cm^{-1} to 823.0 cm^{-1} spectral range from both the updated HITRAN (black) and GEISA (red) spectral databases.

Total Pressure (Torr)	Total Pressure (mb)	Temperature (K)
67.8	90.4	195
119.5	159.2	215
351	467.9	250
760	1013.1	292

Table 2.2. Ethane spectroscopy measurements representative of atmospheric conditions

In order to investigate this difference further and to provide improved measurements of the ethane spectral parameters, Vander Auwera et al. [2007] have performed a series of measurements at 296 K and 278 K. It was found that the integrated band intensity calculated at 296 K for the HITRAN2004 and GEISA line lists were respectively a factor of 1.57 larger and 1.44 smaller than the values that were observed. Vander Auwera et al. [2007] proposed their own set of ethane spectral parameters for inclusion into the HITRAN databases. These have been implemented for the work in this thesis and are referred to as the"HITRAN+Update" values throughout this thesis. These updates have now been included into the HITRAN2008, just released at the time of writing.

Figure 2.4 shows a comparison between these updated line parameters and the original values in the GEISA database and it can be seen that the agreement is now much closer than it was previously in Figure 2.2.

2.4.2.1 Preliminary Ethane Lab Spectra

In order to further assess the quality of the current knowledge of ethane spectroscopy available from HITRAN and GEISA, as part of this thesis, preliminary ethane spectroscopic measurements were performed at the Molecular Spectroscopy Facility (MSF) at the Rutherford Appleton Laboratory. It was decided to concentrate on the C_2H_6 molecule as opposed to C_2H_2 due to the extent of the uncertainty in the C_2H_6 spectral parameters as shown from the conflicting data in the HITRAN and GEISA databases (see Section 2.4.2).

High spectral resolution (0.015 cm^{-1}) measurements were made at four sets of temperatures and pressures which were chosen to be representative of conditions found in the real atmosphere. These measurement conditions are shown in Table 2.2. Ethane with a minimum purity of 99.995% was used and in all of these cases an ethane pressure of 3.5 Torr was chosen in order to provide a high signal for the strongest ethane lines without saturating any of the lines. The total pressure was achieved by the addition of high purity "dry air".

The main issue encountered with these preliminary measurements was that they exhibited a large degree of spectral channelling. as shown in Figure 2.5. This channelling was a result of reflections between optical components such as the cell windows and optical filters and can be observed in the measured interferogram

(Fig. 2.6) of both the sample and background measurements. While adjustments allowed it to be reduced, it was not possible to remove it completely during the measurements.

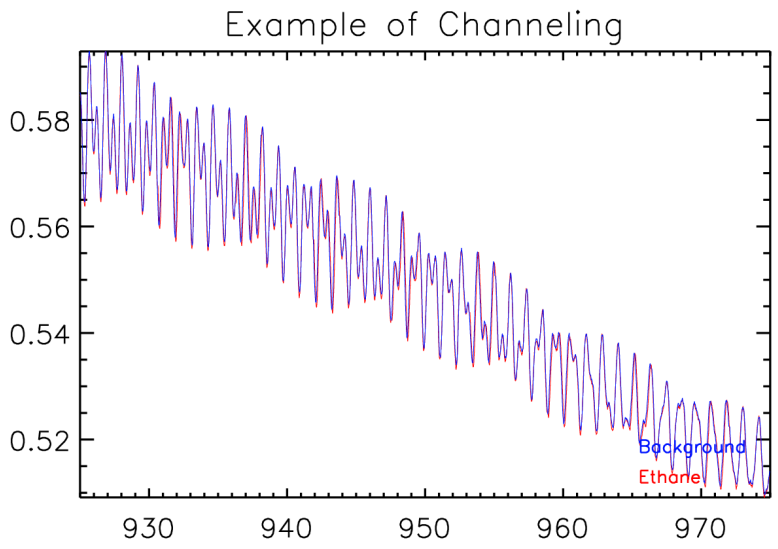

FIGURE 2.5. An example of unwanted spectral channelling caused by reflections between optical components within the interferometer observed in both the measurement and background spectra.

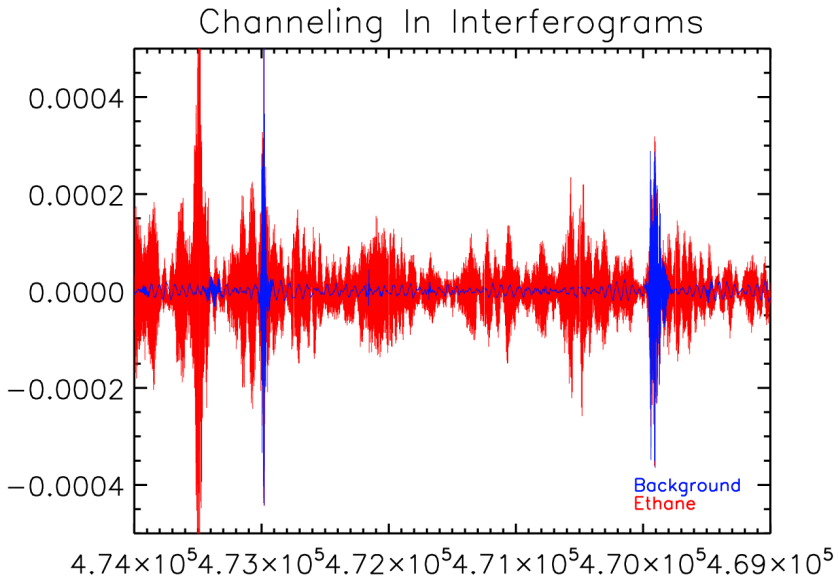

FIGURE 2.6. The recorded interferograms for both the measurement and background scans showing the additional peaks in the interferogram caused by the spectral channelling. As these peaks are present in both the background and measurement, it is possible to identify and remove them to some degree, limiting the effect of the channelling.

As this channelling is clearly identifiable in both measurements, it is possible to flatten these sections of the interferogram in an attempt to remove the channelling features. If the channelling is consistent as it is in this case, when calculating the transmission of the measurement against the background, this channelling effect should be further reduced. Care must be taken that this technique does not significantly alter other components of the spectra, introducing errors into the analysis.

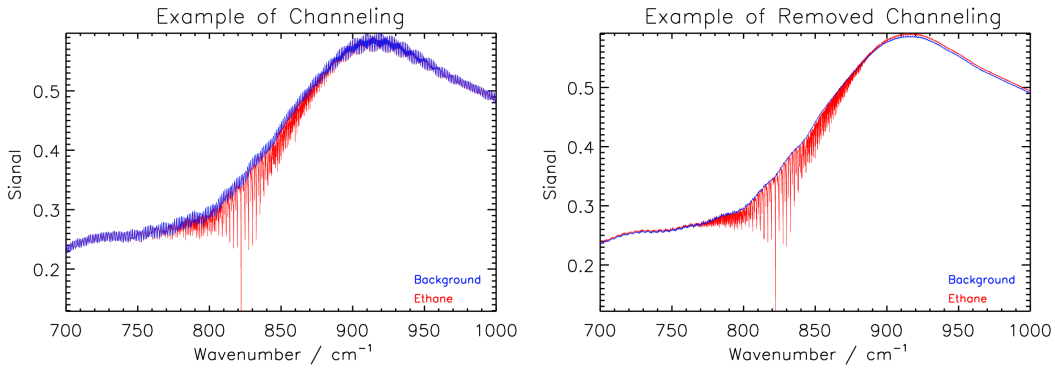

(a) Original Measurement

(b) After Removal Of Channelling

FIGURE 2.7. An example of spectral channelling and the resulting spectra once an attempt have been made to minimise it.

Figure 2.7 shows the sample (red) and background (blue) measurements before and after the removal of the spectral channelling.

This technique was applied to each of the measurements and was deemed to have successfully removed the majority of the observed channelling.

The transmission was calculated from the measurements for each of the scenarios outlined in Table 2.2 and compared to simulations of the expected transmission using the Oxford Reference Forward Model (see Section 2.5). These simulations were performed using both the original HITRAN2004 C_2H_6 spectroscopic data as well as the updated line information provided by Vander Auwera et al. [2007].

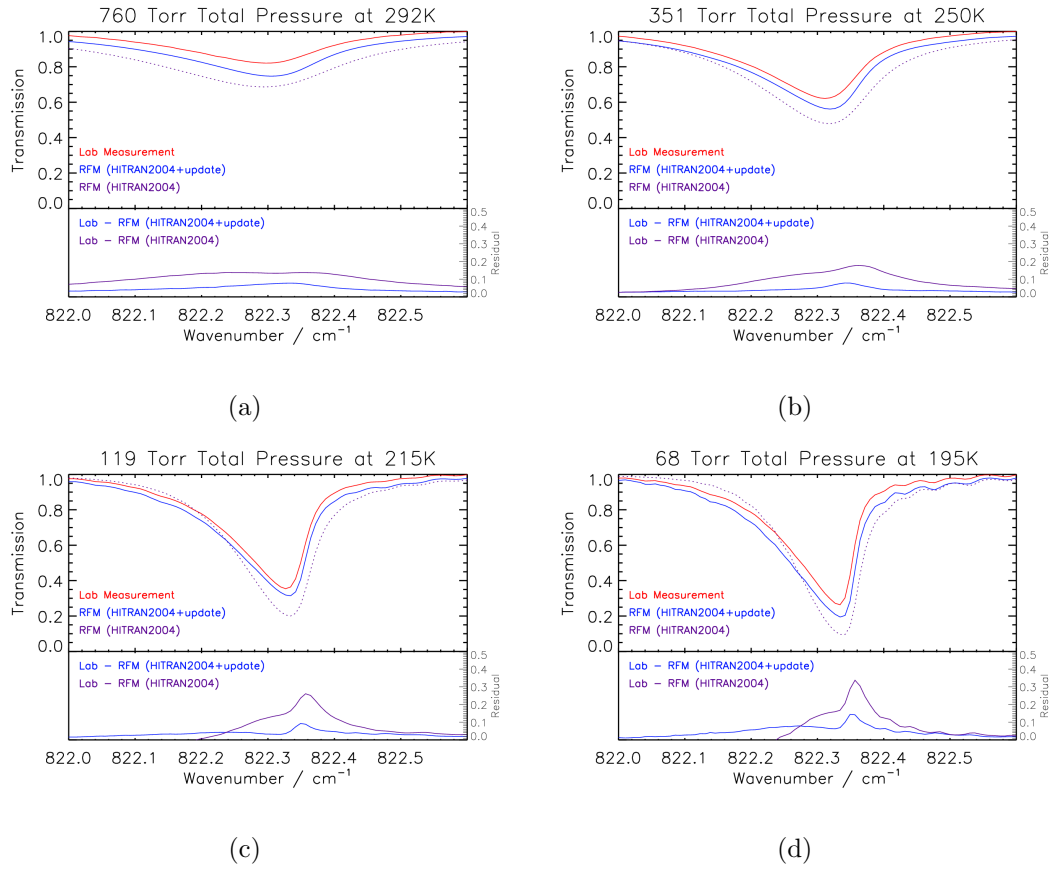

FIGURE 2.8. FTIR measurement at a spectral resolution of 0.015 cm^{-1} between 822.0 cm^{-1} and 822.6 cm^{-1} of 3.5 Torr of ethane in: (a) a total pressure of 760 Torr at room temperature (292 K) - (b) a total pressure of 351 Torr at 250 K - (c) a total pressure of 119 Torr at 215 K - (d) a total pressure of 68 Torr at 195 K. The lower panel shows the spectral residual between the lab measurement and the simulations.

Figure 2.8(a) shows the measured transmission of 3.5 Torr of ethane in a total pressure of 760 Torr at 292 K (room temperature) between 822.0 cm^{-1} and 822.6 cm^{-1} and compares to the simulations performed with the same conditions. The residual between the laboratory measurement and each of the simulations is also shown in the lower panel. It can be seen that for these conditions, the line is considerably broadened and the residual with the original HITRAN 2004 data (purple, lower panel) shows that the simulation differs from the measurement in both shape and offset. The improved ethane spectroscopy provided by Vander Auwera et al. [2007] is shown to significantly reduce both of these differences although a residual still exists.

When decreasing the temperature and pressure to 250 K and 351 Torr to simulate mid-tropospheric conditions (Fig. 2.8(b)), the line broadening is reduced and the difference in quality between the original data and the updated information is further highlighted. Whilst the original data has a maximum transmission residual to the laboratory measurements of 0.2, the improved spectroscopy differs by a maximum of only 0.07.

The case where the pressure is 119 Torr and the temperature is 215 K represents typical upper tropospheric conditions which are the most relevant to the work performed in this thesis. The transmissions and residuals for this scenario are shown in Figure 2.8(c) and the large residual of 0.27 for the HITRAN2004 data is considerably larger than the 0.09 residual for the updated spectroscopy. From these residuals it can also be seen that the position of the peak in the residual is altered slightly, suggesting that the wavenumber position in the updated spectroscopy is closer to the one observed in the laboratory measurements than the older HITRAN2004 data but still not exactly the same.

Finally, Figure 2.8(d) shows the results for a pressure of 68 Torr and a temperature of 195 K. Again, the updated ethane spectroscopy is shown to be much closer to the measurements than the original data but still with significant differences.

Simulations for typical upper tropospheric conditions were performed and it was found that even though the spectroscopy of ethane has been significantly improved, the difference between the improved spectroscopy and our laboratory measurements is equivalent to as much as a 15% reduction in the amount of ethane. It follows therefore that any retrieval using the current ethane spectroscopy may be underestimating the amount of ethane responsible for a measured spectral signature. This obviously has implications for any accurate retrieval of ethane and requires future work to perform improved measurements of the ethane spectroscopy, particularly for scenarios of pressure and temperature relevant to upper tropospheric measurements.

2.5 The Oxford Reference Forward Model

The Oxford Reference Forward Model (RFM) is a line by line radiative transfer code based on the GENLN2 code [Edwards, 1992]. The RFM was initially designed to

solve the radiative transfer equation for the purpose of producing simulations of atmospheric limb emission spectra for the MIPAS instrument although its use has now been extended to simulate a wider variety of scenarios including laboratory and nadir satellite spectra.

In order to perform a simulation, various user defined inputs are required specific to the simulation. These inputs include the wavenumber range and resolution of the required simulation as well as the atmospheric species within this spectral region. In addition, in the case of simulations for limb-viewing instruments the measurement tangent height and instantaneous field-of-view (IFOV) are also required. Spectroscopic information for each of the species is taken either from the HITRAN spectral database or for heavier molecules, from cross-section files. To perform accurate simulations, the instrument line shape (ILS) must also be provided.

Finally, in order to perform simulations of atmospheric spectra with the RFM, the temperature, pressure and volume mixing ratios of all relevant species must be input. These are typically taken from the reference climatologies. In this case, work by Remedios et al. [2007] has provided reference states of 36 species on a common altitude, pressure, and temperature grid from 0 to 120 km along with both means and estimates of variability (maximum, minimum and one sigma values).

Once these inputs have been provided, the RFM simulates the observed radiances within the spectral region by calculating the transmittance for contributing species. These calculations are first performed on a coarse 0.5 cm^{-1} grid and then a calculation on a 0.0005 cm^{-1} fine mesh grid is performed. This calculation is performed up to 25 cm^{-1} from the line centre and ensures that effects from overlapping wings are sufficiently modelled. These calculations are performed over the spectral range and output on to a regular grid defined by the user.

2.6 Retrieval Theory

In comparison to an in situ measurement of the atmosphere, remote sensing from satellites is capable of providing almost simultaneous global measurements of atmospheric constituents.

In order to achieve this, there are first considerable difficulties which must be overcome. The main difficulty is the fact that the measured radiance is often a complicated function of the variable which we are attempting to obtain as well as various other parameters which we may or may not accurately know. Therefore the retrieval of an atmospheric profile via satellite remotely-sensed data is often ill-posed (with no unique solution). As well as the fact that the nature of these problems often leads to more than one solution, some of these may be inconsistent with observations and unrealistic compared to the real atmosphere and it often becomes necessary to constrain the solution with additional prior information.

Retrieval theory is dealt with in extensive detail in Rodgers [2000] with some key aspects are outlined below.

2.6.1 Definitions

The measurement vector, y, relates to a set of m measurements. The state of the atmosphere (typically temperature, pressure or volume mixing ratios) is then defined as x and it is this state vector which we wish to retrieve. The relationship between y and x is given by the forward model:

$$\mathbf{y} = \mathbf{f}(\mathbf{x}, \mathbf{b}) + \epsilon \tag{2.13}$$

where

- The state vector x, with n elements, denotes the parameter(s) to be retrieved
- The measurement vector, y, contains the radiances that are inverted to retrieve x, e.g. the measured MIPAS spectral radiances at each tangent altitude.
- The forward function f represents the relationship between the measurement vector and the state vector. This is approximated by the Forward Model, F(x,b).
- The forward function parameters, b, represent all of the other factors which can affect the measurement but which are not in the state vector and hence not retrieved e.g. atmospheric profiles of mixing ratios or instrument line shape.
- The measurement noise, ϵ is the random error due to instrument noise.

2.6.2 Weighting Functions

The general remote sensing problem is often non-linear and requires the forward model to be linearised with respect to a reference state, x_0 giving:

$$y - F(x_0) = \frac{\partial F(x)}{\partial x}(x - x_0) \tag{2.14}$$

where the partial derivative, $\frac{\partial F(x)}{\partial x}$, represents the sensitivity of the forward model to a change in the state vector, x. This quantity is known as the weighting function or Jacobian matrix K and contains m forward model elements by n state vector elements. This weighting function matrix therefore relates the sensitivity of each element of F to each element of the state vector and in the situation where there are more elements in the measurement vector than unknowns in the state vector (i.e. m gt n) the retrieval can be described as being over-constrained. In contrast, when there are less measurements than unknowns, the retrieval is described as under-constrained or ill-posed.

2.6.3 Covariance Matrix

The covariance matrix describes how the knowledge relating to the error or noise in the real measurements, estimates or retrievals is described within the retrieval scheme.

S_y is the measurement error covariance matrix with the diagonal elements being the variances of the individual elements of y whilst the off-diagonal values indicate the covariance between the different elements of y. A similar covariance matrix is used to describe the covariance of the a priori data (S_a).

2.6.4 Retrieval Approach

A well-determined remote sensing problem can be considered as a set of simultaneous equations where there are the same number of measurements (and hence equations) as there are unknowns. In this case the number of elements in the state vector (n) is equal to the number of elements in the measurement vector (m).

In general, it is important to understand that the number of unknowns in the state vector and the number of measurements define the problem that we are attempting to solve. As explained above, in the case where there are less measurements than unknowns (i.e. $m < n$), the problem is said to be under-constrained as we, for example, only one equation but two unknowns. In this case, there may be multiple possible solutions and in order to reach a reasonable solution it may be necessary to utilise prior information relating to the unknowns, referred to as a priori.

In the case where there are more measurements than unknowns (i.e. $m > n$) then the problem is said to be over-constrained. In the ideal case, the extra measurement information does not provide any additional information that was not already known. However, in reality, it is more likely that there is no solution that agrees with all of the measurements as each measurement will have an error associated with it. In this case where we have an over-constrained problem with measurement noise, an optimal estimation approach is used to find the best solution.

2.6.5 Optimal Estimation

In the case where we have measurement noise which leads to amplifications of the errors and hence instabilities in the retrieved profiles it is possible to use an optimal estimation which takes into consideration an a priori estimate of the state vector to constrain the result to a reasonable solution which might not be possible from the measured radiances alone.

Although the problem will still not have a unique solution, the best (or optimal) solution can be found. There are two possibilities for the best solution. This can either be the most probable state where

$$\frac{\partial P(x \mid y)}{\partial x} = 0 \tag{2.15}$$

or the expected state, $\tilde{x}$ which is the mean state averaged over its probability density function (PDF):

$$\tilde{x} = \int x P(x \mid y) dx \tag{2.16}$$

With the assumption that the probability fits a Gaussian model and that the PDF is therefore symmetric about its maximum, the most probable state is the same as the expected state.

The value of the most probable state is achieved by minimising a cost function which depends upon optimising the difference between the measured and modelled radiances as well as the difference between the state vector and the a priori. This cost function takes the form:

$$\chi^2 = (y - Kx)^T S_y^{-1} (y - Kx) + (x - x_a)^T S_a^{-1} (x - x_a) \tag{2.17}$$

The most probable state is then given by the following:

$$\tilde{x} = x_a + (K^T S_y^{-1} K + S_a^{-1})^{-1} K^T S_y^{-1} (y - K x_a) \tag{2.18}$$

where S_a is the covariance of the a priori estimate of the state vector, x_a.

2.6.6 Gain Matrix

The measurement contribution function represents how the solution of the state vector, x, is affected by a change in the measured radiances, y. The contribution function is often termed the measurement gain matrix, G and is defined as:

$$G = \frac{\partial \tilde{x}}{\partial y} \tag{2.19}$$

In the case where a priori data are used this becomes:

$$G = (K^T S_y^{-1} K + S_a^{-1})^{-1} K^T S_y^{-1} \tag{2.20}$$

The most probable state vector given in Equation 2.18, where the value of χ^2 is at a minimum, is then:

$$\tilde{x} - x_a = G(y - Kx) \tag{2.21}$$

2.6.7 Averaging Kernel

The averaging kernel describes how the retrieval has smoothed the true atmospheric profile and is defined as:

$$A = \frac{\partial \tilde{x}}{\partial x} \tag{2.22}$$

The averaging kernel can be regarded as an indication of the weighting of the final retrieval between the measurement and the a priori information such that

$$\tilde{x} = Gy + (I_n - GK)x_a \tag{2.23}$$

where

$$A = GK \tag{2.24}$$

giving

$$\tilde{x} = Ax + (I - A)x_a \tag{2.25}$$

In the ideal case where the a priori has no influence, the averaging kernel would be a unit matrix but in reality the averaging kernel elements peak at the appropriate level and have a half-width associated with the vertical resolution of the retrieval.

2.6.8 Iterative Approach To Non-Linearity

In order to minimise the cost function in Equation 2.17, an iterative technique is used. Assuming that the problem is not too non-linear the Gauss-Newton iteration takes the form

$$x_{i+1} = x_i + (S_a^{-1} + K_i^T S_y^{-1} K_i)^{-1}(K_i^T S_y^{-1}[y - F(x_i)] + K_i[x_i - x_a]) \tag{2.26}$$

where for the initial iteration, the value of x_0 is usually set to the a priori value, x_a. This iteration should move the solution in the direction which minimises the cost function. However, if the iterative process is unstable, for example when the initial guess is too far from the solution or when there is increased non-linearity, then the Gauss-Newton iteration may be insufficient and an adjustment to the Gauss-Newton method is required. This adjustment is the Levenburg-Marquardt iteration where an adjustable damping factor, γ, is used to aid convergence. The iteration becomes:

$$x_{i+1} = x_i - (S_a^{-1} + K_i^T S_y^{-1} K_i + \gamma D)^{-1}(-K_i^T S_y^{-1}[y - F(x_i)] + S_a^{-1}[x_i - x_a]) \tag{2.27}$$

with D a scaling matrix usually set to S_a^{-1}. This method works by either decreasing or increasing the value of γ depending on whether the value obtained for χ^2 is increased or decreased. If the value of χ^2 is increased by the iteration step, then γ is increased without updating x_i and the same calculation is attempted again. If χ^2 decreases after the iteration, the value of x_i is accepted and γ is decreased for the next iteration.

2.6.9 Testing For Convergence

The iterations described above require a test for whether the retrieval is deemed to have converged on the optimal solution and hence has finished or whether further iterations are required. A common test for convergence is to calculate the change in the χ^2 value between one iteration and the next. This change in χ^2 is calculated using

$$\chi_n^2 = \frac{1}{n}(x_{i+1} - x_i)^T(S_x(x_{i+1} - x_i)) \tag{2.28}$$

with S_x in this case being the covariance of the $x_{i+1}th$ atmospheric state.

Convergence is said to have been reached when the change in χ^2 is less than a threshold value which determines that the residual (the difference between the measurement and the forward model, $F(x) - y$) is the same order of magnitude as the instrument noise. This prevents the retrieval attempting to fit the measurement noise as signal.

Whilst the absolute value of χ^2 should itself not be used as a test for convergence, it is still a useful indicator of whether a completed retrieval has converged on a reasonable solution and has not instead become stuck in a local minimum rather than the global minimum which identifies the optimal solution. Ideally this value should be equal to the number of elements in the state vector, n.

2.7 Summary

This chapter has outlined some of the key theoretical aspects associated with the work in this thesis. The general principles of radiative transfer and remote sensing were discussed, of particular relevance to the limb-viewing of the Earth's atmosphere from space. This included a description of basic spectroscopic theory relating to line intensities and the broadening of spectral lines in the atmosphere caused by both pressure and collisional effects.

The spectroscopy of C_2H_2 and C_2H_6 was discussed and it was shown they have appropriate spectral features in the MIPAS spectral range from which to retrieve. In order to successfully retrieve information from atmospheric spectra, it is necessary to have a good understanding of the spectroscopic parameters such as line intensities

and positions. There are several large databases which contain such spectroscopic information, namely HITRAN and GEISA.

Although the C_2H_2 spectroscopy is estimated to have errors of less than 5% [Jacquemart et al., 2003], in relation to C_2H_6 the current knowledge of its spectroscopic parameters has been shown to be poor, with large discrepancies between the HITRAN and GEISA databases in both line positions and intensities. Whilst the work in this thesis was being undertaken, Vander Auwera et al. [2007] have also performed further spectroscopic measurements of C_2H_6. The preliminary ethane measurements performed as part of the work for this thesis have shown that the work of Vander Auwera et al. [2007] has significantly improved the ethane spectroscopy but differences do still exist which may translate into biases of as much as 15% in any retrieved ethane VMR. This has shown that further work is required to perform improved measurements of the ethane spectroscopy, particularly for scenarios of pressure and temperature relevant to upper tropospheric measurements.

The remainder of this chapter has dealt with the simulation of and retrieval from atmospheric spectra. The Oxford Reference Forward Model was described which allows simulations of MIPAS limb-emission spectra to be performed. Following on from this, retrieval theory was discussed in detail and focused on explaining the basic theory behind the retrieval approach utilised in this thesis to retrieve both C_2H_2 and C_2H_6 from MIPAS L1B spectra.

Chapter 3

The Michelson Interferometer For Passive Atmospheric Sounding (MIPAS)

3.1 The Envisat Satellite

The ENVIornmental SATellite is a European Space Agency mission with the main objective of improving Europe's capabilities for the remote sensing of the Earth from space. One of the mission's primary objectives is the continuation of the observations of the Earth's land, sea, ice and atmosphere performed by its predecessors, the European Remote Sensing satellites (ERS-1 and ERS-2) in order to provide long-term continuous datasets to understand environmental and climate systems. ENVISAT was launched from Kourou, French Guiana on 1st March 2002 onboard a ESA Ariane-5 rocket into a sun-synchronous polar orbit at a mean altitude of 800 km and an inclination of 98.55°. ENVISAT has an orbital period of 100 minutes with a 35 day orbital repeat cycle and a descending node equator crossing with a mean local solar time of 10.00 am. It is expected that the ENVISAT mission will continue until at least 2013 with the determining factor being fuel supply. This would effectively double the original expected mission lifetime of five years up to over ten years.

The Envisat payload comprises ten instruments contributing a total payload mass of 2.1 tonnes towards ENVISAT's total mass of 8.1 tonnes. These instruments offer a wide range of complementary measurement techniques including passive radiometers, active radars and altimeters that allow many significant aspects of the Earth's system to be observed. Table 3.1 lists each of these instruments; their location onboard the ENVISAT satellite is shown in Figure 3.1.

This work primarily uses high spectral resolution data obtained from the MIPAS instrument which is described in detail in the following section.

Instrument	Objective
AATSR (Advanced Along Track Scanning Radiometer)	Accurate sea and land surface temperature, vegetation indices, aerosol, cloud parameters
ASAR (Advanced Synthetic Aperture Radar)	Ocean waves, sea ice extent and motion, land surface (deforestation, desertification)
DORIS (Doppler Orbitography and Radiopositioning Integrated by Satellite)	Precise satellite positioning
GOMOS (Global Ozone Monitoring by Occultation of Stars)	Monitoring and understanding of ozone depletion in the stratosphere
MERIS (Medium Resolution Imaging Spectrometer)	Ocean colour monitoring (chlorophyll, yellow substance, suspended matter) and vegetation status
MIPAS (Michelson interferometer for Passive Atmospheric Sounding)	Ozone chemistry, monitoring of global distribution of major greenhouse gases, atmospheric dynamics, clouds (including polar stratospheric clouds)
MWR (Microwave Radiometer)	Total atmospheric water column measurement for correction of RA measurements
RA-2 (Radar Altimeter 2)	Ocean topography, marine geoid characteristics, wind speed and wave height)
SCIAMACHY (Scanning Imaging Absorption Spectrometer for Atmospheric Cartography)	Global distribution of trace gases, air pollution, aerosols, clouds and stratospheric ozone chemistry
LRR (Laser Retro-Reflector)	Verification of spacecraft stability and positioning

Table 3.1. Table showing the entire ENVISAT Instrument Payload along with a brief description of each instrument

3.1.1 Introduction To The MIPAS Instrument On ENVISAT

MIPAS on ENVISAT is a high spectral resolution Fourier Transform Infrared Spectrometer which views the atmosphere using a limb geometry (see Chapter 2) in order to measure atmospheric emission spectra. The first MIPAS-type instrument obtained stratospheric emission spectra from a balloon-borne platform between 1989 and 1992. Since then various versions of the MIPAS instrument, developed by the Institute for Meteorlogie und Klimaforschung (IMK), have been successfully deployed on ground, aircraft and balloon-borne platforms.

The MIPAS instrument is a core payload on the ENVISAT Satellite (sometimes referred to as MIPAS-E, to differentiate from the MIPAS-B balloon instrument) and although there have been interruptions in operations it has continued to provide important scientific information on the atmosphere since 2002.

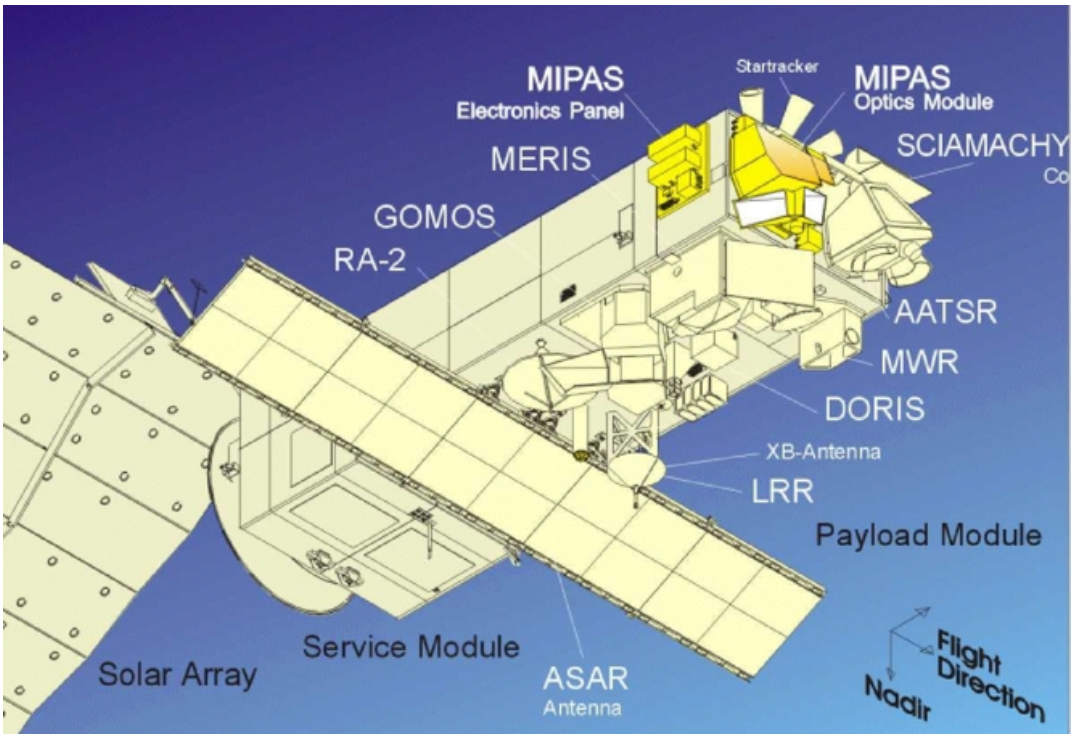

FIGURE 3.1. Instruments onboard the ENVISAT module. Source: ESA [2007].

The MIPAS instrument was designed to perform continuous measurements over a five year lifetime. In March 2004, after less than two years of operation, MIPAS temporarily ceased performing measurements due to an increased number of instrument anomalies. These included an issue with the interferometer mirror drive unit which developed sliding velocity errors.

Two phases of MIPAS operations can be distinguished relating to this period of unavailability. Prior to March 2004, MIPAS operated in a full-spectral resolution (FR) mode (0.025 cm^{-1} unapodised). After a period of inoperation, from January 2005 to present MIPAS has operated in a "reduced-spectral resolution" (RR) mode (0.0625 cm^{-1} unapodised). The reduction in the maximum path difference caused by the issues with the motion of the interferometer mirrors has led to a 40% reduction in the spectral resolution. However as a consequence of this reduction in spectral resolution, the shorter scanning time allows additional measurements to be taken which increases both the vertical and along-track spatial resolution.

For the purposes of this thesis, it is the data obtained via the "full-spectral resolution" mode at a resolution of 0.025 cm^{-1} (unapodised) which is used. The potential for the application of this work to the reduced resolution data is briefly discussed in Chapter 7

3.1.1.1 Background and Objectives

The main objective of the MIPAS mission is to study the chemistry and dynamics of the upper troposphere, stratosphere, mesosphere and lower thermosphere [Fischer

et al., 2008]. This main objective is broken down into several scientific objectives which are discussed in more detail in Fischer et al. [2008].

1. Stratospheric chemistry and dynamics: specifically the study of stratospheric ozone depletion and its effect on the physical structure of the stratosphere.

2. Stratosphere-troposphere exchange: observing the transport through the tropical transport layer (TTL) and the exchange processes.

3. Chemistry and physics of the upper troposphere: the study of the transport of natural and anthropogenic species (such as those from biomass burning) from the lower troposphere into the upper troposphere/lower stratosphere (UTLS) region.

4. Physics and chemistry of the upper atmosphere: observations of temperature, CO, CO_2, O_3 and other key species in the mesosphere and lower thermosphere (MLT) region

5. Climatology and weather forecasting: high vertical resolution observations of water vapour and ozone in the UTLS to improve data assimilation for weather forecasting. Observations of polar stratospheric clouds (PSCs) and cirrus clouds to understand their global distribution and effect on the Earth's radiation budget, and effects on atmospheric chemistry.

3.1.1.2 Viewing Geometry And Observation Modes

MIPAS observes mid-infrared atmospheric limb radiance emissions with an unapodised spectral resolution of 0.025 cm^{-1} between 685 cm^{-1} and 2410 cm^{-1} (14.6 and 4.5 microns). This covers the region of the atmospheric spectrum where there are a variety of molecules with well-defined absorption bands, and in many cases well-resolved lines [Fischer et al., 2008]. In full resolution mode measurements are made with a nominal mode of 17 tangent altitudes at 68 km, 60 km, 52 km, 47 km, 42 km and then every 3 km until the final mid-tropospheric measurement at 6 km.

These measurements are made in the rearward, along-track direction with a 3 km x 30 km instantaneous field of view (IFOV) with an atmospheric path length between the instrument and the tangent position of approximately 3000 km. This viewing geometry is shown in Figure 3.2. With each integration at a given tangent altitude taking 4.45 seconds, a complete set of all 17 tangent altitudes requires approximately 76 seconds, leading to 75 such profiles being measured per orbit. In MIPAS terminology, the measurement at each tangent altitude is termed a "scan" and a set of 17 scans constitute a "sweep" or vertical profile.

MIPAS is also capable of operating in a variety of "special" modes which include the ability to measure through a sideways cross-track FOV to observe specific events such as volcanic eruptions. A full list of the different observation modes in the full spectral resolution mode is detailed in Table 3.2. MIPAS operated in nominal mode

Mode	Description	Objective
N/A	Nominal	Stratospheric chemistry and dynamics
S1	Polar winter chemistry	Polar chemistry and dynamics
S2	Tropospheric-stratospheric exchange	Exchange between troposphere and stratosphere, tropospheric chemistry
S3	Impact of Aircraft emissions	Study of major air traffic corridor
S4	Stratospheric dynamics	To identify and observe transport processes within the stratosphere
S5	Diurnal changes	Diurnal changes near the terminator
S6	Upper troposphere/ lower stratosphere	Study of important dynamical processes in the upper troposphere and lower stratosphere region of the atmosphere
UA1	Validation	Confirmation of predicted non-LTE effects on the retrieval of pressure, temperature and the six target species
UA2	Upper polar vortex dynamics	Stratosphere mesosphere exchange and dynamics
UA3	Radiative energy budget of the mesosphere and lower thermosphere	Hydrogen, nitrogen and carbon budgets in the upper atmosphere, mesospheric dynamics and non-LTE studies
UA4	Non-LTE studies of NO	Radiative cooling of the thermosphere

Table 3.2. Table showing the various observation modes of MIPAS "full resolution" mode up until March 2004. MIPAS operated in nominal mode approximately 80% of the time with the remainder dedicated to performing special observations.

approximately 80% of the time, with the remainder dedicated to performing these special observations.

3.2 The MIPAS Interferometer

A variant of a classical Michelson interferometer forms the basis for the MIPAS instrument. A Michelson interferometer consists of an angled beamsplitter and two plane mirrors, one moving and one fixed. The beamsplitter allows a collimated beam from an external source to be both partially transmitted to the moving mirror and partially reflected to the fixed mirror. These two beams then return to the beamsplitter where they interfere and produce an interferogram (see Chapter 2).

There are several key advantages in using a FTS compared to spectrometers with dispersive elements such as prism or grating-based spectrometers. These advantages include:

1. The Fellgett (or Multiplex) Advantage - In a single-element grating spectrometer all of the wavelengths are measured successively, whereas in an interfer-

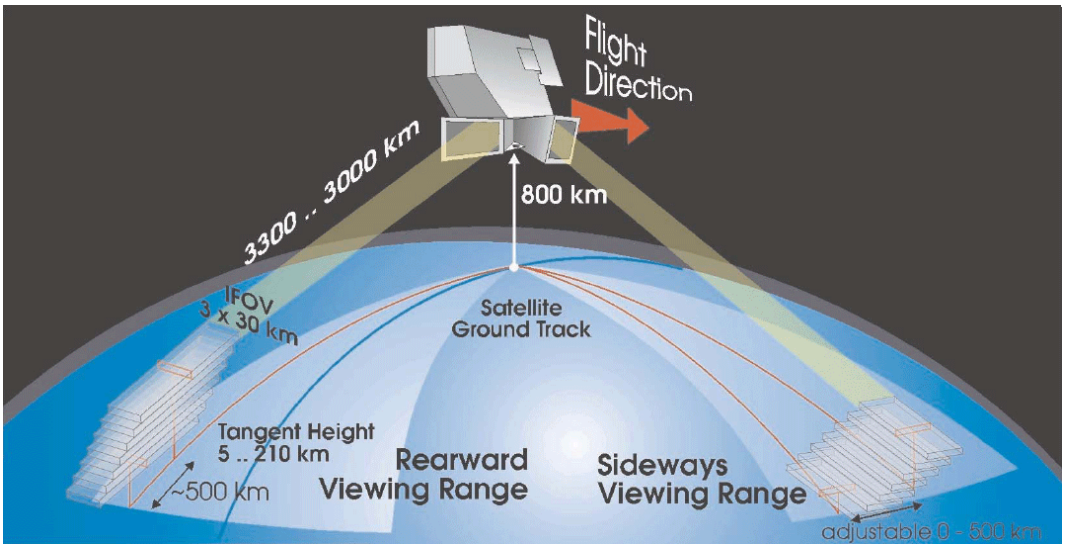

FIGURE 3.2. MIPAS viewing geometry showing both the nominal observation mode geometry (rearward, along-track) and the special observation mode which utilises a sideways cross-track field of view to examine special events. Source: Fischer et al. [2008].

ometer system, they are measured simultaneously. Not only does this mean that the spectral signatures of a wide range of species can all be identified in the same measurement but this also leads to the signal to noise ratio being much higher for an FTIR instrument compared to equivalent recording times for a wavelength scanning grating system.

2. The Jacquinot (or Throughput) Advantage - As there are no slits employed by an interferometer system, the radiation throughput is much higher than in a dispersive system which must compromise between radiation input and the increase in spectral resolution afforded by a narrowing of the grating width.

3. The Connes Advantage - Finally, due to the simultaneous wavelength measurement with a HeNe laser, the wavelength calibration and stability of an interferometer system is in principle much greater than that of dispersive systems.

The major disadvantage with an FTS system is the complexity of the mechanical operations that it is required to perform, specifically the precision requirements for the movement of the optical elements in the system.

In the case of the interferometer used in the MIPAS instrument, there are several modifications to the classical Michelson interferometer to meet the specific radiometric, spectroscopic and size requirements of space flight. To minimise the amount of mechanical movement necessary, these modifications include two corner-cube reflectors that each move 10 cm giving a maximum path difference of 20 cm, and hence the required unapodised spectral resolution of 0.025 cm^{-1}.

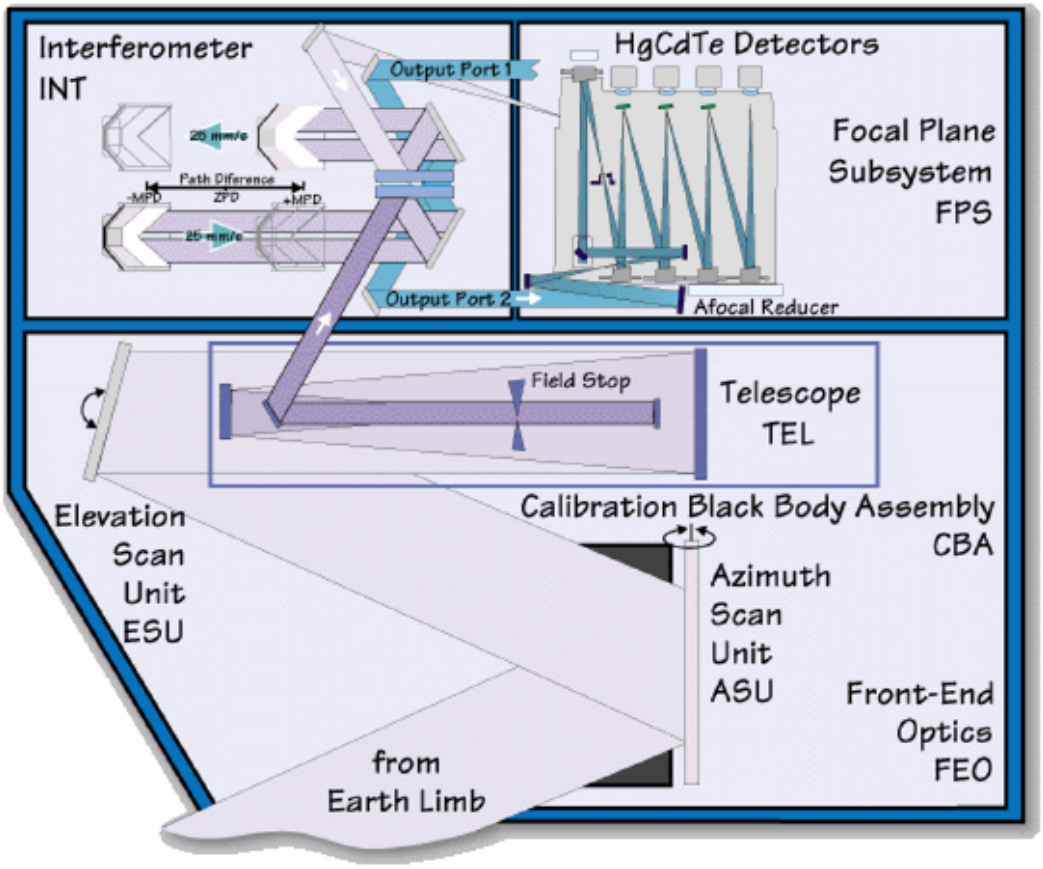

FIGURE 3.3. The MIPAS instrument layout showing the arrangement of the telescope, interferometer and detectors inside the MIPAS instrument. Figure taken from Fischer et al. [2008].

Figure 3.4 shows the arrangement of the optical system. Atmospheric radiation enters the instrument from the anti-sunward side of the ENVISAT satellite through the input telescope where it is collimated and directed into the MIPAS optics module via the input port. Once inside the MIPAS optics modules, the infrared radiation reaches the beamsplitter whose design allows half of the radiation to be transmitted through its semi-transparent mirror, with the remaining half being reflected. In this way the beam is split in two, each of which is then reflected into a corner-cube retro-reflector which reflects the beam back towards the beamsplitter where it is recombined. A pair of Mercury Cadmium Telluride (MCT) detectors measure the interference pattern caused by the recombination of the beams which will be at a maximum when there is constructive interference between the two beams and minimum when there is destructive interference.

The variation of the optical path difference, via the movement of the corner-cube reflectors, allows the detector to measure the intensity due to both the constructive and destructive interference patterns, which is referred to as an interferogram. It is this interferogram which is converted into the measured radiance spectra by a Fourier transform calculation, meaning that it is possible to measure across the

entire spectral range simultaneously (referred to above as Fellgett's advantage).

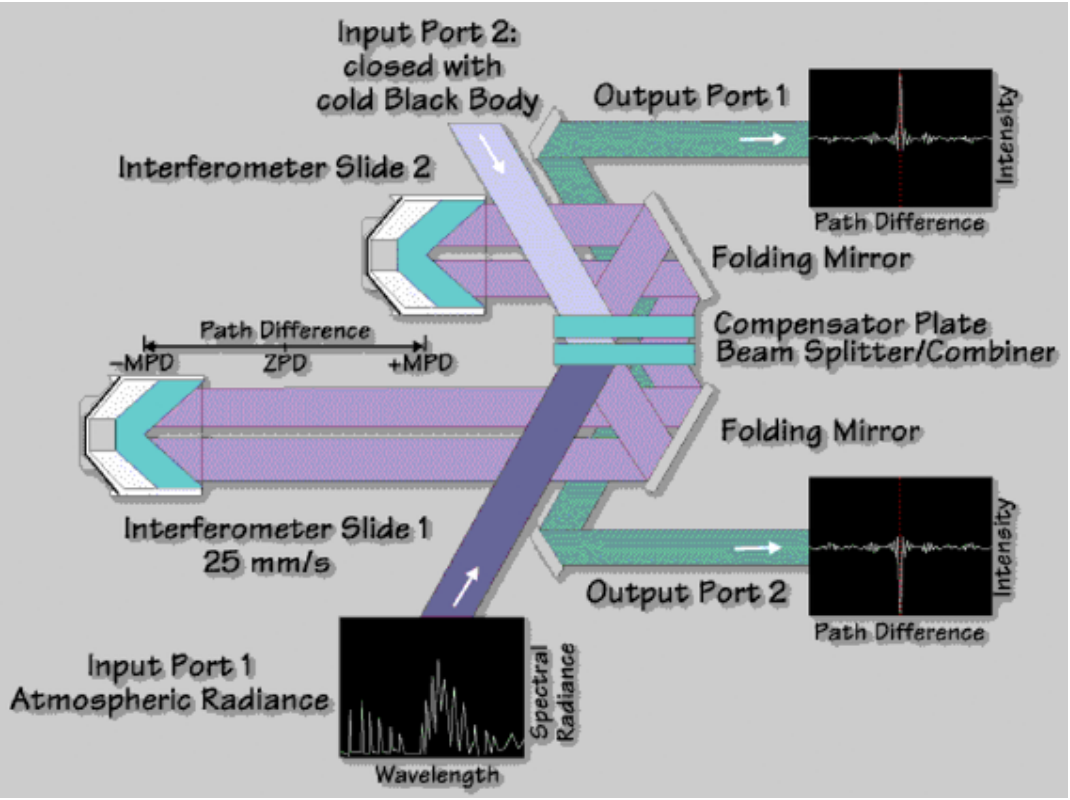

FIGURE 3.4. A schematic view of the MIPAS interferometer system. Figure taken from ESA [2007].

In order to achieve the best radiometric sensitivity and to increase the signal to noise ratio as well as to provide redundancy in case of failure, MIPAS uses four detectors in each of the interferometer output ports, giving a total of eight detectors, designated A, B, C and D. These are optimised for maximum sensitivity to each of the five spectral bands (A, AB, B, C and D). In both ports, detectors A, C and D are identical. This arrangement allows the signals from the pairs of detectors to be co-added to improve the signal to noise ratio and provide redundancy. If a detector in one of the output ports fails, the measurement from the corresponding detector in the other output port can still provide data. The exception to this are detectors B1 and B2 which are optimised for a different spectral range in each port, referred to as bands AB and B respectively. This arrangement can be seen schematically in Figure 3.4 and is outlined in Table 3.3.

To measure the long-wave infrared region (14.6 to 7 microns), photo-conductive HgCdTe (PC-MCT) detectors are used in order to meet the low noise and electronic bandwidth requirements of the instrument but for the short-wave region (7 to 4 microns), photo-voltaic (PV-MCT) detectors are preferred due to linearity and noise performance. The noise contribution from the detectors is temperature dependent and so the focal plane arrays are cooled through the use of two Stirling cycle coolers, maintaining a temperature of 70K.

Band	Detector	Spectral range (cm^{-1})
A	A1 A2	685-970
AB	B1	1020-1170
B	B2	1215-1500
C	C1 C2	1570-175
D	D1 D2	1820-2410

Table 3.3. Details of the 5 spectral bands measured by MIPAS ranging from 685 cm^{-1} to 2410 cm^{-1}.

3.3 MIPAS Performance

3.3.1 Radiometric Calibration And Offset

In order to provide the accurate spectral measurements required, the instrument performance must be carefully characterised. In particular, radiometric calibration must be performed to take into account any self-emission from the instrument itself and to be able to assign radiance units ($nW/cm^2 \cdot sr \cdot cm^{-1}$) to the raw signal counts. This is achieved by performing calibration measurements of both an internal blackbody at a temperature of 224K and a deep space measurement with negligible source emission. These calibration measurements are performed at the start of each nominal measurement sequence.

Further deep space measurements are performed to determine the instrument offset value which is the contribution to the measured signal from the self-emission of the instrument. These measurements are performed approximately 20 times per orbit and allow the thermal emission of the instrument to be subtracted from each atmospheric measurement. The offset value has been found to change by less than 10% of the Noise Equivalent Spectral Radiance (NESR) between two consecutive measurements [Kleinert et al., 2007]. Absolute offset variations are believed to be less than 2 $nW/cm^2 \cdot sr \cdot cm^{-1}$ [Fischer et al., 2008].

3.3.2 Gain

The instrument responsivity, or gain, is another important quantity which must be characterised. To perform measurements of the instrument gain in each channel, the internal blackbody is heated to 250K where it has an emissivity of greater than 99.6% and a total of 1200 low resolution measurements are made, 600 of which are of the internal blackbody and the remaining 600 are out to deep space. The stability of the radiometric gain has been shown to be better than 1.5 % per week [Fischer et al., 2008] and was monitored on a daily basis prior to March 2004 but once the temporal variation was well quantified, these measurements were reduced to once every two days.

3.3.3 NESR

The Noise Equivalent Spectral Radiance (NESR) is used to quantify the amount of noise observed in the spectra and thus the radiometric sensitivity of the measurement. The $NESR_0$ is the lowest possible NESR value for a scene of zero radiance. During flight, this $NESR_0$ is calculated from the standard deviation of measurements performed during deep space observations at 210 km. It has been reported by Kleinert et al. [2007] that there has been no observed degradation of the NESR with time (Fig. 3.5). The value of the NESR is wavenumber dependent and generally values range between 50 $nW/cm^2 \cdot sr \cdot cm^{-1}$ in band A, down to 3 $nW/cm^2 \cdot sr \cdot cm^{-1}$ in band D which is well within the specified requirements Fischer et al. [2008]. As can be seen from Figure 3.5, NESR values between 800 cm^{-1} and 1000 cm^{-1} are typically found to be between 30 $nW/cm^2 \cdot sr \cdot cm^{-1}$ and 40 $nW/cm^2 \cdot sr \cdot cm^{-1}$.

With regards to the detection of spectral signatures discussed in Chapter 4, quantification of the NESR becomes important as often weak spectral signatures may be of the same order as the noise. The implications of estimating the NESR for the detection algorithm are discussed in Section 4.1.6.

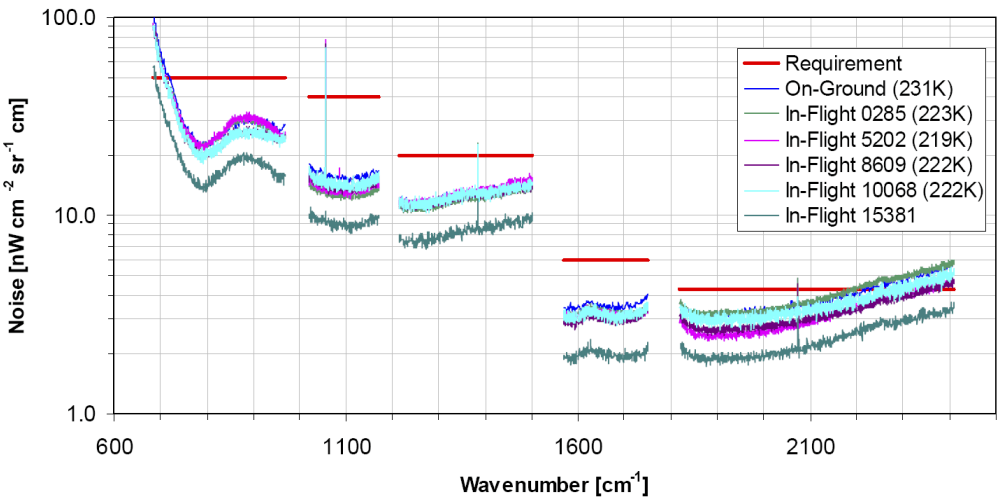

FIGURE 3.5. MIPAS $NESR_0$ before launch and in-flight. The figure is taken from Kleinert et al. [2007] who report no systematic evolution of the NESR with time.

3.3.4 Spectral Calibration

Spectral calibration of the measurements is performed through the retrieval of spectral lines with well known wavenumber positions. The lines used operationally are shown in Table 3.4. These are compared to reference spectral lines which allow calibrated wavenumber values to be assigned to the measured spectra. The spectra are then calibrated by shifting the wavenumber values until the measured spectra are in agreement with the reference spectra. In order to obtain a wavenumber

Band	Target gas	Peak position (cm^{-1})	Spectral interval (cm^{-1})	Tangent altitude (km)	Number of coadditions	Used in ILS calibration	Used in spectral calibration
A	O_3	802.5074	802.40 - 802.62	30	1	yes	yes
AB	O_3	1125.2085	1125.10 - 1125.30	30	1	yes	no
B	H_2O	1409.9686	1409.85-1410.08	50	1	yes	yes
C	H_2O	1672.4750	1672.40 - 1672.55	50	1	yes	yes
D	H_2O	1966.2615	1966.00 - 1966.50	50	1	yes	yes

Table 3.4. Reference lines and spectral windows used for spectral calibration and ILS retrieval. Source [ESA, 2007]

accuracy of better than 0.001 cm^{-1}, the calibration is performed every four limb sequences. With a variation of only approximately 5 ppm between July 2002 to March 2004, no significant spectral shift has been observed and the spectral calibration is considered to be very stable [Kleinert et al., 2007].

3.3.5 Pointing And Line Of Sight Calibration

In order to provide accurate retrievals of atmospheric profiles, the atmospheric path through which the measurement is being made must be well quantified. For this reason, the calibration of the pointing and line of sight (LOS) of the instrument are important factors which must be considered. The line of sight calibration is performed by comparing the observations of stars passing through the instrument field of view with the expected trajectory of these stars with respect to the orbital position of ENVISAT and correcting for any differences between the values.

A study of the pointing performance of MIPAS performed by Kiefer et al. [2007], comparing the retrieved altitudes with the engineering altitudes derived from ENIVSAT positional data, showed that the MIPAS engineering altitudes are between 0 km and 1.8 km higher, leading to a systematic pointing difference of 1.5 to 2 km between the tropics and the poles.

Figure 3.6 shows this pointing bias as a function of orbit number between August 2002 and April 2005.

For the data from 2003 used in this thesis (enclosed by red lines in Fig. 3.6), it can be seen that the variation in the pointing bias was at its largest. After an update to the on-board software on 12th December 2003 (Orbit 9321) the amplitude of the variations in the pointing bias was drastically reduced. Prior to this a correction

of the attitude was performed twice a day to minimise the effect of this pointing drift.

Despite the application of these corrections, caution must be used when dealing with MIPAS engineering altitudes and ideally retrieved pressure should be used to distinguish between vertical levels.

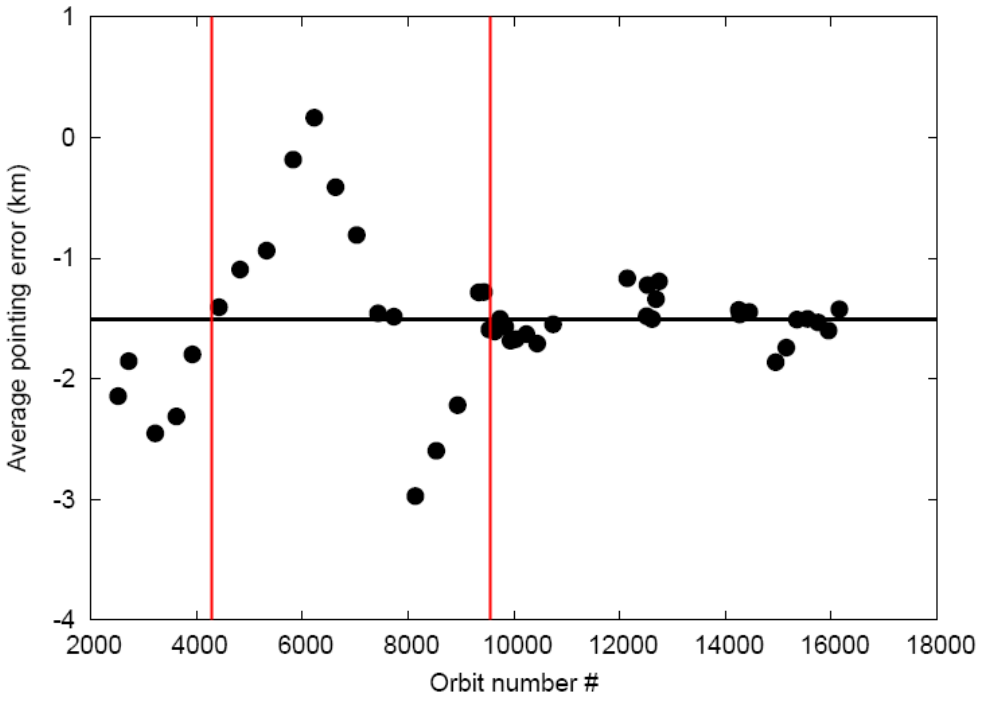

FIGURE 3.6. MIPAS pointing bias as a function of orbit number from August 2002 to April 2005. The solid line represents the average value of the pointing bias with negative values indicating a bias towards lower altitudes. The two red lines identify the start (Orbit 04380) and end (Orbit 09603) of 2003. Figure modified from Kiefer et al. [2007].

3.3.6 Instrument Line Shape

The instrumental line shape (ILS) is the area-normalised spectral response function of the spectrometer and characterises the shape and width of the observed spectral lines. The maximum path difference (MPD) of the instrument is the major factor which defines the ILS, with a greater MPD giving a thinner ILS.

In order to retrieve the ILS, a retrieval method called the Parametric ILS Fitting Method is used (PIFM). This method involves the selection of a reference peak of a species with a well-defined wavenumber and simulating the spectral line in the microwindow (Table 3.4). The ILS is then retrieved by minimising the residual between this simulation and measured spectra. Due to the computationally intensive

nature of this retrieval, the ILS is only retrieved once per orbit and is limited to the coaddition of just 5 measurements. For the purposes of the Level 2 processing, this is not sufficient due to a poor singal-to-noise and instead a fixed reference ILS based on the coaddition of a full orbit of data is used.

3.4 MIPAS Data

The operational data processing of MIPAS is organised in the following way (Fig. 3.7). Initially the onboard processing is performed, which includes numerical filtering, decimation and digitisation of the data, with the resulting source packets transmitted to the ground stations in ESRIN Italy (via Svalbard) and Kiruna Sweden ready for the ground-based processing to commence.

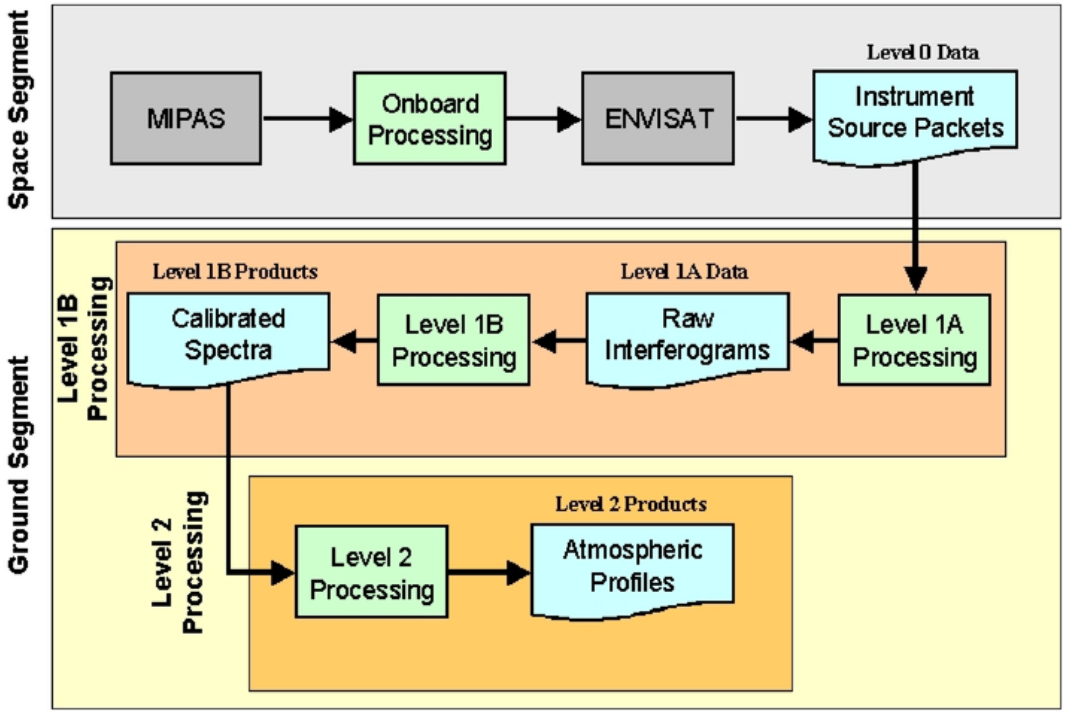

FIGURE 3.7. A schematic of the MIPAS data processing chain showing the various stages of data processing from Level 1A (raw interferograms) to the Level 2 profiles of operationally retrieved species. Source: ESA [2007].

The Level 0 (L0) instrument source packets received from ENVISAT are processed into the Level 1A data, the raw interferograms, by the ground segment. These in turn are then processed into the Level 1B (L1B) data where they are converted into spectrally and radiometrically calibrated (see Sections 3.3.1 and 3.3.4 respectively), geolocated radiance spectra of the atmosphere.

The Level 2 (L2) data are then retrieved from the L1B spectra using the Optimised Retrieval Module (ORM) [Raspollini et al., 2006], giving atmospheric profiles of pressure and temperature along with key atmospheric constituents: water vapour

(H_2O), ozone (O_3), methane (CH_4), nitric acid (HNO_3), nitrogen dioxide (NO_2) and nitrous oxide (N_2O).

The following sections provide more details on both the L1B and L2 data products.

3.4.1 MIPAS L1B Data

The main objective of the MIPAS Level 1B data processor [Kleinert et al., 2007] is to provide geolocated and spectrally and radiometrically calibrated atmospheric measurements with the main output being atmospheric radiance spectra as a function of wavenumber. This calibration process is described in Sections 3.3.1-3.3.3 for the radiometric calibration and Section 3.3.4 for the spectral calibration.

The two inputs to the L1B processor are the measurement data contained in the L0 product and auxiliary data files used to calibrate the measurement data. These auxiliary data files, as well as containing the data used in calibration, contain information on the status of the instrument along with the timing and position of the measurements. The L1B product output from the processing consists of geolocated atmospheric spectra, calibrated both radiometrically and spectrally and accompanied by data calibrations, data assessments and data quality validation information.

For each measurement sweep, calibrated spectra are generated by the Fourier Transform of the L1A raw interferograms for each of the 5 spectral bands and are then output into the Level 1B data product along with the sweep information header. Specific header information is also included for each individual elevation sequence within the sweep.

A full description of the MIPAS L1B processing algorithm can be found in Kleinert et al. [2007].

3.4.2 MIPAS L2 Data

The MIPAS L2 data processor utilises the L1B data to produce pressure, temperature and concentration profiles for H_2O, O_3, CH_4, HNO_3, NO_2 and N_2O. This data is produced through the use of the Optimised Retrieval Module (ORM), the L2 retrieval code developed by an ESA-led international consortium with the aim of producing Near Real-Time (NRT) retrievals of the L2 products within 3 hours of the measurement. The ORM uses a non-linear least-squares global fit of a theoretical model to the observation as described in Raspollini et al. [2006] in order to process the large amount of data necessary within the time constraints.

The NRT L2 retrieval has the following convergence criteria [Raspollini et al., 2006]: The maximum relative difference between the projected state from the previous iteration and the actual value is less than a threshold, T1; The maximum variation between iterations is less than a threshold, T2; The number of iterations

has not exceeded a maximum threshold. Even without reaching convergence due to the first two criteria, the retrieval is stopped after the maximum number of iterations is reached.

In order to provide the NRT retrieval in a timely manner, it is necessary for the above convergence criteria to be relatively relaxed. This however results in a relatively large convergence error (the difference between the profile at convergence and the profile obtained after 10 iterations).

In addition to the production of NRT data, the ORM also allows offline processing for re-analysis of MIPAS data. Whilst in the case of the NRT data, a compromise is necessary between accuracy and speed, the offline processing allows the retrieval to iterate until convergence is reached using stricter convergence criteria. For example, typical values for T1 in NRT data are less than 0.15 but the offline processing uses much stricter values of less than 0.02. This means that whilst the convergence error in the NRT may be as significant as the random error, in the offline retrieval the convergence error will be negligible. In addition the offline processing descends to the lower levels (6 km and 9 km) omitted from the NRT retrieval.

It should be noted that the work in this thesis does not use MIPAS L2 data but instead to ensure consistency the MORSE algorithm (as described in Section 3.6.1) is used to retrieve the necessary pre-requisite variables such as pressure, temperature, H_2O, O_3 and HNO_3.

3.5 Cloud Detection From MIPAS

In order to utilise the MIPAS spectra to their potential, it is vital that cloud contaminated data are identified and removed from the dataset. In order to do this, a cloud detection algorithm was devised that uses the ratio between two regions (or microwindows) of the spectra to calculate a cloud index value. The operational microwindows used for the determination of this cloud index for MIPAS (see Table 3.5) are taken from Spang et al. [2004] where microwindows are defined for bands A, B and D.

The operational cloud detection algorithm operates hierarchically and primarily uses band A for cloud detection and only progresses to bands B and D if band A is unavailable. Throughout this thesis, any discussion of cloud index is referring to the cloud index in band A (CI-A). The two microwindows in this band are 788.20 cm^{-1} to 796.25 cm^{-1} (MW1)and 832.3 cm^{-1} to 834.4 cm^{-1} (MW2). The first of these is dominated by CO_2 and O_3 emissions. In comparison, the second region is dominated by cloud and aerosol emissions. The cloud index for this band (CI-A) is calculated from the ratio MW1/MW2.

Spang et al. [2004] found that for optically thick cloud in band A, the cloud index value (CI-A) was close to 1 whereas for clear sky conditions the CI-A is typically greater than 4. Intermediate values suggest that either optically thin cloud is

CI Band	MW1 (cm^{-1})	MW2 (cm^{-1})	CI threshold	Altitude range [km]
CI-A	788.20 - 796.25	832.3 - 834.4	1.8	12 - 40
CI-B	1246.3 - 1249.1	1232.3 - 1234.4	1.2	12 - 40
CI-D	1929.0 - 1935.0	1973.0 - 1983.0	1.8	12 - 30

Table 3.5. The MIPAS Cloud Index thresholds for bands A, B and D

present (and hence some useful spectral information may still remain in the data) or that a cloud is only partially filling the MIPAS field of view. Operationally, a cloud index threshold of 1.8 is used to distinguish between cloudy and non-cloudy scans between 6 km and 45 km, with a value less than 1.8 being deemed cloud contaminated and screened from the L1B data before the L2 processing is begun [Raspollini et al., 2006].

The effect of cloud filtering the data used in this thesis has been investigated in Chapters 4 and 5. A cloud index of greater than 4 (corresponding to clear sky measurements - [Spang et al., 2004]) is used but the potential for applying the detection algorithm to either partially cloudy ($1.8 < CI < 4$) or fully cloudy ($CI < 1.8$) scenes is also discussed in Chapter 7.

3.6 MIPAS L2 Operational Retrieval And Offline Retrievals

Figure 3.8 shows the spectral range covered by the MIPAS instrument and identifies the positions in the spectrum of some of the key atmospheric species in each of the MIPAS bands.

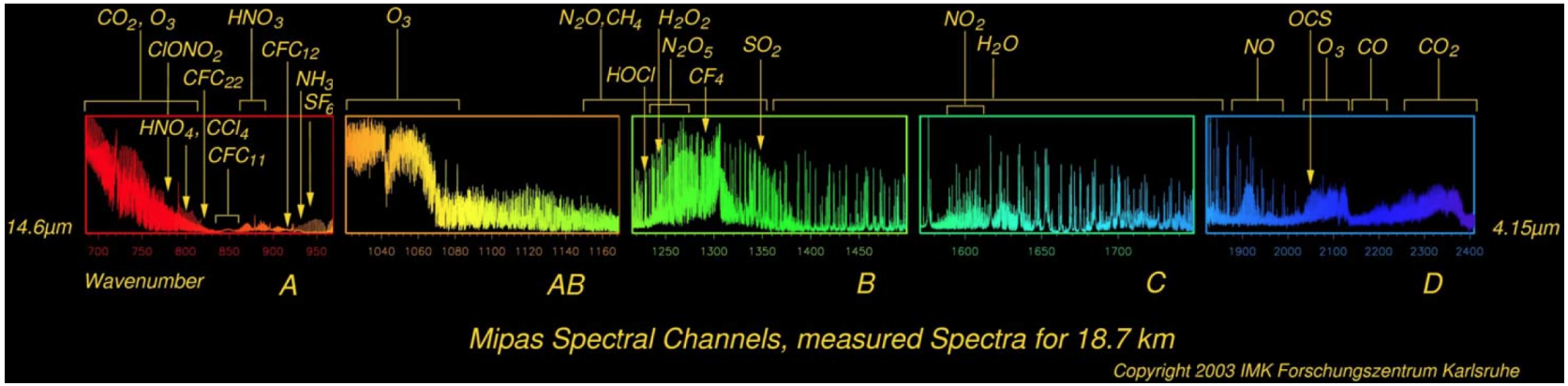

FIGURE 3.8. MIPAS spectral range taken from Fischer et al. [2008] showing the region of the infrared spectrum which MIPAS measures over, 685 cm^{-1} to 2410 cm^{-1}, and the various key atmospheric constituents which it is possible to measure in this region. Source: Fischer et al. [2008]

As discussed in Section 3.4, MIPAS is able to detect a wide range of trace species and is operationally used to retrieve pressure, temperature, O_3, H_2O, CH_4, HNO_3, N_2O and NO_2 from 6 to 68 km. The quality of these retrievals and error analyses can be found in Raspollini et al. [2006] where the L2 processing is described in detail. Discussions on these operational products and their validation are given by Cortesi et al. [2007] (O_3), Wang et al. [2007] (HNO_3) and Wetzel et al. [2007] (NO_2) all of which are available in the MIPAS Atmospheric Chemistry and Physics Special Issue [MIPAS ACP Special Issue, 2006].

In addition to the operationally retrieved species above, various research groups have developed their own distinct retrieval software for exploiting MIPAS spectra. A comparison between different algorithms was performed under the Advanced MIPAS Level 2 Data Analysis (AMIL2DA) project [von Clarmann et al., 2003], which included algorithms from Institut für Meteorologie und Klimaforschung (IMK) with their Retrieval Control Program (IMK-RCP); Oxford University with their Processor To Invert MIPAS Observations (OPTIMO), a precursor to the MORSE scheme used in this thesis; Deutsches Zentrum für Luft- und Raumfahrt (DLR) with two algorithms DLR-a and D-PAC; Istituto di Fisica Applicata Nello Carrara (IFAC) with the Optimized Retrieval Algorithm (ORM), a prototype for the operational retrieval software and Rutherford Appleton Laboratory (RAL) with RET2D. In addition to the algorithms discussed in relation to AMIL2DA, additional schemes are now available such as the Forschungszentrum Jülich (FZJ) [Hoffmann et al., 2005], the OPERA code at the University Of Leicester [Moore and Remedios, 2008] and the GMTR code by Bologna University [Carlotti et al., 2006].

Although these retrieval schemes may differ considerably, each using their own forward model, they are all based on a minimisation of the cost function (as described in Chapter 2). However, there are several distinct differences between the schemes.

- The radiative transfer calculation is performed either by a line-by-line calculations (using the RFM in the case of OPTIMO, MORSE and OPERA), by precalculated absorption cross-sections (in the case of the ORM-based codes) or by less accurate parametric radiative transfer codes (as in the case of the FZJ algorithm).

- The inversion method is also different between schemes. For example, the ORM code retrieves on an altitude grid defined by the tangent altitudes of each individual limb scan whilst other codes operate on a fixed altitude grid.

- The majority of the retrieval codes use a microwindow technique as discussed in this thesis but some codes such as OPERA, RET2D and FZJ operate on broadband spectral radiances much wider than the typical microwindows.

- Apart from for the ORM-based and GMTR codes, the atmospheric state variables are constrained by a regularisation term. This has the benefit of helping to prevent instabilities in the retrieved profile but does mean that some a priori information is contained in the results. OPTIMO, OPERA and FZJ use

the optimal estimation approach from Rodgers [2000] as discussed in Chapter 2, whilst MORSE uses a modified version of this termed sequential estimation (see Section 4.3.2.3). The remaining codes use some variant of Tikhonov regularisation [Tikhonov, 1963]. For the ORM and GMTR codes, global fit approaches are employed which currently have no explicit constraints.

- Finally, some retrieval schemes such as RET2D and GMTR avoid the assumption of a horizontally homogeneous atmosphere by updating the a priori information based on the result of the previous limb scan using a horizontal sequential estimation technique.

The comparison study performed as part of the (AMIL2DA) project [von Clarmann et al., 2003] found that the various different retrieval algorithms were all capable of accurately retrieving known atmospheric states for all of the MIPAS operational species to a level consistent with their error estimates.

These retrieval algorithms have subsequently been used to retrieve a variety of scientific products in addition to the six key species retrieved operationally.

MIPAS is noted as being particularly capable of measuring a number of species relating to the NOy budget including HNO_3, NO, NO_2, $ClONO_2$, N_2O_5, HO_2NO_2 and PAN. In relation to the atmospheric sulphur budget, SO_2 from volcanic plumes [Burgess et al., 2005], OCS [Burgess et al., 2005] and SF_6 [Burgess et al., 2006] have all been successfully retrieved. In addition to these, various other trace species have been detected and retrieved from MIPAS spectra including PAN [Glatthor et al., 2007], HCFC-22 [Moore and Remedios, 2008] and HCN [Glatthor et al., 2009].

3.6.1 MORSE

The MIPAS Orbital Retrieval using Sequential Estimation (MORSE) retrieval algorithm used in this thesis is a 1-dimensional line-by-line optimal estimation algorithm which uses sequential estimation.

For the retrieval from limb measurements, a sequential approach can be taken where each limb measurement is retrieved in turn, from the highest to the lowest altitudes and the retrieved state vector can be incorporated into the retrieval for the next level. The advantage of this approach is that the inversion of the weighting function matrix can be performed faster due to its smaller size. This approach applied sequentially to all altitudes is the same as the simultaneous retrieval of all measurement altitudes but less computationally expensive.

The rationale for the selection of the MORSE algorithm for this thesis was that the advantage of the MORSE scheme is that the sequential estimation technique, by stepping down from high altitudes, helps to prevent instabilities in the retrieved vertical profile and can damp vertically propagating errors in the upwards direction. This technique also leads to the reduction in the size of the matrix which is required for inversion, simplifying the calculation considerably. MORSE also uses the RFM

as the forward model component which is a code developed specifically for the simulation of MIPAS radiances and has been extensively studied previously both within our group and the wider MIPAS community [von Clarmann et al., 2003]. Additionally, practical constraints were also taken into consideration, MORSE is capable of running using pre-calculated look-up tables in order to speed up the computationally expensive radiative transfer calculations and is heavily optimised in order to use a minimal amount of computational resources, allowing it to run alongside other processes (A. Dudhia, personal communication).

3.7 Summary

This chapter introduces the MIPAS instrument, outlining the background and objectives of the mission as well as describing how the instrument performs its measurements of atmospheric limb emission radiances. The measurement geometry and the various observation modes are discussed, although it should be noted that the majority of work performed in this thesis uses full spectral resolution nominal measurements.

Detailed information on the performance and calibration of the instrument is presented, with particular reference to the offset, gain, ILS and NESR quantities and how they impact upon the performance of the instrument.

The data processing chain is briefly described, outlining the process by which raw interferograms are converted into Level 1B atmospheric limb emission spectra and ultimately into the Level 2 geophysical quantities. In addition to this, the process for screening cloud-contaminated data by calculating a cloud index from the ratio between two spectral region is discussed.

Finally, a discussion of both operational and scientific retrieval algorithms summarises the various approaches towards retrieving atmospheric constituents from MIPAS spectra. These different schemes have been shown in the literature to be capable of retrieving scientific products from MIPAS data such as SO_2, PAN and HCFC-22.

Justification for the selection of the MORSE retrieval scheme used throughout this work has been provided and has been stated in terms of its ability to use the sequential estimation approach not only to prevent retrieval instabilities but also in terms of the computational requirements of the algorithm.

Chapter 4

Detection Of C_2H_2 And C_2H_6

4.1 Detection Methodology

In Chapter 3, it was noted that the retrieval processing can take considerable time and require substantial computing resources. This chapter discusses the development of a fast detection algorithm which is capable of identifying the spectral signature of both C_2H_2 and C_2H_6 in MIPAS data. It shows that the use of such a detection algorithm is:

- Computationally simple and hence very fast, especially when compared to a computationally expensive optimal estimation retrieval code.
- Capable of reflecting information on the signature of the gas observed in the spectra.
- Capable of identifying interesting geophysical features which can be explored further using a more rigourous retrieval approach.

The development of this detection algorithm is discussed in detail and the results of its application to both C_2H_2 and C_2H_6 spectral signatures are shown.

4.1.1 C_2H_2 Microwindow And Contaminating Species

A simulated MIPAS spectrum is shown in Figure 4.1 where the contributions from C_2H_2 and each interfering species to the total radiance (black) are presented. The Oxford Reference Model (RFM) [Dudhia, 2005] was used to model the spectra as observed by MIPAS at 12 km. The RFM is a line-by-line radiative transfer model based on the GENLN2 model [Edwards, 1992] and can simulate the MIPAS infrared spectra taking into account the instrument lineshape and field of view. The spectroscopic information is taken from the HITRAN 2004 spectral database [Rothman et al., 2005; Jacquemart et al., 2003] and in this case the simulation

uses the RAMStan (Reference Atmospheres for MIPAS: Standard atmospheres) standard atmospheric climatology [Remedios et al., 2007] with an enhancement of C_2H_2 typical of biomass burning based on profiles from Rinsland et al. [2005].

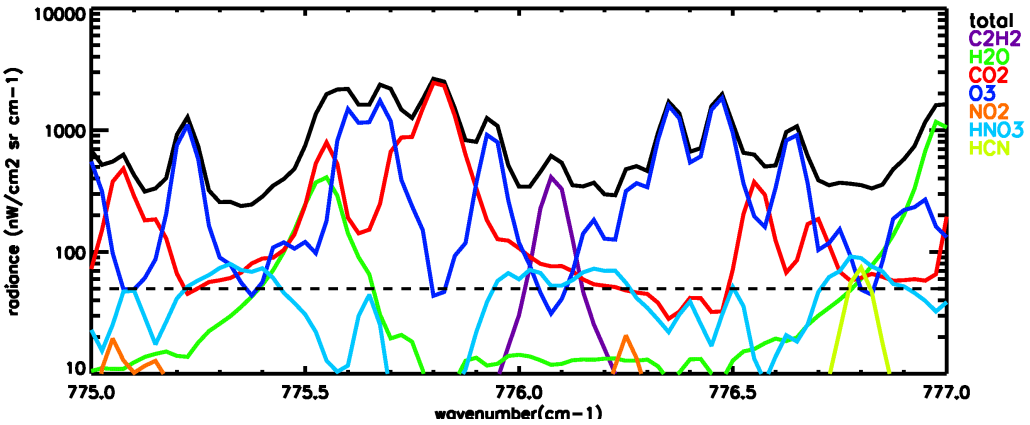

FIGURE 4.1. RFM simulation of a 12 km MIPAS spectrum at a 0.025 cm^{-1} resolution covering a 2 cm^{-1} range around the prominent C_2H_2 feature at 776.075 cm^{-1}. This shows the contribution to the C_2H_2 microwindow from interfering species and uses a standard atmosphere background with an enhanced C_2H_2 profile typical of biomass burning observations.

The ν_5 C-H bend centred at 730 cm^{-1} C_2H_2 peak (purple) can be seen as the dominant feature in the 776.0 cm^{-1} to 776.15 cm^{-1} spectral range (Fig. 4.2) and unlike the other C_2H_2 absorption lines in this region at 755 cm^{-1}, 762 cm^{-1} and 766.7 cm^{-1} the line is not masked by a strong ozone feature [Rinsland et al., 1998]. The clear absorption line within the microwindow allows the unambiguous identification of enhanced C_2H_2 in MIPAS L1B spectra. In addition the feature may also be distinguished, albeit with some difficulty due to noise, at background concentrations.

4.1.2 Automated Detection Scheme

As the C_2H_2 spectral signature is readily detected in MIPAS L1B spectra it is possible to use the estimated peak intensity of the signature to qualitatively indicate the amount of C_2H_2 present in the atmosphere at the tangent altitude.

The following two examples show a strong and weak C_2H_2 signal respectively. Both examples are from clear spectra with a cloud index of over 5 at the 12 km MIPAS nominal tangent altitude. Figure 4.3 shows an example of a MIPAS L1B spectrum where the peak intensity of the C_2H_2 is on the order of 250 $nW/cm^2 \cdot sr \cdot cm^{-1}$ and represents a strong C_2H_2 spectral signal. In contrast, Figure 4.4 shows a weak C_2H_2 signal which is barely distinguishable from the baseline and with an apparent peak of just 20 $nW/cm^2 \cdot sr \cdot cm^{-1}$ is below the estimated 40 $nW/cm^2 \cdot sr \cdot cm^{-1}$ noise

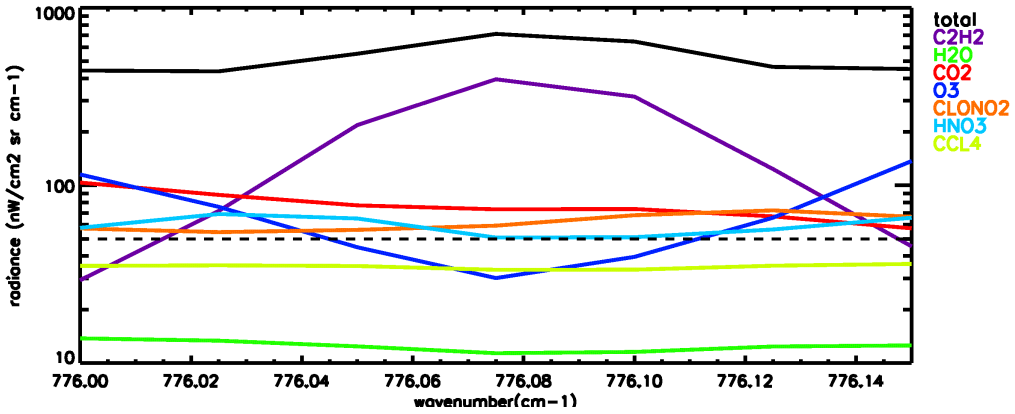

FIGURE 4.2. RFM simulation of a 12 km MIPAS spectrum at a 0.025 cm^{-1} resolution showing the contribution to the C_2H_2 microwindow (776.0 cm^{-1} to 776.15 cm^{-1}) from interfering species using a standard atmosphere background and an enhanced C_2H_2 profile typical of biomass burning observations.

limit. The fact that a signal appears to be apparent below the estimated noise limits suggests that either the value for the noise is conservative and in reality it is much less or that the noise may be correlated due to apodisation effects. An analysis of the noise and its implications on the detection scheme is discussed in Section 4.1.6.

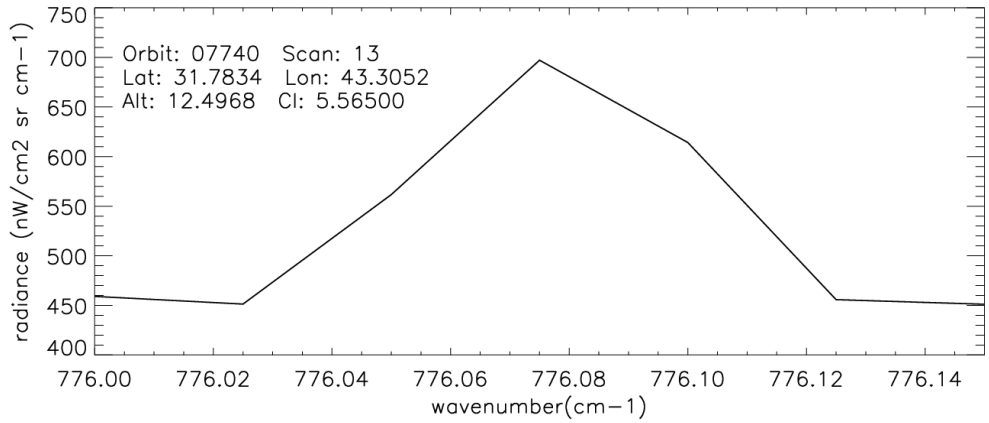

FIGURE 4.3. An example of a MIPAS spectrum identified as containing a strong C_2H_2 signal at a 12 km nominal altitude from Scan 13 Orbit 07740 on 23rd August 2003 over the Middle East.

Although the above has shown that it is clearly possible to identify qualitatively the amount of C_2H_2 present in a given MIPAS measurement, there is a significant

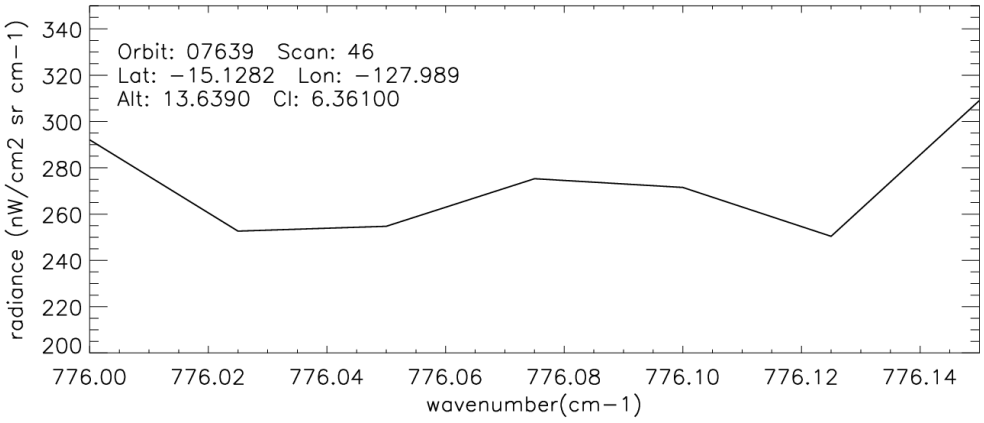

FIGURE 4.4. An example of a MIPAS spectrum identified as potentially containing a weak C_2H_2 signal at a 12 km nominal altitude from Scan 46 Orbit 07639 on 16th August 2003 over the South Pacific Ocean.

problem in utilising this to provide global C_2H_2 distributions, namely the requirement to analyse each of the large number of measurements which MIPAS produces. At each altitude, MIPAS obtains approximately 74 scans per orbit and with 15 orbits per day it can be considered that whilst looking manually at single events it may be trivial to qualitatively identify the amount of C_2H_2 present. When analysing days, months or even years of data it becomes necessary to automate and optimise the methodology employed.

An automated detection scheme requires the ability to perform basic pattern recognition to distinguish the strength of a C_2H_2 spectral peak. In addition, it must be robust enough to handle the large variations in MIPAS radiance spectra resulting from partially cloudy scenes ideally without producing false positives where no peak is present.

Figure 4.5 shows a schematic of the detection algorithm applied to a spectrum containing a strong C_2H_2 peak radiance signal. The detection algorithm developed first reads the MIPAS L1C spectra between 776.0 cm^{-1} and 776.15 cm^{-1} containing seven spectral points. For all cloud-free scenes (CI $\geq$ 4 [Spang et al., 2004]), a baseline is then generated by calculating an average value from a point either side of the C_2H_2 peak (776.025 cm^{-1} and 776.125 cm^{-1}) in this microwindow. The radiance from this baseline to the C_2H_2 peak at 776.075 cm^{-1} is then calculated. If this value is greater than a threshold value, the C_2H_2 peak can be distinguished from MIPAS noise (which has a conservative value of 40 $nW/cm^2 \cdot sr \cdot cm^{-1}$ [Kleinert et al., 2007]) then the spectrum is flagged as containing C_2H_2. For all spectra flagged as containing C_2H_2, the value of the peak radiance above the baseline is used to quantify the strength of the C_2H_2 peak. Note that the final detected signal is in radiance units ($nW/cm^2 \cdot sr \cdot cm^{-1}$). This process is outlined in Figure 4.6.

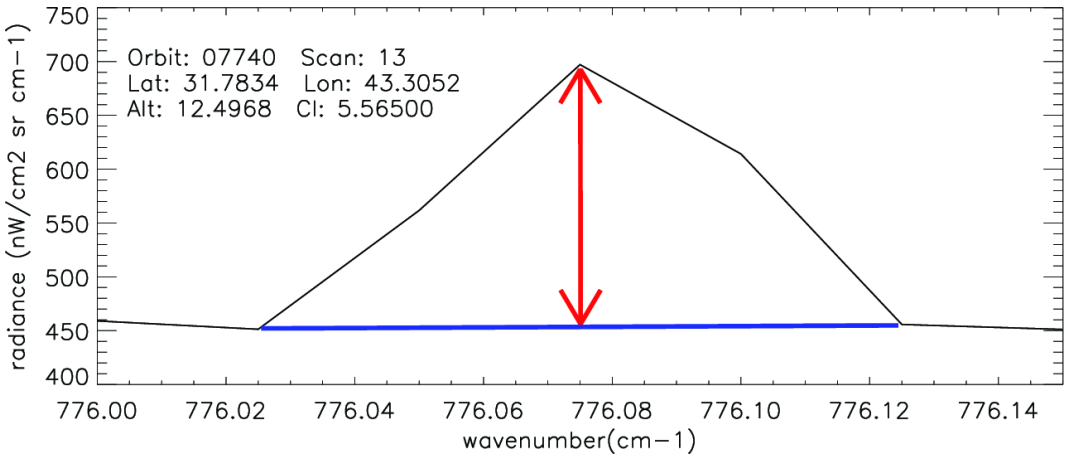

FIGURE 4.5. Example showing the approach taken in identifying the C_2H_2 signal. First a baseline is calculated for the specific case of C_2H_2 in this microwindow (blue line). Next the difference between the C_2H_2 peak and the baseline is calculated (red line). This value is referred to throughout as the C_2H_2 peak radiance signal and a high value identifies a spectrum as containing a significant contribution from C_2H_2.

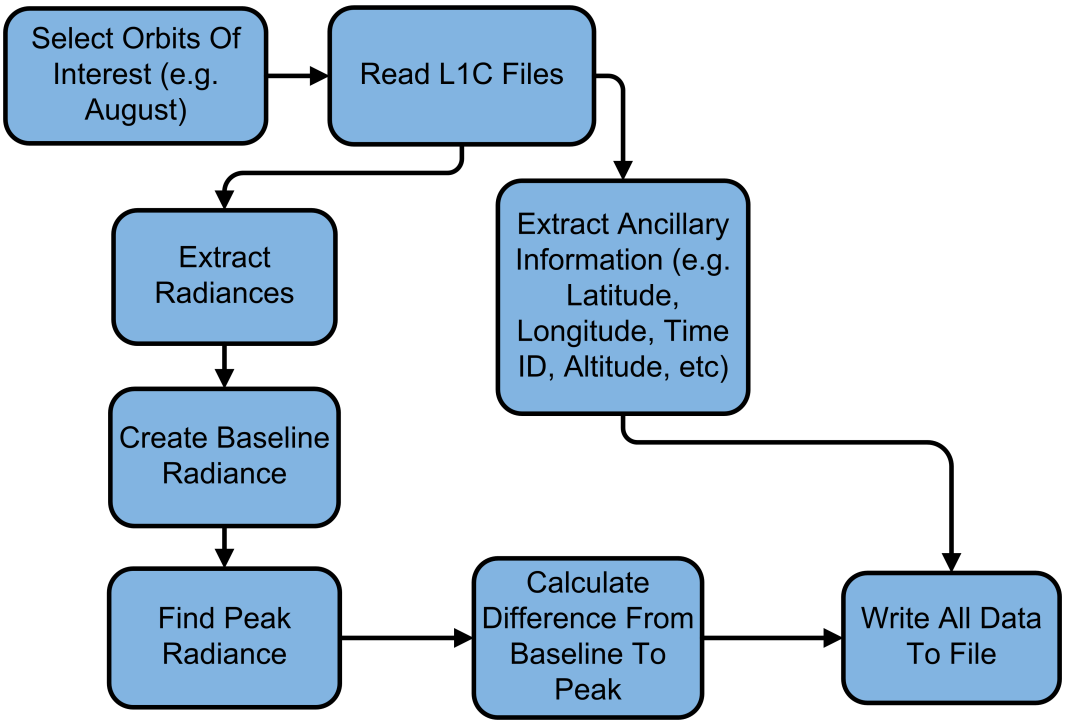

FIGURE 4.6. A flowchart detailing the detection algorithm process. The spectrum is read in, a baseline is generated within the designated C_2H_2 microwindow and the distance to the C_2H_2 peak is calculated. This data along with ancillary information such as the time and geolocation of the measurement point are recorded to a data file.

4.1.3 Analysis Of Noise

As discussed in Section 3.3.3, the MIPAS NESR is calculated and made available as a product in the L1B data file. Figure 4.7 shows the frequency distribution for the MIPAS NESR values for the 12 km nominal tangent altitude for all of the August 2003 data calculated within the C_2H_2 microwindow between 776.0 cm^{-1} and 776.15 cm^{-1}. The maximum NESR value was found to be 73.7 $nW/cm^2 \cdot sr \cdot cm^{-1}$ with the smallest value just 22.1 $nW/cm^2 \cdot sr \cdot cm^{-1}$. The distribution was found to be approximately Gaussian as expected with a mean of 29.4 $nW/cm^2 \cdot sr \cdot cm^{-1}$ which is lower than the conservative estimate of 40 $nW/cm^2 \cdot sr \cdot cm^{-1}$.

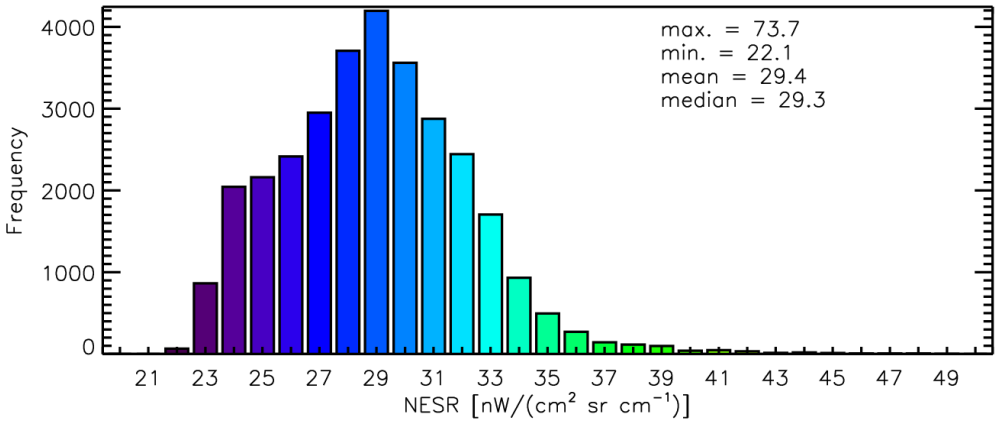

FIGURE 4.7. Frequency distribution of MIPAS NESR values for the 12 km nominal tangent altitude for August 2003.

However, a further significant issue with the noise estimate is that the NESR is calculated for an unapodised spectrum. As it is necessary to apodise the spectra in order to suppress spectral "ringing" due to the sinc function associated with the fourier transformation of the truncated interferogram, this apodisation effect must be taken into consideration.

In order to examine the effect of apodisation on a noisy spectrum, a random Gaussian distribution was generated with a mean of 2000 $nW/cm^2 \cdot sr \cdot cm^{-1}$ and a standard deviation, or sigma, of 40 $nW/cm^2 \cdot sr \cdot cm^{-1}$. The standard deviation was then calculated separately for the distribution and found to be approximately the expected 40 $nW/cm^2 \cdot sr \cdot cm^{-1}$. The distribution was apodised (Fig. 4.8) in the same way that the MIPAS L1B spectra are apodised before use and the resulting standard deviation was found to have reduced to approximately 25 $nW/cm^2 \cdot sr \cdot cm^{-1}$. This analysis was repeated with various distributions using different initial standard deviations and in each case the standard deviation once apodised was found to be approximately 60% of the original value.

Having shown that the effect of apodisation of the MIPAS L1B spectra is effectively to reduce the average value of the noise to 60% of the original value, this

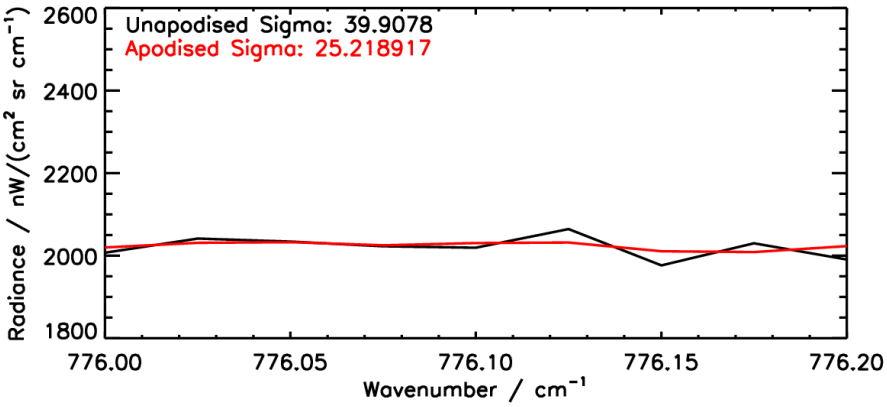

FIGURE 4.8. The effects of apodising a random Gaussian distribution with a mean of 2000 nW/cm^2·sr·cm^{-1} and a standard deviation of 40 nW/cm^2·sr·cm^{-1}. The standard deviation is reduced from 40 nW/cm^2·sr·cm^{-1} to approximately 25 nW/cm^2·sr·cm^{-1}.

implies that although Figure 4.7 gives a mean noise value of 29.4 nW/cm^2·sr·cm^{-1}, the value once apodised may be as low as 17 nW/cm^2·sr·cm^{-1}. The minimum value of 22.1 nW/cm^2·sr·cm^{-1} may be just 13 nW/cm^2·sr·cm^{-1}. The implications of this are that whilst 40 nW/cm^2·sr·cm^{-1} is a conservative estimate of the NESR, there may exist a detectable signal below this threshold so some care must be taken when choosing an appropriate noise threshold. However, as in the case of C_2H_2, due to the fact that a typical background concentration is above even a conservative noise threshold the effect that this has is minimal. It does however become important when attempting to perform the detection of species with a weaker spectral signature which may be the case in the future.

4.1.4 Dependence Of Detection Algorithm On Temperature

Some care must be taken when interpreting detection results over multiple seasons on a global scale as the C_2H_2 peak radiance has some temperature dependence which will result in a higher peak radiance being calculated for higher temperatures.

A series of simulated spectra were produced with the RFM for the same C_2H_2 concentrations using the equatorial and mid-latitude MIPAS reference atmosphere temperature and pressure profiles. These simulations suggest that the temperature dependence of C_2H_2 is relatively small. The maximum variation of 8 nW/cm^2·sr·cm^{-1} is significantly less than the estimated MIPAS spectral noise of 40 nW/cm^2·sr·cm^{-1}.

Additionally the temperature jacobian was calculated and it was found that for a 1 K change in temperature at 12 km, the C_2H_2 peak radiance will increase by

approximately 3 nW/cm^2·sr·cm^{-1}. Assuming that the temperature dependence is linear, a reasonable temperature variation of 10 K will result in an increase in the peak radiance of approximately 30 nW/cm^2·sr·cm^{-1}, again similar to the estimated MIPAS noise.

This result indicates that the observations of strongly enhanced C_2H_2 peak radiances (often greater than 200 nW/cm^2·sr·cm^{-1}) can not be attributed to temperature changes and that a large amount of C_2H_2 must be present. However, a small temperature effect is present and the potential for systematic biases in the detected peak radiance between seasons must be considered carefully. The discussion of the removal of this effect using the MIPAS L2 temperature data is discussed in the future work section of Chapter 7.

4.1.5 Dependence Of Detection Algorithm On Cloud

In order to assess the effect of cloud-contamination on the detected peak radiance signal a sensitivity study was performed. A background aerosol extinction profile was modified in order to introduce a cloud at the 12 km tangent altitude with varying extinction values, ranging between $5x10^{-5}$ and $1x10^{-1}$ km^{-1}; the cloud was defined between 10 and 14 km as a trapezoid with identical values at 11,12 and 13 km, falling away to the background values above and below. These profiles were then used as input into the RFM along with the MIPAS specific characteristics (such as FOV, ILS, etc) to simulate atmospheric spectra with varying degrees of cloud contamination. The MIPAS Cloud Index [Spang et al., 2004] was calculated for these spectra and the detection algorithm was used to obtain the C_2H_2 peak radiance values.

Starting with a C_2H_2 peak radiance of 247 nW/cm^2·sr·cm^{-1} in the non-cloudy case, the effect of introducing cloud is shown in Figure 4.9 which plots the obtained C_2H_2 peak radiance against the CI value for each simulation. For the case where no cloud is present the C_2H_2 peak radiance was found to be 247 nW/cm^2·sr·cm^{-1}. The effect of adding a cloud with a corresponding CI value of 4 caused a reduction in this value of 19 nW/cm^2·sr·cm^{-1}, down to 228 nW/cm^2·sr·cm^{-1}. This is the maximum effect that cloud would have on the C_2H_2 peak radiance as any stronger effects (i.e. CI < 4.0) are removed via filtering out the lower CI values; note simulations for CI < 1.8 (i.e. thick cloud) should be treated with caution as scattering is not included in these RFM calculations.

4.1.6 Dependence Of Detection Algorithm On Interfering Species

As for the case of cloud, a sensitivity study was performed for the various interfering species in the C_2H_2 microwindow (see Fig. 4.2). The VMR of each gas was perturbed by 300% of the nominal RAMStan reference atmosphere value and the radiance in the C_2H_2 microwindow was simulated for each case (Fig. 4.10). As

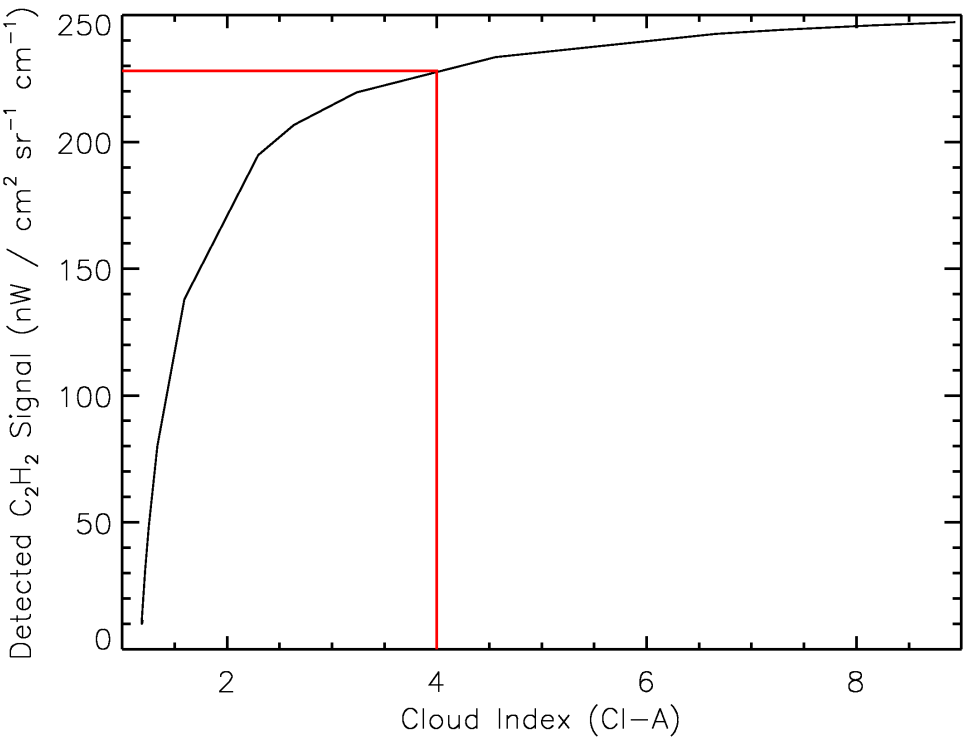

FIGURE 4.9. C_2H_2 peak radiances (nW/cm^2·sr·cm^{-1}) against MIPAS CI value for simulated cloudy spectra with varying cloud extinction profiles. The red line denotes a CI value of 4 and the corresponding C_2H_2 peak radiance which would be detected for that degree of cloud. The effect of cloud is found to be minimal to the detected peak radiances, with a maximum influence of reducing the value by 19 nW/cm^2·sr·cm^{-1}.

expected it was found that the majority of interfering species had little effect. For those that did produce an effect (H_2O, CO_2, CCl_4), the result was a similar shift in both the baseline and peak leading to the detected peak radiance signal being largely unaffected.

Table 4.1 shows the value of the detected C_2H_2 peak radiance (in nW/cm^2·sr·cm^{-1}) in each case where the interfering gas has been perturbed, along with the difference from the unperturbed case. The largest differences between the perturbed and unperturbed cases were -7 nW/cm^2·sr·cm^{-1} for H_2O and +6.3 nW/cm^2·sr·cm^{-1} for CO_2, with the remaining differences on the order of 1 nW/cm^2·sr·cm^{-1}. It should also be noted that a 300% perturbation is in some cases far more than even a very extreme realistic perturbation. This section has therefore shown that the detection algorithm is robust enough to remain unaffected by interfering species. This is mainly due to the fact that the C_2H_2 microwindow is only 0.15 cm^{-1} wide and that any interfering species are relatively flat over this range, leading to a similar shift

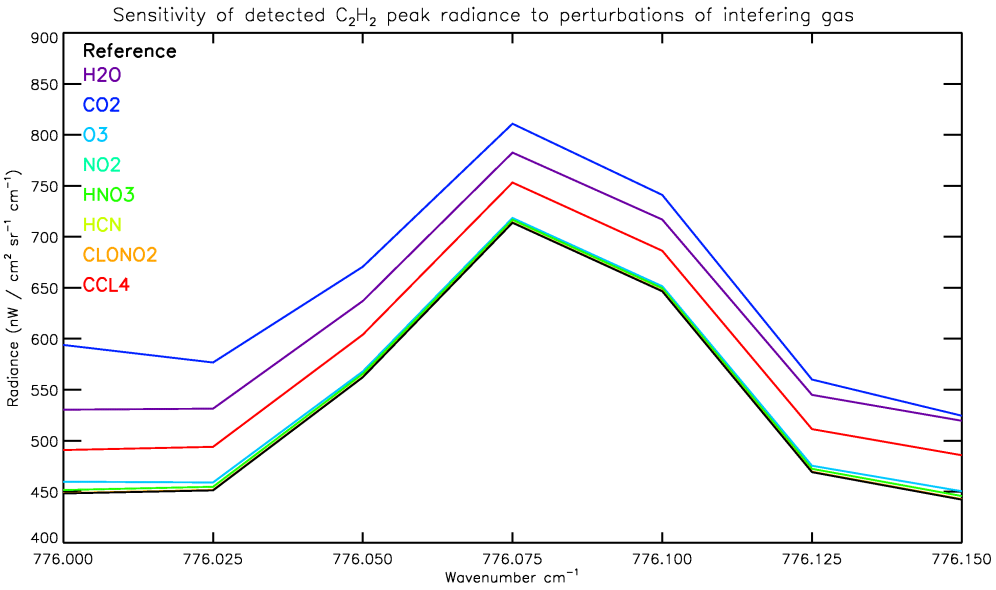

FIGURE 4.10. Simulated spectra in the C_2H_2 microwindow between 776.0 cm^{-1} and 776.15 cm^{-1} where each interfering species (see legend) has been increased to 300% of its RAMStan reference atmosphere value.

in both the baseline and peak.

Gas	Detected Peak Radiance	Difference From Reference
	$nW/cm^2 \cdot sr \cdot cm^{-1}$	$nW/cm^2 \cdot sr \cdot cm^{-1}$
None (ref)	244.6	N/A
H2O	237.6	-7
CO2	250.9	6.3
O3	243.0	-1.6
NO2	244.5	-0.1
HCN	244.2	-0.4
CLONO2	244.5	-0.1
CCL4	244.5	-0.1

Table 4.1. Effect on the C_2H_2 detected peak radiance for the cases shown in Figure 4.10 where each interfering species has been increased to 300% of its RAMStan reference atmosphere value. This effect was found to be minimal for all of the interfering species, with a maximum effect of 7 $nW/cm^2 \cdot sr \cdot cm^{-1}$ for H_2O.

4.2 C_2H_2 Detection Results

The detection algorithm described above was applied to MIPAS data from October 2003 MIPAS L1B spectra for the 12 km nominal MIPAS tangent altitude. All of the results shown in this chapter are for the 12 km nominal tangent altitude.

As the detection algorithm requires a clearly identifiable C_2H_2 peak, the detection limit here is higher than for a retrieval which is capable of fitting much lower concentrations. Even so, due to the large difference in radiance between high and low C_2H_2 amounts of several hundred $nW/cm^2 \cdot sr \cdot cm^{-1}$, it is possible to clearly detect large C_2H_2 peak values above the 40 $nW/cm^2 \cdot sr \cdot cm^{-1}$ conservative estimates of the noise levels. It was shown in Section 4.1.6 that once apodised the noise levels may be lower than 20 $nW/cm^2 \cdot sr \cdot cm^{-1}$, allowing weaker spectral signatures to be distinguished from the noise.

4.2.1 Case study - 21st October 2003

The following case study will show the detection algorithm applied firstly to a single MIPAS orbit, then a whole day and finally a whole month. In viewing the detection in this way it is possible to demonstrate the effects of coverage and cloud/aerosol contamination on the final data set as well as to provide a full walkthrough of the process.

Figure 4.11 shows the results for each of the 71 scans performed by MIPAS in orbit number 08585 on 21st October 2003. This orbit begins off the southern west coast of Africa and ascends over Eastern Africa and Eastern Europe, reaching the North Pole and then descending over Alaska and the Pacific Ocean down to

the South Pole and finally ending over south-west Africa. In order to reduce the influence of cloud contamination on the spectra, any scan where the cloud index (as described by Spang et al. [2004]) is less than 4.0 is removed from the process and no further analysis is made of it. The effect of applying this cloud filter is that out of the original 71 scans in the orbit, 16 are removed, leaving 55 scans to apply the detection algorithm to. In the case of orbit 08585, and in MIPAS observations in general, the majority of the scans removed as cloudy were located over the equator/tropics.

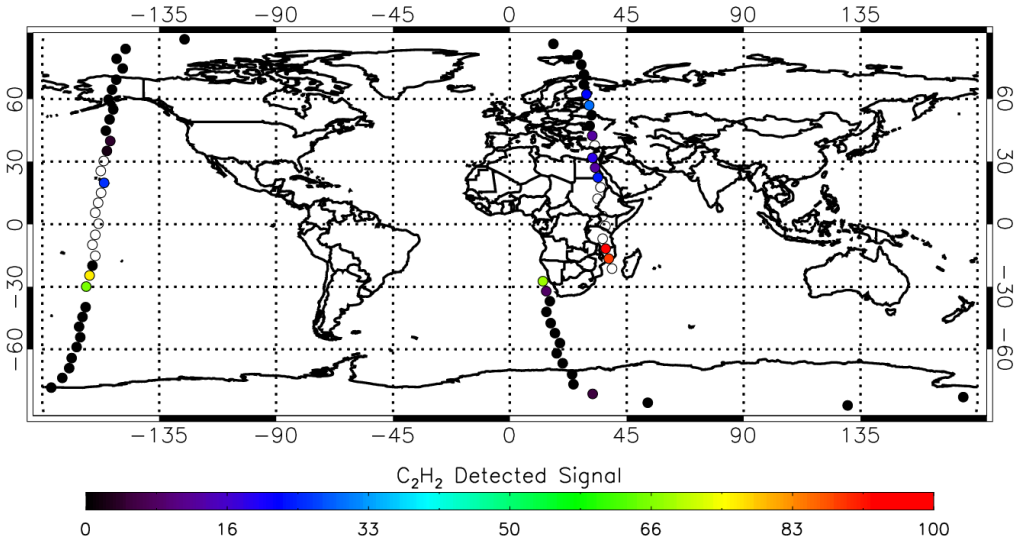

FIGURE 4.11. The C_2H_2 detected signal (nW/cm^2·sr·cm^{-1}) for the whole of Orbit 08585 on 21st October 2003. The high values observed over South-East Africa coincide with biomass burning outflow during this period.

The detection algorithm was applied to the remaining 55 scans for orbit 08585 and the value of the detected C_2H_2 peak radiance for these scans is shown. A signal of over 100 nW/cm^2·sr·cm^{-1} was observed for two scans (scan numbers 02 and 03), both over South-Eastern Africa, where various species have previously been identified in the biomass burning outflow passing over the Madagascar region [Glatthor et al., 2007]. To verify that the detection algorithm is functioning correctly and is successfully picking out the strong signals, the L1B MIPAS spectrum for scan 03 is shown in Figure 4.12 and shows the strong C_2H_2 peak radiance signal that was identified. Moderate values of C_2H_2 peak radiances between 30 nW/cm^2·sr·cm^{-1} and 70 nW/cm^2·sr·cm^{-1} are also observed both off the coast of Southern Africa and in the Pacific Ocean.

The next step in utilising the detection algorithm was to apply it to an entire day of data, in this case the 21st October 2003, which amounted to 14 orbits with approximately 74 scans each. These results are shown in Figure 4.13. As can be seen from just a single day of data, there is reasonable coverage in the polar and

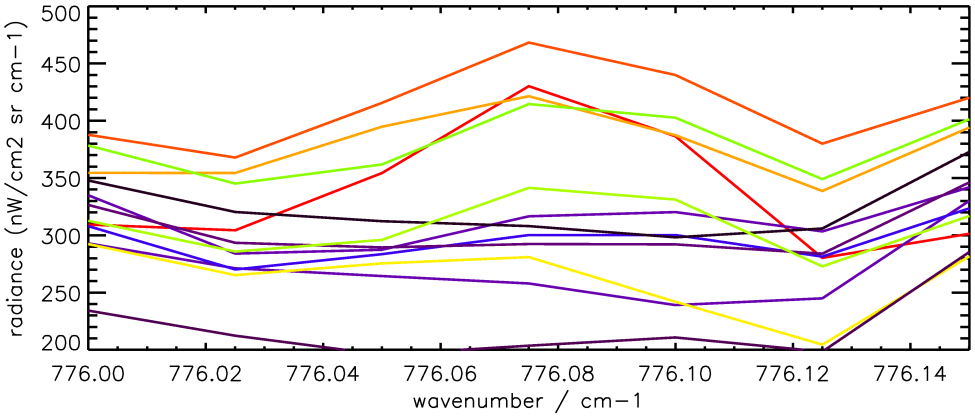

FIGURE 4.12. The MIPAS L1B apodised spectra in the C_2H_2 microwindow for a selection of scans from Orbit 08585 at the 12 km nominal altitude coloured by peak radiance signal. The difference in the C_2H_2 spectra relating to high and low concentrations of C_2H_2 is clearly shown. A high C_2H_2 peak radiance signal of 149.9 nW/cm^2·sr·cm^{-1} is observed over South-East Africa (see Fig. 4.11) whilst much lower values with no significant C_2H_2 peak are observed elsewhere.

mid-latitude regions but far less coverage in the tropics due to cloud. Hence an accumulation of data from multiple days or weeks becomes necessary to achieve the required data coverage.

Various strong C_2H_2 peak radiance signals with values over 100 nW/cm^2·sr·cm^{-1} are identified over Southern Africa, India, China and North-Western Australia, all of which are typical biomass burning regions. One important feature to note from this result is the consistency in the strength of the detected C_2H_2 signal, not only between adjacent scans in an orbit but also between scans from different orbits over the same area. This consistency can clearly be seen over South-East Africa where four adjacent scans, taken from two different orbits, form a cluster of high (red) values. The same consistency is seen over Western Australia where two high values from different orbits coincide against a much lower background. It is not only the consistency between the location of high C_2H_2 values which is important but also the consistency between the other ranges of values. For example, in the middle of the Atlantic Ocean between South America and Africa there is a cluster of four intermediate measurements with values between 50 and 60 nW/cm^2·sr·cm^{-1}. The fact that there is such good agreement even though again the cluster is comprised of measurements from different orbits gives confidence that there is consistency with our methodology.

Figure 4.14 shows the detection algorithm applied to data for the whole of October 2003 with the results gridded using a weighted distance mean (see Section 4.2.2). Overall there is reasonable global coverage, albeit with gaps due to cloud

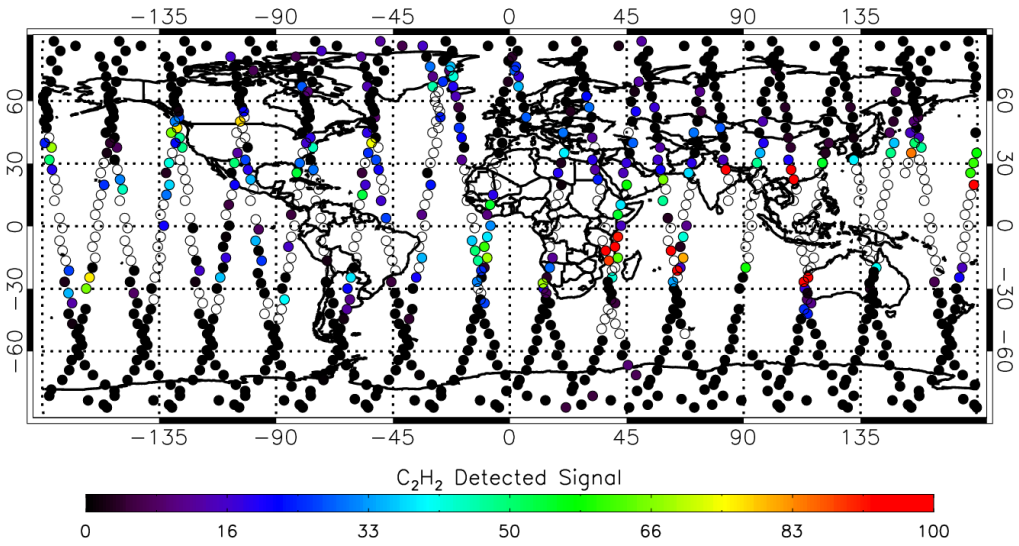

FIGURE 4.13. The C_2H_2 detected peak radiance signal for the entire day, 21st October 2003. High values are observed over Southern Africa, India, China and North-Western Australia, all locations identified as biomass burning regions.

over equatorial regions. It should also be noted that these regions with poor spatial coverage due to cloud or aerosol, namely Central Africa, South-East Asia and the Amazon region of South America, are also regions that typically exhibit strong biomass burning during October. Even with the reduced coverage, significant enhancements of C_2H_2 are observed over Southern-Africa and South-East Asia. Substantial transport between Asia and North America is observed with large C_2H_2 enhancements over the North of the Pacific Ocean. In addition, transport from Africa to both Australia and South America is clearly evident.

4.2.2 Weighted-Distance Mean Gridding Of C_2H_2 Detection Results

As in the case of Figure 4.14 and all other averaged plots presented in this thesis, a weighted-distance mean gridding technique is used.

This technique uses a regular grid with a 5° resolution. MIPAS observations within 10° of the centre of each grid box contribute towards the final value for that grid box with the weighting of their contribution falling off as a function of the square of the distance from the centre of the grid box. In this case the specific distance-weighting function used was $1 - {x_g}^2/r^2$ where x_g is the distance from the centre of the grid box and r is the radius of influence which in this case was chosen to be 10°. Figure 4.15 shows the relative contribution that each point would make towards the final value for a grid box.

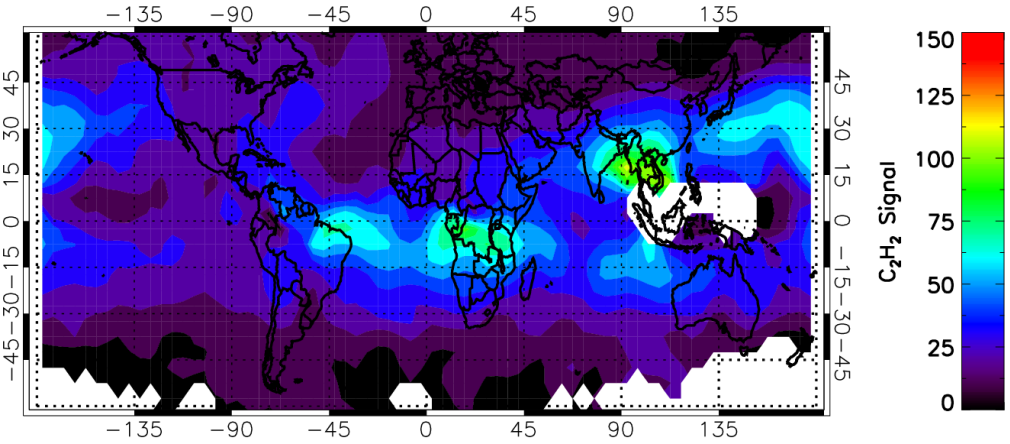

FIGURE 4.14. The monthly 5° gridded C_2H_2 detected signal for the October 2003. The African and South-East Asian regions are the most dominant biomass burning regions during this time of year and a clear C_2H_2 enhancement is observed over these areas.

The combination of this function with the selected gridding resolution produces an optimal weighting with a large contribution from any values falling within the grid box and a suitably lower weighting to values outside the grid box. This means that the gridded average is not inappropriately weighted by the MIPAS measurement which happens to fall at the centre of a grid box but that the nearby measurements are also taken into account giving a more realistic average of the detection value within each grid box. If instead, the value associated with each grid box was simply the average of the values inside it, this would result in unphysical gradients in the C_2H_2 distribution at the edge of each grid box. This method ensures this is not the case and effectively smooths the distribution between grid boxes whilst maintaining a robust average of the individual observation values. In order to produce plots of the distributions, these weighted-distance mean gridded values are then used to produce contour plots.

4.2.3 C_2H_2 Detection For 2003

Having demonstrated that this detection approach provides reasonable and consistent results for October 2003, the detection algorithm was applied to MIPAS L1B spectra for the whole of 2003 to examine the variability in the C_2H_2 distribution and intensity throughout the year with particular focus on the Asian monsoon anticyclone. The results were subsequently separated into months and are discussed in the following section.

Figure 4.16 shows the C_2H_2 detection results for the months of January, February, March and April 2003. Strong enhancements are observed over biomass burning

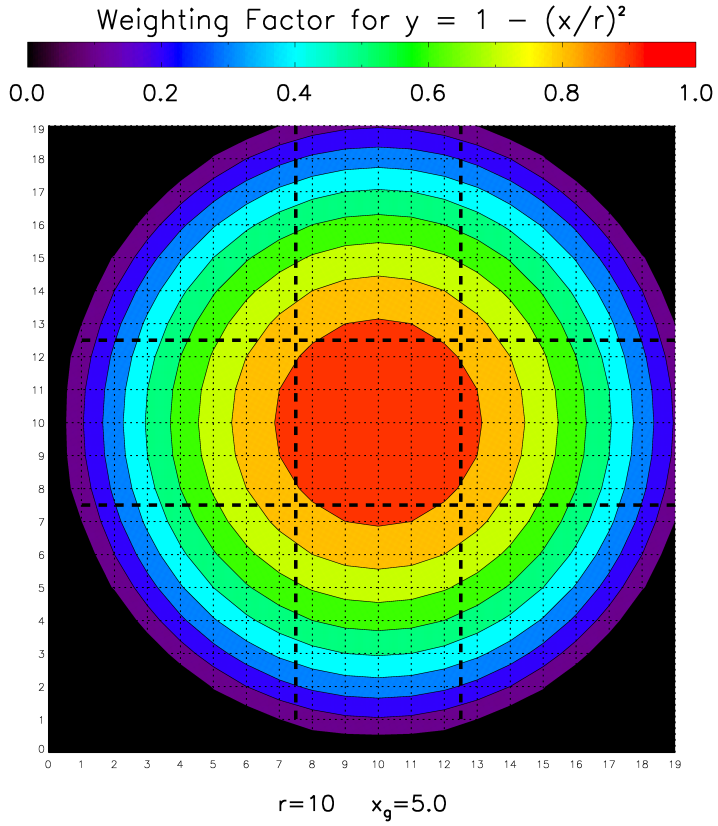

FIGURE 4.15. The weighted-distance mean relative contribution in a 5° grid box for points within a 10° radius of the grid box centre.

regions in Northern Africa, Southern Africa and Asia. As well as these enhancements, considerable outflow from these regions occurs with the strength of the Asian transport towards North America particularly notable at this time, in March and April. This transport appears to almost encompass the sub-tropics, passing over Central and North America and merging with more local emissions before continuing eastwards into the Atlantic Ocean. Liang et al. [2007] note that this long-range transport of Asian pollution across the Pacific is expected to reach a maximum in spring due to the strong westerly winds and occurs in the middle to upper troposphere [Bey et al., 2001].

The AATSR fire map for April 2003 (Fig. 4.19) confirms that there is significant fire activity in the sub-tropics at this time, with a large number of detected fires not only in Asia but also in Central America and Africa. This suggests that whilst Asia is the main source for the enhancements observed transported over the Pacific Ocean, the emissions from Central America and Africa also contribute to the enhancement seen across the whole of the sub-tropics.

As outlined in Chapter 1, the Asian monsoon anti-cyclone is a dominant feature in the summer months in the Northern Hemisphere, with its influence beginning

around late May and persisting until early September. In contrast to earlier in the year, the distribution of C_2H_2 during the monsoon period from May until August is significantly different (Fig. 4.17) and demonstrates the dominant influence of the anticyclone in unprecedented detail. In the Northern Hemisphere, the monsoon anticyclone leads to a clear chemical isolation over the Middle East and Asian regions where a particularly strong enhancement of C_2H_2 is observed throughout the summer (as noted by Park et al. [2008]). Large C_2H_2 enhancements are still observed over regions such as Southern Africa and Asia and some zonal transport still exists, particularly in the Southern Hemisphere from Southern Africa towards Australia and in the Northern Hemisphere from Asia towards North America. However, the formation of the monsoon anticyclone acts as a barrier to much of the Northern Hemisphere zonal transport observed in previous months with significantly less C_2H_2 observed over North America and the Atlantic Ocean.

This chemical isolation caused by the monsoon anticyclone clearly persists over the whole of the summer while the anticyclone is still active. As the monsoon reaches its end during September, the barrier to transport is removed but due to the much lower levels of biomass burning in the sub-tropics in October and November, the large-scale zonal transport of C_2H_2 is not as evident as it was before the monsoon (Fig. 4.18). Instead there is a relatively uniform distribution with low C_2H_2 values and only a few areas of moderate enhancements such as over South-East Asia.

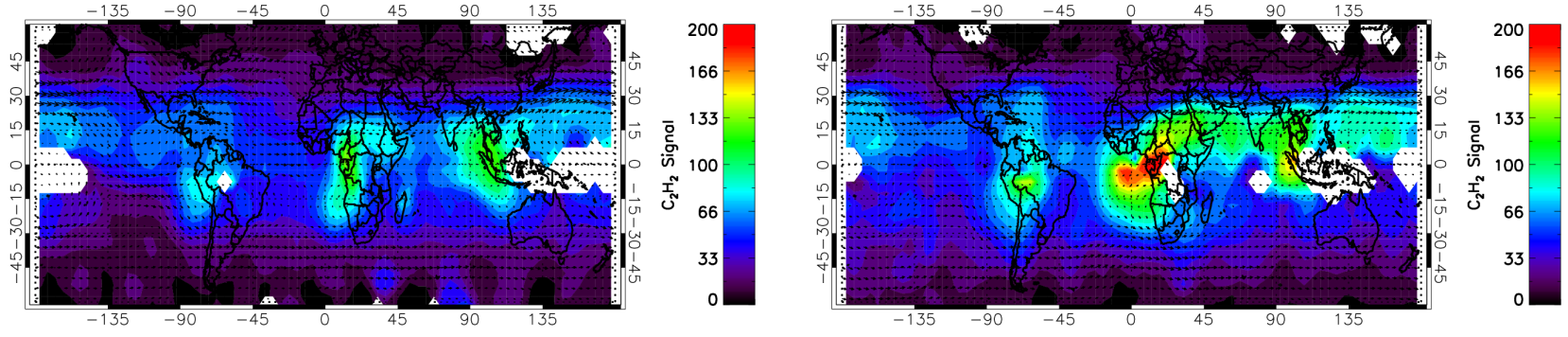

(a) January

(b) February

(c) March

(d) April

FIGURE 4.16. C_2H_2 detection results for January, February, March and April 2003 showing strong C_2H_2 enhancements over Northern Africa, Southern Africa and Asia associated with biomass burning. Significant eastwards transport of C_2H_2 is also observed from Asia during March and April.

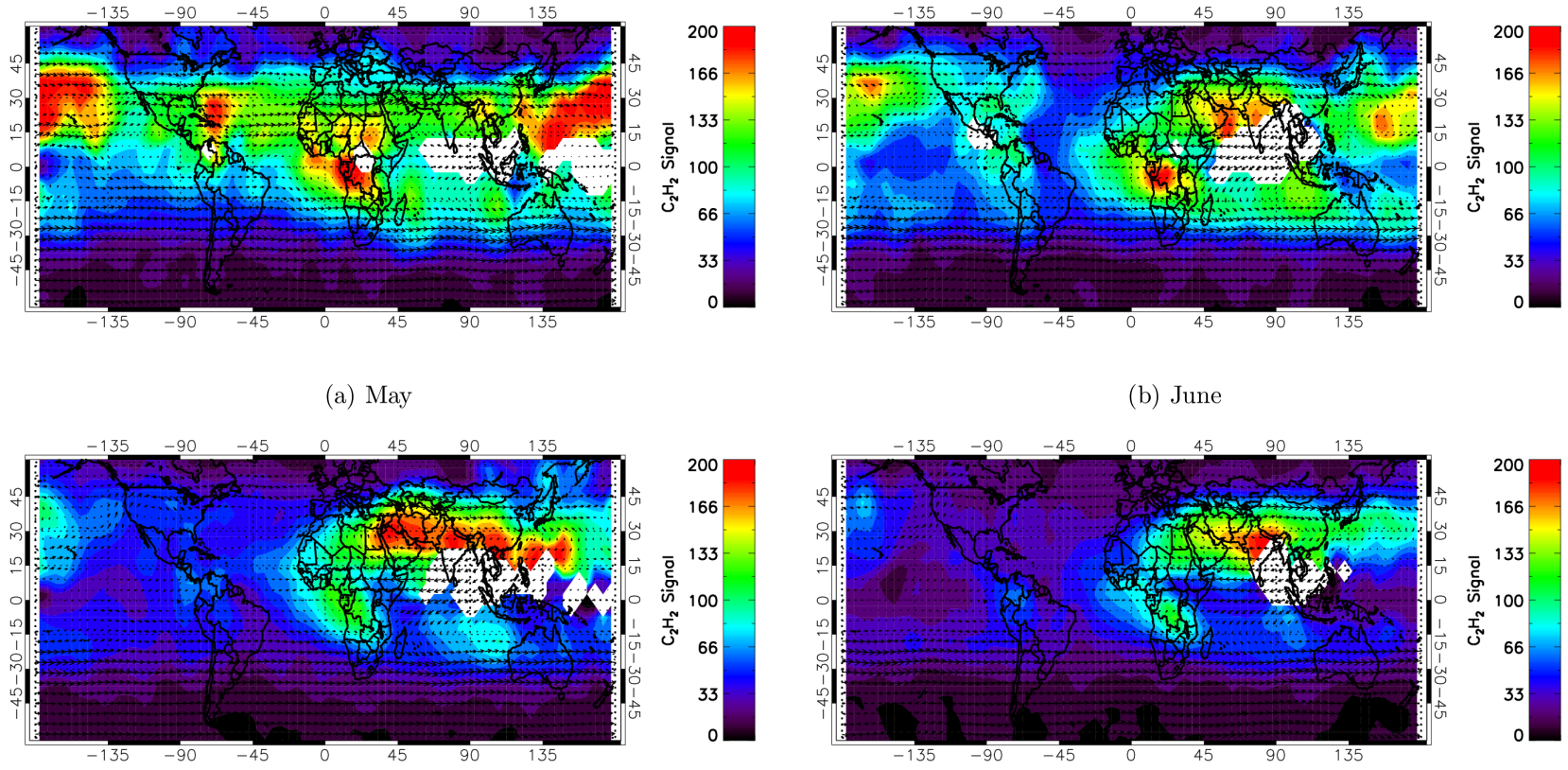

(a) May

(b) June

(c) July

(d) August

FIGURE 4.17. C_2H_2 detection results for May, June, July and August 2003 showing the strong chemical isolation over the Asian monsoon anticyclone as well as biomass burning transport in Southern Africa.

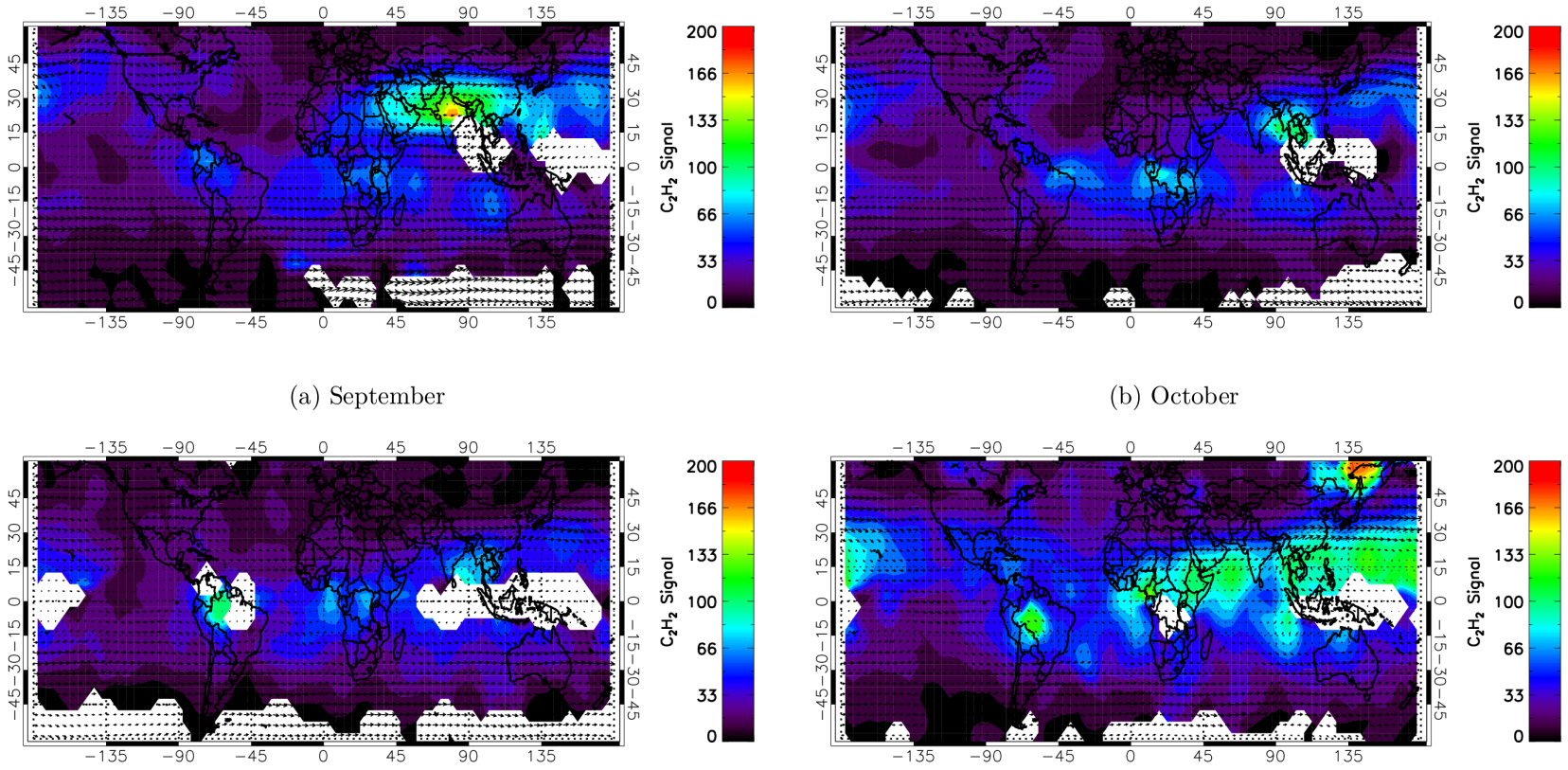

(a) September

(b) October

(c) November

(d) December

FIGURE 4.18. C_2H_2 detection results for September, October, November and December 2003 showing no significant enhancements of C_2H_2 after the dissipation of the monsoon anticyclone during September.

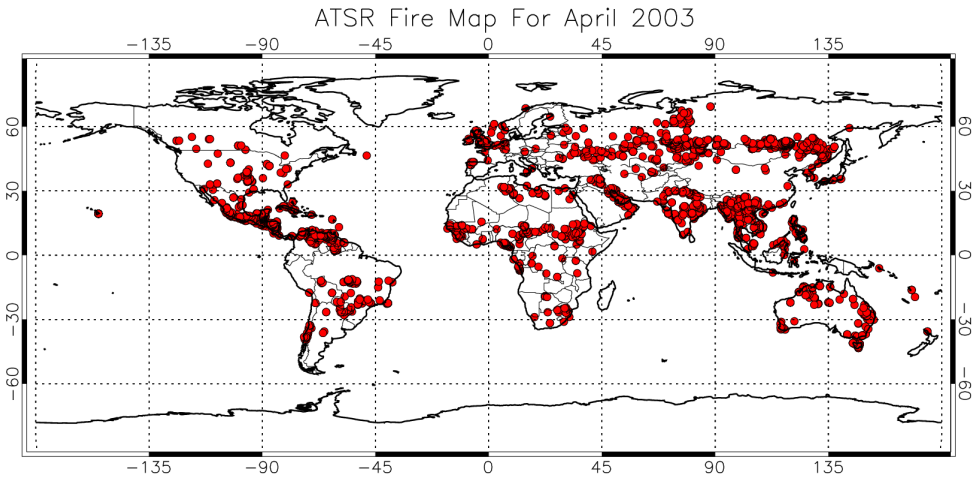

FIGURE 4.19. AATSR Fire Maps for April 2003 showing the fire distribution. In April, there are a large number of fires detected between 10°N and below 30°N coinciding with the enhanced C_2H_2 observed in Figure 4.16

In order to analyse the details of the detection data in more detail, the data was analysed in conjunction with 150 hpa ECMWF wind vectors and AATSR fire detections. In addition NCEP OLR contours for 240 W/m^2 (orange), indicative of moderate convective activity, and for 205 W/m^2, indicative of deep convection (red) are displayed.

4.2.3.1 January 2003

Figure 4.20 shows the detection for January 2003 and includes the additional information on fires, wind fields and OLR outlined above.

Over South America, moderately enhanced C_2H_2 is observed around the region of deep convection located over the Amazon region. During January the majority of fires in South America occur further North which may account for the lack of significant C_2H_2 enhancements over this region. In addition, the wind vectors show strong 150 hpa winds moving clean air eastwards from the ocean towards the coast, preventing the small enhancement of C_2H_2 from extending out over the ocean.

Although OLR is used as an indicator for convection, it is also instructive to consider the altitude of the cloud top heights (CTH) as identified from the MIPAS data. In order to calculate the CTH, the MIPAS cloud index (see Section 3.5) is used to determine the highest MIPAS level in which the cloud index is less than 1.8. The CTH for January 2003 is shown in Figure 4.21 and the location of the high altitude cloud is in strong agreement with the location of the convective activity identified by the OLR (red and orange contours in Figure 4.20). Particularly high cloud (over 16 km) and low OLR values are observed over Central South America and Northern Indonesisa/Pacific Ocean.

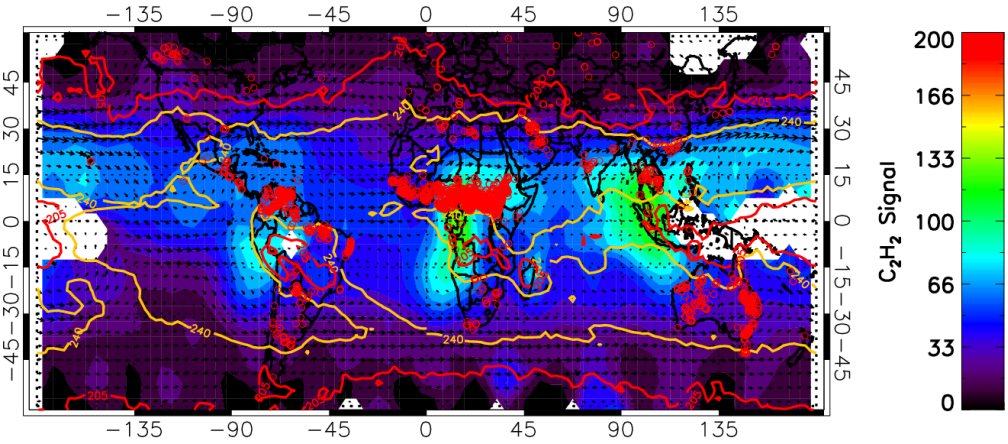

FIGURE 4.20. C_2H_2 detection results for January 2003 for the 12 km MIPAS nominal altitude. ECMWF 150 hpa wind vectors and AATSR fire detections are included. NCEP OLR 240 W/m^2 (orange) and 205 W/m^2 (red) contours identify regions of convection and deep convection respectively.

Over southern Africa, the CTH values are around 14 km with relatively small regions of deep convection over southern Africa and Madagascar and the majority of fires occurring to the north of the convection zone, above the equator. The 150 hpa wind vectors passing over southern Africa circulate cyclonically containing the enhancement over the west coast, whilst the wind vectors to the north carry clean air from the Atlantic and prevent the enhancement moving further north than 15°N. Additionally a small enhancement of C_2H_2 with a value around 80 nW/cm^2·sr·cm^{-1} is observed over Madagascar and appears to be associated with the localised convective activity identified by the low OLR values.

The final significant enhancement for January is observed over Indonesia and South-East Asia where a large amount of deep convection is observed. The values observed here of between 90 nW/cm^2·sr·cm^{-1} and 130 nW/cm^2·sr·cm^{-1} appear to be transported eastwards into the Pacific where values between 60 nW/cm^2·sr·cm^{-1} and 80 nW/cm^2·sr·cm^{-1} are observed. Due to the spatial extent of the deep convection over this region it is more difficult to identify the source of the C_2H_2. Although a large number of fires are observed over South-East Asia which could potentially contribute to the C_2H_2 enhancement, the wind vectors suggest that the source is actually to the south within the deep convection zone over Indonesia. Unfortunately due to the large amount of cloud over this region, neither fire detections nor MIPAS observations are possible.

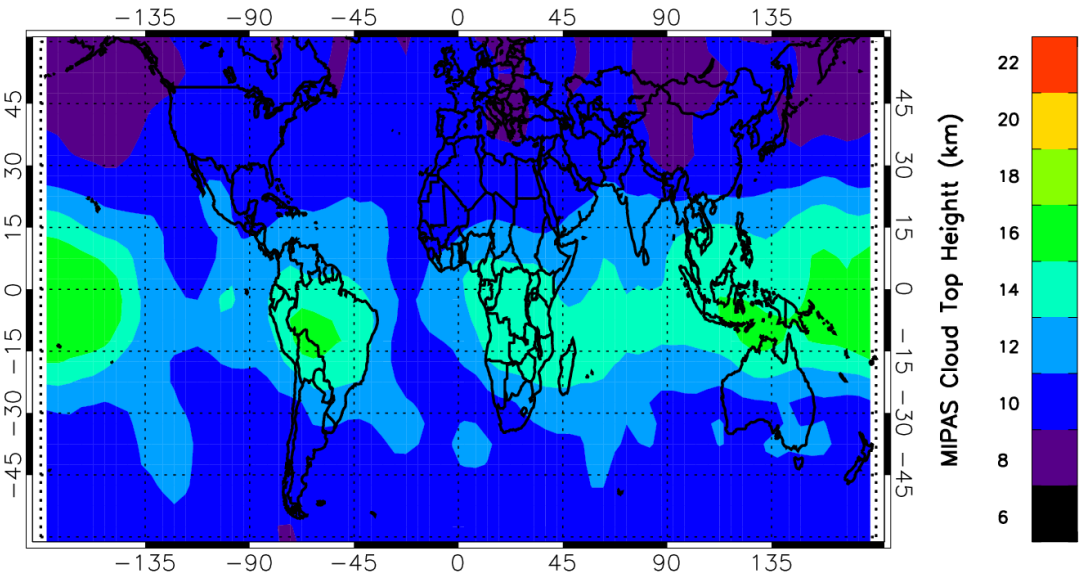

FIGURE 4.21. MIPAS Cloud Top Height for January 2003 showing the highest MIPAS nominal altitude where a cloud index of less than 1.8 was present in the sweep.

4.2.3.2 February 2003

In February (Fig. 4.22), the enhancement over South America appears to be stronger and is centred over the larger region of deep convection. The lack of AATSR fire detections over this region again suggest that open biomass burning/forest fires may not be the source of the C_2H_2 and instead it may be domestic biofuel burning which is being uplifted by the deep convection.

In comparison to January, the enhancement of C_2H_2 over Africa is considerably larger in February and this appears to be largely attributable to the alteration of the wind flow over Africa. Instead of moving strictly eastwards from the Atlantic across northern Africa as in January, the wind vectors over Central Africa for February move north-eastwards from the biomass burning and convection regions towards the Middle East and then eastwards towards India and South-East Asia. In addition, the wind vectors off the west coast of Africa are much weaker and no longer prevent the extension of the enhancement westwards where a significant enhancement is now observed over the South Atlantic.

The strong deep convection is still present over Indonesia and appears to contribute to the C_2H_2 enhancement but is now merged with the enhancement travelling from Africa towards South-East Asia and then eventually across the Pacific.

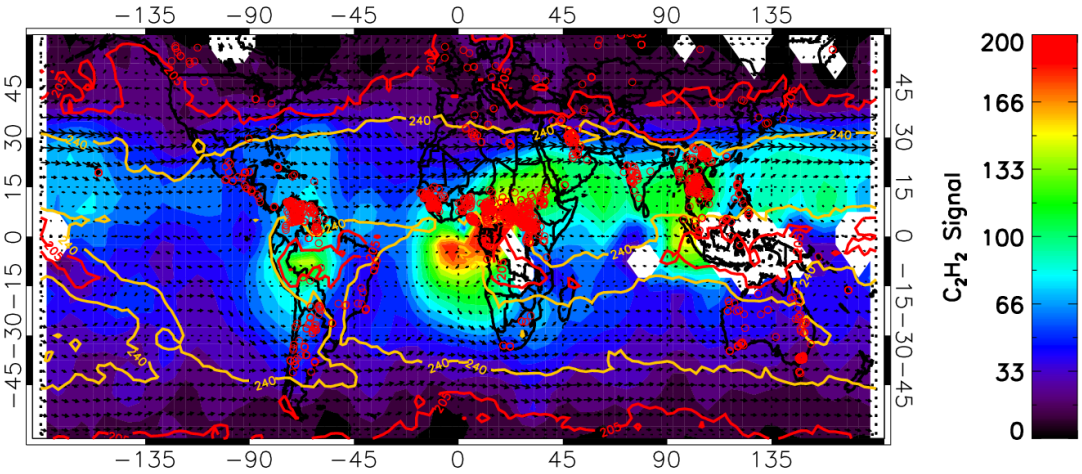

FIGURE 4.22. C_2H_2 detection results for February 2003 for the 12 km MIPAS nominal altitude. ECMWF 150 hpa wind vectors and AATSR fire detections are included. NCEP OLR 240 W/m^2 (orange) and 205 W/m^2 (red) contours identify regions of convection and deep convection respectively.

4.2.3.3 March 2003

The C_2H_2 distribution for March (Fig. 4.23) is largely similar to February with a significant amount of C_2H_2 transported from Central Africa, north-eastwards to the Middle East and then eastwards over South-East Asia and into the Pacific.

The major difference to February is the enhancement over Central America which corresponds to the large number of fires now detected in the region. The wind vectors indicate that this enhancement over Central America is transported south-eastwards along the north-eastern coast of South America into the Atlantic.

Although a minor enhancement, another interesting feature observed in March not identified in earlier months is the moderate enhancement of around 100 ppbv on the southern edge of the deep convective region over Indonesia. This enhancement off the north-eastern coast of Australia appears to be linked to the deep convection region, offering possible confirmation that it is through this deep convection mechanism that the enhanced C_2H_2 is uplifted in this region.

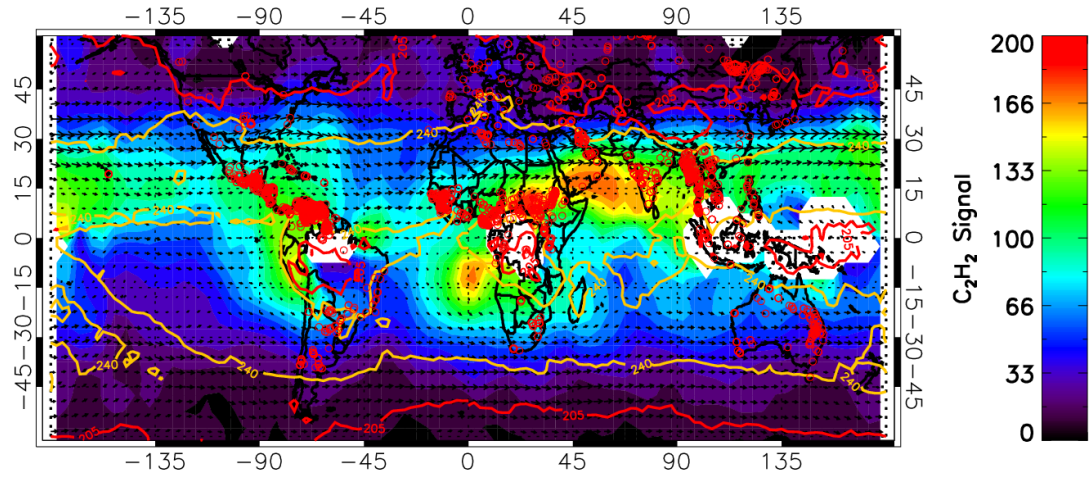

FIGURE 4.23. C_2H_2 detection results for March 2003 for the 12 km MIPAS nominal altitude. ECMWF 150 hpa wind vectors and AATSR fire detections are included. NCEP OLR 240 W/m^2 (orange) and 205 W/m^2 (red) contours identify regions of convection and deep convection respectively.

4.2.3.4 April 2003

April sees a significant increase in the amount of C_2H_2 observed via the detection method (Fig. 4.24). This increase appears to be related to the fact that strong eastward winds are present between 10°N and 40°N around the circumference of the Earth and significant fire activity is observed on all of the major landmasses within this band. As observed in March, both Central America and Central Africa experience biomass burning but in addition to this, the number of fires observed in South-East Asia is greatly increased. This region is entirely covered by fire detections in Figure 4.24 coinciding with the location of strongly enhanced C_2H_2 with peak radiance values of over 200 nW/cm^2·sr·cm^{-1}. The combination of the intense fire activity and strong wind vectors leads to significant enhancements of C_2H_2 transported over the Pacific Ocean towards North America. Again, the gradient in the wind vectors over the North Pacific strongly coincides with the boundary between enhanced C_2H_2 above 130 nW/cm^2·sr·cm^{-1} and the much lower values of around 50 nW/cm^2·sr·cm^{-1} further to the north. This distinct shape to the C_2H_2 distribution is consistent with the location of the tropopause at this altitude as determined from NCEP tropopause pressure.

As well as the large scale distribution of C_2H_2 discussed above, there are several interesting smaller features observed in April which should be commented upon.

There are two regions of localised C_2H_2 enhancements over Central Africa at 15°N which coincide with two separate areas of localised biomass burning activity on the northern edge of the convection zone. This seems to suggest that the emission from these fires is directly observed as enhancements of C_2H_2. Furthermore this suggests that uplift is happening on a relatively quick time-scale as the enhancements are observed directly over the fire regions and have not yet been transported eastwards.

Another interesting feature which provides further evidence that C_2H_2 is acting as a tracer of biomass burning is that during April the strong westerly winds transport C_2H_2 from southern Africa across the Indian Ocean towards Australia. This effect is not observed in previous months as the strong westerly winds are not present and instead the southern part of the Indian Ocean contains low amounts of C_2H_2 consistent with background levels.

Finally, it should be noted that despite the large number of fires detected over the Siberian region above 45°N, no enhancements of C_2H_2 are observed the 12 km MIPAS nominal altitude observations at these higher latitudes are in the lower stratosphere.

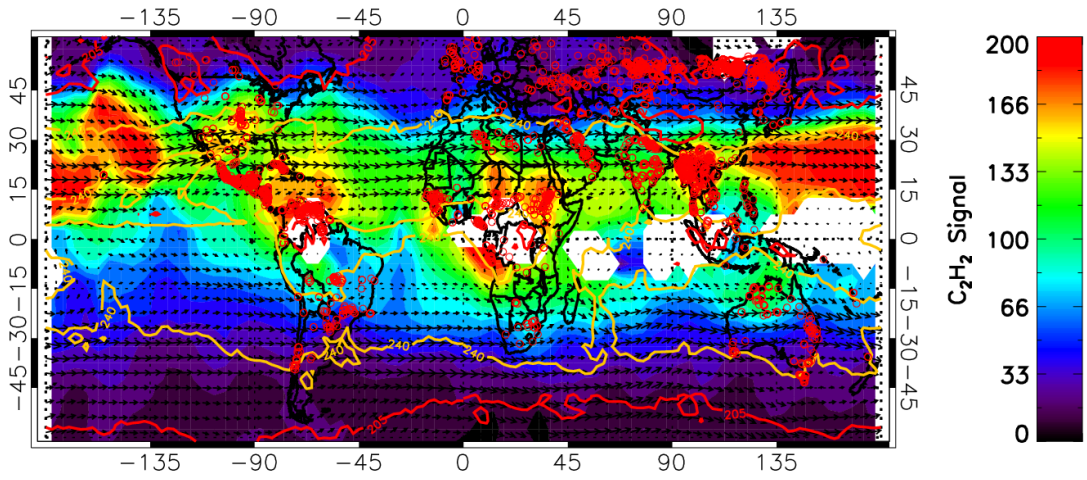

FIGURE 4.24. C_2H_2 detection results for April 2003 for the 12 km MIPAS nominal altitude. ECMWF 150 hpa wind vectors and AATSR fire detections are included. NCEP OLR 240 W/m^2 (orange) and 205 W/m^2 (red) contours identify regions of convection and deep convection respectively.

4.2.3.5 May 2003

The C_2H_2 distribution for May is largely similar to that of April with only subtle differences such as the wind vectors over southern India indicating the onset of the Asian Monsoon anticyclone which forms during the end of May.

The deep convection previously present over Africa at the equator weakens, leading to a decrease in the number of cloudy scenes and hence an increase in MIPAS observations. These observations continue to show the strong enhancement in C_2H_2 over the African equatorial region but now the full extent of the enhancement region can be observed.

One notable feature is the strong enhancement of C_2H_2 in the Caribbean region which could potentially be associated with the fire detections in the region but is more likely associated with the much greater amount of biomass burning present in Mexico, transported over the Caribbean sea towards the Atlantic Ocean.

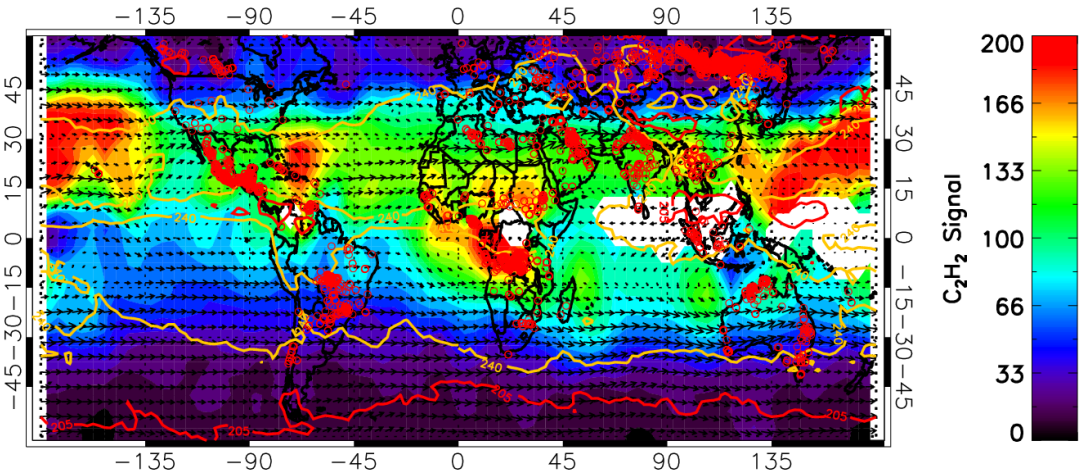

FIGURE 4.25. C_2H_2 detection results for May 2003 for the 12 km MIPAS nominal altitude. ECMWF 150 hpa wind vectors and AATSR fire detections are included. NCEP OLR 240 W/m^2 (orange) and 205 W/m^2 (red) contours identify regions of convection and deep convection respectively.

4.2.3.6 June 2003

Effects related to the start of the Asian Monsoon anticyclone at the end of May start to become apparent in the C_2H_2 distribution for June. A strong anticyclonic system is evident from the 150 hpa wind vectors over Asia, extending over the Middle East and north-east Africa. In addition, the OLR identifies two regions of deep convection over the Indian Ocean. The major effect of the formation of the anticyclone on the C_2H_2 distribution is that rather than being transported eastwards across the Asian continent into the Pacific, a large proportion of the C_2H_2 is recirculated westwards across the Indian Ocean towards Africa. This leads to an enhancement of C_2H_2 over the Middle East and Indian regions of over 150 nW/cm^2·sr·cm^{-1} whilst the amount of C_2H_2 observed over the Asian-Pacific region is significantly lower, reducing from over 200 nW/cm^2·sr·cm^{-1} to below 150 nW/cm^2·sr·cm^{-1}.

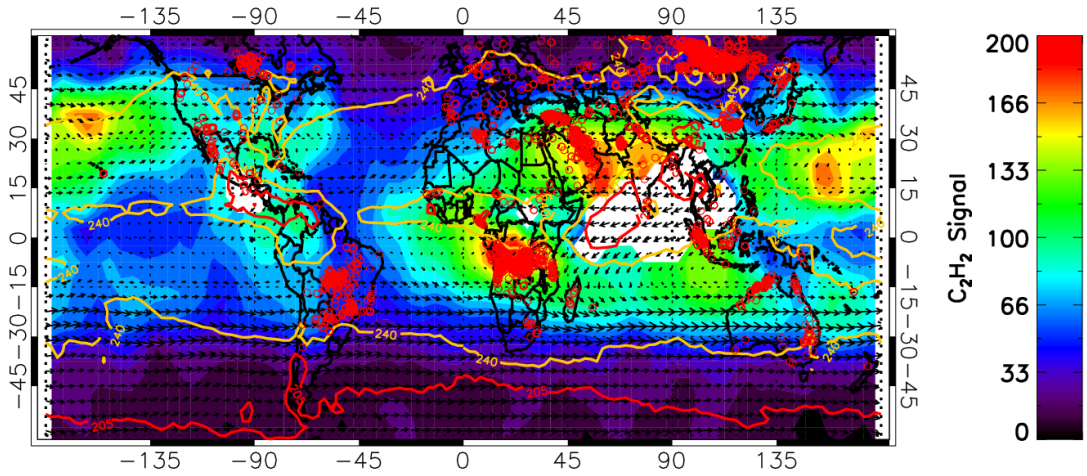

FIGURE 4.26. C_2H_2 detection results for June 2003 for the 12 km MIPAS nominal altitude. ECMWF 150 hpa wind vectors and AATSR fire detections are included. NCEP OLR 240 W/m^2 (orange) and 205 W/m^2 (red) contours identify regions of convection and deep convection respectively.

Although no significant deep convection is observed over Southern Africa, the large number of fire detections between 0°N and 15°S coincide with a strong enhancement of C_2H_2, possibly suggesting that the uplift here is produced at least partially from pyro-convection. This enhancement is then transported eastwards over Madagascar where it encounters airmasses leaving the Southern edge of the anticyclone before being transported towards Australia.

As discussed in Chapter 1, pyro-convection is capable of uplifting air into the UTLS, on both local and regional scales [Damoah et al., 2006]. This land type in this region can be considered as one of three main biome types: forest, savanna or grassland (Fig. 4.27). Freitas et al. [2005] discuss the effect that the vegetation type has on the pyro-convective activity and note that the size of the fire affects the

plume rise height through decreasing the role of entrainment. It follows that the heat flux of the fire (and hence the fire size) is distinctly different for the different types of vegetation with the minimum (maximum) heat fluxes for forest, savanna, and grassland fires being 30.0 (80.0), 4.4 (23), and 3.3 (3.3) kWm^{-2}, respectively [Guan et al., 2007].

Despite a large number of fire detections over South America, no enhancements of C_2H_2 are observed. This may be due to the lack of convective activity in the region, which instead is much further north around Central America, but also appears to be possibly related to the vegetation type in this area which is identified from MODIS land surface type data (Fig. 4.27) as being savannas/woody savannas. Interestingly in previous months when fires were present over the more forested areas to the north in the Amazon region, some C_2H_2 enhancement was observed although as deep convection was also present it is difficult to conclude that it is purely the land type influencing the C_2H_2 emissions and whether this is simply due to the pyro-convective behaviour of this land type. Furthermore, Freitas et al. [2007] discuss how the horizontal wind speed can affect the entrainment and potentially limit the injection height that these fires are capable of causing.

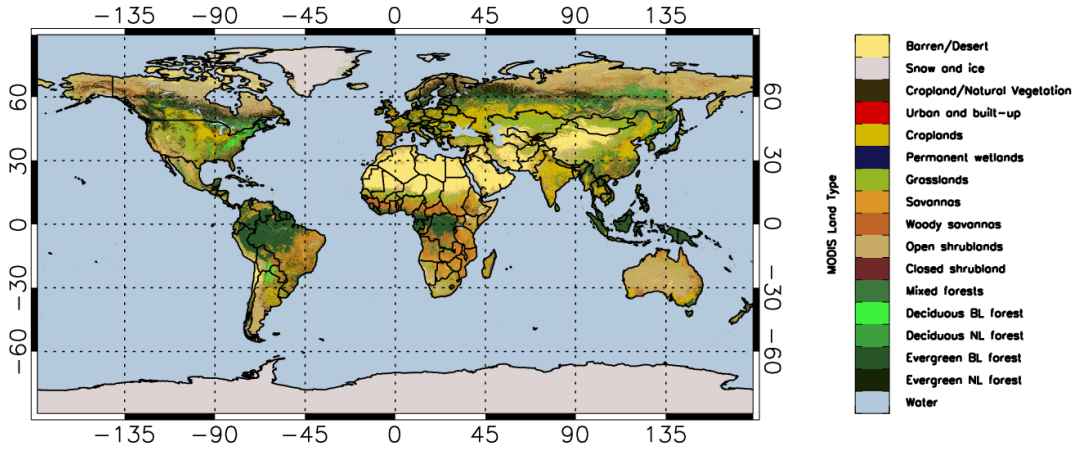

FIGURE 4.27. MODIS Land Surface Type taken from the International Geosphere-Biosphere Programme (IGBP) 1-Minute Land Ecosystem Classification Product showing the variation in surface type.

4.2.3.7 July/August/September 2003

The C_2H_2 distributions for July, August and September are considered together as due to the dominance by the Asian monsoon anticyclone, the distributions for these three months are very similar. Almost no enhancements are observed over the Western Hemisphere with all of the C_2H_2 isolated inside the anticyclone. Due to the implications of this strong chemical isolation, the effect of the Asian monsoon anticyclone on the C_2H_2 distribution is considered in detail in Section 4.2.4.

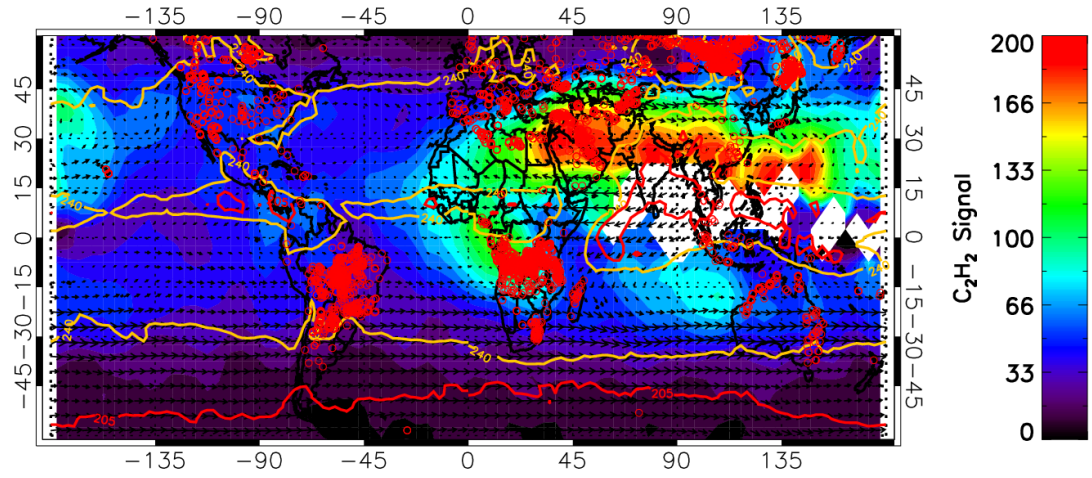

FIGURE 4.28. C_2H_2 detection results for July 2003 for the 12 km MIPAS nominal altitude. ECMWF 150 hpa wind vectors and AATSR fire detections are included. NCEP OLR 240 W/m^2 (orange) and 205 W/m^2 (red) contours identify regions of convection and deep convection respectively.

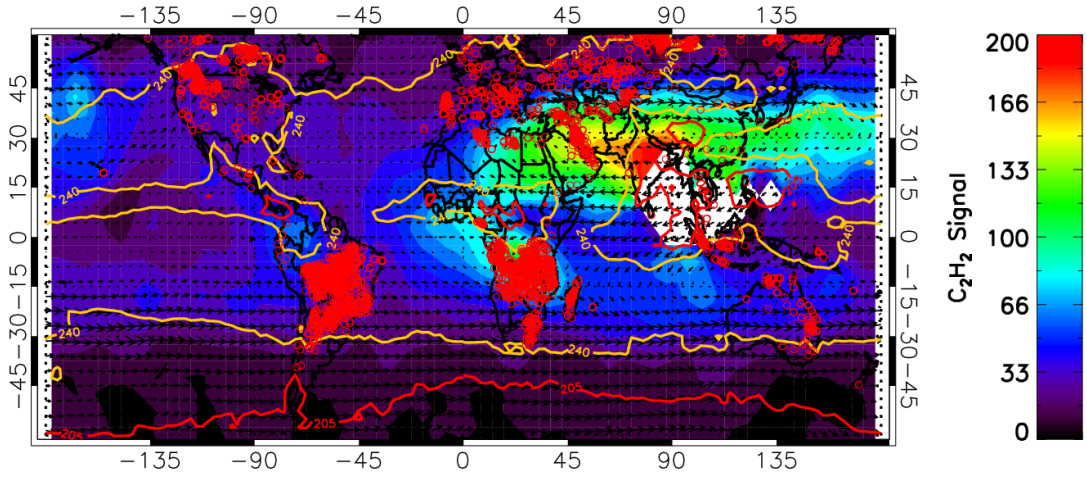

FIGURE 4.29. C_2H_2 detection results for August 2003 for the 12 km MIPAS nominal altitude. ECMWF 150 hpa wind vectors and AATSR fire detections are included. NCEP OLR 240 W/m^2 (orange) and 205 W/m^2 (red) contours identify regions of convection and deep convection respectively.

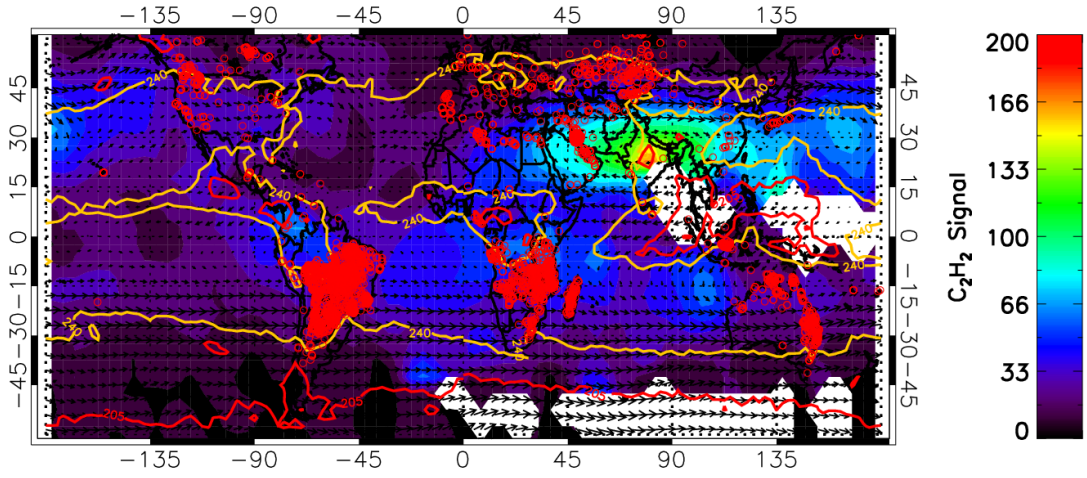

FIGURE 4.30. C_2H_2 detection results for September 2003 for the 12 km MIPAS nominal altitude. ECMWF 150 hpa wind vectors and AATSR fire detections are included. NCEP OLR 240 W/m^2 (orange) and 205 W/m^2 (red) contours identify regions of convection and deep convection respectively.

4.2.3.8 October 2003

As the Asian Monsoon anticyclone dissipates at the end of September, the C_2H_2 enhancements observed in October are relatively small. The largest of which, at around 120 nW/cm^2·sr·cm^{-1}, is over the South-East Asia region just to the north of the deep convective region. Despite the large number of fire observations in the Southern Hemisphere over South America, Southern Africa and Australia there are no significant enhancements of C_2H_2 observed with only moderate enhancements observed from the South American and West African coasts passing into the Atlantic. This distribution and plume shape is however in agreement with the results from von Clarmann et al. [2007] who observe enhanced C_2H_6 attributed to African Savannah and Amazonian Forest biomass burning during October 2003.

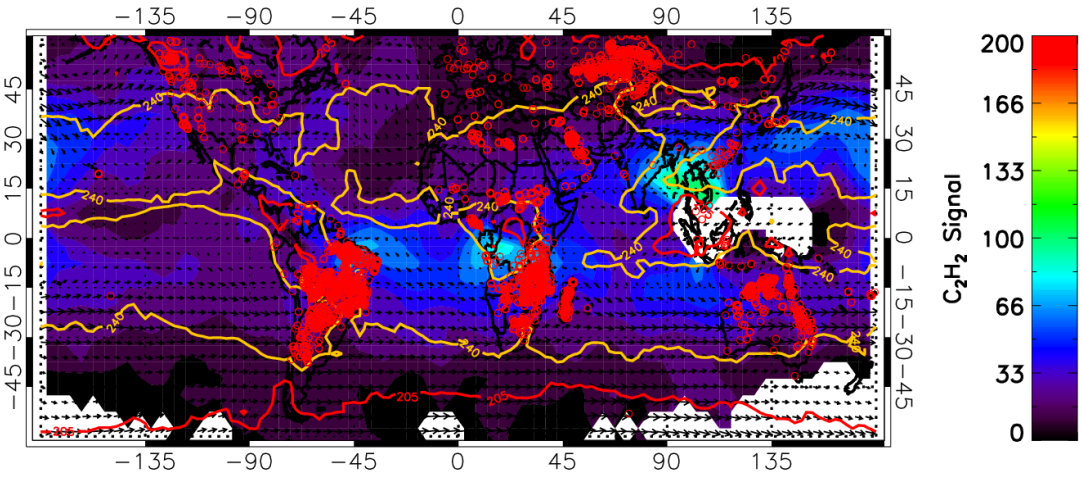

FIGURE 4.31. C_2H_2 detection results for October 2003 for the 12 km MIPAS nominal altitude. ECMWF 150 hpa wind vectors and AATSR fire detections are included. NCEP OLR 240 W/m^2 (orange) and 205 W/m^2 (red) contours identify regions of convection and deep convection respectively.

The fact that there are very few fires in the 0°N to 40°N latitude band (Fig. 4.54) may partially be responsible for this. In order to investigate this further, in future work it may prove useful to examine other indicators of fire activity and surface conditions such as burnt area index and seasonal vegetation data as one possibility is that the intensive fires previously in the year have resulted in less biomass being available for production of C_2H_2.

4.2.3.9 November 2003

As already noted for October, November also displays no signs of large C_2H_2 enhancements. The only real feature of note is the moderate C_2H_2 enhancement of around 120 nW/cm^2·sr·cm^{-1} over the Amazon region of South America close to both regions of deep convection and fire activity. With reference to the MODIS land surface type (Fig. 4.27), the C_2H_2 enhancement seems to be confined to the evergreen broadleaf rainforests of the Amazon region.

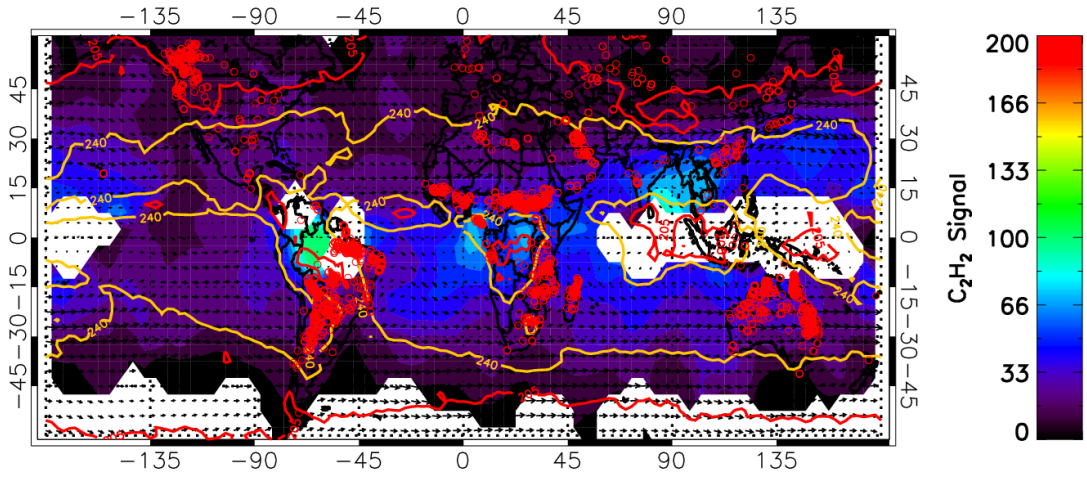

FIGURE 4.32. C_2H_2 detection results for November 2003 for the 12 km MIPAS nominal altitude. ECMWF 150 hpa wind vectors and AATSR fire detections are included. NCEP OLR 240 W/m^2 (orange) and 205 W/m^2 (red) contours identify regions of convection and deep convection respectively.

4.2.3.10 December 2003

Finally, the C_2H_2 distribution for December is analysed and several interesting features are apparent. Firstly, the large number of fires detected in South-East Asia lead to an enhancement of C_2H_2 being transported into the Pacific. Likewise, the biomass burning in Central Africa is far more intense than it was in November and results in C_2H_2 being transported into the Indian Ocean. An enhancement is still observed over the Amazon region associated with the deep convection and biomass burning in the region.

However, perhaps the most interesting feature is the strong enhancement of over 150 nW/cm^2·sr·cm^{-1} observed above 45°N at 135°E. According to NCEP tropopause pressure, the average pressure of the tropopause in this region for December is around 300 hpa (Fig. 4.34), meaning that MIPAS observations at around 12 km are viewing the stratosphere. This implies that the strong enhancement is actually within the stratosphere and may be a result of convection "overshooting"

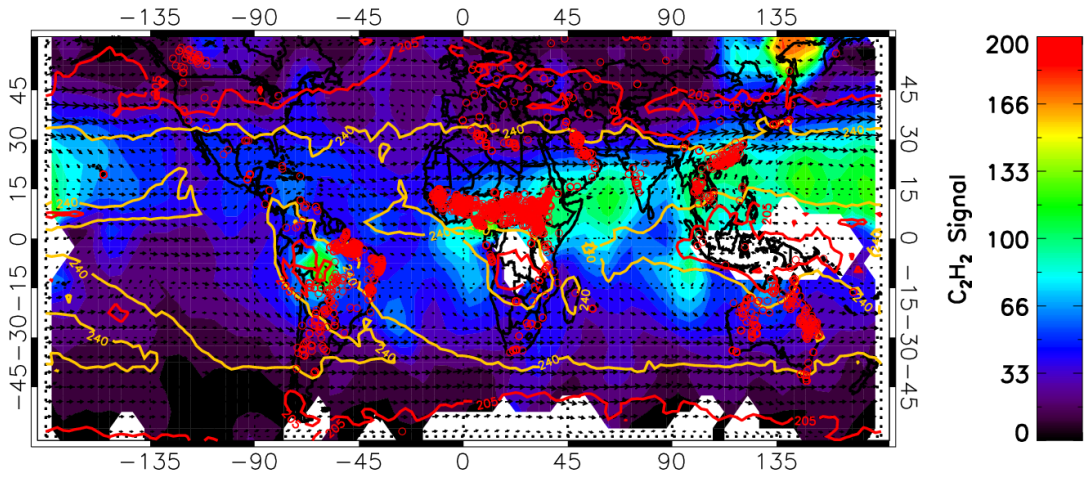

FIGURE 4.33. C_2H_2 detection results for December 2003 for the 12 km MIPAS nominal altitude. ECMWF 150 hpa wind vectors and AATSR fire detections are included. NCEP OLR 240 W/m^2 (orange) and 205 W/m^2 (red) contours identify regions of convection and deep convection respectively.

the tropopause [Chung et al., 2008]. In order to examine this effect further, a full retrieval would be necessary to allow the vertical structure of the C_2H_2 to be examined but nevertheless the detection technique has proved useful in identifying this as a region of potential further study.

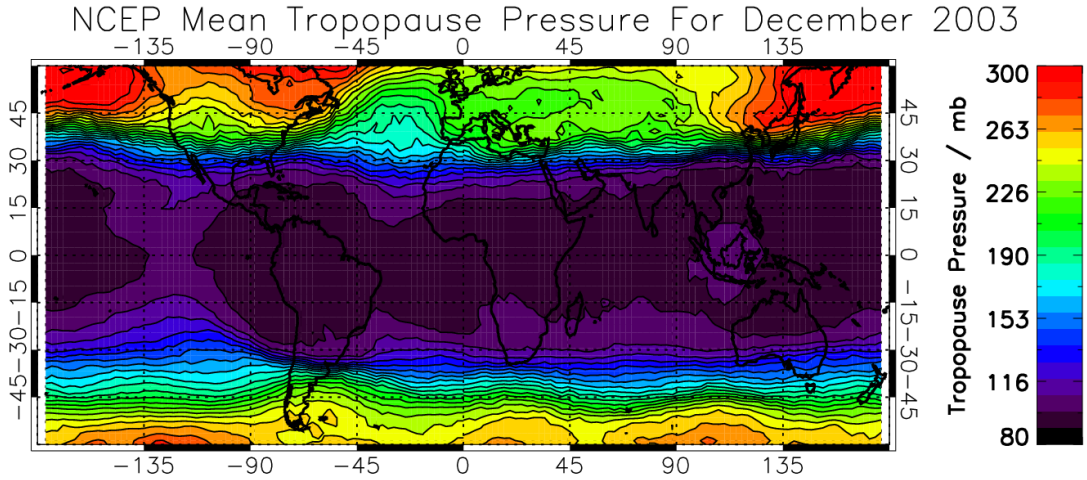

FIGURE 4.34. NCEP Tropopause Pressure for December 2003.

4.2.4 The Formation Of The Asian Monsoon Anticyclone

The analysis above has shown that not only is it possible to use the detection algorithm to discuss the distribution and transport of C_2H_2 throughout the year but also that C_2H_2 can be used to identify important dynamical effects such as the onset and subsequent chemical isolation related to the Asian monsoon anticyclone and how this acts as a barrier to zonal transport during the Northern Hemisphere summer. In order to analyse this effect in more detail, the following section will concentrate on the region affected by the monsoon anticyclone and use monthly averages of ECMWF wind vectors to show how the C_2H_2 enhancement is isolated during the formation of the anticyclone, persisting over the summer and dissipating as the anticyclone fades. The C_2H_2 detected peak radiances are displayed here as individual measurements rather than monthly averages in order to show the variability in the data as well as highlight the consistency observed over the Asian Monsoon anticyclone region. The plots are now restricted to the latitude and longitude ranges of 0°N to 60°N and 0°E to 180°E.

As expected, the analysis of January (Fig. 4.35) for both the wind vectors and C_2H_2 distribution shows that there is no anticyclone present in the region at this time of year and no resulting chemical isolation. Instead, the wind vectors and C_2H_2 distribution suggest that any North African and Middle Eastern biomass/biofuel burning is transported through Asia and into the Pacific Ocean. This leads to a latitudinal dependence on the C_2H_2 strength, with all of the values south of 30°N being considerably higher than the values to the North. From the wind vectors it is apparent that there is fast eastward transport and below 30° N this transports any enhancements from the African and Middle Eastern regions eastwards, whereas to the North there are neither the sources nor the meteorology to deliver similar C_2H_2 concentrations.

The analysis for April (Fig. 4.36) shows that although the wind vectors remain largely unchanged over the region, the increase in biomass and biofuel burning leads to a considerable increase in the amount of C_2H_2 that is transported zonally with large enhancements observed globally in the sub-tropics. In particular, significant eastward transport is observed from South-East Asia into the Pacific.

Examining the mean ECMWF wind vectors for June (Fig. 4.37(a)) shows the start of the monsoon anticyclone formation over Asia and the Middle East. A sharp gradient is observed in the C_2H_2 distribution along the western and northern edges of the anticyclone as defined by the wind vectors. The formation of the anticyclone clearly acts as a barrier to zonal transport across Northern Africa and the Mediterranean with a strong C_2H_2 enhancement isolated over the Middle East.

This chemical isolation continues throughout June, July and August (Fig. 4.37) where the sharp gradient in C_2H_2 distribution continues to follow the edge of the anticyclone as defined by the wind vectors. This is consistent with the behaviour of CO within the Asian monsoon anticyclone as observed from the Microwave Limb Sounder (MLS) by Barret et al. [2008]. Barret et al. [2008] went on to show using assimilations of this data into the MOCAGE chemical transport model that South-

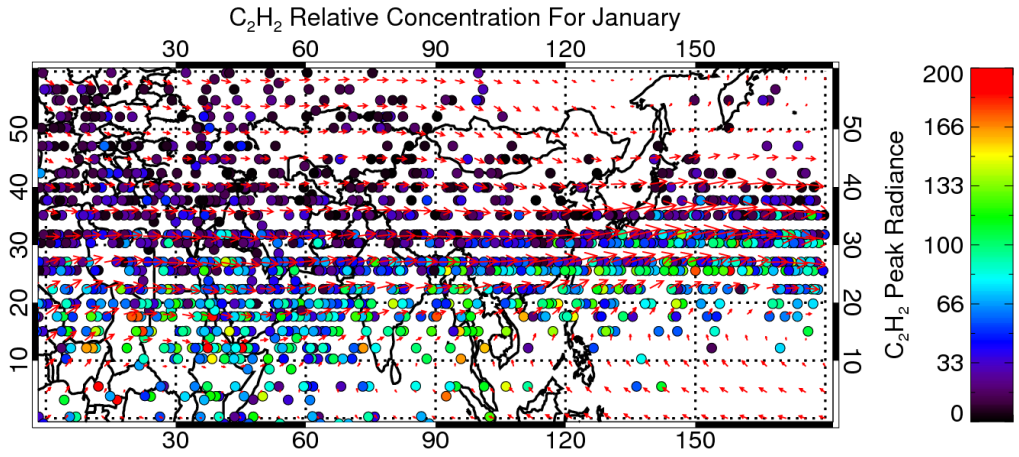

FIGURE 4.35. C_2H_2 detected peak radiances (nW/cm^2·sr·cm^{-1}) and ECMWF wind vectors over the Asian monsoon anticyclone region for January 2003 showing no monsoon at this time of the year and instead showing zonal transport from Northern Africa towards South-East Asia.

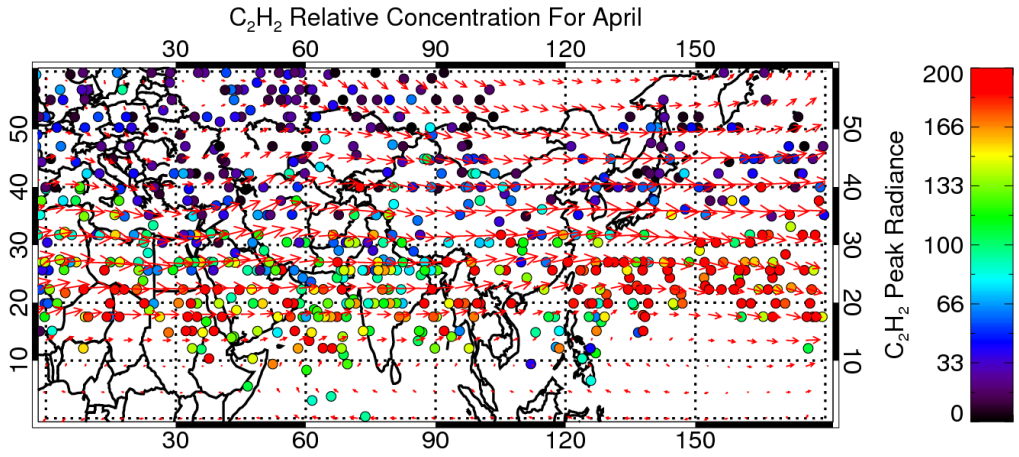

FIGURE 4.36. C_2H_2 detected peak radiances (nW/cm^2·sr·cm^{-1}) and ECMWF wind vectors over the Asian monsoon anticyclone region for April 2003 showing a much stronger degree of eastward transport with enhanced C_2H_2 observed over the Pacific.

East Asian pollution is uplifted into the upper troposphere and trapped within the Asian monsoon anticyclone where it is circulated over Northern Africa, behaving in the same way as the C_2H_2 isolation and transport observed here.

By September 4.38(a) the anticyclone had begun to weaken and this is shown in the C_2H_2 distribution by a reduction in the C_2H_2 enhancement and an eastward shift as the centre of the anticyclone moves east.

Finally by October, the anticyclone has dissipated and the C_2H_2 distribution no longer shows an isolated enhancement with only the signal due to the South-East Asian biomass burning still present (Fig. 4.38(b)).

The geopotential height anomaly (the deviation of the geopotential height from the zonal mean value) has previously been used as a tracer to identify the location of the Asian monsoon anticyclone by Park et al. [2008]. Figure 4.39 shows the NCEP geopotential height anomaly for August 2003 along with the average wind vectors. As can be seen, the geopotential height anomaly and the wind vectors agree with each other as to the location of the monsoon boundary. This boundary strongly matches the location of the isolation of the C_2H_2 values in Figure 4.39(b). Not only is the general location of the anticyclone in agreement with the enhanced C_2H_2 values but also specific features such as the distinct shape of the northern edge bounded by the Himalayas and the tongue extending out over the Pacific.

A similar plot comparing the geopotential height anomaly to the detected C_2H_2 peak radiances for September 2003 shows that the reduction in intensity of the anticyclone is matched by the reduction in intensity of the C_2H_2 isolation. In addition, the core of the anticyclone is clearly identified as being located over Northern India which coincides with the maximum in the detected C_2H_2 peak radiance.

Whilst the geopotential height anomaly can act as a tracer for the anticyclone boundary, the outgoing longwave radiation (OLR) can be used as a proxy for the location of the actual region of deep convection as it was used previously in this chapter. It has already been noted by Park et al. [2008] that the location of the anticyclone and the deep convection are distinctly separate regions, with the majority of the deep convection occurring at the South-Eastern edge of the anticyclone, rather than in the centre. Figure 4.41 shows the NCEP OLR for August 2003. An OLR value below 205 W/m^2 is considered to be indicative of deep convection and is outlined by the white contour lines in Figure 4.41. Whilst the OLR also indicates that there is moderate convective activity over by Africa and Central America, the South-East Asia region contains the majority of the deep convection. It is from the surface in this region where the enhanced C_2H_2 observed isolated within the anticyclone is originating from.

In order to understand this behaviour more clearly, a latitude band ranging from 0°N to 40°N was taken which allowed the Southern Hemisphere biomass burning variability to be disregarded and instead focus on the effect of the monsoon anticyclone. The C_2H_2 signal values were then binned into 20° longitude bands and a meridional mean for each of these bands was taken. This was repeated for each

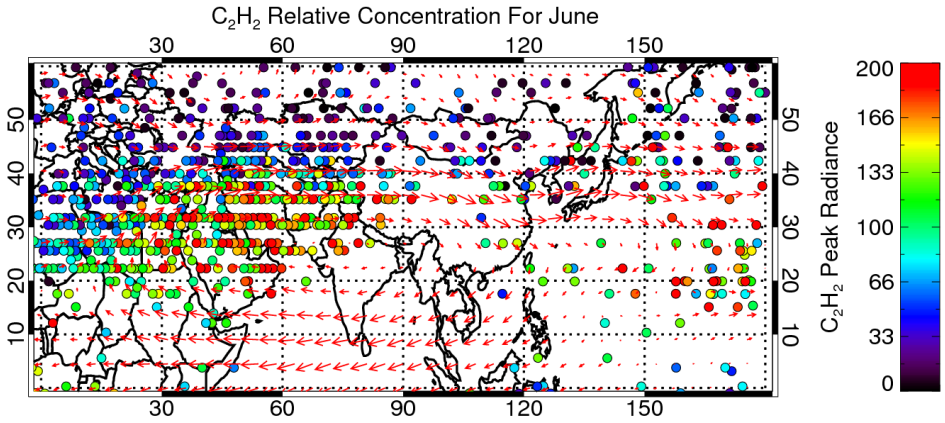

(a) June

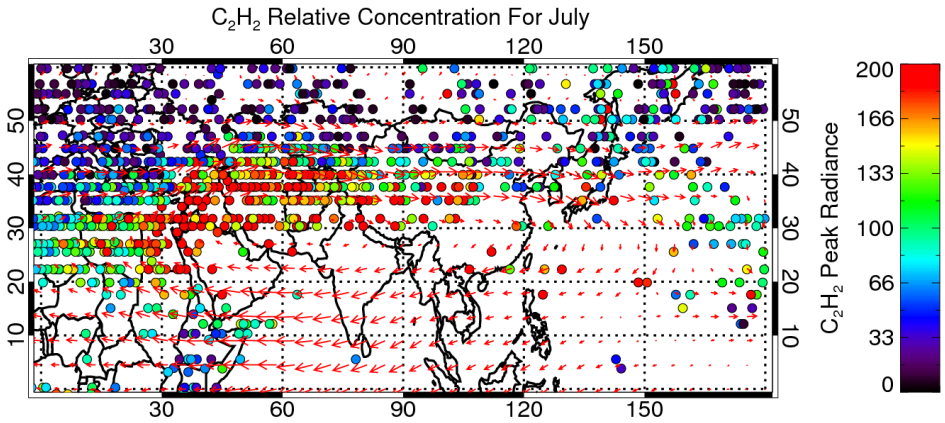

(b) July

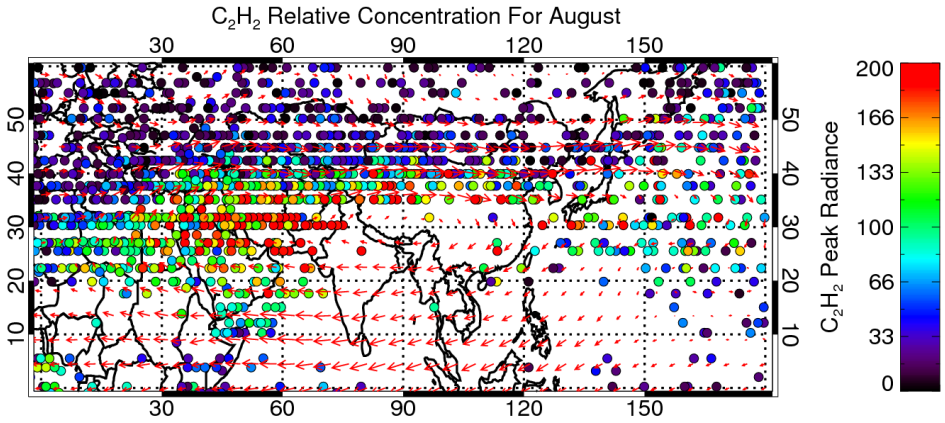

(c) August

FIGURE 4.37. C_2H_2 detection results for June, July and August 2003 showing the persistence of the monsoon anticyclone and the resulting chemical isolation of C_2H_2 for the Northern Hemisphere summer period.

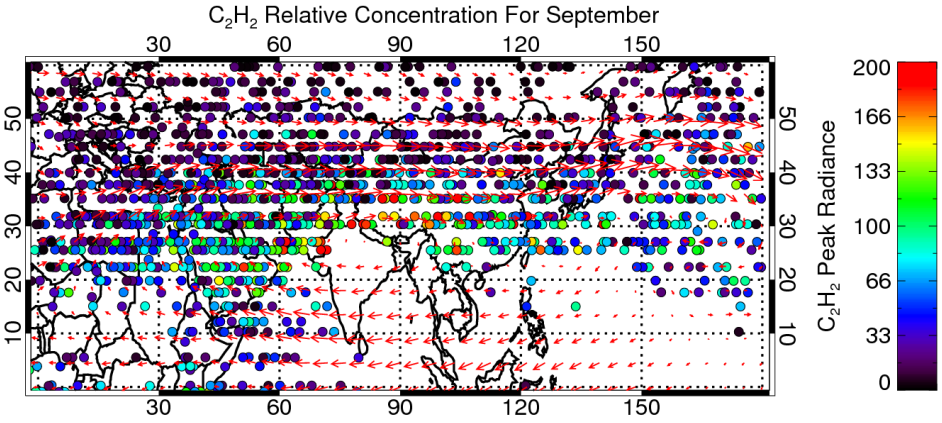

(a) September

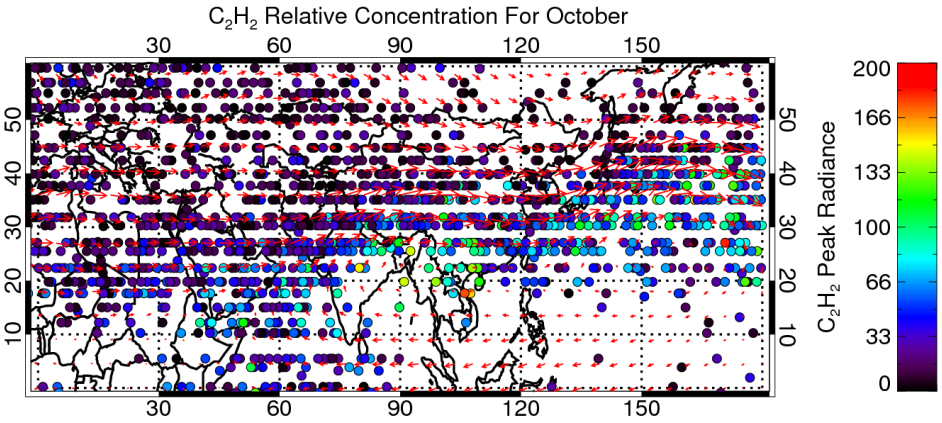

(b) October

FIGURE 4.38. C_2H_2 detection and ECMWF wind vectors over the Asian monsoon anticyclone region for September and October 2003 showing the end of the monsoon anticyclone, leaving only the signal associated with the South-East Asian biomass burning.

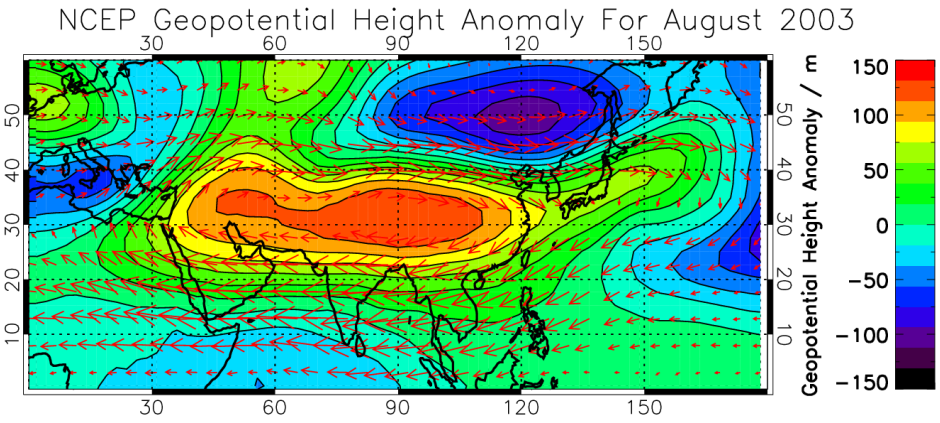

(a) NCEP Geopotential Height Anomaly

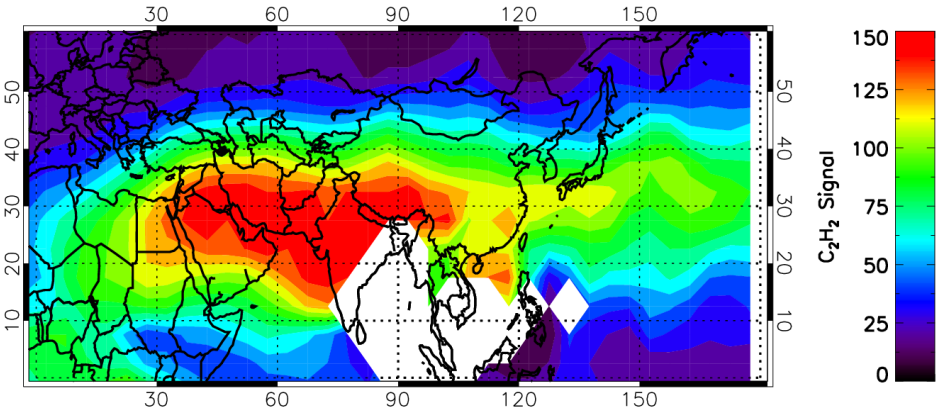

(b) C_2H_2 Detected Peak Radiance

FIGURE 4.39. The NCEP Geopotential Height Anomaly (above) and the C_2H_2 detected peak radiance (below) for August 2003. The geopotential height anomaly is used as an indication for the anticyclone location and is shown to be in strong agreement with the enhanced C_2H_2 detected peak radiance chemically isolated by the monsoon anticyclone.

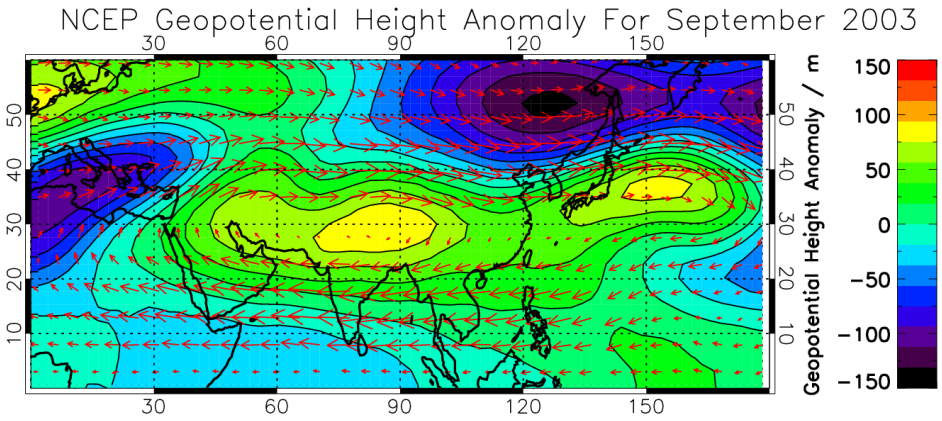

(a) Geopotential Height Anomaly

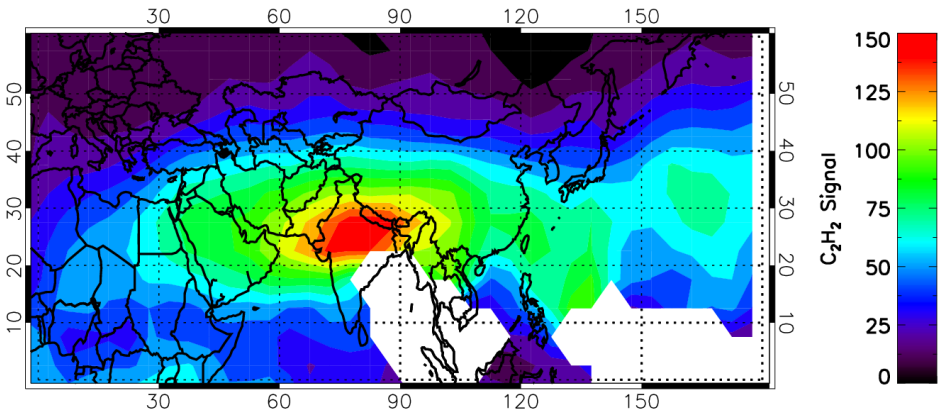

(b) C_2H_2 Detected Peak Radiance

FIGURE 4.40. Geopotential Height Anomaly for September 2003 (above) and the C_2H_2 detected peak radiance (below). As the anticyclone reaches an end, the geopotential height anomaly shows the core to be centred over Northern India, in the same location as the enhancement in the C_2H_2 Detected Peak Radiance. Again the agreement can be seen in considerable detail, including the similarity in location of the secondary enhancement off the eastern coast of Japan which is related to the extended section of the anticyclone.

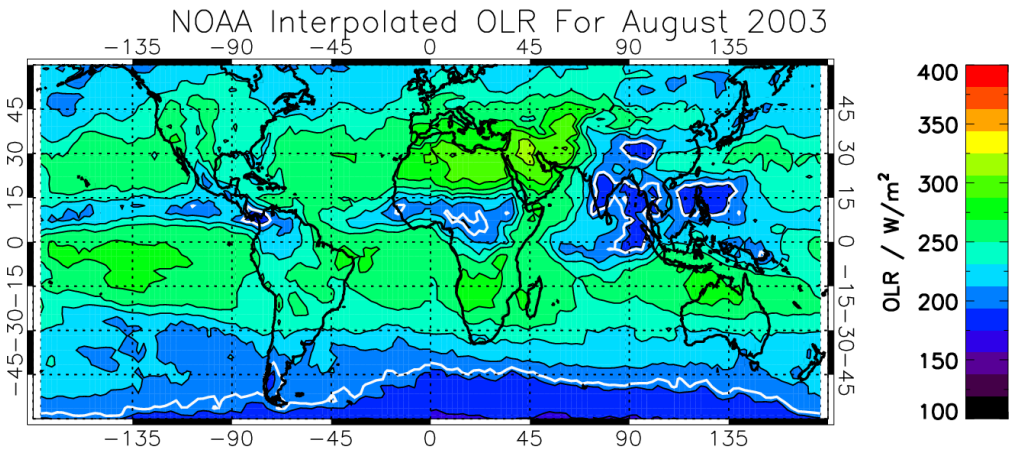

FIGURE 4.41. NCEP OLR for August 2003. Areas of deep convection (i.e. OLR < 205 W/m^2) are outlined by the white contour lines and show the large area of deep convection over India and South-East Asia, on the South-Eastern edge of the Asian monsoon anticyclone.

month, resulting in information on the monthly meridional distribution for the latitude band affected by the monsoon anticyclone for the whole of 2003. This data is shown in Figure 4.42.

The meridional distribution of C_2H_2 for January and February is seen to be both low and uniform across the entire latitude band. For the period from March until May, the distribution increases due to the increase in biomass burning but remains uniform across the latitude bands with the exception of the Asian-Pacific transport which is seen to increase. However, once the monsoon anticyclone begins to form in June, there is a significant reduction in the C_2H_2 values at other longitudes and a large increase between 30°E and 120°E corresponding to the region of the monsoon anticyclone's influence. This effect grows stronger as the anticyclone persists and by August the majority of the C_2H_2 observed is isolated inside this region with very low levels at other longitudes. As the anticyclone dissipates from September onwards, the meridional distribution returns to a more uniform shape and the isolation seen during the peak of the monsoon begins to disappear.

4.3 Ethane Detection

After successfully applying the automated detection algorithm to C_2H_2 it was decided that the algorithm had proven itself to be robust enough to allow the detection of ethane from the 12 km MIPAS nominal tangent altitude.

The C_2H_6 spectroscopy is discussed in detail in Section 2.3.2 and the detection algorithm utilises the same C_2H_6 peak located at 822.3 cm^{-1} (Fig. 4.43).

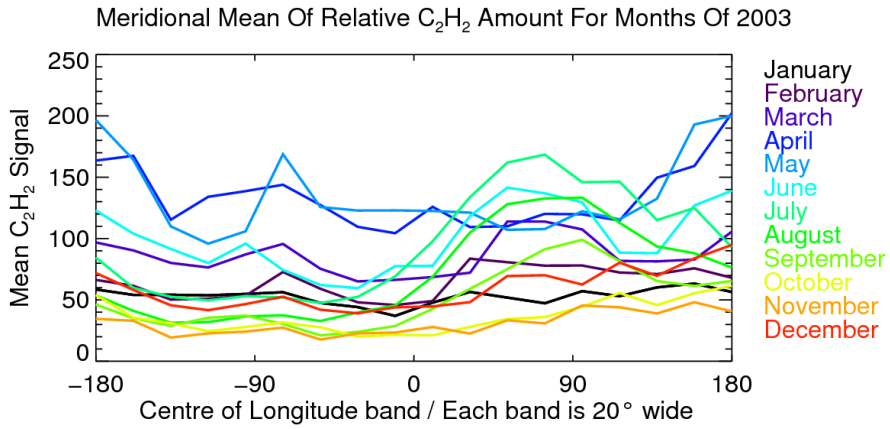

FIGURE 4.42. Meridional mean C_2H_2 detected peak radiances ($nW/cm^2 \cdot sr \cdot cm^{-1}$) for 2003 divided into 20°-wide longitude bands and monthly timesteps in order to illustrate how the meridional distribution of C_2H_2 changes throughout the year in the 0°N-40°N latitude band. The isolatory influence of the Asian monsoon anticyclone is observed from the end of June when C_2H_2 builds between 30°E and 120°E and persists until the anticyclones dissipation in September.

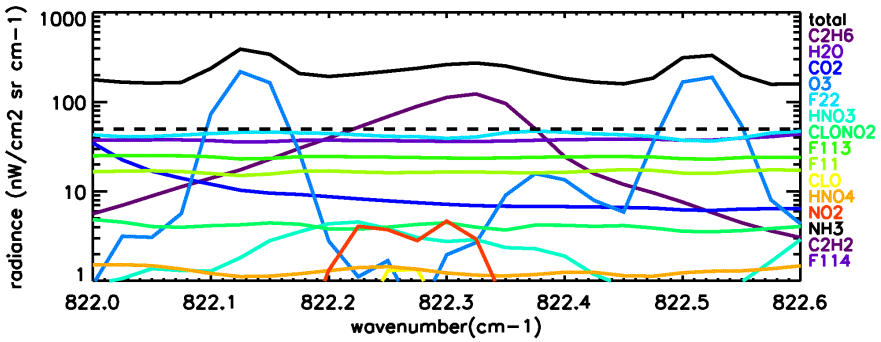

FIGURE 4.43. RFM simulation of a 12 km MIPAS spectrum at a 0.025 cm^{-1} resolution showing the contribution in the region of the C_2H_6 peak between 822.0 cm^{-1} and 822.6 cm^{-1}) from interfering species using a standard atmosphere background.

4.3.1 Ethane Detection Results

Figures 4.45, 4.46, 4.47 show the detected C_2H_6 signal for each month of 2003.

The detection results look reasonable with a clear distinction between the biomass burning influenced latitudes and the clearer latitudes above 30°N and below 30°S.

Between March and July, as well as enhancements relating to the Asian, South American and Southern African biomass burning, there is a strong latitude band of enhanced C_2H_6 between 0°N and 30°N. This distribution is similar to that observed above for C_2H_2 (Fig. 4.16).

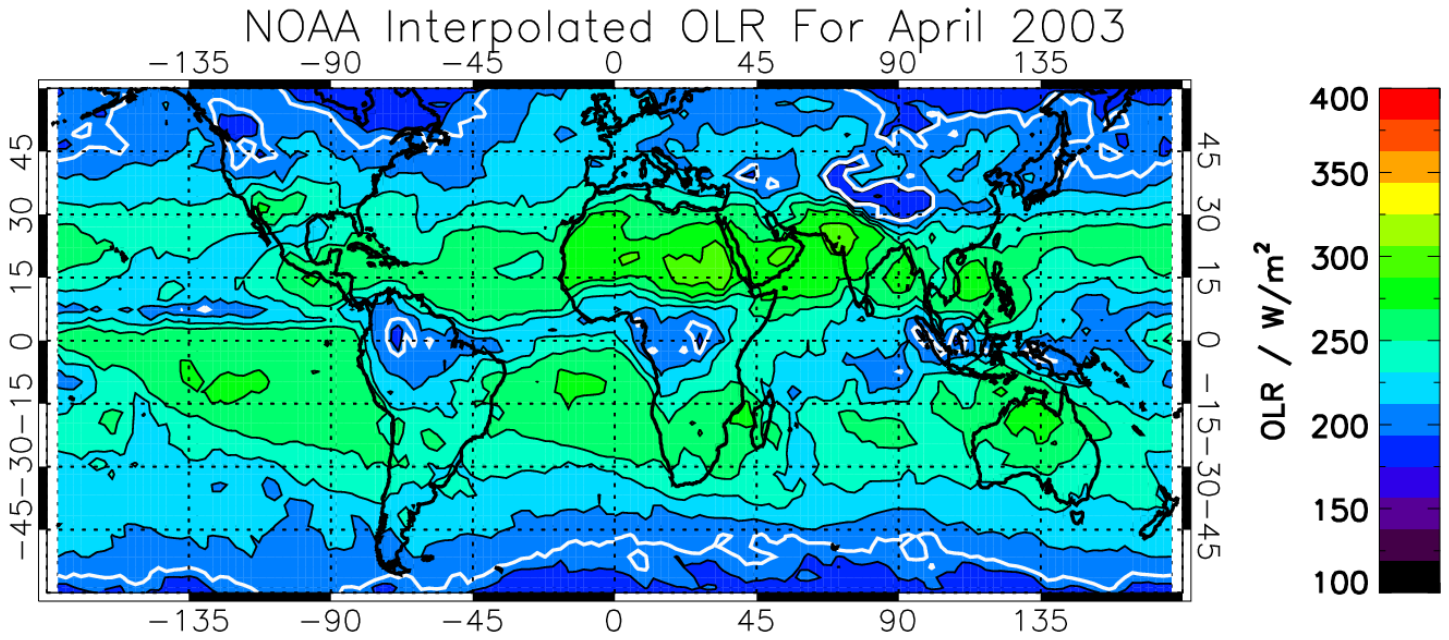

FIGURE 4.44. NCEP OLR for April 2003. Areas of deep convection (i.e. OLR < 205 W/m^2) are outlined by the white contour lines. Significant deep convection is observed in South America, Africa and South-East Asia as well as in the Siberian region.

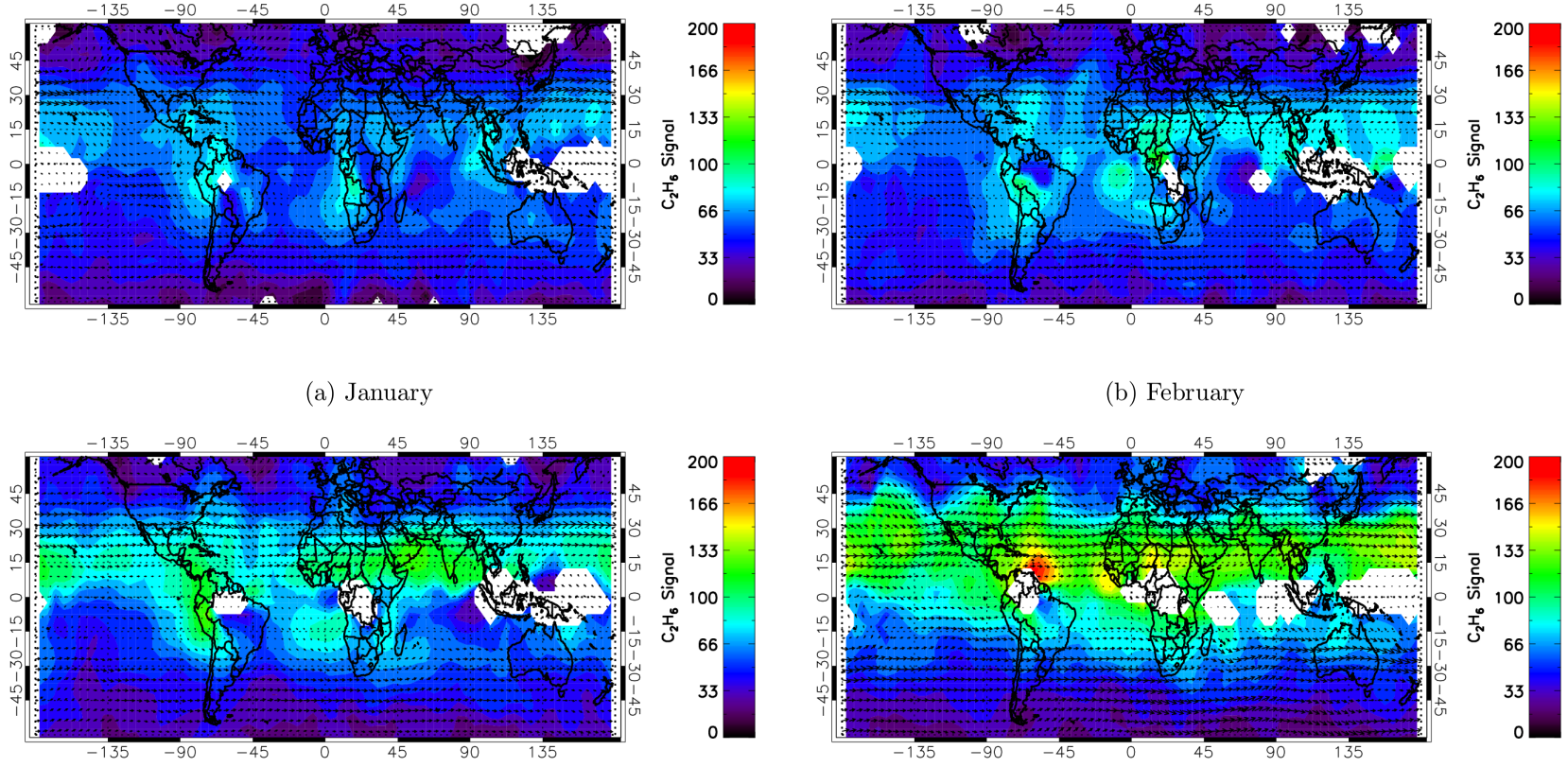

(a) January

(b) February

(c) March

(d) April

FIGURE 4.45. C_2H_6 detected peak radiance results for January, February, March and April 2003 showing a strong latitude band of enhanced C_2H_6 forming between approximately 0°N and 30°N. This enhancement is observed increasing until a large portion of the Northern Hemisphere shows an enhancement in C_2H_6.

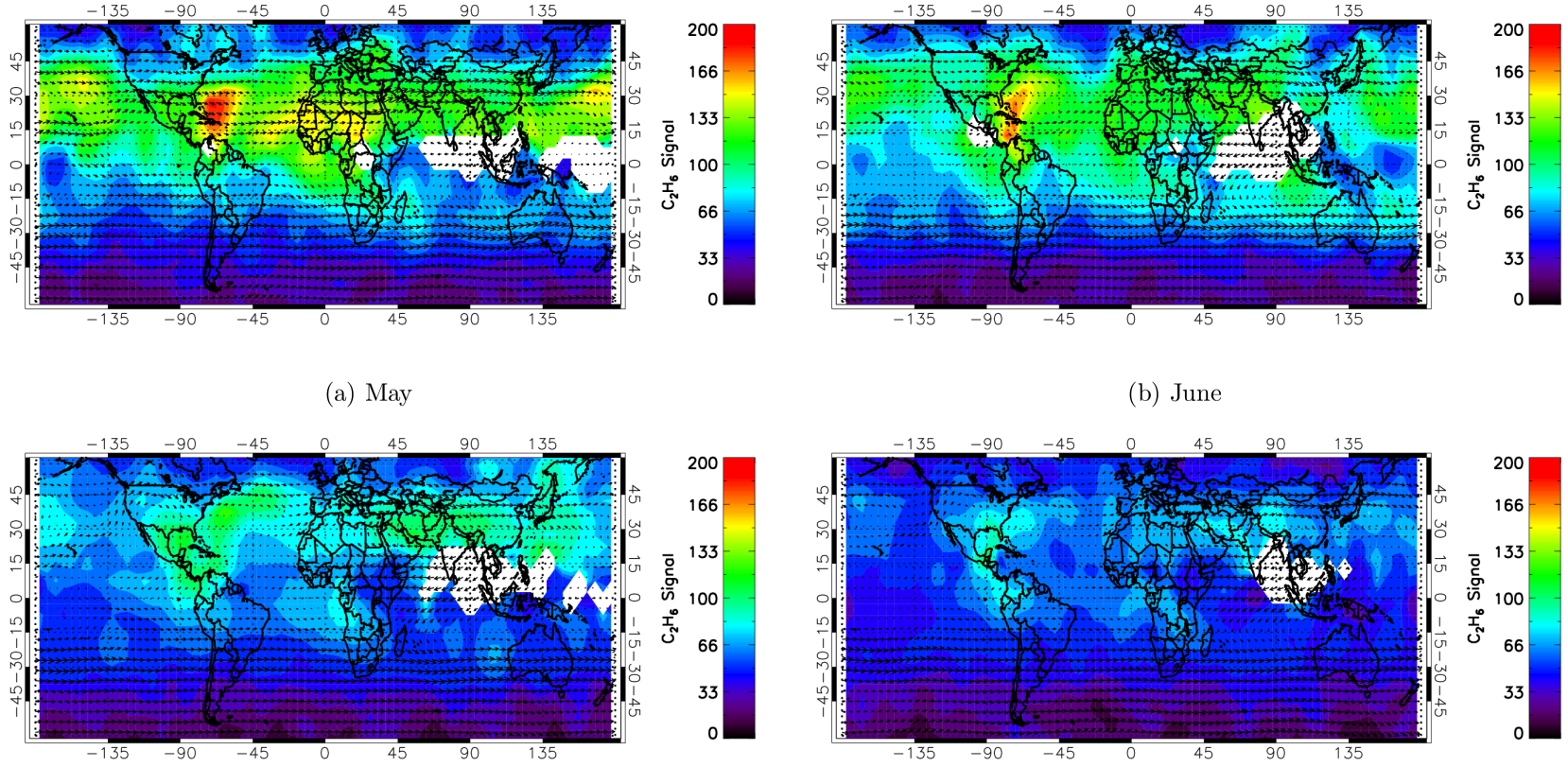

(a) May

(b) June

(c) July

(d) August

FIGURE 4.46. C_2H_6 detected peak radiance results for May, June, July and August 2003 showing first the continued expansion of the C_2H_6 enhancement before it begins to lessen during July. During August the enhancement is again confined to Central America, Southern Africa and the monsoon anticyclone region.

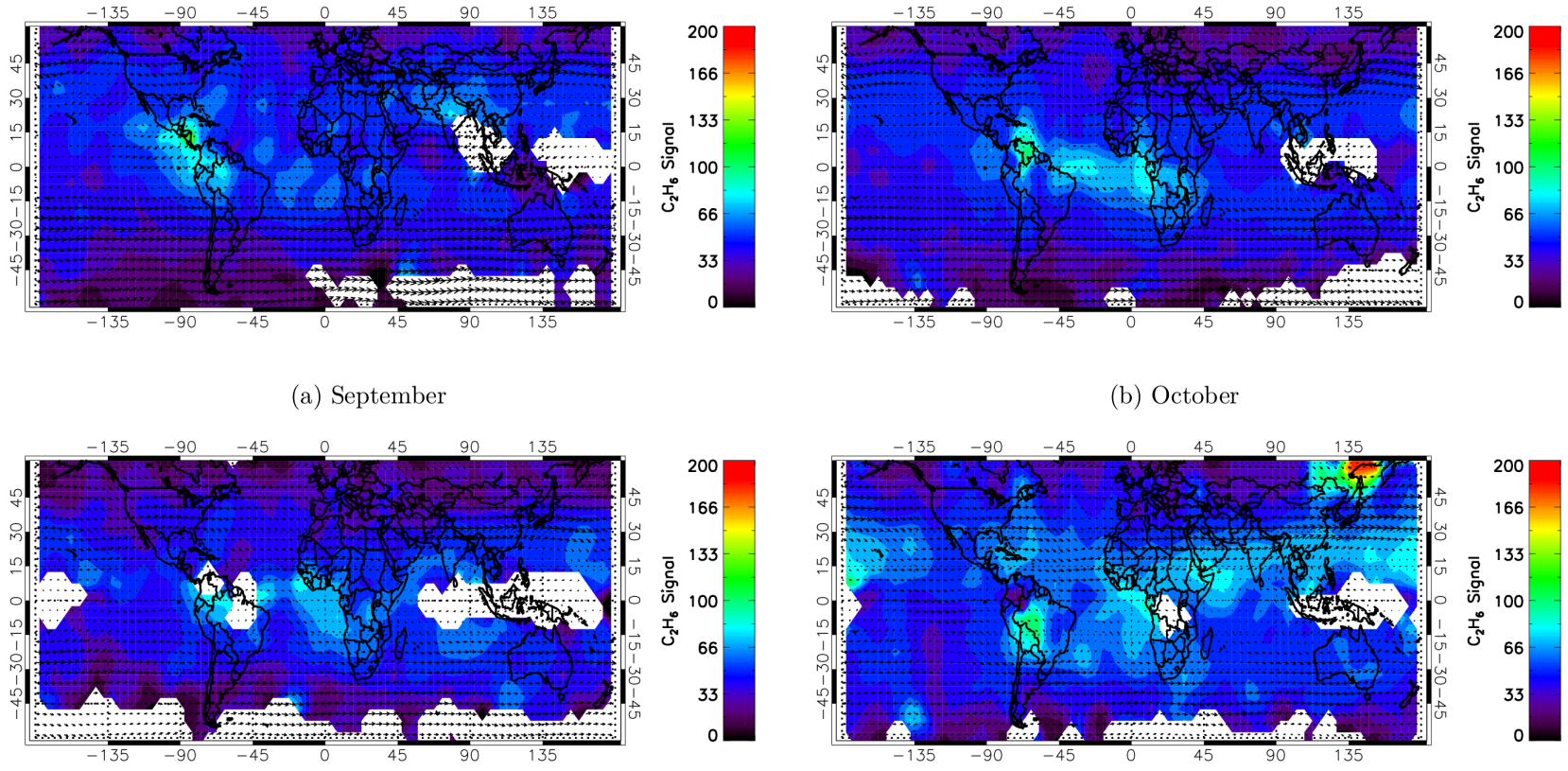

(a) September

(b) October

(c) November

(d) December

FIGURE 4.47. C_2H_6 detected peak radiance results for September, October, November and December 2003 showing enhancements of C_2H_6 over biomass burning regions in Central and South America and Africa.

In order to explain this large enhancement which seems to exist on a global scale, Figure 4.44 shows the OLR for April. As discussed above, OLR values below 205 W/m^2 act as a proxy for deep convection and in this case there is significant deep convection all along the equator in South America, Africa and South-East Asia.

In addition to deep convection, examination of the AATSR fire map for April 2003 (Fig. 4.19) shows a large number of fires detected over these regions with Central America, Central Africa, India, Siberia and South-East Asia all showing intense fire activity. It is around these regions of both intense fire activity and deep convection where the C_2H_6 enhancements seem to originate from before moving to cover the entire latitude band.

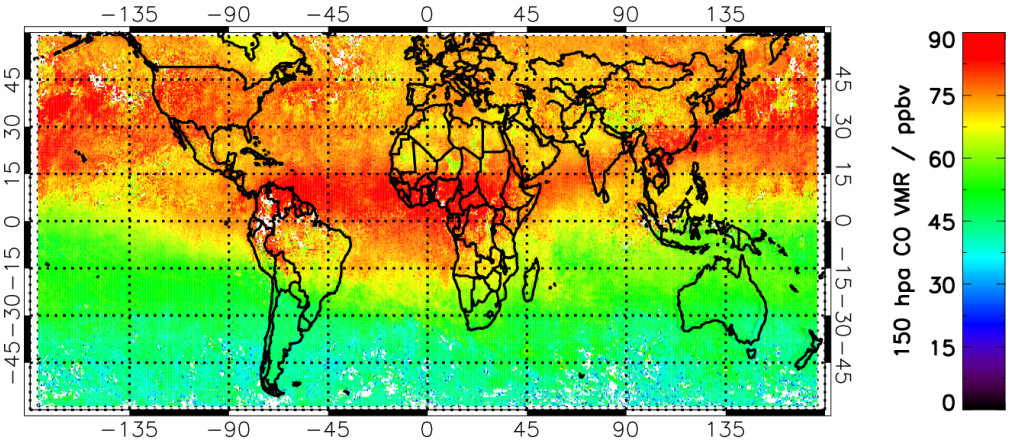

FIGURE 4.48. 150 hpa MOPITT CO for April 2003 showing the high CO enhancements due to the increased fire activity in the 0°N and below 30°N latitude band.

In addition to analysing the AATSR fire maps, the 150 hpa MOPITT CO data is shown in Figure 4.48 and shows the strong zonal enhancement of CO between 0°N and below 30°N caused by the observed fires, 150 hpa MOPITT data typically has a vertical resolution of 4 km (Kanawade, personal communication) This provides further agreement that the source of the large zonal enhancement of both C_2H_2 and C_2H_6 which is observed between 0°N and below 30°N in April 2003 is related to the distribution of fires at this time.

4.3.2 Comparisons Of C_2H_6 And C_2H_2 Detection

4.3.2.1 April

The C_2H_6 distributions above have not been analysed in as much detail as the C_2H_2 distributions in Section 4.2.3. This is partly due to the fact that there are a lot

of similarities between the two distributions due to similar sources and dynamical behaviour. However, the short analysis above has revealed some interesting features which the following will highlight through a comparison to the C_2H_2 distributions.

In April, both the C_2H_2 and C_2H_6 distributions show a similar enhancement in the 0°N to 40°N latitude band associated with the eastwards transport from the multiple biomass burning regions. However, whilst both species show enhancements over the Pacific, the large enhancement of C_2H_2 which originate from the biomass burning in South-East Asia appears much stronger than the C_2H_6 which is only moderately enhanced over the Pacific. Instead, it is the South American enhancement around the convection region at the top of South America which provides the largest C_2H_6 signal observed in April and which may be associated with the production of fossil fuel and natural gas rather than biomass burning.

Similarly, the strong localised enhancements observed over Africa at the equator for C_2H_2 are also present in the C_2H_6 but appear relatively much weaker. This result could potentially just be related to the fact that C_2H_6 possesses a weaker spectral signature and is therefore harder to detect. However, multiple-level retrievals would allow the vertical structure of the distributions to be determined but in order to probe the lower troposphere where pyro-convective injection would typically take place, aircraft measurements may be a better choice.

4.3.2.2 August

August provides the most distinct differences between the C_2H_2 and C_2H_6. As discussed above, the C_2H_2 is strongly isolated within the Asian Monsoon anticyclone. Interestingly the C_2H_6 peak radiance only shows a weak enhancement inside the anticyclone of around 80 $nW/cm^2 \cdot sr \cdot cm^{-1}$. A similar level of C_2H_6 enhancement of between 80 $nW/cm^2 \cdot sr \cdot cm^{-1}$ and 100 $nW/cm^2 \cdot sr \cdot cm^{-1}$ is observed over Central America and the South-East United States where no C_2H_2 enhancement is observed at all. This behaviour again appears to be related to the non-biomass burning sources of C_2H_6 discussed in Chapter 1, namely the fossil fuel production of natural gas.

Despite these large qualitative differences between the two species, when the two quantities are correlated (see Section 4.3.3) the background and moderate values are shown to correspond very well and it is only the enhancements which differ.

4.3.2.3 December

In contrast to August, there is a strong agreement between the two distributions for December. In particular, an enhancement over the Amazonian deep convection region is present in both the C_2H_2 and C_2H_6 distributions. However, the most interesting aspect of the distributions is that the apparent stratospheric enhancement observed above 45°N at 135°E discussed in Section 4.2.3.10 is seen for both the C_2H_2 and C_2H_6 with a very similar spatial distribution.

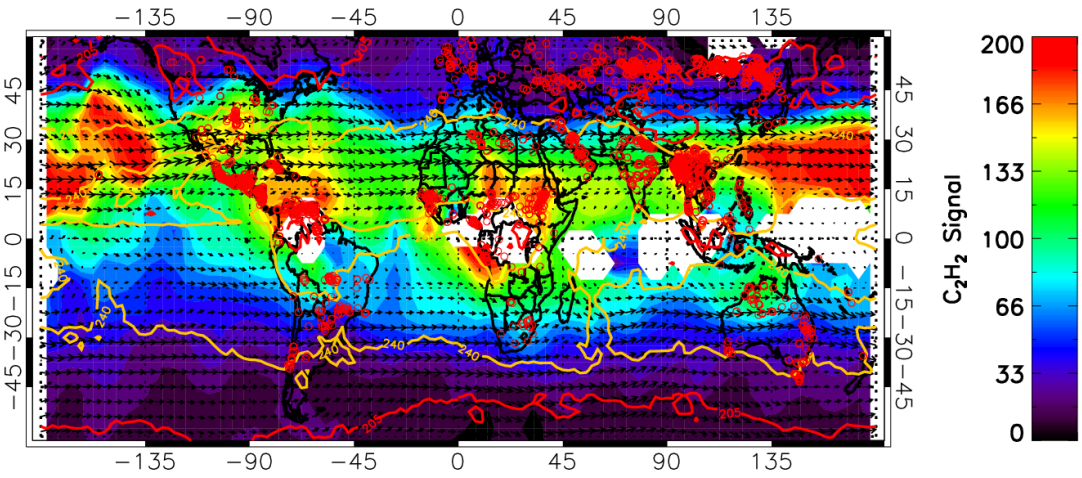

(a) C_2H_2 Detection For April 2003

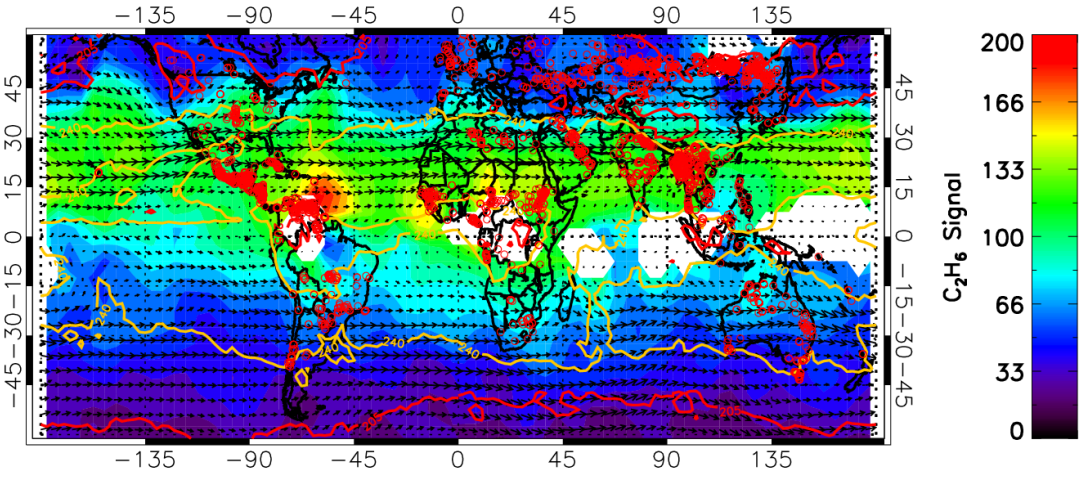

(b) C_2H_6 Detection For April 2003

FIGURE 4.49. C_2H_2 and C_2H_6 detection results for April 2003 for the 12 km MIPAS nominal altitude. ECMWF 150 hpa wind vectors and AATSR fire detections are included. NCEP OLR 240 W/m^2 (orange) and 205 W/m^2 (red) contours identify regions of convection and deep convection respectively.

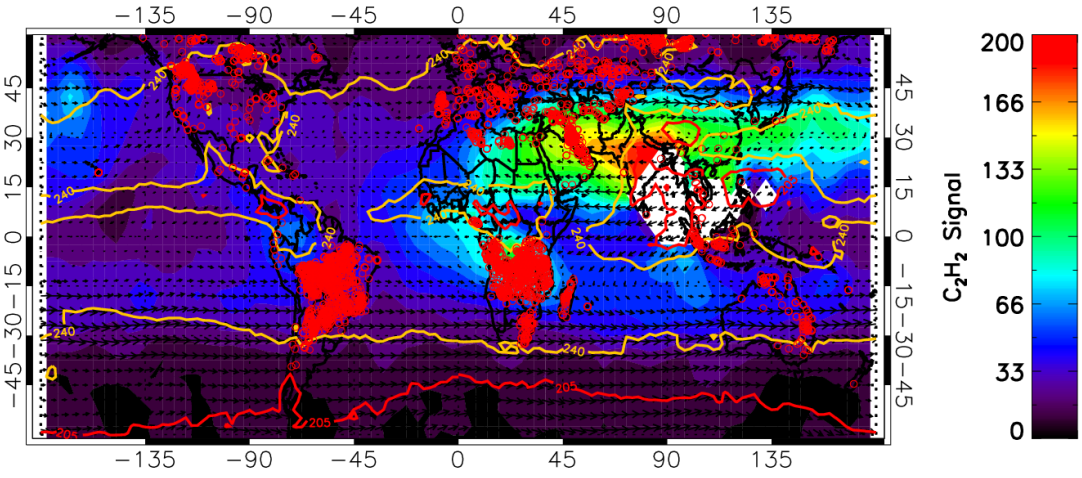

(a) C_2H_2 Detection For August 2003

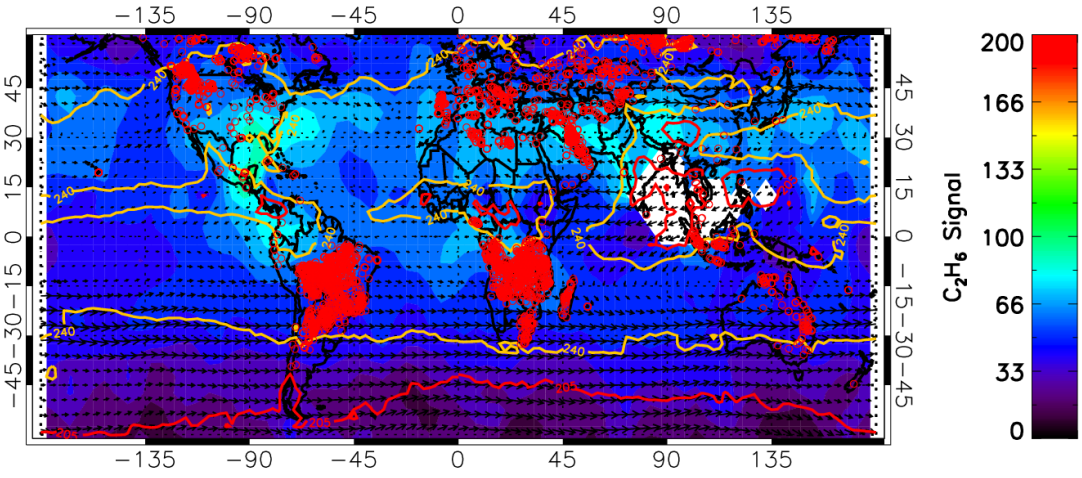

(b) C_2H_6 Detection For August 2003

FIGURE 4.50. C_2H_2 and C_2H_6 detection results for August 2003 for the 12 km MIPAS nominal altitude. ECMWF 150 hpa wind vectors and AATSR fire detections are included. NCEP OLR 240 W/m^2 (orange) and 205 W/m^2 (red) contours identify regions of convection and deep convection respectively.

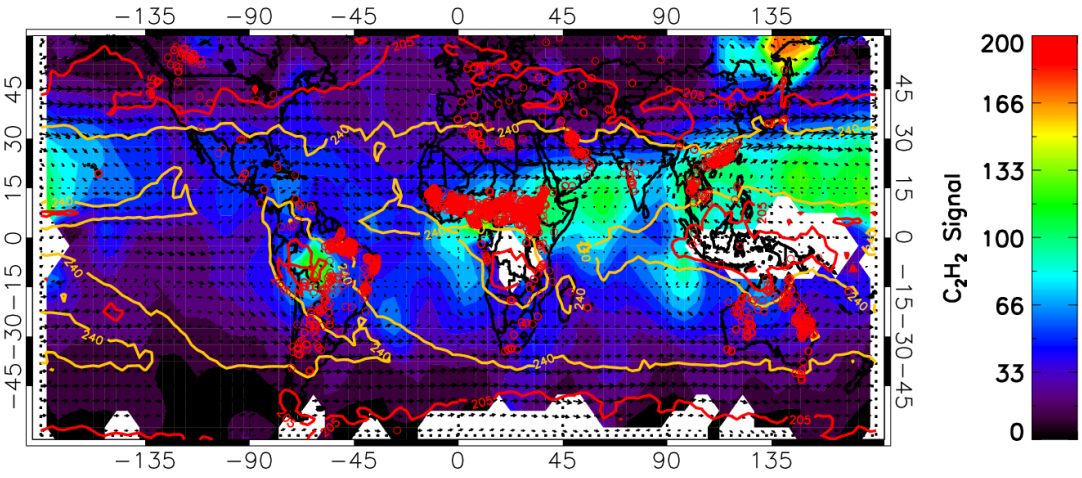

(a) C_2H_2 Detection For December 2003

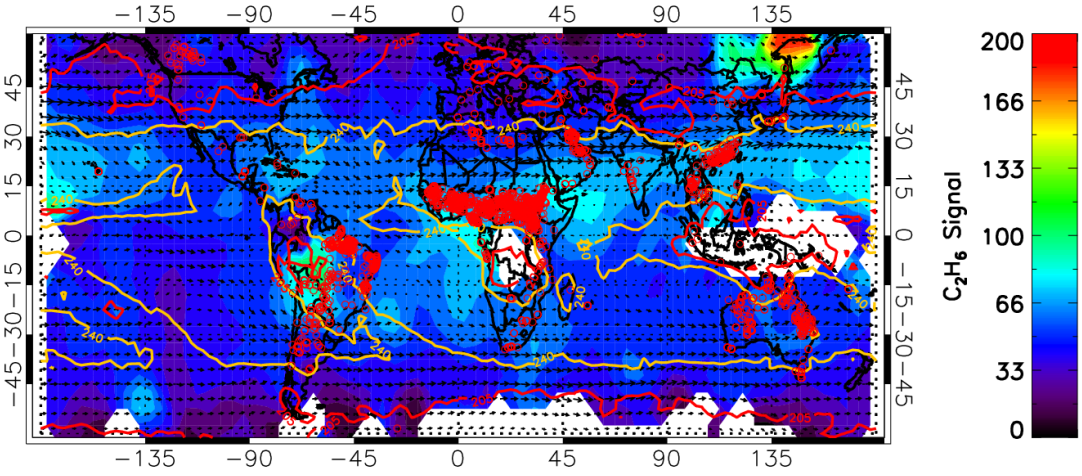

(b) C_2H_6 Detection For December 2003

FIGURE 4.51. C_2H_2 and C_2H_6 detection results for December 2003 for the 12 km MIPAS nominal altitude. ECMWF 150 hpa wind vectors and AATSR fire detections are included. NCEP OLR 240 W/m^2 (orange) and 205 W/m^2 (red) contours identify regions of convection and deep convection respectively.

4.3.3 Correlations Between C_2H_6 And C_2H_2 Detection

In order to correlate the C_2H_6 detection results against the C_2H_2 detection discussed in Section 4.2.3 it was necessary to filter both datasets to only contain points where both C_2H_2 and C_2H_6 were successfully detected from the same measurement. The results of this correlation between C_2H_2 and C_2H_6 for each month of 2003 is shown in Figures 4.52 and 4.53.

The spread in these correlations is consistent with the instrument noise of approximately 40 nW/cm^2·sr·cm^{-1} (see Section 3) but despite this a strong correlation exists between the C_2H_2 and C_2H_6 detection for most months when considered globally with the correlation coefficient peaking in April with 0.931 and having a minimum in August with 0.702.

The distribution of the correlations also differs between months. Specifically, the distribution "forks" due to high C_2H_6 being observed over Central and North America, related to fossil fuel production of C_2H_6, where there is no significant C_2H_2 enhancement.

As C_2H_6 and C_2H_2 can have similar sources from biomass burning but also have different lifetimes, it may be expected that the seasonality of biomass burning may have an effect on the relationship between the two, however this is further complicated due to the large C_2H_6 emissions associated with fossil fuel production. Figure 4.54 shows the seasonal cycle in AATSR fire counts separated for the same scenarios as the correlations discussed above. It is apparent that the Northern Hemisphere biomass burning dominates the global distribution for much of the year, from April until August, peaking in July.

The location of this biomass burning is spread out over the whole Northern Hemisphere with Siberian fires in Russia being the major source but also with North America and Europe both contributing significantly. The majority of this burning in the Northern Hemisphere happens at relatively high latitudes which can be seen by examining the 0°N and 40 °N latitude band which shows both a low fire count and almost no seasonal cycle in the total fire count. The reason for this apparent lack of seasonality, is that within this latitude band, different areas become dominant at different stages of the year. The large African fires seen in January disappear and are replaced by South-East Asian fires in February, March and April. Hence, the locations of the biomass burning regions change but when considering the latitude band as a whole, the resulting total fire count remains roughly the same throughout the year.

In contrast to the Northern Hemisphere, the Southern Hemisphere biomass burning seasonality (Fig. 4.54, blue line) has a distinctive cycle to it with a minimum in March with almost no fires and a maximum in October.

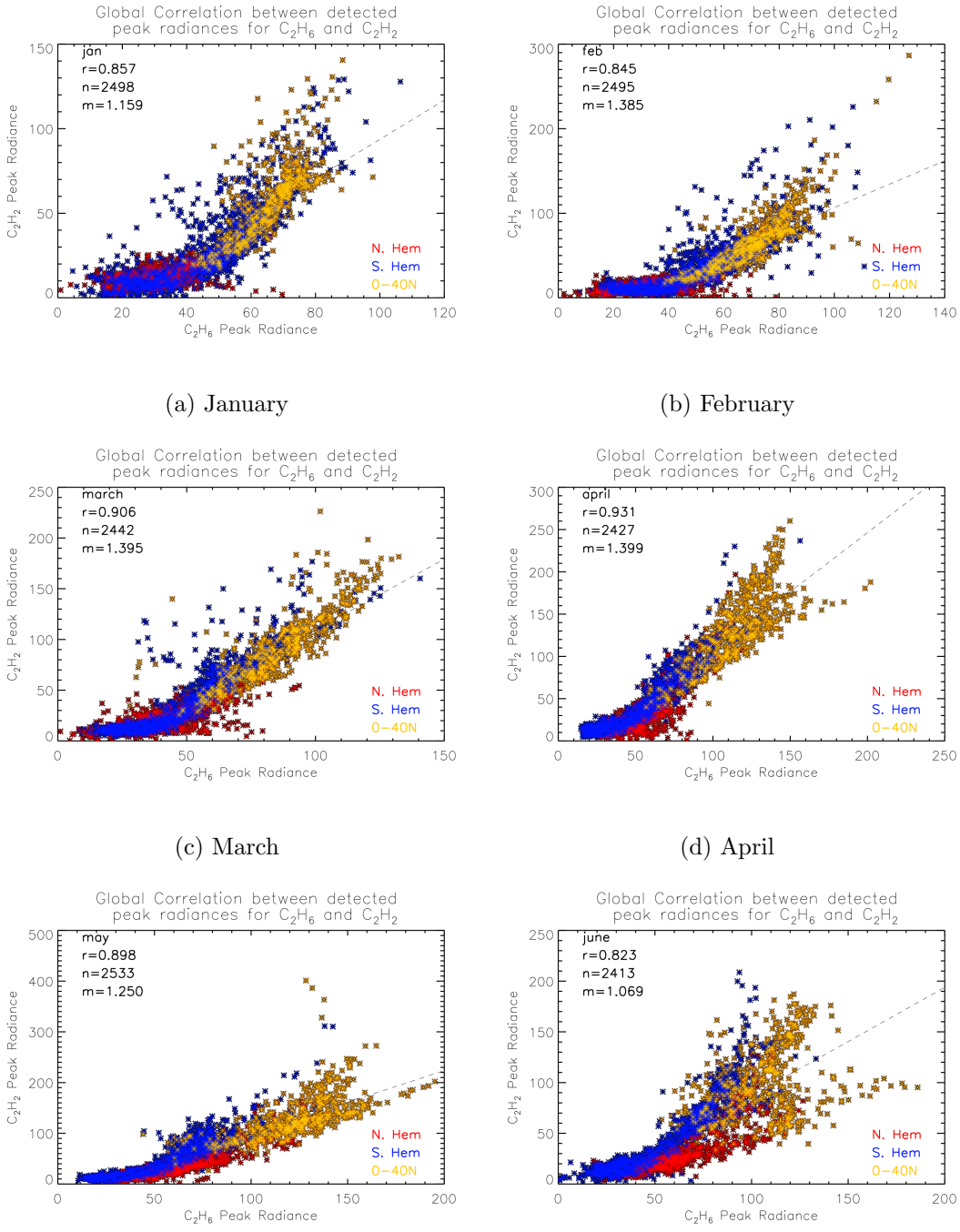

(a) January

(b) February

(c) March

(d) April

(e) May

(f) June

FIGURE 4.52. The global correlation between the detected peak radiances for C_2H_6 and C_2H_2 for January to June 2003 showing a strong correlation for most months but with a distinct "fork" to the correlation relating to the enhanced C_2H_6 detected over Central America where no C_2H_2 enhancement is observed. The data is separated into Southern Hemisphere (blue), 0-40°N region (orange) and the remainder of the Northern Hemisphere (red).

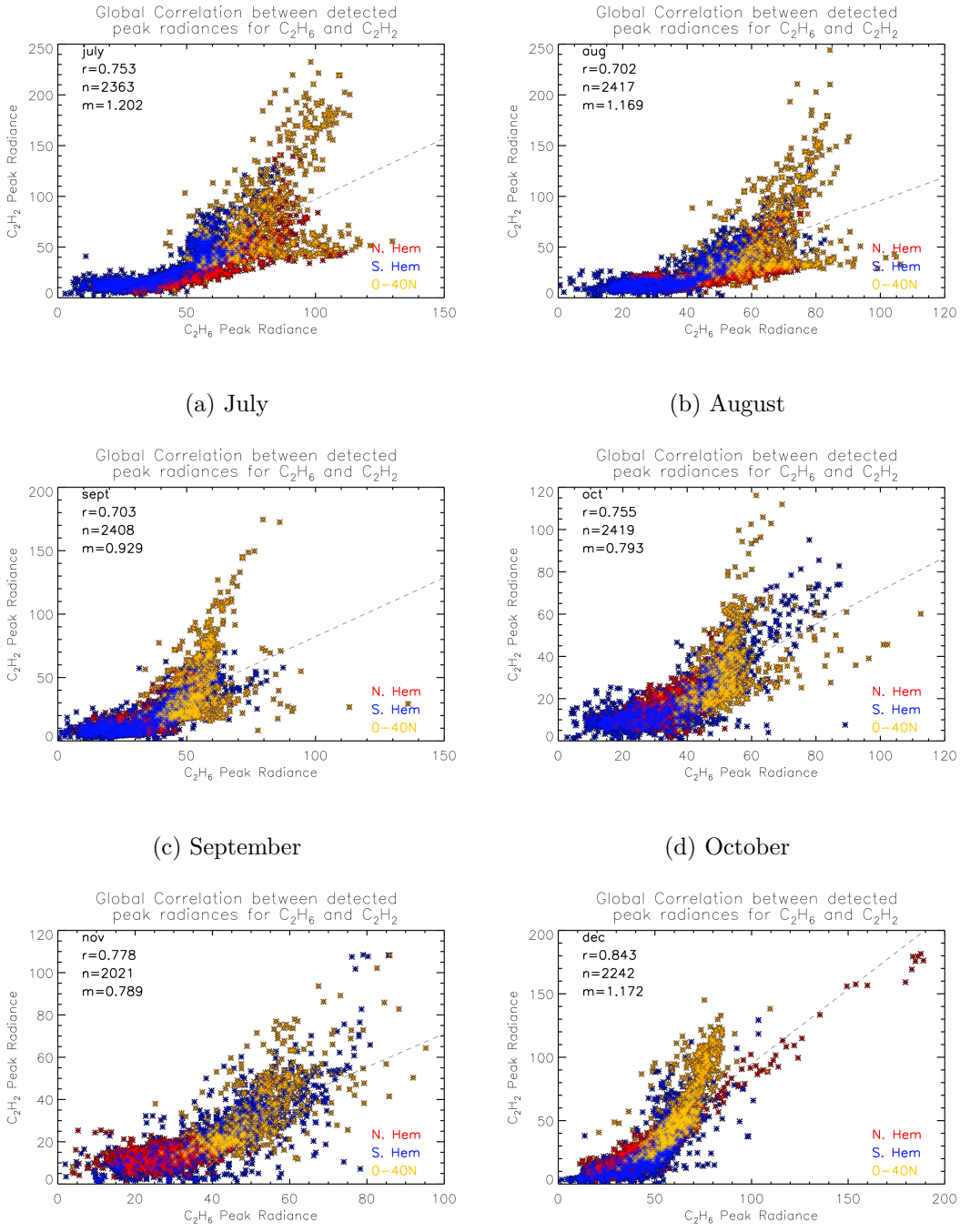

(a) July

(b) August

(c) September

(d) October

(e) November

(f) December

FIGURE 4.53. The global correlation between the detected C_2H_6 and C_2H_2 for July to December 2003. Although generally a strong correlation is observed, significant enhancements in C_2H_6 over Central America with no corresponding enhancements in C_2H_2 do produce poorer correlations for some months. Again, the data is separated into Southern Hemisphere (blue), 0-40°N region (orange) and the remainder of the Northern Hemisphere (red).

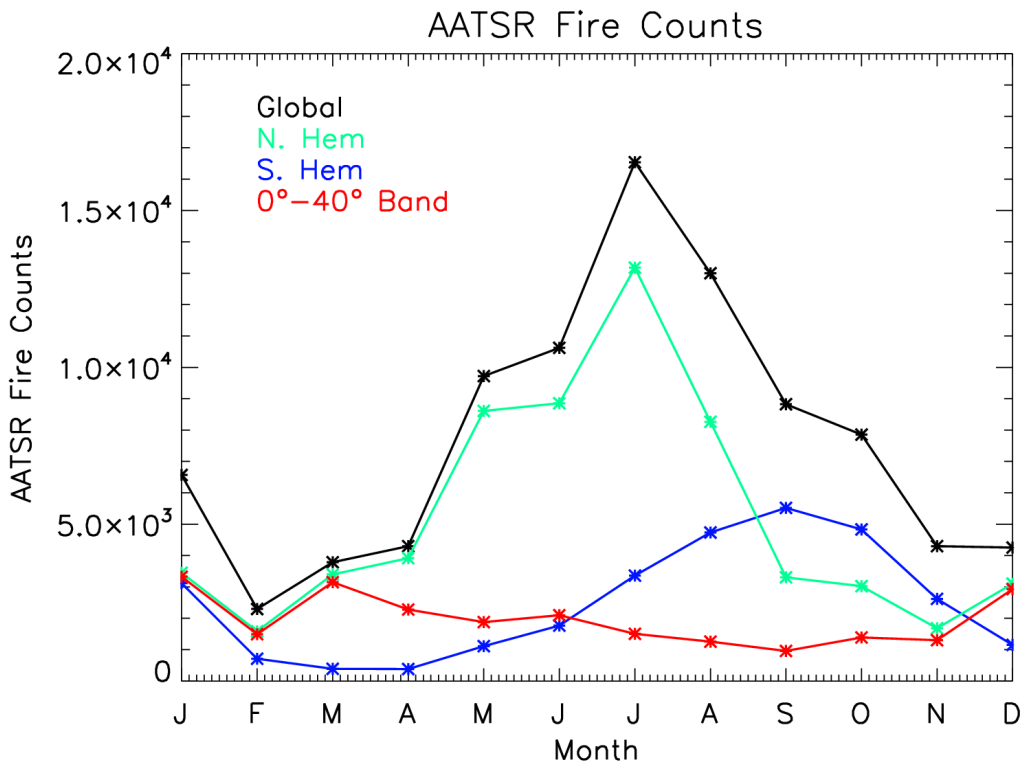

FIGURE 4.54. The seasonal cycle of biomass burning characterised by AATSR fire counts. The figure contains the seasonal cycle for the global data (black) as well as for the Southern Hemisphere (blue), 0-40°N region (red) and the whole of the Northern Hemisphere (green). The dominant feature in the global data relates to the Siberian fires that occur during the Northern Hemisphere summer but which may not be observed in the 12 km detected peak radiances as at those latitudes the tropopause height may be too low. Instead, it is the biomass burning in the Southern Hemisphere and in the 0-40°N band which is observed in the detection data.

4.4 Summary

This chapter has outlined the development of a fast detection algorithm which is capable of identifying the spectral signature of C_2H_2 and C_2H_6 in MIPAS L1B spectra. The use of such a detection algorithm is favourable to using a full optimal estimation retrieval when performing an initial analysis due to the long amount of time and computational expense which would be required to apply a full retrieval to such a large number of measurements. Whilst not a replacement for a full retrieval, the detection algorithm has been successfully applied to the entire MIPAS dataset for 2003 and has produced a variety of interesting results.

Section 4.2.3 discussed the detection results for the whole of 2003 and showed that the monthly C_2H_2 distribution could be mapped in order to highlight biomass

burning sources and transport regimes. An in-depth analysis of the C_2H_2 distribution for each month included examination of the ECMWF 150 hpa wind vectors, NCEP OLR as a proxy for deep convection, AATSR fire counts and MIPAS cloud top heights. The C_2H_2 enhancements could be explained in terms of fire emissions, convection and transport giving confidence that the detection methodology is producing reasonable results and furthermore that C_2H_2 can successfully act as a useful tracer for biomass burning.

Following on from this, Section 4.2.4 focused on the Asian monsoon anticyclone and showed with the use of ECMWF wind vectors that the C_2H_2 enhancement is isolated during the formation of the anticyclone, persisting over the summer and dissipating as the anticyclone fades. Figure 4.39 demonstrated the extent to which the C_2H_2 enhancement captures the boundary of the anticyclone region and Figure 4.42 showed how the anticyclone formation had an effect on the C_2H_2 distribution across the entire latitude band. Geopotential height anomaly (Fig. 4.39 and 4.40) and OLR (Fig. 4.41) maps were produced in order to define the monsoon boundary and convection region. The C_2H_2 isolation was again shown to be strongly correlated to the anticyclone region both during the height of the monsoon in July and August as well as when the intensity began to fall in September.

Section 4.3.1 dealt with the application of the detection algorithm to C_2H_6, producing similar global distributions to C_2H_2 albeit with some notable differences such as the C_2H_6 feature observed over Central America which is not apparent in the C_2H_2 data and may be attributed to fossil fuel production. The signature of this effect was observed as a "fork" in the correlations between the two species and was shown to not be present during the whole year, but instead these features were attributed to possible differences between the source regions and lifetimes for the two species. However, in order to discuss this in more detail, mixing ratio profiles for the two species are required and will be discussed further in regards to the retrieval results in Chapter 6.

Chapter 5

Retrieval Of C_2H_2 And C_2H_6

This chapter discusses the retrieval of C_2H_2 and C_2H_6 using the MIPAS Orbital Retrieval using Sequential Estimation (MORSE) retrieval code which was described in Section 3.6.1. Before the results of the retrieval can be discussed, a thorough analysis of both the retrieval errors and the quality of the retrieval results must be performed. This chapter therefore concentrates on analysing the quality of the retrieval results and includes comparisons to the detection algorithm discussed in the previous chapter.

5.1 C_2H_2 MORSE Retrieval Setup

The MORSE retrieval scheme as described in Chapter 2 was applied to MIPAS L1B data for August 2003 in order to retrieve C_2H_2. The C_2H_2 microwindow between 776.0 cm^{-1} to 776.15 cm^{-1} described in Section 4.1.1 was selected for the retrieval.

In order to successfully retrieve C_2H_2, it was necessary to first use MORSE to retrieve pressure, temperature, H_2O, O_3 and HNO_3 using the MIPAS operational microwindows described by Raspollini et al. [2006]. Once retrieved, these values were used as the a priori for the C_2H_2 retrieval to constrain the result to a reasonable solution, as discussed in Section 2.6. The a priori for the other species were taken from the RAMStan (Reference Atmospheres for MIPAS: Standard atmospheres) standard atmospheric climatology [Remedios et al., 2007]. A C_2H_2 a priori profile typical of biomass burning was used, based on profiles from Rinsland et al. [2005]. In order to allow for the large variation in C_2H_2 signal observed globally, it was necessary to use an a priori covariance of 1000%.

5.2 C_2H_2 Retrieval Errors

The systematic forward model parameter and instrument errors shown for each parameter are 1σ values calculated from measured biases in the MIPAS L2 data

Variable	Uncertainty
H_2O	20%
CO_2	1%
O_3	10%
HNO_3	10%
NO_2	50%
CCL_4	5%
Temperature	1%
Pressure	2%
Gain	2%
Shift	4%
Spread	2%
Spec	5%
Offset	2 nW/cm^2·sr·cm^{-1}

Table 5.1. Table showing the uncertainties of the various inputs to the retrieval error calculations. In the case of the instrument parameters and pressure/temperature, these inputs are 1σ values calculated from measured biases in the MIPAS data and were taken from Fischer et al. [2008]. The remaining parameters (H_2O, O_2 and HNO_3) were taken from previous MIPAS work outlined in the text.

and were taken from Fischer et al. [2008]. Uncertainties of 2% were assumed for pressures and 1K for temperatures. Water vapour was taken to have an uncertainty of 20% (Lahoz et al., 2004), with 10% for O_3 (Cortesi et al., 2007) and HNO_3 (Wetzel et al., 2007) and 5% for CCL_4 . The errors associated with the Gain (see Section 3.3.2) and the instrument line shape effects of Shift (the uncertainty in the spectral calibration or central position of the ILS) and Spread (the uncertainty in the width of the ILS) were calculated using perturbations to the instrument line shape of 4%, 2% and 4% respectively and an offset error of 2 $nW/cm^2 \cdot sr \cdot cm^{-1}$ was estimated, with these figures again taken from Fischer et al. [2008]. The error relating to the C_2H_2 spectroscopy was conservatively estimated to be 5% with Jacquemart et al. [2003] giving an error of between 2% and 5% for line intensities. All of these uncertainties which act as inputs to the error calculation are summarised in Table 5.1.

The errors relating to the Gain, Shift and Spread discussed above can be considered as direct convolutions of the high resolution atmospheric spectra with transformations of the nominal ILS as shown in Figure 5.1 as described in Dudhia [2004].

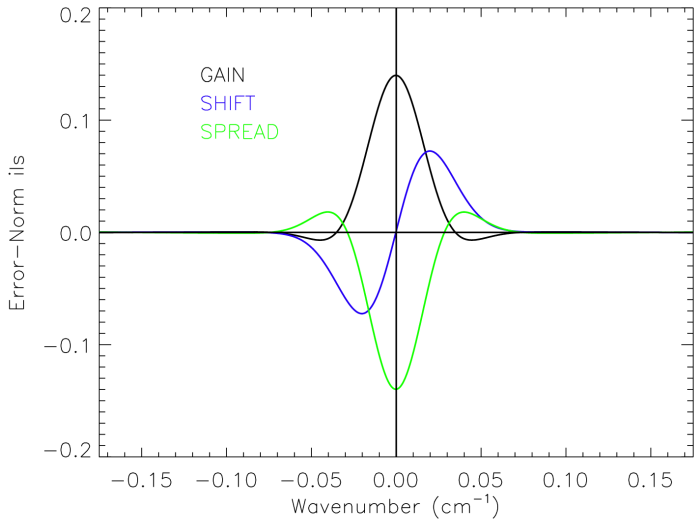

FIGURE 5.1. Difference between the nominal ILS and the perturbed ILS representing a change in the Gain, Shift and Spread respectively.

Figure 5.2 shows the final errors calculated for the retrieval between 9 km and 18 km (310 hpa to 76 hpa), showing the total calculated error (solid line), along with the random component (dotted line) and the systematic component (dashed line). Contributions to the C_2H_2 retrieval error from the various error components discussed above are also shown. As the C_2H_2 profile decreases rapidly with altitude, at pressures below 120 hpa there is a greatly reduced signal and hence the random error increases substantially and dominates the single profile retrieval error. At lower altitudes (pressures above 300 hpa), the uncertainty in water vapour VMR

has a much larger affect and at high altitudes the O_3 and HNO_3 uncertainties dominate the overall systematic error.

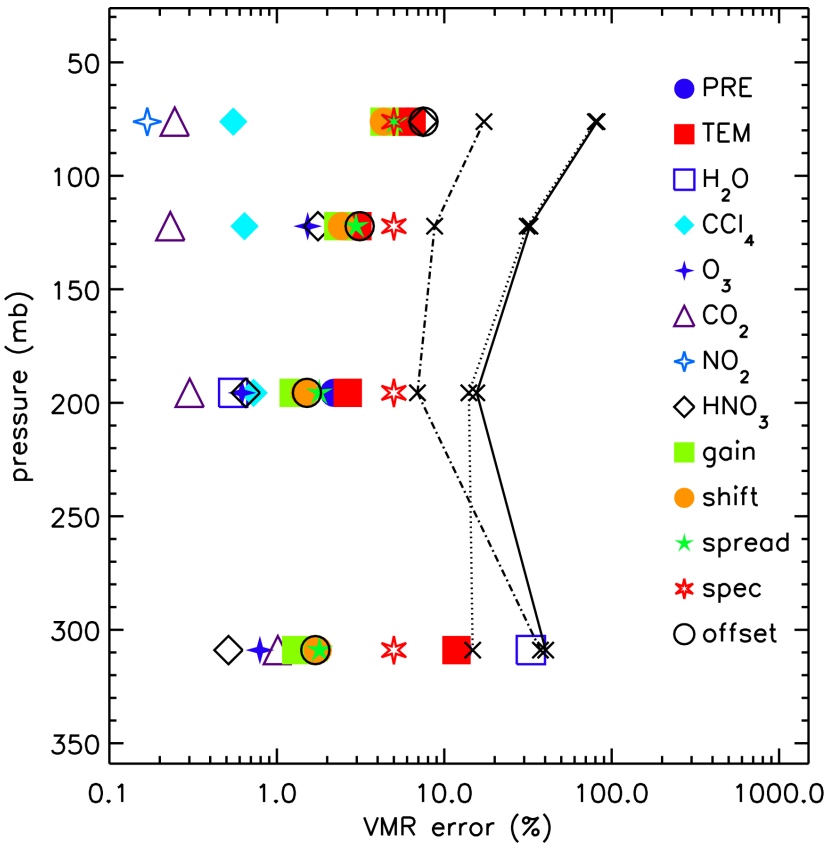

FIGURE 5.2. Contributions to the C_2H_2 retrieval error. The total error (solid line), random error (dotted line) and the systematic error (dashed line) are all shown as well as the various components to the systematic error such as the Instrument Line Shape and spectroscopic errors.

Table 5.2 summarises the calculated errors for each of the components discussed above and includes a total systematic and random error value as well as a final total error. The total error on the retrieved VMR was estimated to be 16% at 200 hpa, with the majority being related to the random retrieval noise (14%) and only 7% related to the systematic errors. Of those systematic errors, the uncertainty in the C_2H_2 spectroscopy and instrument line-shape effects along with the uncertainty in the pressure and temperature are the dominant contributors with a minimal contribution from the uncertainty in the VMRs of other species in this spectral window.

	Pressure Level (hpa)			
Error Component	308.96	195.62	122.2	76.15
P	12.05	2.2	2.59	6.09
T	11.83	2.65	3.03	6.38
H_2O	32.92	0.55	0.07	0.06
CCL_4	1.49	0.73	0.64	0.55
O_3	0.79	0.62	1.53	4.38
CO_2	1.01	0.3	0.23	0.25
NO_2	0.03	0.02	0.05	0.17
HNO_3	0.51	0.65	1.76	7.47
GAIN	1.31	1.26	2.33	4.4
SHIFT	1.75	1.47	2.44	4.35
SPREAD	1.8	1.79	2.97	5.06
SPEC	5	5	5	5
OFFSET	1.7	1.51	3.13	7.52
Total Systematic (%)	37.53	6.92	8.76	17.28
Total Random (%)	14.78	14.02	31.29	79.95
Total Error (%)	40.34	15.64	32.49	81.80

Table 5.2. Table showing the calculated errors for the each component of the error analysis for the four retrieval levels between 9 km and 18 km. The final percentage systematic, random and total errors are also shown.

5.3 C_2H_2 Data Quality

Before it is possible to use the retrieval results, it is necessary to examine the various indicators of retrieval quality. This section first deals with the effects of vertical sensitivity and cloud contamination on the retrieved C_2H_2 VMRs before going on to examine the data filtering in detail.

5.3.1 Averaging Kernels

Typical averaging kernels for the retrieval over the monsoon anticyclone region where high C_2H_2 concentrations are observed are shown in Figure 5.3 and clearly show strong peaks at 300 hpa and 200 hpa. The fact that there is no significant C_2H_2 signal at pressures below 120 hpa is also shown. The 200 hpa averaging kernel peaks with a value of 0.72, indicating that there is a significant amount of information arising from the measurements.

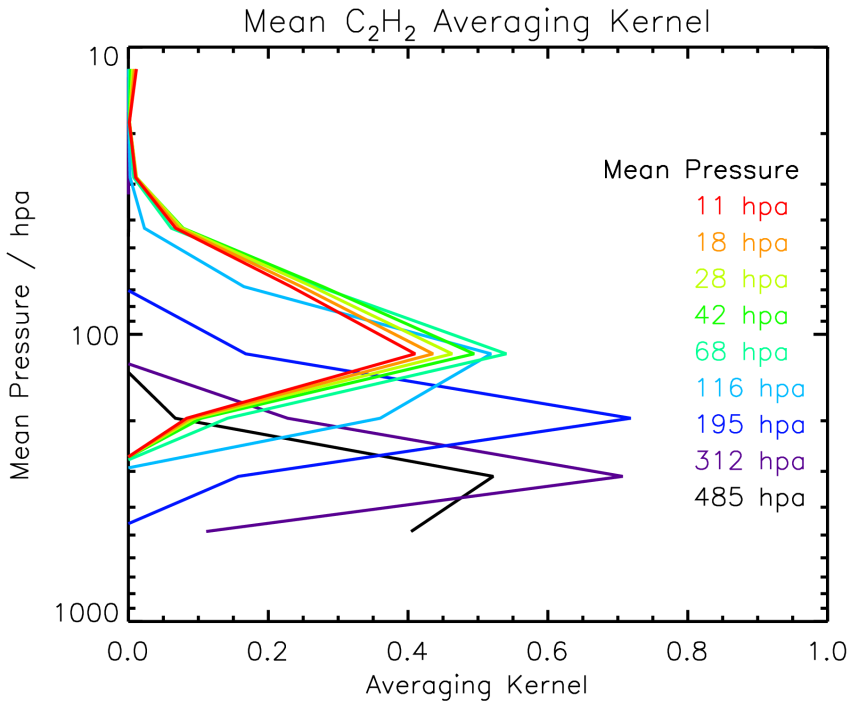

FIGURE 5.3. Mean averaging kernels over the monsoon anticyclone showing the quality of the retrieval at 200 hpa and 300 hpa. Note that there is no discernible C_2H_2 signal above 100 hpa as expected.

5.3.2 Cloud Index

In order to remove any poor quality or biased retrievals it is important to consider the impact of cloud filtering upon the retrieval results. Note that a retrieval is only attempted if the cloud index is greater than 1.8, otherwise no attempt is made to retrieve information from a scan and instead the retrieval moves on to the next non-cloudy scan.

Figure 5.4(a) shows the MIPAS cloud index (as discussed in Section 3.5) for every C_2H_2 retrieval that successfully converges.

The majority of measurements with a cloud index between 1.8 and 4.0 occur on the edge of cloudy (white) regions, suggesting that a more rigourous cloud threshold is required to remove these partially cloud-affected measurements.

Figure 5.4(b) shows the cloud index values with a cloud index threshold of 4 (cloud-free, [Spang et al., 2004]), along with a C_2H_2 CHISQ ≤ 2 and a Pressure CHISQ ≤ 10. This more stringent quality filtering does not significantly affect the data coverage. The main effect is the removal of measurements made at the boundary of cloudy areas where partially cloud-contaminated measurements may have otherwise affected the retrieval results. The following section will examine the data filtering in more detail.

5.3.3 Data Quality Filtering

The quality filtering of the C_2H_2 retrieval results must be carefully considered. In this section the effect of each additional filter on the final C_2H_2 "acceptable" values is discussed. The effect on the final C_2H_2 distribution by the addition of each subsequent filtering parameter is shown in Figure 5.5. Figure 5.5(a) shows the C_2H_2 distribution with no additional filtering. The only data filtering applied here is that the condition that the cloud index of the scan is greater than 1.8 is checked before the retrieval is started. The gaps in data, such as the large areas over Central America, Africa and South-East Asia, are purely due to the cloudiness of the data in these regions and are well correlated with areas of convective activity.

As shown above, a cloud threshold of 4 as opposed to 1.8 provides more confidence that partially cloudy scenes have been removed that may otherwise still be present and have an effect upon the retrieval. As can be seen in Figure 5.5(b), the effect of increasing the cloud index threshold to 4.0 does not significantly alter the C_2H_2 spatial distribution regionally, but instead just enlarges the areas that were already identified as cloudy. This is in agreement with the analysis of the cloud index in Section 5.3.2 where it was noted that the majority of measurements with a cloud index between 1.8 and 4.0 occur on the edge of the large cloud areas.

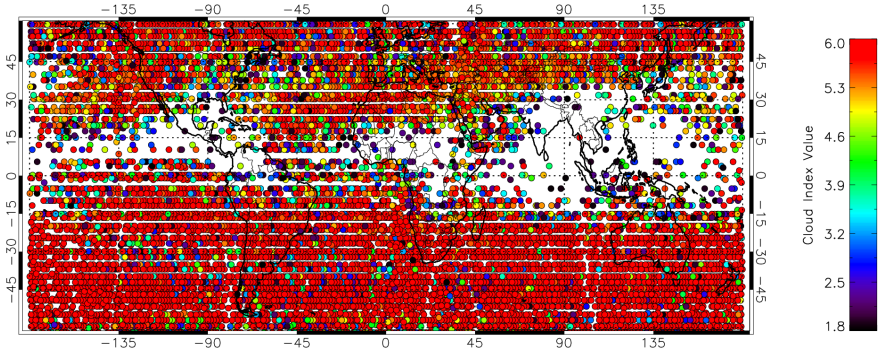

(a) Unfiltered

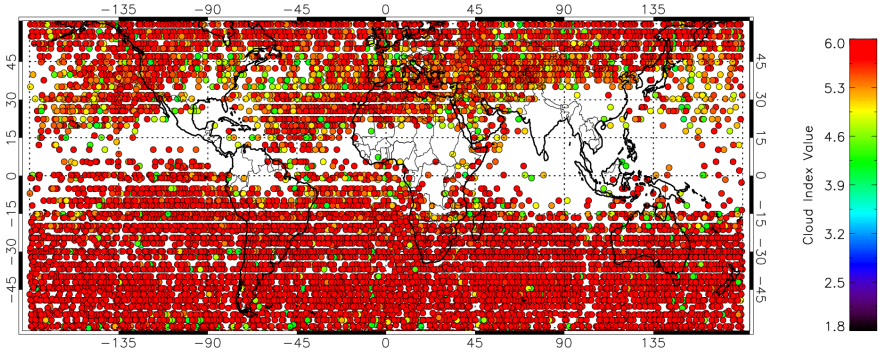

(b) Filtered

FIGURE 5.4. (a) Unfiltered 200 hpa Cloud Index Map and (b) Filtered 200 hpa Cloud Index Map With CI ≥ 4, CHISQ ≤ 2 and Pressure CHISQ ≤ 10 showing that the majority of points remaining once a cloud index threshold of 1.8 has been applied are located on the boundary of the cloudy regions. This shows that in order to fully remove the effect of cloud, a tightened cloud index threshold of 4.0 is more suitable.

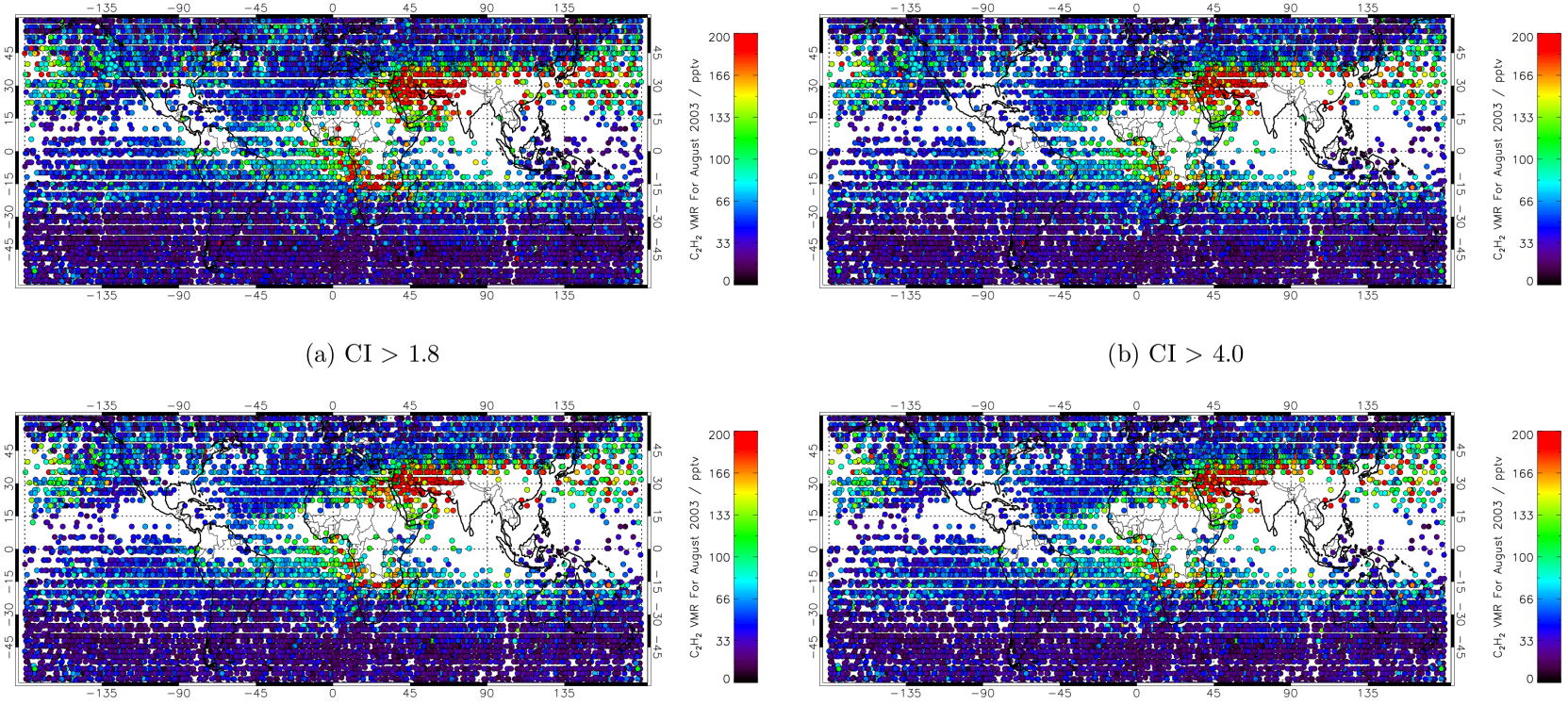

(a) CI > 1.8

(b) CI > 4.0

(c) CI > 4.0 and CHISQ < 2.0

(d) CI > 4.0,CHISQ < 2.0 and PCHISQ < 10

FIGURE 5.5. The 200 hpa C_2H_2 retrieval results for August 2003. The 4 figures indicate different stages of filtering with: a) Only the minimum cloud index filter of 1.8 applied - b) A higher cloud index threshold of 4.0 - c) A CI threshold of 4.0 and a CHISQ filter of 2.0 on the C_2H_2 retrieval - d) The same as the previous filtering but with an additional filter of a CHISQ filter of 10.0 on the Pressure retrieval.

Aside from the use of the cloud index to filter the retrieval results, one of the most important quality indicators that comes from the retrieval itself is the CHISQ value. From an analysis of the C_2H_2 retrieval results, a CHISQ filter of 2.0 was chosen so as to remove the few anomalous C_2H_2 values where the spectral fit between the measurement and simulation was found to be poor. The effect of applying this CHISQ filter in addition to a cloud index threshold of 4.0 is shown in Figure 5.5(c). There is no significant change in the C_2H_2 distribution when applying this extra level of filtering. The few high C_2H_2 measurements in regions of otherwise low values, such as below 30°S, are removed.

Finally, the last filtering condition used is that the CHISQ for the initial pressure retrieval must be less than 10. Whilst this condition does not directly relate to the quality of the C_2H_2 retrieval, it does ensure that the value that the C_2H_2 uses as its a priori pressure value is a realistic value with a good spectral fit to the measurement. It was found that even with an a priori value for the initial pressure taken from a poorly-fitted retrieval, the C_2H_2 retrieval was still capable of converging upon a reasonable answer. In order to remain cautious of such cases and to only use the C_2H_2 retrievals where the pressure is well-fitted, a CHISQ value for the pressure retrieval of less than 10 was used. This threshold of 10, whilst high, does ensure that the worst pressure retrievals are omitted. As can be seen from Figure 5.5(d), this filter again does not significantly affect the distribution of the C_2H_2 retrieval but does give more confidence that the values of the retrieved C_2H_2 VMRs are correct.

Although the above discussion, along with Figure 5.5, has shown the effect of applying the different stages of filtering on the C_2H_2 distribution, it is also necessary to quantify the effect of this filtering. It should be noted that the values of the CHISQ filtering criteria discussed above are somewhat arbitrary and based empirically on the statistics of the retrieval results. Therefore, future work would entail a wider exploration of these values to optimise them further. However, the following section will show the effect of these filtering criteria on the data and how they successfully lead to the removal of the poorer quality retrievals.

5.3.4 Spectral Residual As Indicator Of Data Quality

The residual calculated from the spectral fit of the final simulated spectrum against the measured spectrum provides information on how well the retrieval has worked. This indicator for how well the retrieval is performing is possibly the one of most use as it tells us whether the simulation using the retrieved C_2H_2 VMR agrees with the measured spectra. If there is a large disagreement here, despite the other quality indicators implying that the retrieval was successful, then there is clearly a problem with the retrieval process either in the initial setup of the a priori or in the actual retrieval parameters such as the microwindow range or the amount that the a priori covariance allows the residual to be minimised.

The frequency distribution of the C_2H_2 spectral residual for the peak at the centre of the C_2H_2 microwindow at 776.075 cm^{-1} is shown in Figure 5.6. The

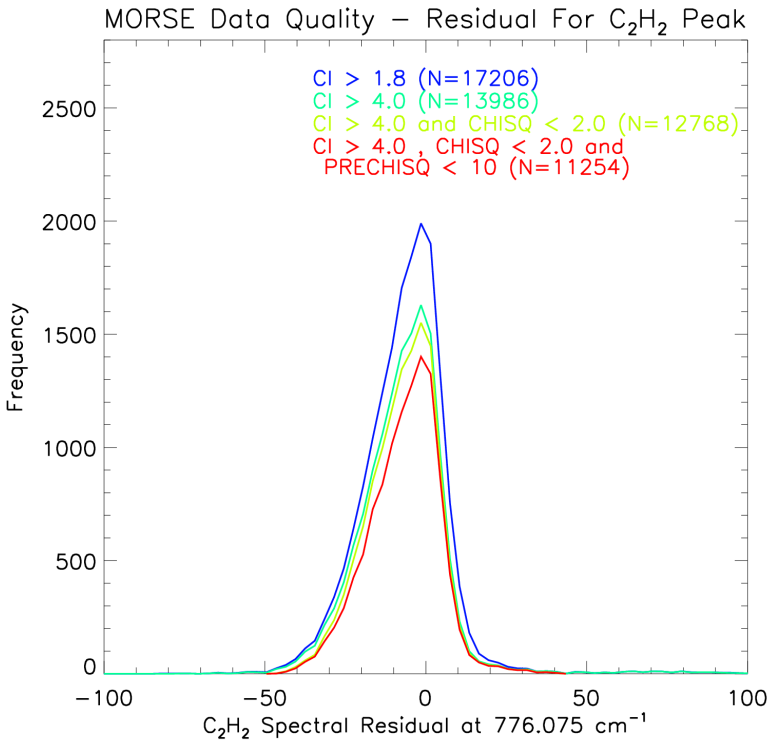

FIGURE 5.6. Frequency distribution showing the spectral residual values of the C_2H_2 peak at 776.075 cm^{-1} for the C_2H_2 retrieval and the effect that the quality filtering has. The majority of the distribution ranges from -50 $nW/cm^2 \cdot sr \cdot cm^{-1}$ to +40 $nW/cm^2 \cdot sr \cdot cm^{-1}$ which is within the MIPAS noise and indicates that the retrieval is converging on a result which leads to an extremely good fit to the measurement.

fact that this distribution peaks at a value of 0 is encouraging and suggests that the retrieval is obtaining an extremely good fit between the simulation using the retrieved C_2H_2 VMR and the measured spectra. In addition to this, even for the case where no additional filtering is applied, the fact that the majority of the distribution ranges from -50 $nW/cm^2 \cdot sr \cdot cm^{-1}$ to +40 $nW/cm^2 \cdot sr \cdot cm^{-1}$ shows no significant spread on the residual values. The noise on the MIPAS measurement is expected to be approximately 40 $nW/cm^2 \cdot sr \cdot cm^{-1}$ (reduced to approximately 25 $nW/cm^2 \cdot sr \cdot cm^{-1}$ for the apodised spectra - see Section 4.1.6). This means that the distribution of the residual is primarily within the noise of the measurement and the retrieval is generally fitting the spectra as well as possible. The application of the full filtering conditions do not alter the residual distribution, instead they reduce the peak value as expected and remove the very small number of outlying values where the residual is not being correctly fitted and has a value greater than $\pm$ 50 $nW/cm^2 \cdot sr \cdot cm^{-1}$.

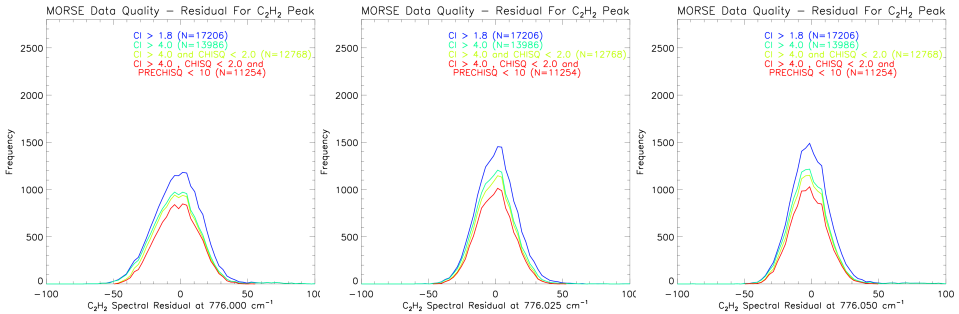

(a) 776.000 cm^{-1} (b) 776.025 cm^{-1} (c) 776.050 cm^{-1}

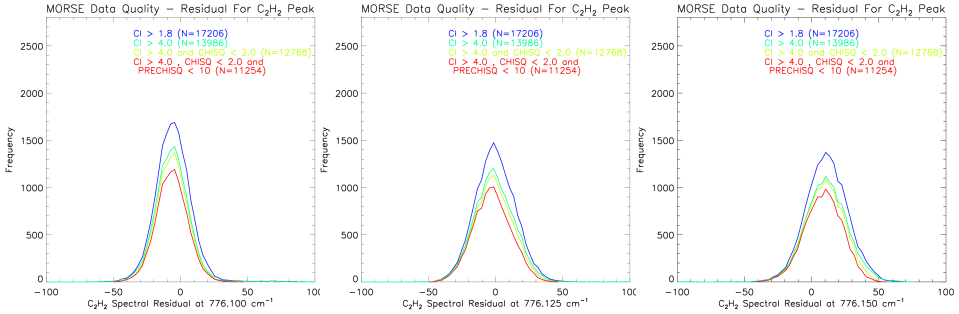

(d) 776.100 cm^{-1} (e) 776.125 cm^{-1} (f) 776.150 cm^{-1}

FIGURE 5.7. Histogram showing the distribution of C_2H_2 Residual values for each of the other 6 spectral points in the C_2H_2 microwindow. The fact that the majority of the residuals for each spectral point in the microwindow is within the MIPAS noise shows that the retrieval is providing a good fit to the measurement.

Although the analysis of the residual for the centre of the C_2H_2 peak shows that there is an extremely good fit between the measurement and simulation using the retrieved C_2H_2 VMRs, it is also necessary to consider the residual for the remaining 6 points in the microwindow and to ensure that the spectral fit here is just as good and no contaminant species are affecting the C_2H_2 microwindow.

Figure 5.7 shows the same type of frequency distribution as shown in Figure 5.6 but for each of the remaining 6 spectral points in the C_2H_2 microwindow. Despite small difference in the distributions in terms of height and width, all of the distributions are centred approximately around 0. The distributions all have a range less than -50 nW/cm^2·sr·cm^{-1} to + 50 nW/cm^2·sr·cm^{-1}, with the majority of the values being within 40 nW/cm^2·sr·cm^{-1} of the centre. The effect of filtering is the same as it was for the centre of the C_2H_2 peak, the peak of the distribution is reduced but all of the outlying values are also removed. These plots have shown that the fit between the measurement and the retrieval is good and is within the measurement noise for the majority of the retrievals.

In order to emphasis the quality of the spectral fit and to justify further the use of the various filtering conditions, all of the spectral residuals are plotted together with the colour used to distinguish between different measurements (Fig. 5.8). As there are a huge number of measurement residuals plotted (17206 in the case of no additional filtering), it is not the purpose of these plots to show the details of the retrievals which have a small spectral residual and have hence achieved a good fit between the measurement and the retrieval. Instead the purpose of this plot is to highlight the few cases where the fit between the measurement and the retrieval is poor and to show the affect that filtering can have on such cases.

Figure 5.8(a) shows all of the C_2H_2 residuals, with the dashed line showing the mean value of all of the residuals and the dash-dot line showing the ± 40 nW/cm^2·sr·cm^{-1} values indicating the measurement noise. Ideally all of the points of the residuals would be within this noise boundary. As can be seen, for the case where no additional filtering is applied this is clearly not the case. Although the majority of points are within the noise values (as also shown from the frequency distributions), there are several retrievals where the residual is extremely poor with some of the points having a spectral fit several hundred nW/cm^2·sr·cm^{-1}s apart. It should be noted that when compared to the total of 17206 retrievals, these cases where the residual is poor are relatively tiny but nevertheless should be taken into account. In addition to these points, there appears to be a systematic problem fitting the 776.015 cm^{-}1 spectral point for a number of retrievals.

The application of the stricter cloud index threshold (Fig. 5.8(b)) does not seem to effect either of these problems, suggesting that it is not an issue with cloud-contamination but instead is an issue with the retrieval itself. When applying the C_2H_2 CHISQ filter (Fig. 5.8(c)), data affected by these issues is removed and almost all the remaining residuals lie within the MIPAS noise level of ± 40 nW/cm^2·sr·cm^{-1}. This has shown that whilst it is the filtering of cloud-contaminated measurements using the cloud index threshold that has the largest effect on factors such as the DOFS and removes the most measurements from the

dataset, the CHISQ value is an important parameter which can be used to ensure that only the data with a good fit between the measured and simulated spectra is used. In the case of C_2H_2, even without using the CHISQ value to filter the results, the data is still of a high quality when only filtered for cloud, however to remove the relatively small number of poor retrievals it has been shown that the CHISQ filter is an important part of the data quality process.

This section has shown that a good spectral fit is achieved between the measurement and simulation once the cloud index, C_2H_2 CHISQ and Pressure CHISQ are suitably filtered. In order to investigate the effects of this filtering further, the change in distributions of the VMR, CHISQ and DOFS due to this filtering will be examined.

5.3.5 VMR Distribution As Indicator Of Data Quality

Figure 5.9 shows the frequency distribution of the C_2H_2 retrieved VMRs for each of the filtering conditions used in Figure 5.5. As can be seen from the unfiltered case, with the cloud index just greater than 1.8, there are 17206 successful C_2H_2 retrievals with the peak of the distribution occurring at around 40 pptv and the majority of the retrieved VMRs below 100 pptv. Whilst the distribution has the minimum value confined by the condition that the retrieved VMR must be greater than 0, there is no such constraint on the maximum value which leads to a significant tail on the front of the distribution, extending out to 400 pptv with ever-decreasing frequency. As it is the enhanced values of C_2H_2 that are of most interest with, i.e. those with a value over 100 pptv, it is the values that exist in this tail away from the background value of 40 pptv that we are interested in.

With the adjustment of the cloud index threshold from 1.8 to 4.0, the number of successful retrievals is reduced from 17206 to 13986. As can be seen from Figure 5.9, this stricter cloud filtering does not significantly effect the tail of the distribution above 100 pptv, instead its largest effect is seen around the peak of the distribution. With the stricter cloud filtering, there are approximately 300 less measurements at the peak of the distribution at 40 pptv. This result is in agreement with the analysis of the C_2H_2 distribution maps above. The effect of altering the cloud index threshold from 1.8 to 4.0 mainly affects the background or low C_2H_2 values as high concentrations of C_2H_2 would not have been capable of converging for cloud-contaminated measurements

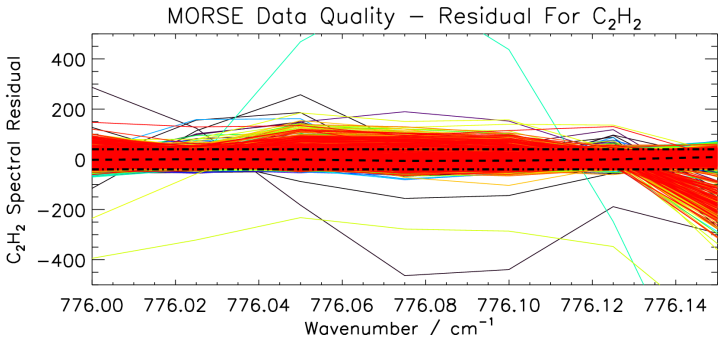

(a) CI > 1.8

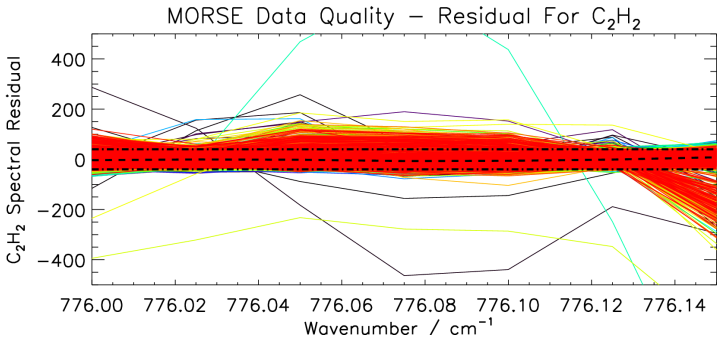

(b) CI > 4

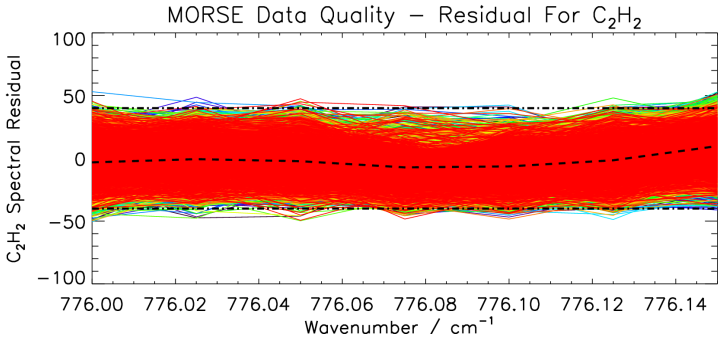

(c) CI > 4 and CHISQ < 2

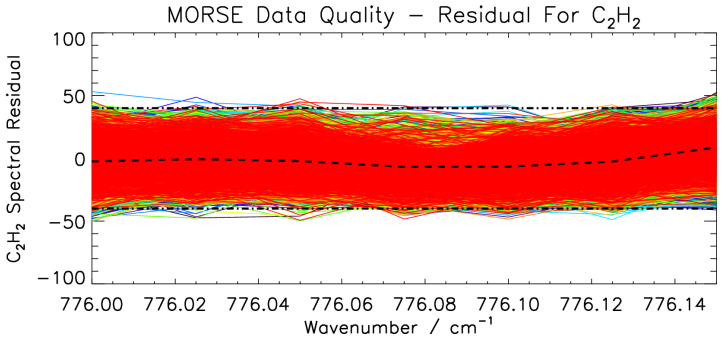

(d) CI > 4, CHISQ < 2 and PCHISQ < 10

FIGURE 5.8. Residuals for the C_2H_2 retrieval and the effect of the different filtering scenarios. The dashed line shows the mean value of all of the residuals and the dash-dot line shows the ± 40 nW/cm^2·sr·cm^{-1} values indicating the measurement noise. After application of the full filtering scenario, all of the retrieval residuals lie within the MIPAS noise (Fig. 5.8(d)).

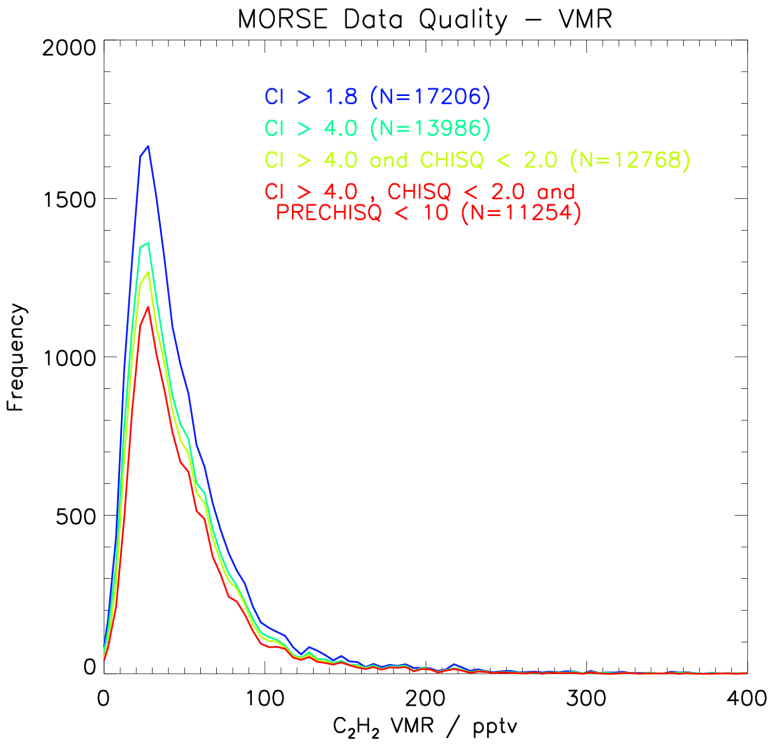

FIGURE 5.9. Histogram showing distribution of C_2H_2 VMRs for cases described in Figure 5.5. This distribution peaks at a value of around 50 pptv which is the background C_2H_2 VMR. The majority of the data are between 0 pptv and 100 pptv, with only a relatively small amount of data having a significantly enhanced VMR of over 100 pptv.

The effect of applying the C_2H_2 CHISQ filter can also be seen in Figure 5.9 and leads to the additional removal of just over 1200 points. After the application of the final filtering condition (Pressure CHISQ ≤ 10.0), the number of measurements is further reduced to 11254. This last filtering removed 1500 measurements where the pressure retrieval was not deemed to be suitable.

Although a small peak around 200 pptv is removed by the application of the cloud index threshold, it has been shown above that to achieve a good spectral fit this cloud index threshold is necessary. The important aspect to note is that apart form this, the tail of the distribution where the C_2H_2 enhancements are to be found remains largely unaffected by any of the filtering applied. This suggests that when a strong C_2H_2 VMR is present, the size of the peak in the spectra is strong enough so that a successful retrieval can be performed. The next sections take a further look at the indicators or retrieval quality and the effect that filtering has on these.

5.3.6 CHISQ As Indicator Of Data Quality

As discussed above and in Section 2.6.9, the CHISQ value is an important output from the retrieval which is capable of acting as an indicator of the quality of the retrieval. Figure 5.10(a) shows the CHISQ value for each C_2H_2 retrieval with the only filtering applied being the cloud index threshold of 1.8. Although the majority of CHISQ values are below 2, there is considerable noise in the plot with some values greater than 10 and no apparent pattern in the distribution of these points. The application of a stricter cloud index threshold as well as filtering the C_2H_2 and pressure CHISQ values as previously described, results in the plot shown in Figure 5.10(b). Here the upper limit on the CHISQ value of 2.0 is imposed by the filtering conditions and again there does not appear to be any bias between the geo-location of the measurement and the CHISQ value that results from the C_2H_2 retrieval.

In order to analyse this further, the frequency distribution of the CHISQ values is plotted (Fig. 5.11) for the different filtering criteria. For the case where no extra filtering is applied, with only the cloud index threshold of 1.8 being used, the distribution is strongly peaked around a CHISQ value of 1 with a tail extending out to 10. However, the values within the tail in this instance are extremely small with only a negligible number of points with a CHISQ value greater than 4.0. The effect of increasing the cloud index threshold to 4.0 reduces the peak of the distribution but it also has an effect on the CHISQ values in the tail of the distribution, reducing these even further. Whilst this reduction is similar at both the peak and within the tail, considered as a relative amount the reduction in the tail is substantially greater with almost half of the CHISQ values between 2.0 and 4.0 being removed compared to less than a tenth of the values at the peak.

The application of the next stage of the filter, removing points with a CHISQ for the C_2H_2 retrieval greater than 2.0, just applies a cut-off at 2.0 in the frequency distribution plot. The final stage of filtering, applying the condition that the CHISQ value for the initial pressure retrieval must be less than 10, does not greatly effect the shape of the distribution, mainly just reducing the peak further. It has been shown that in the case of the CHISQ frequency distribution for the C_2H_2 retrieval, the application of the various filtering conditions has removed the higher CHISQ values whilst maintaining the shape of the distribution, centred on a CHISQ value of 1.0.

5.3.7 DOFS As Indicator Of Data Quality

The calculation of the Degrees Of Freedom Of Signal for the C_2H_2 retrieval are discussed in Chapter 2. Considering the averaging kernels for the C_2H_2 retrieval shown in Figure 5.3, we would expect a significant signal from the 12 km and 15 km nominal MIPAS altitudes, approximately equivalent to 300 hpa and 200 hpa in the case of the August 2003 retrievals. We might also expect some degree of signal from the 9 km nominal altitude and possibly some from the higher altitudes although the averaging kernels have shown that there is no discernable signal above 100 hpa.

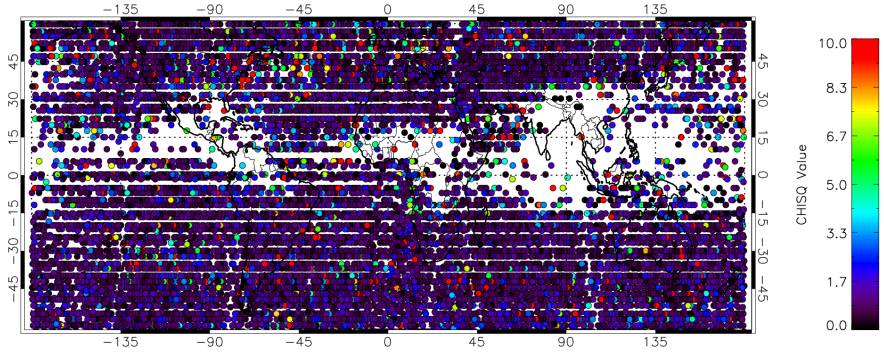

(a) CI > 1.8

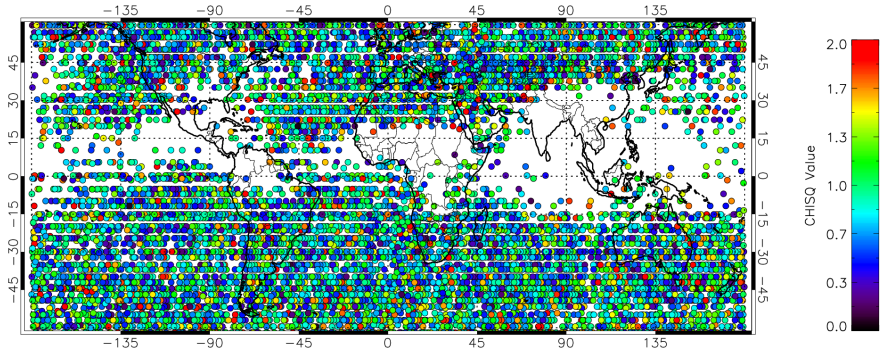

(b) CI > 4.0,CHISQ < 2.0 and PCHISQ < 10

FIGURE 5.10. The CHISQ values for the 200 hpa C_2H_2 retrieval results for August 2003. The top figure has only the minimal cloud threshold of 1.8 applied whereas the bottom figure has the full filtering scenarios discussed above applied (note differing scale). In order to show the variability in the CHISQ values, it should be noted that the two figures require separate scales. There appears to be no systematic bias in CHISQ values over certain regions which would otherwise lead to a possible bias in the retrieval results.

This would lead us to expect a value for the DOFS of approximately 2 with a minimum value of 1 and a maximum of around 3.

Figure 5.12 shows the actual DOFS frequency distribution calculated from the C_2H_2 retrieval data. As can be seen the distribution is much as expected, with the majority of the values distributed between 1 and 3. However, there is a slight skew to the distribution and rather than being centred on a value of 2, the distribution seems to centre on approximately 1.7 instead.

For the case where no additional filtering is applied, there is a large peak superimposed on top of the distribution at a value of 1.3. When the cloud index threshold is increased to 4.0, this peak disappears.

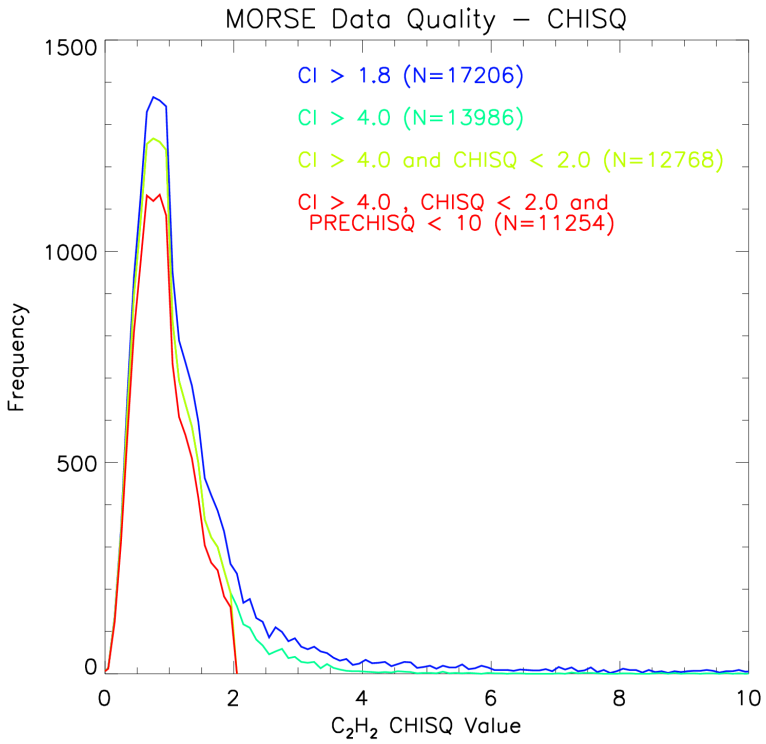

FIGURE 5.11. Histogram showing distribution of C_2H_2 CHISQ values for cases outlined above. The majority of CHISQ values are less than 2.0 and display a distribution centred around a value of 1 as would ideally be expected. Applying a threshold of 2.0 allows the few values with a higher CHISQ value to be removed.

This suggests that there is a link between lower DOFS values in measurements with strong cloud-contamination and that the retrieval may struggle in such cases. The presence of this remaining cloud significantly reduces the degrees of freedom for the measurements where it occurs which may bias the retrieval if it is not taken into consideration. When increasing the cloud index threshold to remove this cloud, some of the skew is removed from the distribution and it becomes more centred with a relatively broad peak between 1.2 and 1.9. This effect is seen even stronger when the full filtering conditions are applied. The majority of the values with a DOFS below 1 are removed as the distribution becomes tightened although still with a slight skew due to the longer tail on the right of the distribution. It follows that when considering the strong enhancements of C_2H_2, the signal is easier to detect at other altitudes and hence we would expect an increase in the DOFS value associated with the enhancements of C_2H_2, leading to the slight tail that is observed in the distribution.

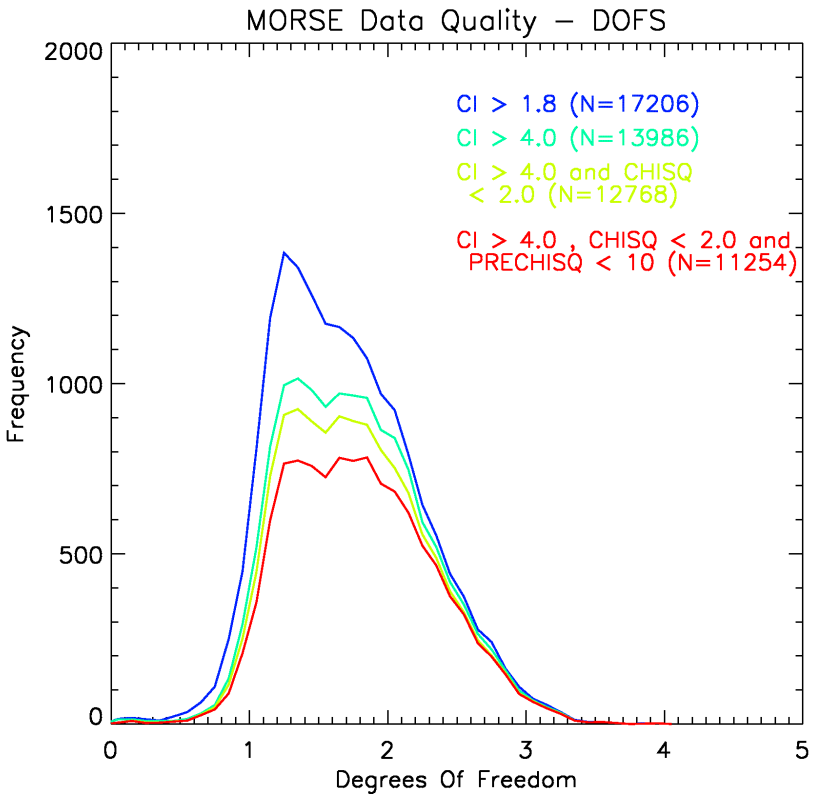

FIGURE 5.12. Histogram showing distribution of DOFS values for the filtering scenarios outlined above. The majority of DOFS values are between 1 and 3 as expected from examination of the averaging kernels in Figure 5.3. The application of more stringent filtering removes some of the bias in the distribution due to cloud.

5.3.8 Summary

The above section has explored the C_2H_2 data quality filtering in detail. It was found that the data filtering does not have a large effect on the distribution of the C_2H_2 enhancements (Fig. 5.5) once cloud-contaminated data has been removed. However, from an analysis of the spectral residuals it was determined that appropriate filtering is necessary to remove the relatively small number of poorly-fitted retrievals (Fig. 5.8). This filtering is primarily achieved by using a CHISQ threshold of 2.0 on the C_2H_2 retrieval which was determined empirically from the CHISQ distribution. A final filtering threshold of 10.0 on the CHISQ for the pressure retrieval ensures that only C_2H_2 results with a reasonable pressure are used.

5.4 Retrieved C_2H_2 VMRs

The MORSE retrieval algorithm has been used to retrieve C_2H_2 for the whole of August 2003. The retrieved data were subsequently filtered as discussed above and retrievals were only kept where the cloud index was greater than or equal to 4.0, the CHISQ value from the C_2H_2 retrieval was less than or equal to 2.0 and the CHISQ value for the initial pressure retrieval was less than 10.0. This filtering used the parameters from the 12 km nominal MIPAS altitude and was then applied to every level.

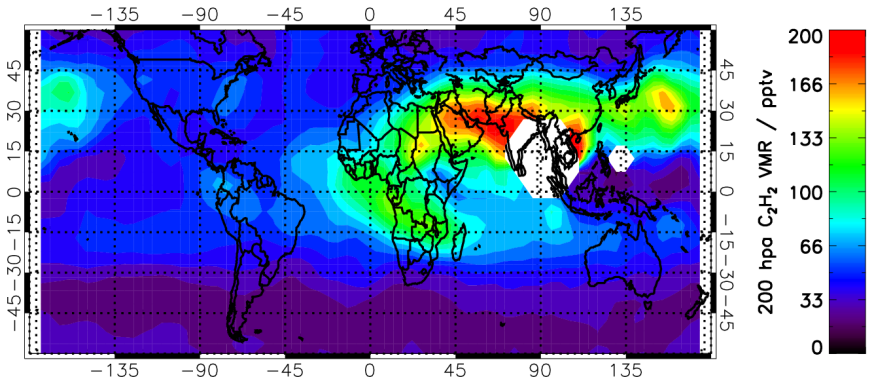

FIGURE 5.13. MORSE retrieved C_2H_2 VMRs for 12 km nominal tangent altitude at 200 hpa mean pressure for August 2003 after application of a cloud filter (CI>4) and retrieval quality filter ($\chi^2 < 2$) showing enhanced C_2H_2 over Asia, Africa and the Middle East.

After the application of the full filtering conditions, the average retrieved pressure for the 12 km nominal altitude was calculated to be approximately 200 hpa. Figure 5.13 shows the all of the retrieved C_2H_2 VMRs for August 2003 for this level. As was the case for the detection of C_2H_2 as discussed in Section 4.39, a large enhancement of C_2H_2 is clearly observed over the monsoon anticyclone region. In addition to this, strong C_2H_2 enhancements are also present over the African biomass burning region as well as in the eastward transport from Asia into the Northern Pacific Ocean. The agreement between the results from this full retrieval and the results from the detection algorithm discussed in Chapter 4 will be discussed in Section 5.5.

5.5 Comparison Between Detection And Retrieval Of C_2H_2 For August 2003

The following section compares the results of the detection algorithm outlined in Chapter 4 with the full retrieval as discussed above. Although the detection algo-

Highest 5 Retrieved C_2H_2 VMRs					
Date	20030806	20030816	20030828	20030805	20030829
Orbit	07492	07640	07800	07478	07814
Scan	13	2	27	14	26
C_2H_2 VMR (pptv)	663	527	461	433	430
C_2H_2 Error (pptv)	109	97	199	76	225
Altitude (km)	12.3	13.1	11.6	12.1	11.6
Lat	31.8	-16.6	79.3	37.7	84.0
Lon	160.4	44.6	151.1	153.4	162.5
Cloud Index	4.15	4.87	6.82	4.32	6.26
CHISQ	0.94	1.02	0.95	1.11	0.37
AVGITR	4	5	1	3	3
Lowest 5 Retrieved C_2H_2 VMRs					
Date	20030831	20030831	20030831	20030830	20030825
Orbit	07854	07848	07845	07832	07764
Scan	23	25	23	27	24
C_2H_2 VMR (pptv)	0.24	0.33	0.48	0.53	0.62
C_2H_2 Error (pptv)	2.28	3.03	4.39	2.67	4.12
Altitude (km)	11.8	11.8	11.8	11.8	11.8
Lat	81.2	81.0	81.2	79.3	86.4
Lon	50.6	24.9	-83.1	66.3	144.8
Cloud Index	6.54	7.38	6.54	6.02	6.69
CHISQ	1.04	0.68	1.37	0.46	1.01
AVGITR	3	3	3	1	3

Table 5.3. Table showing the details for the measurements where the C_2H_2 retrievals have the highest VMRs. C_2H_2 VMRs of over 400 pptv are retrieved. C_2H_2 VMRs of below 1 pptv were retrieved. The error values on these low VMR retrievals are between 2 pptv and 5 pptv which is substantially larger than the VMR values themselves but low in absolute terms. This indicates that although the spectral fit is good and passes the quality filtering above, there is not a sufficient C_2H_2 signal in order to retrieve a VMR and instead the signal is below the detection limit of the retrieval.

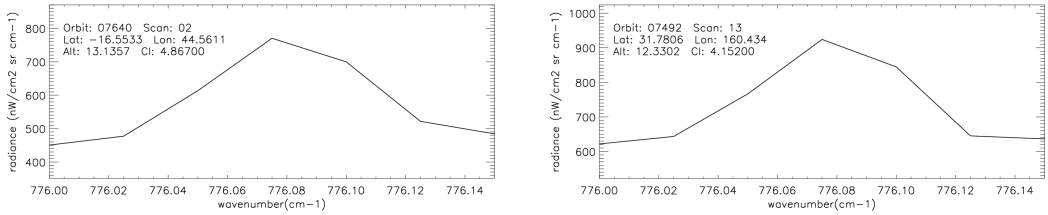

(a) Scan 02 Orbit 07640

(b) Scan 13 Orbit 07492

FIGURE 5.14. The MIPAS L1B spectra for Scan 02 Orbit 07640 and Scan 13 Orbit 07492 confirming that there is a strong C_2H_2 peak in the spectra from which the high C_2H_2 VMRs have been retrieved.

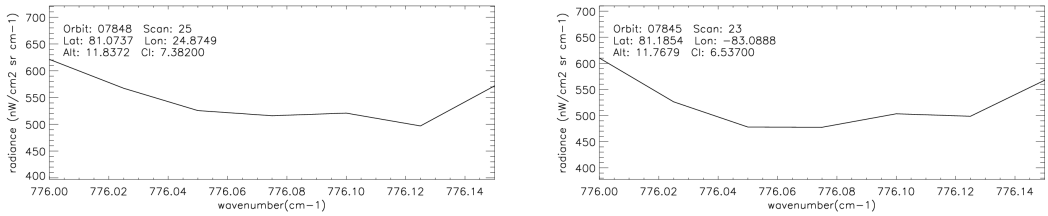

FIGURE 5.15. The MIPAS L1B spectra for Scan 25 Orbit 07848 and Scan 23 Orbit 07845 confirming that there is no visible C_2H_2 peak in the spectra from which the low C_2H_2 VMRs have been retrieved, causing the measurement error to be considerably higher than the retrieved VMR.

rithm should be considered a means for a fast "first look" at the data and not as a robust process on its own, it does offer the major advantage over the full retrieval that it is far less computationally expensive and hence far quicker to run for large amounts of data.

It is expected that the results between the detection and retrieval should be well-correlated (within the detection noise and retrieval error) as both primarily rely on the C_2H_2 spectral signature to obtain information on the amount of C_2H_2 present, however there are several factors which may lead poorer correlations. Cloud or interfering gases in the C_2H_2 microwindow such as high water vapour could lead to a masking of the C_2H_2 spectral signature. Additionally the results may be expected to differ in the presence of multi-layered C_2H_2 enhancements where the MIPAS limb path is sampling across these multiple layers.

For the purposes of this thesis, the results from the detection algorithm for August 2003 will be compared against the MORSE retrieval results for the same period. In order to allow a direct comparison, only measurements that exist both in the retrieval dataset after the application of the filtering criteria and in the detection algorithm dataset are used for comparison.

5.5.1 Correlations Between Detection and Retrieval Globally For August 2003

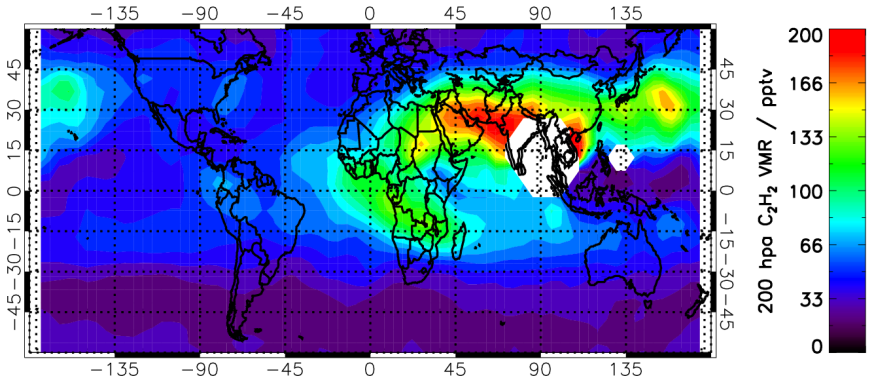

(a) MORSE Retrieved C_2H_2

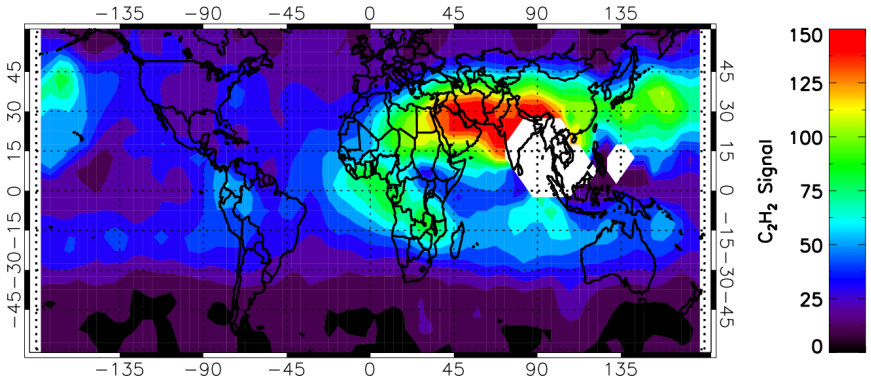

(b) Detected C_2H_2 Peak Radiance

FIGURE 5.16. Global distribution of C_2H_2 for (a) the full MORSE retrieval algorithm (pptv) and (b) the automated detection algorithm ($nW/cm^2 \cdot sr \cdot cm^{-1}$) showing the similarity between the detection and retrieval results for the 200 hpa pressure level for August 2003.

Figure 5.16 shows the global distribution of C_2H_2 for both the full MORSE retrieval algorithm (Fig. 5.16(a)) and for the automated detection algorithm (Fig. 5.16(b)) after filtering to ensure that each dataset only contains measurements that are present in both.

From examination of the two plots it is immediately apparent that there is considerable agreement between the detection and retrieval results. It is important to note here that whilst the retrieval data is in units of pptv, the detection algorithm remains in units of radiance. However, the strong qualitative agreement between the two methods suggests that not only are both methods in strong agreement and hence giving a consistent answer, but also that the detection algorithm could be a

viable alternative to running a full, computational expensive, retrieval in order to analyse the distribution and behaviour of C_2H_2.

In order to investigate this possibility further, a correlation between the detection and retrieval results is shown in Figure 5.17 where 5180 points are considered in the correlation. As shown qualitatively from Figure 5.16, there is a strong correlation between the two methods with a correlation coefficient of 0.853. Applying a linear fit to the correlation gives a line with a gradient of 0.963 and a y-intercept of just 25.6 pptv. Although there is some small spread in the data, this is to be expected as not only does the retrieval data have an average error of approximately 16 % (see Section 5.2) but the detected signal also includes the MIPAS noise of approximately 40 $nW/cm^2 \cdot sr \cdot cm^{-1}$.

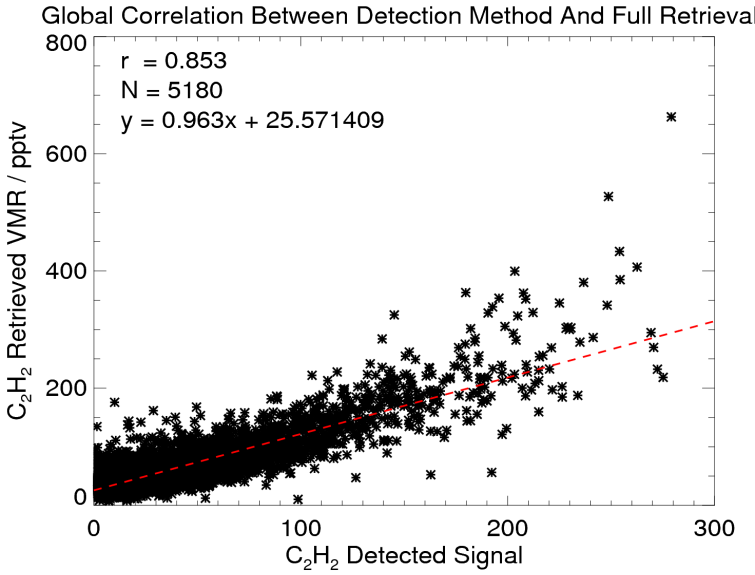

FIGURE 5.17. Correlation between the global distribution of C_2H_2 for the full MORSE retrieval algorithm (pptv) against the automated detection algorithm ($nW/cm^2 \cdot sr \cdot cm^{-1}$). The strong correlation of 0.853 between the two techniques shows that the detection algorithm could be a viable alternative to running a full, computational expensive retrieval.

5.5.2 Correlation For Individual Regions

An obvious potential issue with this relationship is that from Figure 5.16 it can be seen that the enhanced C_2H_2 values are predominantly in the Northern Hemisphere, whereas the low values in the opposite hemisphere. Hence, any such relationship may not be valid when considering the two hemisphere separately. In the following sections, the regional relationships are explored in more detail.

5.5.2.1 Northern Hemisphere

Figure 5.18 shows the Northern Hemisphere C_2H_2 distributions for the two methods. Again, the similarity in results between the two methods is apparent. Although the enhancement over the Asian monsoon anticyclone region dominates this hemisphere, there are also large areas of low background values, particularly over the North Atlantic where the anticyclone acts as a barrier to transport westward.

The correlation between the detection and retrieval methods for the Northern Hemisphere is shown in Figure 5.18(c). Although the number of points is now reduced to 2447, there still exists a strong correlation coefficient of 0.866. In addition to this, the gradient of the line remains close to 1, with a value of 0.966 and the y-intercept remains small at 28.47. The fact that the agreement between the two techniques remains strong when just considering the Northern Hemisphere is not surprising but confirmation of this fact gives greater confidence that the correlation remains strong when fewer points are used.

5.5.2.2 Southern Hemisphere

It is when considering the Southern Hemisphere (Fig. 5.19) that we may expect the agreement to no longer hold due to the lack of any significant enhancement, leading to all the values in the correlation being low and hence giving a flat correlation. The only enhanced C_2H_2 values in the Southern Hemisphere are those from the Southern African biomass burning.

However despite the lack of a significant number of high C_2H_2 values in both the detection and the retrieval results, a strong correlation (Fig. 5.19(c)) does still exist between the lower values. This leads to a correlation of 0.793 with a gradient of 0.899 and a y-intercept of 25.1. Whilst not quite as strong as the correlation in the Northern Hemisphere, there is still significant agreement between the two techniques which gives confidence that the relationship does hold even without a large number of enhanced values being present.

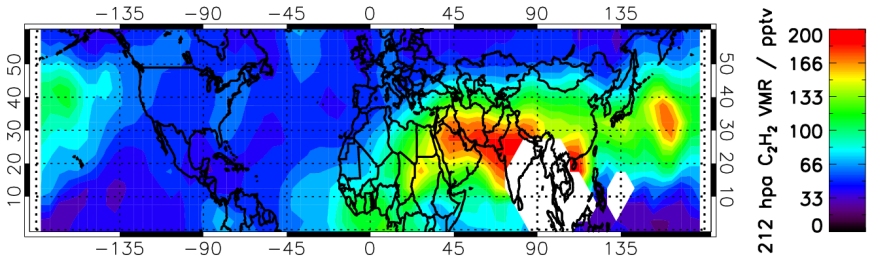

(a) MORSE Retrieved C_2H_2

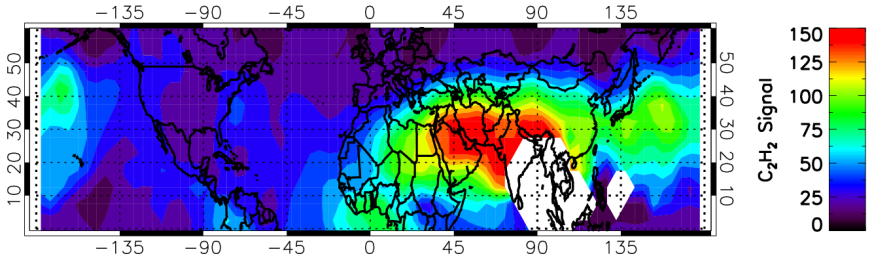

(b) Detected C_2H_2 Peak Radiance

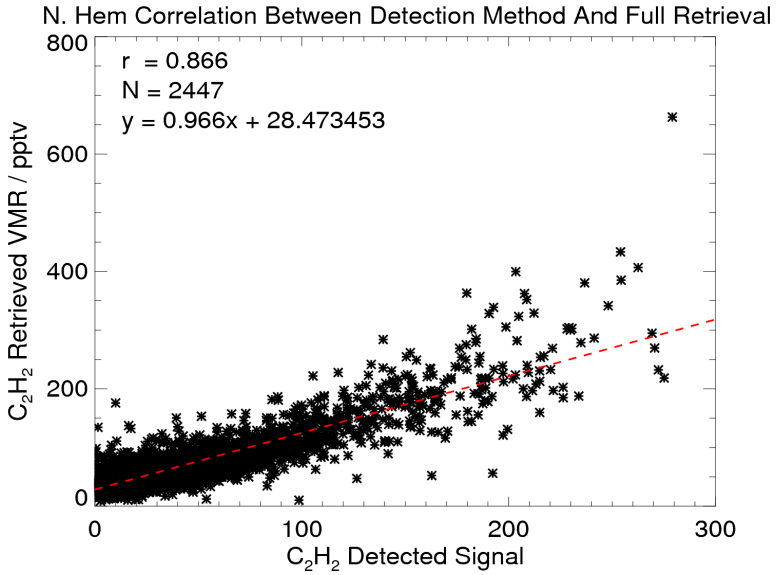

(c) Correlation

FIGURE 5.18. Northern Hemisphere distribution of C_2H_2 for (a) the full MORSE retrieval algorithm (pptv) and (b) the automated detection algorithm ($nW/cm^2 \cdot sr \cdot cm^{-1}$) showing the similarity between the detection and retrieval results in the Northern Hemisphere. Correlation between the Northern Hemisphere distribution of C_2H_2 for the full MORSE retrieval algorithm against the automated detection algorithm giving a strong correlation of 0.866.

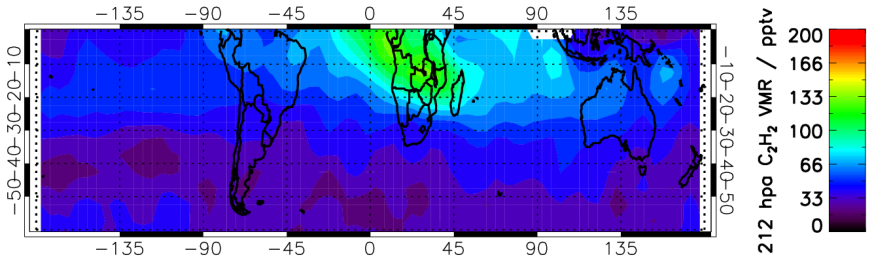

(a) MORSE Retrieved C_2H_2

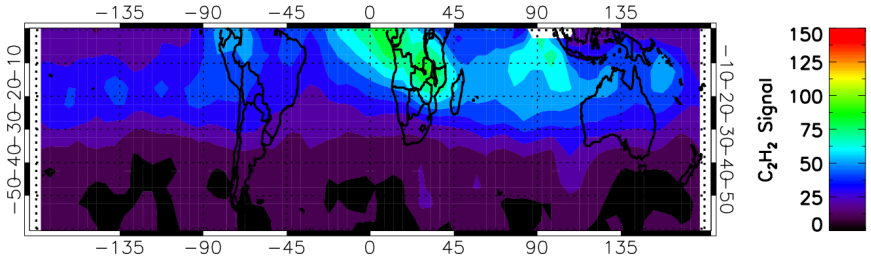

(b) Detected C_2H_2 Peak Radiance

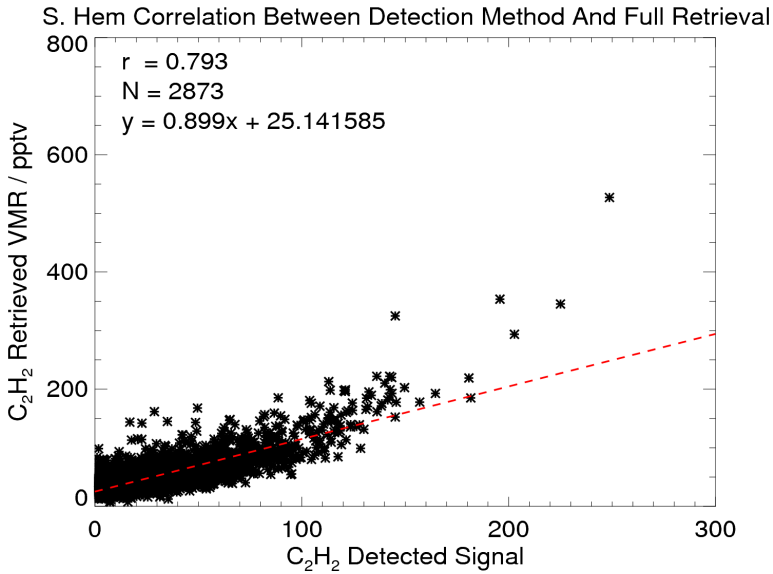

(c) Correlation

FIGURE 5.19. Southern Hemisphere distribution of C_2H_2 for (a) the full MORSE retrieval algorithm (pptv) and (b) the automated detection algorithm (nW/cm^2·sr·cm^{-1}). The lack of a significant enhancement of C_2H_2 in the Southern Hemisphere reduces the similarity between the detection and retrieval results but both do manage to observe the enhancement over Southern Africa. Correlation between the Southern Hemisphere distribution of C_2H_2 for the full MORSE retrieval algorithm against the automated detection algorithm giving a strong correlation of 0.793

5.5.2.3 Southern Africa

Although the correlation between detection and retrieval remains strong when considering a large number of points, it must also be shown that it holds on more regional scales where less measurements are being considered and which may be affected by uplift and transport.

The first region considered is the Southern African region defined as 30°S to 10°N and 30°W to 80°E. This region incorporates a large amount of African biomass burning as well as the transport from the biomass burning source both westward into the Atlantic and eastward towards Australia. In comparing the two techniques (Fig. 5.20), qualitatively the same strong African biomass burning feature is apparent in both although less pronounced in the detection plot (Fig. 5.20(b)). The two separate transport mechanisms in this region can also both be identified through both techniques.

The correlation between the two methods for Southern Africa (Fig. 5.20(c)) shows a strong correlation of 0.843 between the 723 points being considered. Along with a gradient of 1.08 and a y-intercept of 26.0, this shows that the relationship between the detection and retrieval techniques does hold for smaller regions.

5.5.2.4 South America

The next region (Fig. 5.21) considered covers South America and the Southern Pacific Ocean and is defined as 30°S to 10°N, 180°W to 30°W. This region contains no significant enhancement of C_2H_2 at all, with the highest C_2H_2 VMR being just over 150 pptv. This is in contrast to the case where the Southern Hemisphere was considered as a whole where even though the majority of points were low there were still a small number of enhanced points contributed from the Southern African biomass burning.

The fact that this region contains only background and moderate C_2H_2 values leads to the correlation (Fig. 5.21(c)) being worse (0.678) in this region than in the other regions considered so far. A gradient of 0.599 and a y-intercept of 32.2 also suggests that the relationship between the two techniques is not as strong when there are no enhanced values present at all. It can be seen that due to the spread in the data relating to the noise, in order to get a reasonable correlation there must be sufficient variability of the C_2H_2 values in the region being examined and just having a large number of values (in this case 1113) is not enough.

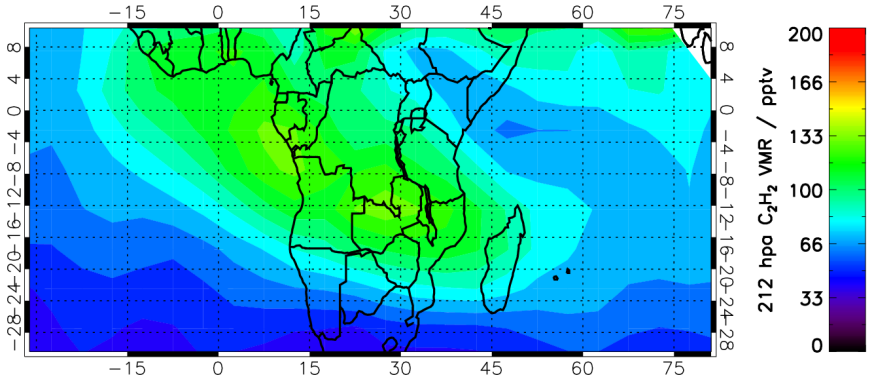

(a) MORSE Retrieved C_2H_2

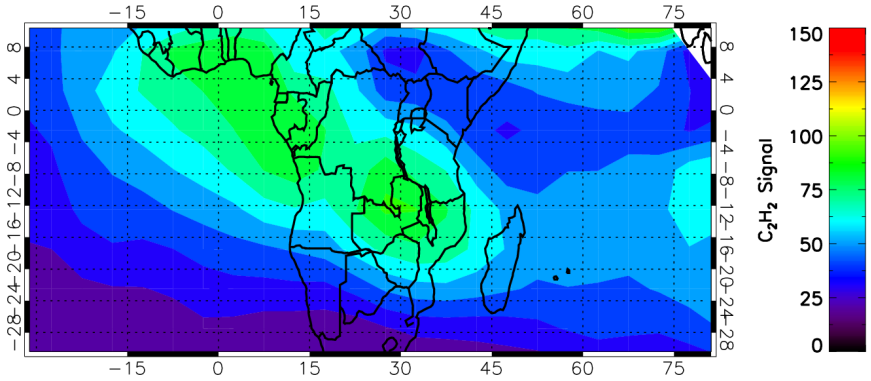

(b) Detected C_2H_2 Peak Radiance

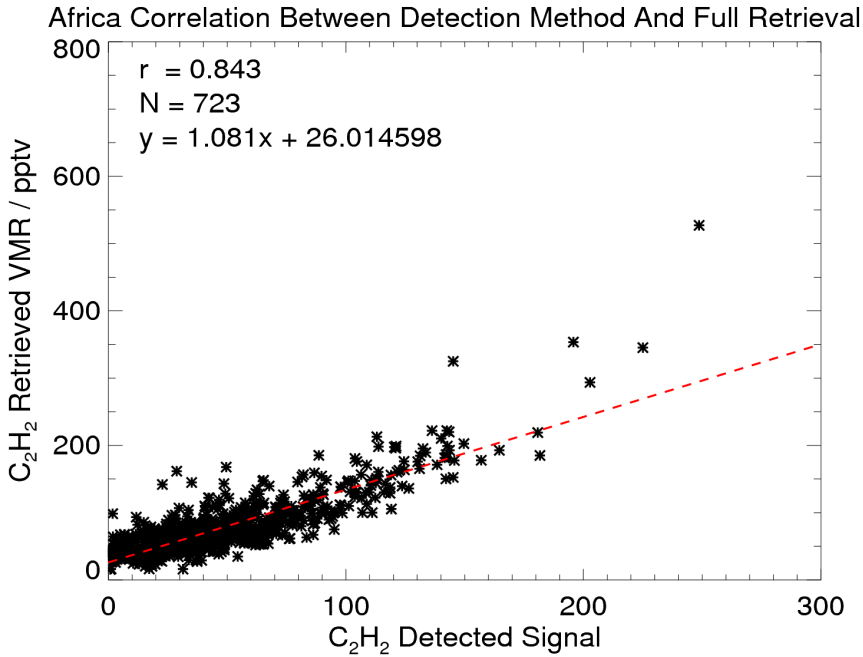

(c) Correlation

FIGURE 5.20. African distribution of C_2H_2 for (a) the full MORSE retrieval algorithm (pptv) and (b) the automated detection algorithm ($nW/cm^2 \cdot sr \cdot cm^{-1}$). The C_2H_2 produced from the African biomass burning region is observed by both techniques. Correlation between the African distribution of C_2H_2 for the full MORSE retrieval algorithm against the automated detection algorithm giving a strong correlation of 0.843.

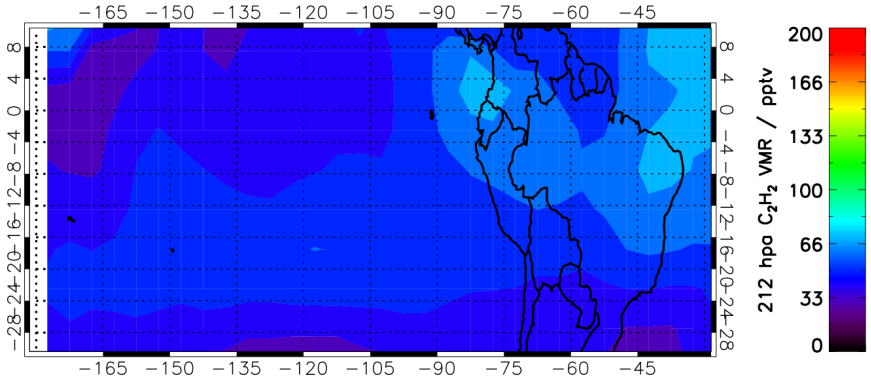

(a) MORSE Retrieved C_2H_2

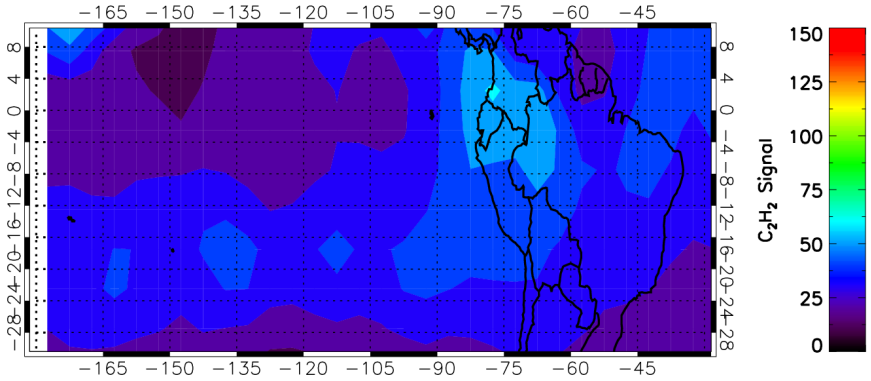

(b) Detected C_2H_2 Peak Radiance

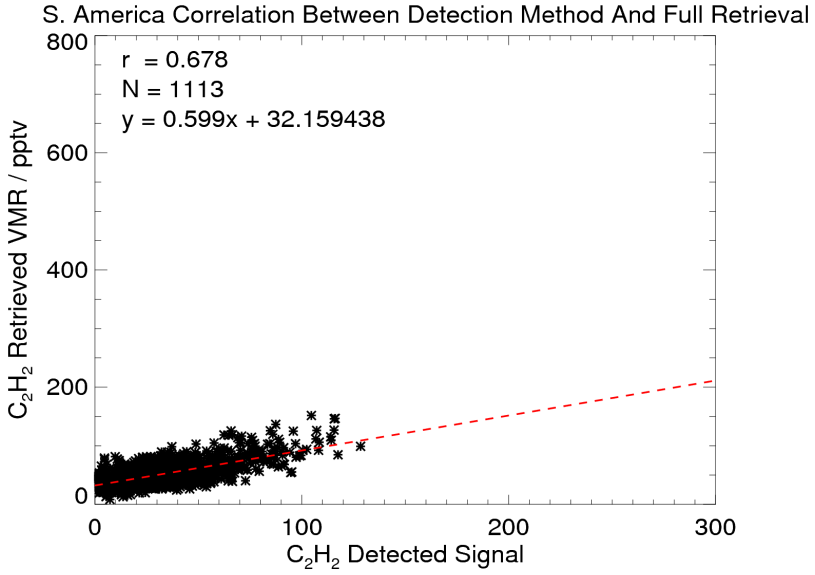

(c) Correlation

FIGURE 5.21. South American distribution of C_2H_2 for (a) the full MORSE retrieval algorithm (pptv) and (b) the automated detection algorithm ($nW/cm^2 \cdot sr \cdot cm^{-1}$). The small C_2H_2 signal from the Amazonian biomass burning is observed by both techniques although the majority of the region consists of relatively clean ocean background. Correlation between the South American distribution of C_2H_2 for the full MORSE retrieval algorithm against the automated detection algorithm giving a strong correlation of 0.678. Due to the clean ocean background there are no real enhancements observed but there still exists a reasonable correlation for the lower VMRs.

5.5.2.5 Asian Outflow

This region covers 10°N to 40°N and 130°E to 110°W and in contrast to the South American case where there were 1113 points to compare, the next case covers the Asian outflow into the Pacific (Fig. 5.22) and only contains 388 points. Despite the low number of points, the similarity between the two techniques is still apparent with the enhancements due to Asian outflow distinct from the lower background values.

Due to the low number of points being compared, the variability between adjacent measurements is more apparent but the correlation between the two techniques (Fig. 5.22(c)) is still strong with a correlation value of 0.872. However, the gradient of 1.2 is steeper than previously seen, suggesting that due to the low number of points, the gradient becomes more influenced by the few high values. This effect is further enhanced by the fact that this region contains a few extremely high values with retrieved VMRs greater than 400 pptv. These value appear to be too high as to no longer completely agree with the linear relationship between the detection and retrieval and show that there may be an upper limit on the use of the detection algorithm for the very high values of C_2H_2.

5.5.2.6 Asian Monsoon Anticyclone

The final region considered is the one of perhaps the most interest as the majority of values are much higher than typical background levels, in contrast to the other regions which contained a relatively small number of enhanced values with considerably more background values. In addition to this, there is no ocean in this region which further removes the number of low background values which are contained in the other regions being considered. In total in this region there are 301 values and as can be seen from Figure 5.23 there is a good agreement between the detection and retrieval techniques.

Figure 5.23(c) shows the correlation over the monsoon anticyclone region. Despite the correlation clearly being dominated by the high values there is still a strong correlation of 0.829 with a gradient of 1.046 and y-intercept of 17. This strong correlation and gradient close to 1 shows that even for this case where the majority of values are enhanced and there is no ocean background to moderate these values, the relationship between the detection and retrieval techniques still remains valid.

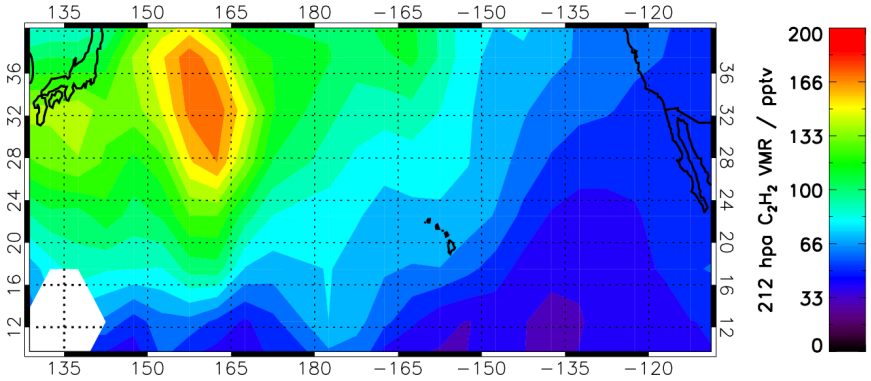

(a) MORSE Retrieved C_2H_2

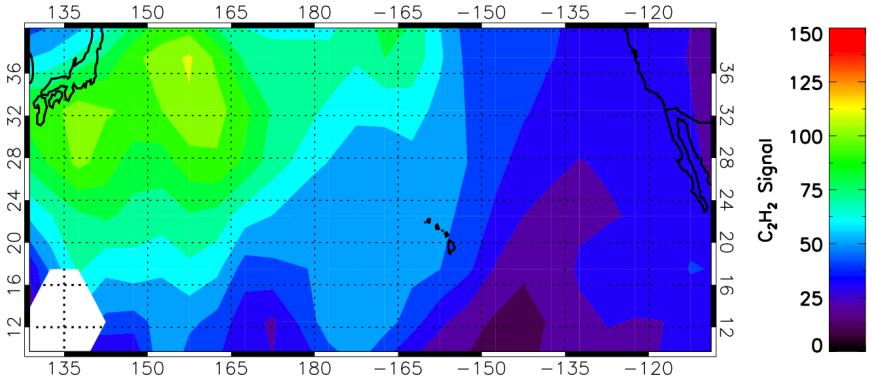

(b) Detected C_2H_2 Peak Radiance

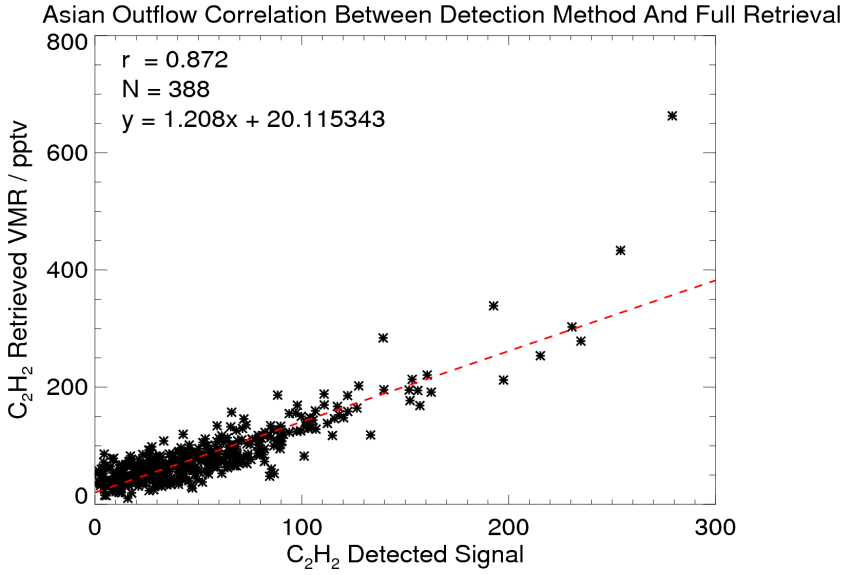

(c) Correlation

FIGURE 5.22. Asian outflow distribution of C_2H_2 for (a) the full MORSE retrieval algorithm (pptv) and (b) the automated detection algorithm ($nW/cm^2 \cdot sr \cdot cm^{-1}$). The outflow of C_2H_2 from Asia is observed over the Pacific Ocean travelling towards North America. Correlation between the Asian outflow distribution of C_2H_2 for the full MORSE retrieval algorithm against the automated detection algorithm giving a strong correlation of 0.872.

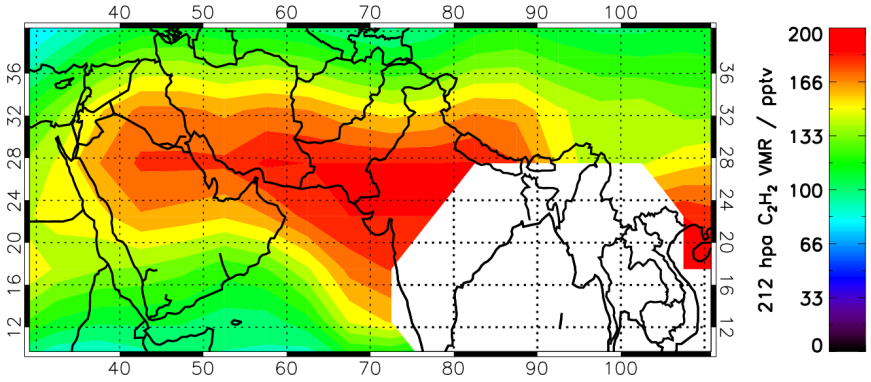

(a) MORSE Retrieved C_2H_2

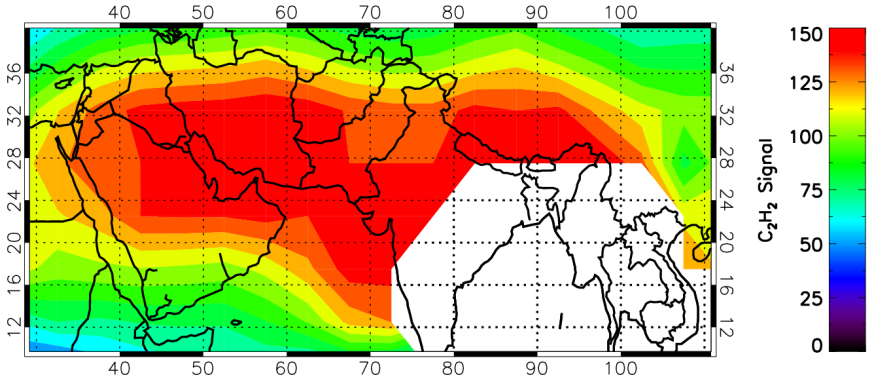

(b) Detected C_2H_2 Peak Radiance

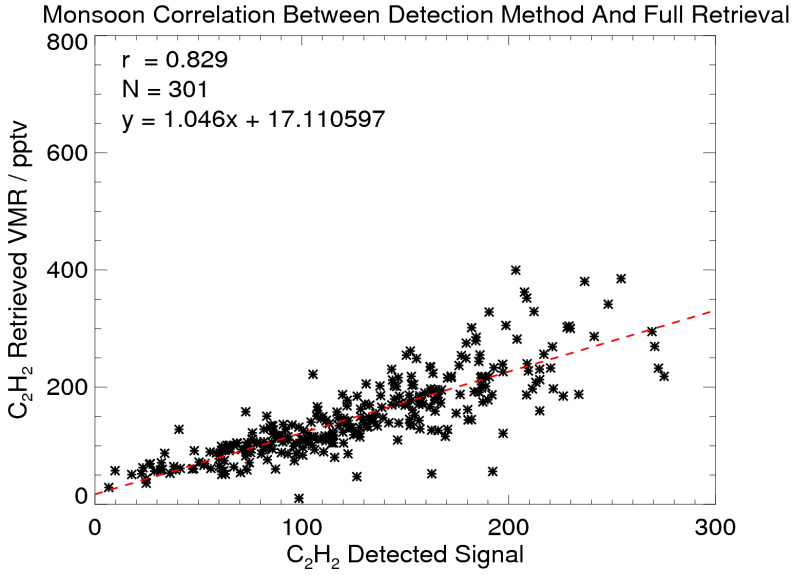

(c) Correlation

FIGURE 5.23. Asian monsoon anticyclone distribution of C_2H_2 for (a) the full MORSE retrieval algorithm (pptv) and (b) the automated detection algorithm ($nW/cm^2 \cdot sr \cdot cm^{-1}$). The strong enhancement of C_2H_2 observed over the anticyclone is observed by both techniques. Correlation between the Asian monsoon anticyclone distribution of C_2H_2 for the full MORSE retrieval algorithm against the automated detection algorithm giving a strong correlation of 0.829.

5.6 Comparison Between Detection And Retrieval Of C_2H_2 For January 2003

The above section has dealt with the comparison between the retrieval and detection for August 2003, mainly due to the interest in the isolation relating to the Asian monsoon anticyclone which is dominant during this period. In order to verify that the detection scheme is still valid for other months, a similar comparison is performed for January 2003.

Figure 5.24 shows the detection and retrieval results for January 2003 and it is immediately evident that there is a strong similarity between the two datasets with very similar features observed over Africa and South-East Asia. The main discrepancy between the two results is that the Central and South American feature is not quite as apparent in the retrieval results, although it is still clearly identifiable.

The correlation between the two techniques for the global data is shown in Figure 5.24(c) with a reasonable correlation of 0.64 between 4233 points. Again, as seen previously the correlation has a thickness to it associated with the measurement noise.

Despite being over a similar number of points, this correlation is worse than the 0.853 value found for August between the detection and retrieval techniques. The main reason for this relates to the fact the for January the detection and retrieval do not completely agree with regards to the feature observed over Central and South America.

When considering the Northern Hemisphere separately as in Figure 5.25 the correlation between the two data sets (Fig. 5.25(c)) increases to 0.741 between 2785 points which although higher than when considering the global data, is not as high as the corresponding correlation for the Northern Hemisphere in August which had a high correlation of 0.866, mainly due to the strong agreement on the location of the monsoon anticyclone feature observed in both the detection and the retrieval.

In contrast, when considering the Southern Hemisphere (Fig. 5.26) the differences observed over the South American region lead to a poor correlation of just 0.530 between 1506 points (Fig. 5.26(c)). This is similar as the result observed for August, considering the Southern Hemisphere on its own generally leads to a poor correlation than if considering it as part of a global correlation. Again, the reason for this is that there are significantly less enhancements observed in the Southern Hemisphere in comparison to the Northern Hemisphere and hence the correlation can be strongly influenced by the few enhanced points which are present.

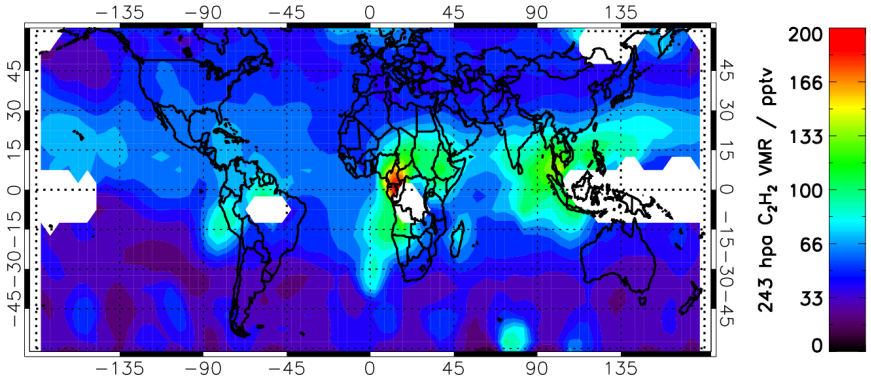

(a) MORSE Retrieved C_2H_2

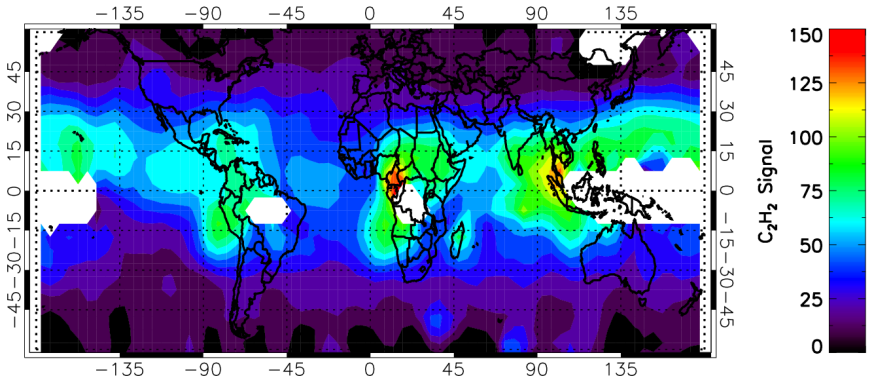

(b) Detected C_2H_2 Peak Radiance

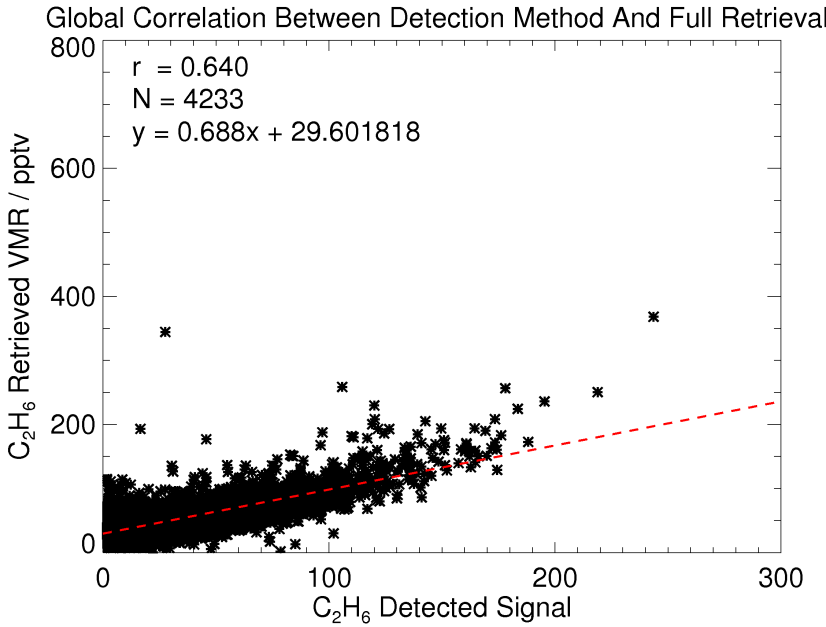

(c) Correlation

FIGURE 5.24. Global distribution of C_2H_2 for (a) the full MORSE retrieval algorithm (pptv) and (b) the automated detection algorithm ($nW/cm^2 \cdot sr \cdot cm^{-1}$) showing the similarity between the detection and retrieval results for January 2003.

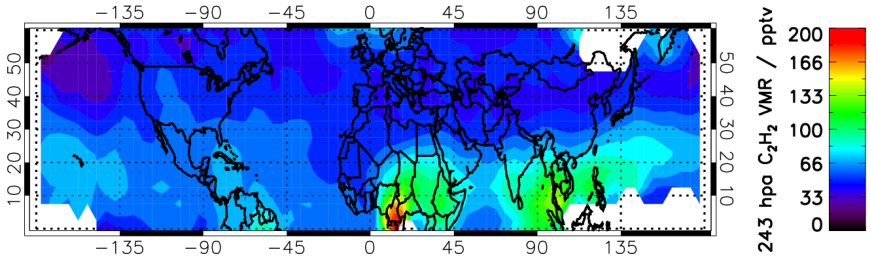

(a) MORSE Retrieved C_2H_2

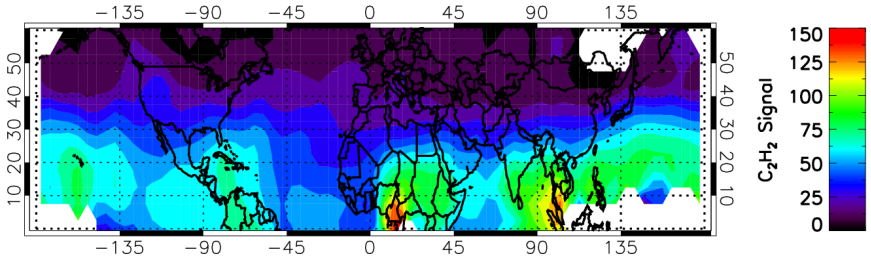

(b) Detected C_2H_2 Peak Radiance

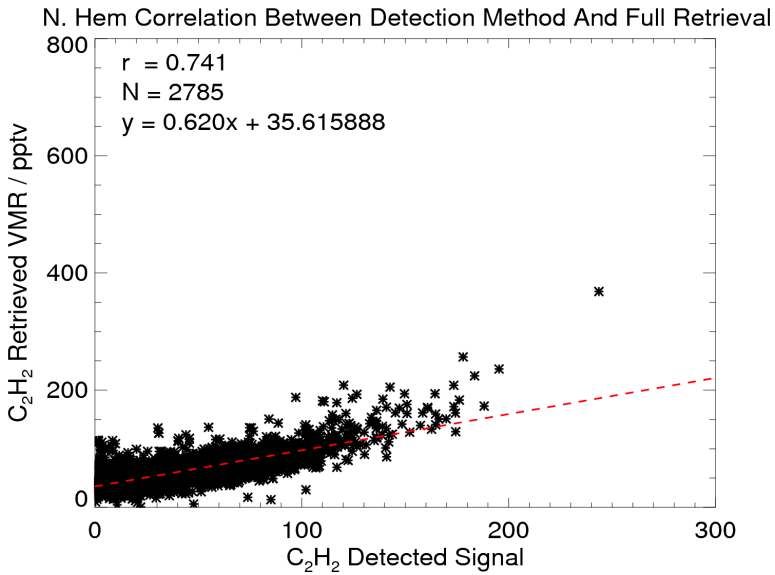

(c) Correlation

FIGURE 5.25. Northern Hemispheric distribution of C_2H_2 for (a) the full MORSE retrieval algorithm (pptv) and (b) the automated detection algorithm ($nW/cm^2 \cdot sr \cdot cm^{-1}$) showing the similarity between the detection and retrieval results for January 2003.

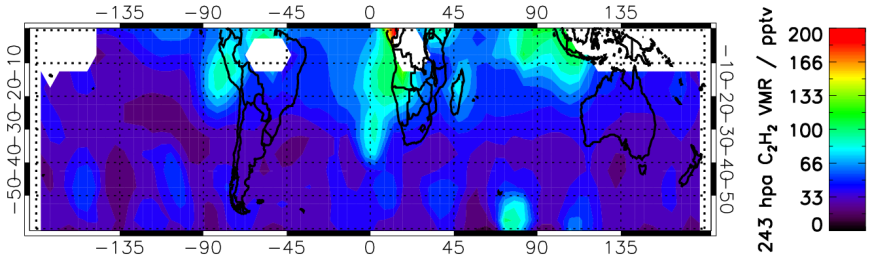

(a) MORSE Retrieved C_2H_2

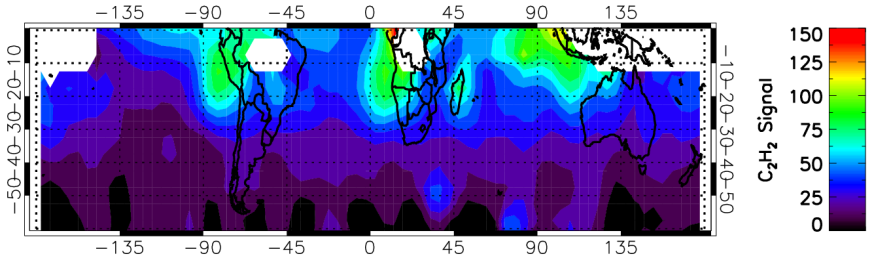

(b) Detected C_2H_2 Peak Radiance

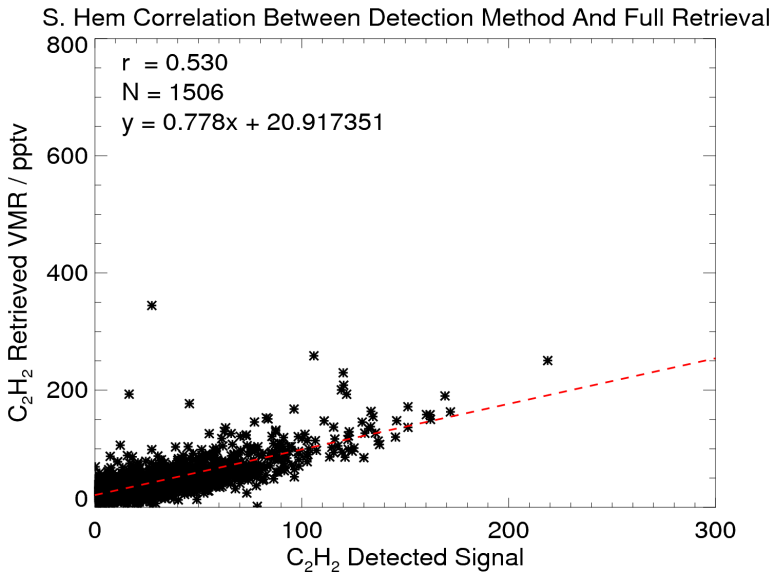

(c) Correlation

FIGURE 5.26. Southern Hemispheric distribution of C_2H_2 for (a) the full MORSE retrieval algorithm (pptv) and (b) the automated detection algorithm ($nW/cm^2 \cdot sr \cdot cm^{-1}$) showing the similarity between the detection and retrieval results for January 2003.

5.6.1 Regional Comparison

A regional comparison was also performed for the same regions as in Section 5.5, namely Africa, South America, Asian-Pacific Outflow and the Asian monsoon anticyclone region.

The comparison for the African region is shown in Figure 5.27. The retrieval (Fig. 5.27(a)) and detection (Fig. 5.27(b)) results for this region are shown to be very similar with both the general distribution as well as a large majority of the details in agreement between the techniques. The strongest signal in both plots has the same shape and is in the same region, located over the Cameroon/Gabon region to the north-west of the cloud/aerosol contaminated area where no analysis was possible. In addition, further enhancements are observed in both datasets over the Madagascan region as well as towards the Indian coast.

As would be expected from the good qualitative agreement, a strong correlation between the individual data points of 0.807 is found (Fig. 5.27(c)) with the majority of values for the detection ranging from 0 $nW/cm^2 \cdot sr \cdot cm^{-1}$ to 150 $nW/cm^2 \cdot sr \cdot cm^{-1}$ and 0 pptv to 200 pptv for the retrieval.

Although these values are similar to the ones found for the August data, the shape of the distribution is quite different. Despite being centred over the same region, for August there was considerable outflow both north-west into the Atlantic and Eastwards towards the Indian Ocean (Fig. 5.27) and eventually Australia. One result from this was that the Madagascan region was directly influenced by this outflow during August, but in January when there does not appear to be the same outflow from the Southern Africa region, Madagascar exhibits its own distinct signal in both the detection and retrieval results.

The comparison for the South American and South Pacific region is shown in Figure 5.28. Again, the retrieval (Fig. 5.28(a)) and detection (Fig. 5.28(b)) plots show a good qualitative agreement between the two techniques with not only the enhanced regions such as the one over Peru being present in both datasets but also the majority of the lower background measurements are in good agreement as indicated by the similar shape of the darker contours over the South Pacific leading to a correlation between the two datasets of 0.829.

This correlation for January is actually considerably higher than the value of 0.678 found for August and this is primarily related to the fact that a much stronger signal is observed over this region in January, relating to the biomass burning present during this time of the year in the north-west of South-America. For August, the maximum detected peak radiance was only 130 $nW/cm^2 \cdot sr \cdot cm^{-1}$ with the maximum retrieved VMR being just 150 pptv. In contrast, for January a detected peak radiance of over 200 $nW/cm^2 \cdot sr \cdot cm^{-1}$ is observed along with a retrieved VMR of over 300 pptv. The good agreement between the two techniques in January relating to this enhancement leads to a stronger correlation than was observed in August.

The comparison for the Asian outflow region is shown in Figure 5.29. As observed for the previous regions, again there is a strong qualitative agreement between the retrieval (Fig. 5.29(a)) and detection (Fig. 5.29(b)). A strong feature relating to the eastwards transport originating from South-East Asia is observed in both datasets with a similar distribution. The correlation between the two datasets was again found to be strong with a value of 0.741.

In comparison to the August data for this region where the enhancements were observed up to 40°N and included the Japanese region, in the case of January the enhancements seem to be confined to the lower latitudes between 15°N and 30°N with much less influence from China and Japan. Instead it is the biomass and biofuel burning in Indonesia and South-East Asia which is the source of the enhancements that are being observed. This implies that any transport of C_2H_2 or biomass burning related products are more likely to be transported towards and have an influence on Central America, as opposed to the effect on North America seen in August.

Finally, the comparison for the Asian monsoon anticyclone region is shown in Figure 5.30. During August this region was of interest due to the chemical isolation of C_2H_2 observed within the monsoon anticyclone but as the anticyclone is not present during January a very different distribution would be expected. The agreement between the retrieval (Fig. 5.30(a)) and detection (Fig. 5.30(b)) appears to be strong with a very similar distribution. Enhancements are observed both over the west of Africa and the South-East Asia/Southern India regions with no enhancements at all over the Middle East or Northern India. The correlation between the two methods is again strong with a value of 0.84 which is comparable to the correlation observed for August of 0.829 despite the large differences between the two periods related to the anticyclone.

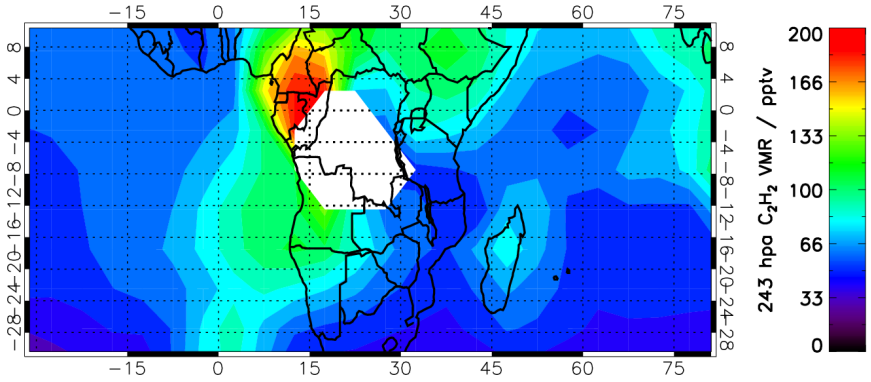

(a) MORSE Retrieved C_2H_2

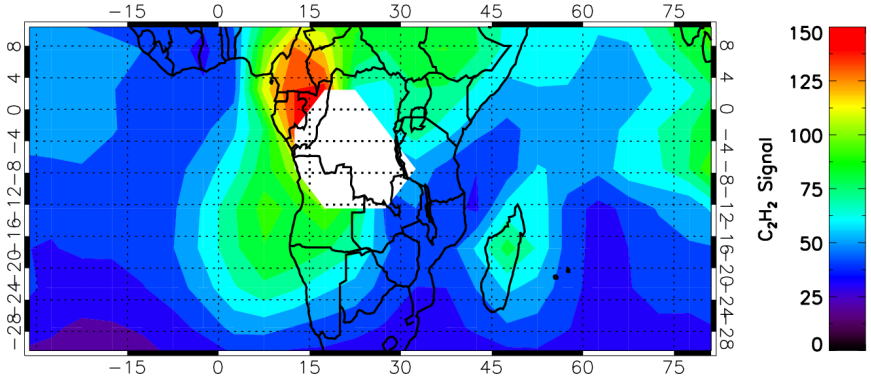

(b) Detected C_2H_2 Peak Radiance

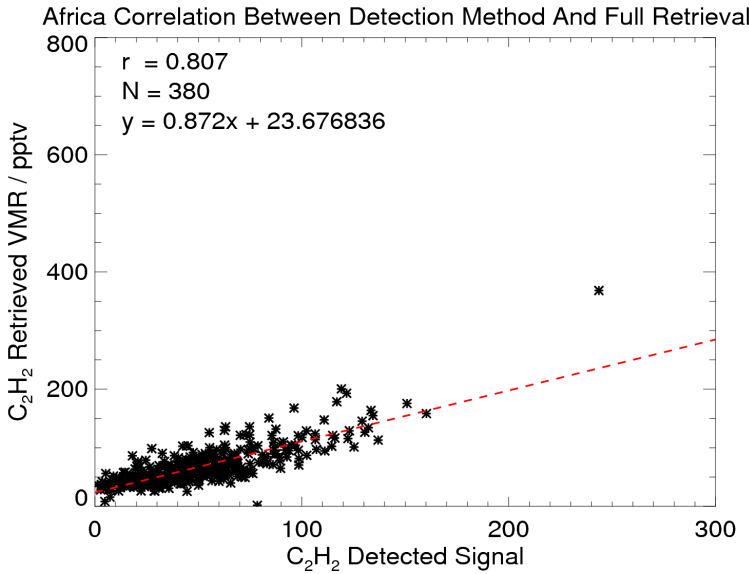

(c) Correlation

FIGURE 5.27. Africa distribution of C_2H_2 for (a) the full MORSE retrieval algorithm (pptv) and (b) the automated detection algorithm ($nW/cm^2 \cdot sr \cdot cm^{-1}$) showing the similarity between the detection and retrieval results for January 2003.

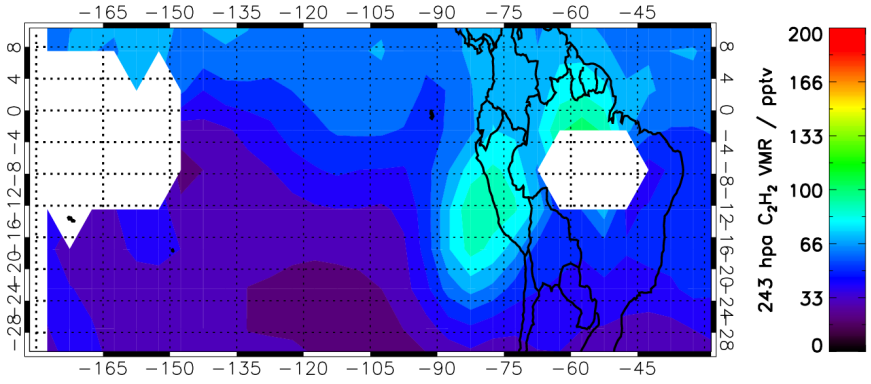

(a) MORSE Retrieved C_2H_2

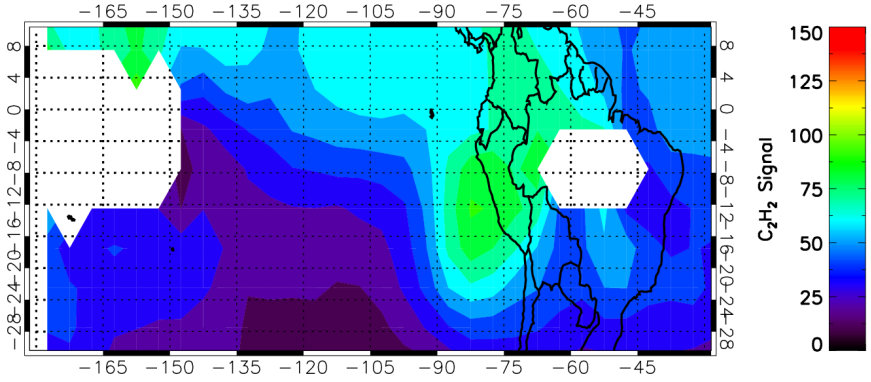

(b) Detected C_2H_2 Peak Radiance

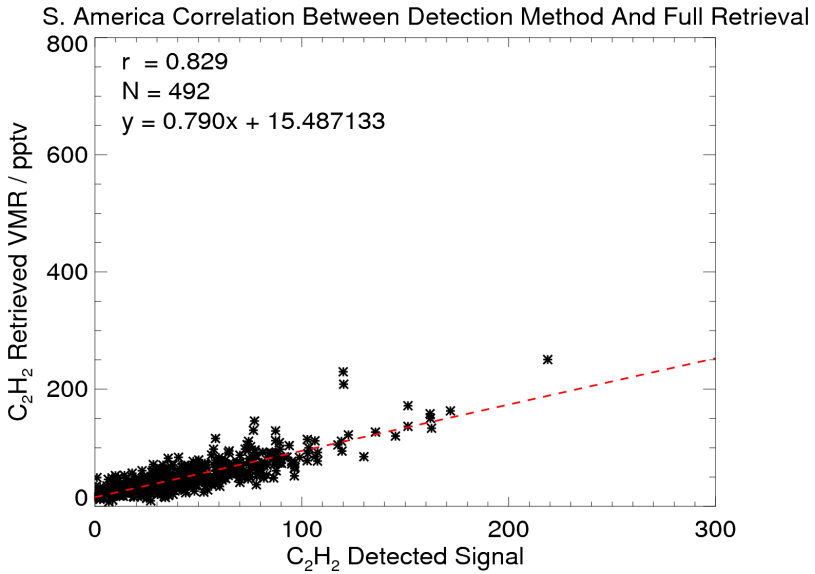

(c) Correlation

FIGURE 5.28. South American distribution of C_2H_2 for (a) the full MORSE retrieval algorithm (pptv) and (b) the automated detection algorithm ($nW/cm^2 \cdot sr \cdot cm^{-1}$) showing the similarity between the detection and retrieval results for January 2003.

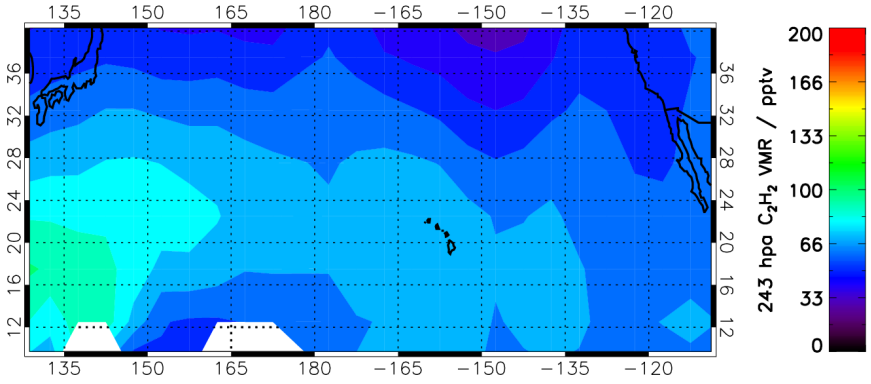

(a) MORSE Retrieved C_2H_2

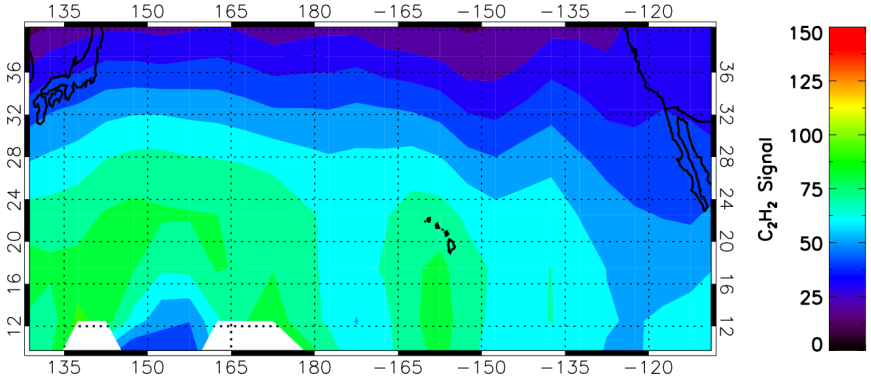

(b) Detected C_2H_2 Peak Radiance

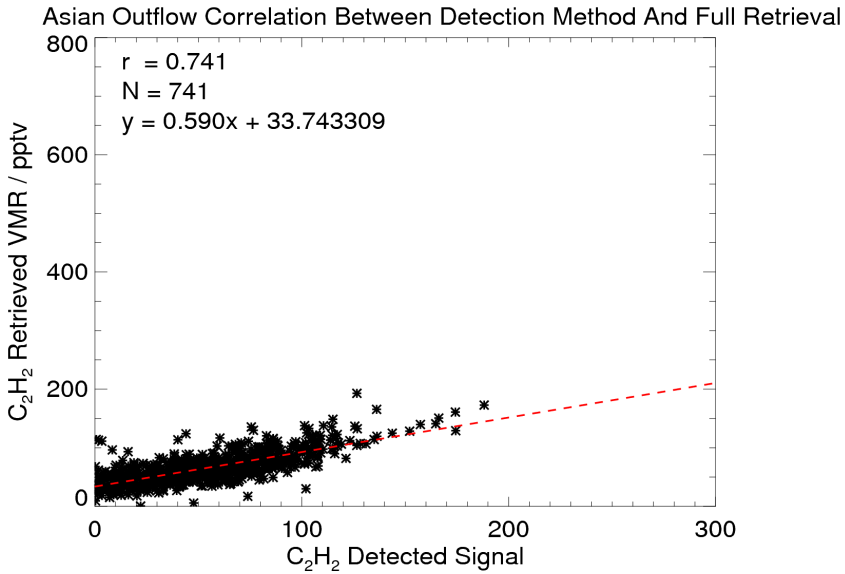

(c) Correlation

FIGURE 5.29. Asian-Pacific outflow of C_2H_2 for (a) the full MORSE retrieval algorithm (pptv) and (b) the automated detection algorithm ($nW/cm^2 \cdot sr \cdot cm^{-1}$) showing the similarity between the detection and retrieval results for January 2003.

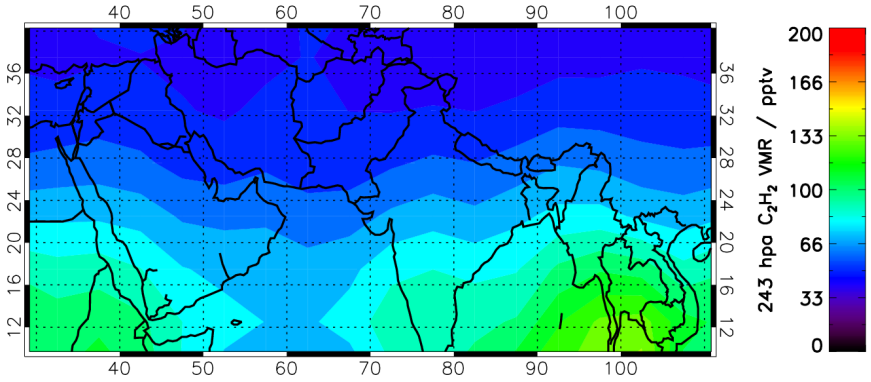

(a) MORSE Retrieved C_2H_2

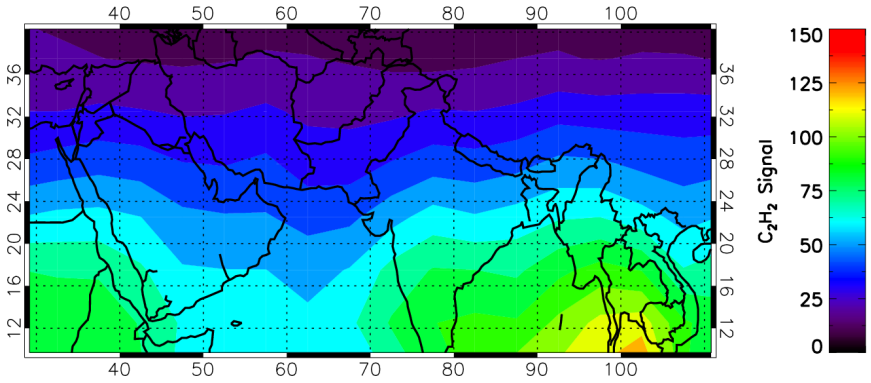

(b) Detected C_2H_2 Peak Radiance

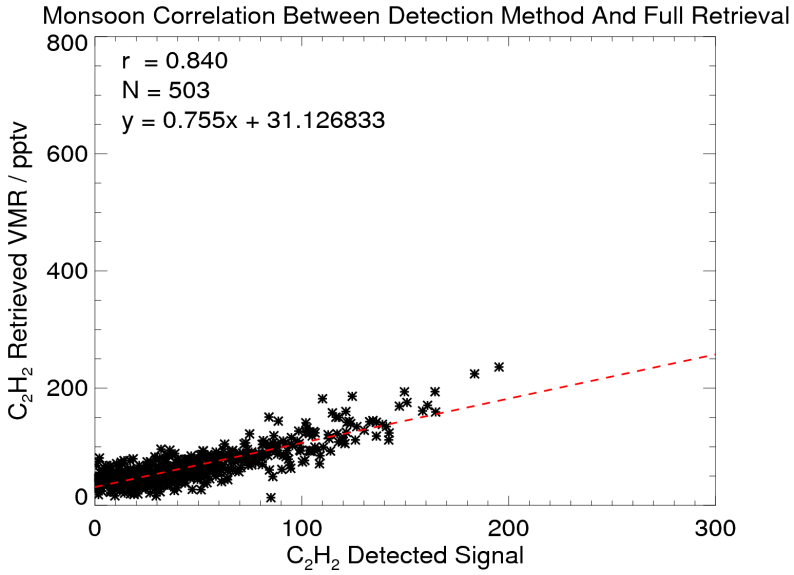

(c) Correlation

FIGURE 5.30. Asian monsoon anticyclone distribution of C_2H_2 for (a) the full MORSE retrieval algorithm (pptv) and (b) the automated detection algorithm ($nW/cm^2 \cdot sr \cdot cm^{-1}$) showing the similarity between the detection and retrieval results for January 2003.

5.6.2 Summary Of Comparisons Between Detection And Retrieval

The above sections have detailed the comparisons between the detection and retrieval techniques on both a global and regional scale for January and August 2003. Overall, it was found that there is a good agreement between the two techniques and in each case the same distributions and features were identifiable with both methods, often to a very high agreement.

By not only performing the comparisons for August when the Asian monsoon anticyclone is the dominant feature but also for January when no such system is present it allowed us to show that the detection result is a valid approach in order to take a "first look" at the data without performing a computationally expensive retrieval. Not only does this help to corroborate the results found from the retrieval but it also gives confidence that it may be possible to extend this technique further to derive not only qualitative peak radiances but actual estimates of the C_2H_2 VMRs.

In order to examine whether this detection approach is robust enough to handle a variety of species, a similar comparison will be performed for C_2H_6 in Section 5.8.

5.7 C_2H_6 Retrieval and Data Quality

The following section details the quality of the C_2H_6 retrieval for August 2003 which was performed using the MORSE retrieval scheme using the same pre-retrieved values for pressure, temperature, H_2O, O_3 and HNO_3 as were used for the C_2H_2 retrieval discussed above.

5.7.1 CHISQ As Indicator Of Data Quality

As shown in Section 5.3.6, the CHISQ retrieval parameter is an important quantity in assessing the quality of the retrieval with an ideal value of 1 but in reality, a distribution centred around 1. Figure 5.31 shows the distribution of the CHISQ values for the C_2H_6 retrieval. The effect of applying the different levels of filtering is similar to that seen for the C_2H_2 retrieval, with the increasing of the cloud index threshold having a large effect. As can be seen, the CHISQ values are somewhat worse for the C_2H_6 retrieval compared to the C_2H_2 retrieval, with a large portion of the distribution between 1 and 4. For this reason and to ensure a suitable number of retrieval points, the CHISQ threshold was set to 10 for C_2H_6 compared to a value of 2 for C_2H_2. Whilst relaxing this CHISQ threshold care must be taken that significantly poor retrievals are not being included in the dataset and for that reason it is also important to consider the other data quality indicators such as the DOFS and the spectral residual fits.

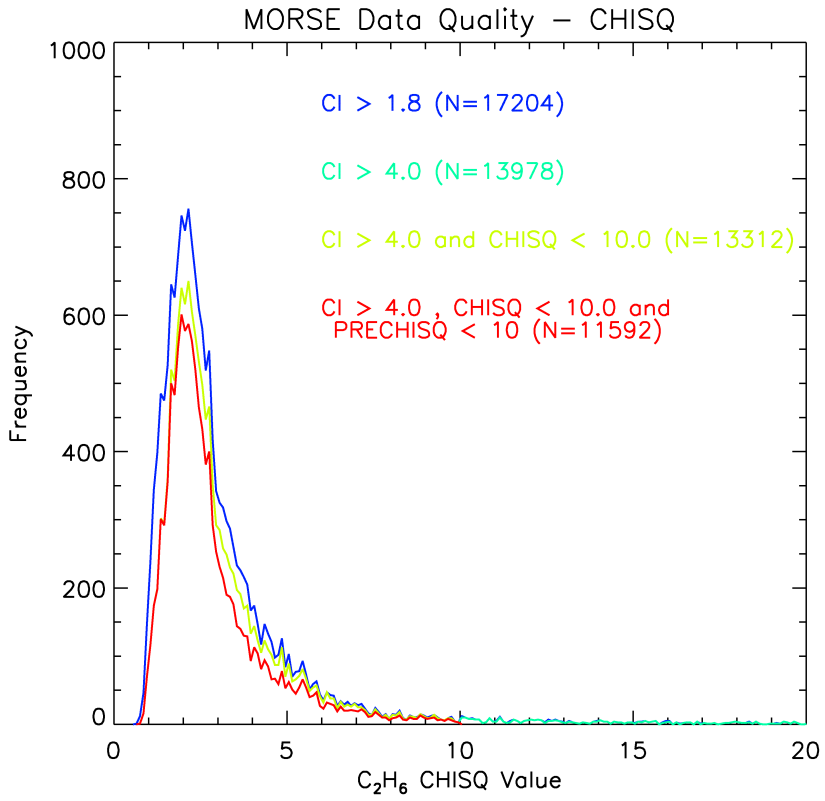

FIGURE 5.31. Histogram showing distribution of C_2H_6 CHISQ values under the different filtering scenarios. The average CHISQ value is shown to be between 2 and 3, which although is worse than for C_2H_2 is still a reasonable value.

5.7.2 DOFS As Indicator Of Data Quality

Figure 5.32 shows frequency distribution of the DOFS for the C_2H_6 retrieval. The majority of the values are between 1 and 3 similar to the DOFS for C_2H_6 (Fig. 5.12). Also similar to the C_2H_2 plot is the fact that there is a peak in the distribution around a value of 1 which is largely removed by the tightening of the cloud index threshold from 1.8 to 4.0.

Although the distribution appears to be slightly more biased towards the lower values than the C_2H_2 retrieval, the data indicates that the retrieval is obtaining between 1 and 3 pieces of information. This corresponds to the fact that we would expect to be able to retrieve from the 9 km, 12 km and 15 km levels similar to C_2H_2 albeit with slightly more difficulty than for C_2H_2 due to the smaller spectral signature and additional interfering species in the C_2H_6 microwindow.

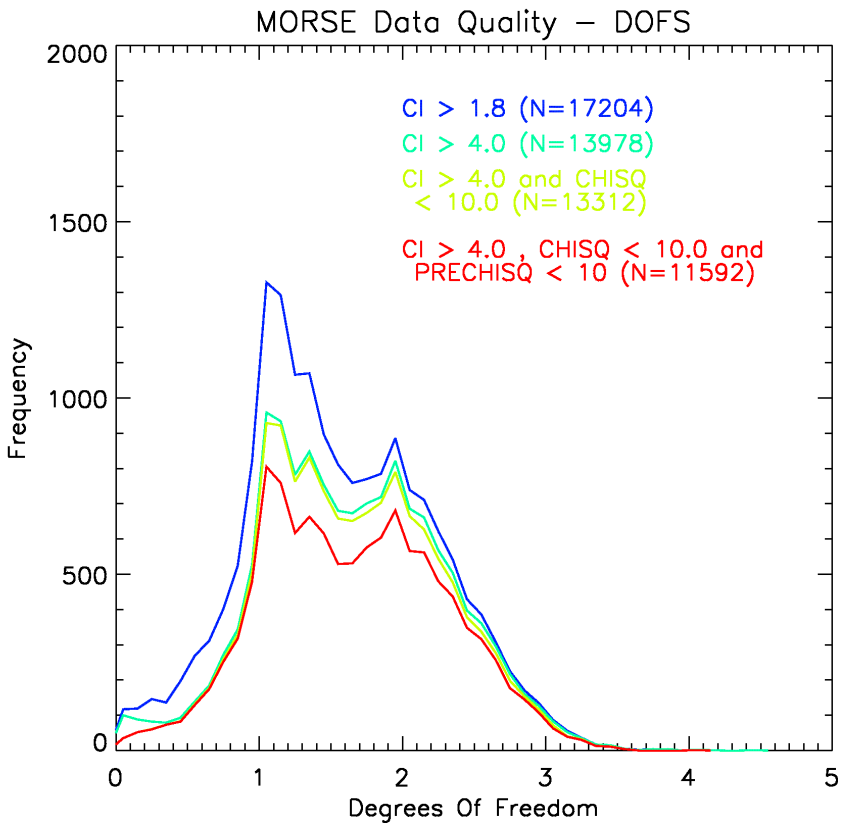

FIGURE 5.32. Histogram showing distribution of the C_2H_6 DOFS values, indicating that typically 1 and 2.5 pieces of information are being retrieved, corresponding to the 9 km, 12 km and 15 km nominal tangent altitudes.

5.7.3 Spectral Residual As Indicator Of Data Quality

As discussed above, due to the necessity of relaxing the CHISQ threshold for C_2H_6 the spectral residuals play an important role in ensuring the quality of the retrieval. The frequency distribution of the residual for the C_2H_6 peak at 822.3 cm^{-1} is shown in Figure 5.33. This distribution indicates that the retrieval is obtaining a good fit between the measurement and the simulation by the forward model, with the centre of the distribution at 0 and the majority less than the noise value of ± 40 $nW/cm^2 \cdot sr \cdot cm^{-1}$. The effect of increasing the strictness of the filtering does not appear to bias the distribution with it staying centred around 0.

To further examine the spectral residuals, Figure 5.34 shows the residuals for all the retrieved scans for each of the filtering scenarios. As shown for C_2H_2, overplotting the residuals on top of each other results in a distribution tightly enveloped by the noise indicating that the retrieval is correctly fitting the simulated spectra to the measurement. However, in the case of C_2H_6 there do appear to be

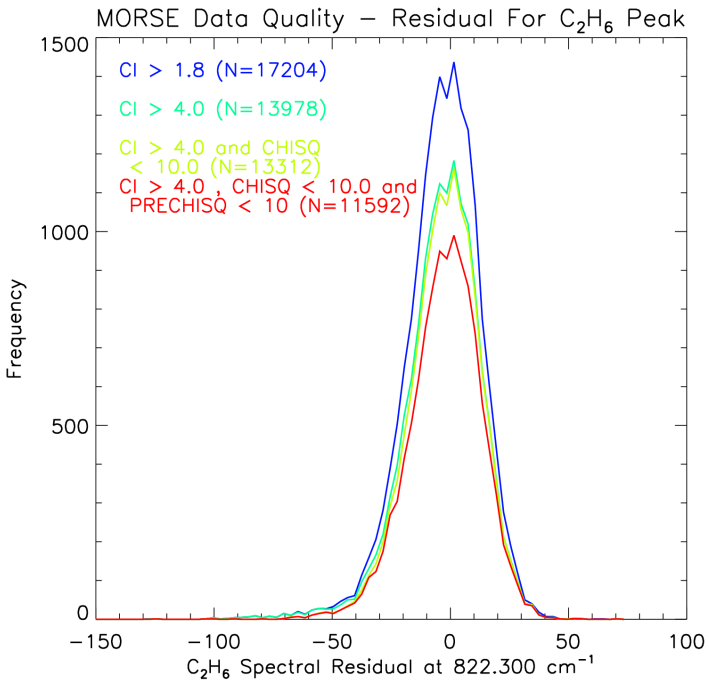

FIGURE 5.33. Frequency distribution showing the spectral residual values of the C_2H_6 peak at 822.3 cm^{-1}. The fit of the simulated forward model to the measurement spectra is shown to be within the MIPAS noise values of ± 40 $nW/cm^2 \cdot sr \cdot cm^{-1}$.

a small number of scans where some features are not being sufficiently fitted and these relate mainly to the ozone lines at either side of the C_2H_6 peak. Although this poor fitting only occurs for a small number of scans, it can be seen that increasing the strictness of the applied filtering helps to reduce this number further but still does not completely remove it. In addition, a very small number of scans (less than 10 out of over 11000) are not correctly fitting the ethane peak itself with a negative residual as high as almost 200 $nW/cm^2 \cdot sr \cdot cm^{-1}$ being observed.

These results suggest that whilst the relatively low CHISQ value and well-fitted spectral residuals indicate that overall the retrieval results are of a high quality, for a small number of scans the retrieval is not performing as well as it could be. By examining the residuals in Figure 5.34 it is apparent that this issue is related to how well the interfering species in the C_2H_6 microwindow are being fit, specifically ozone, and further work may be necessary in the future to reduce these errors.

[p]

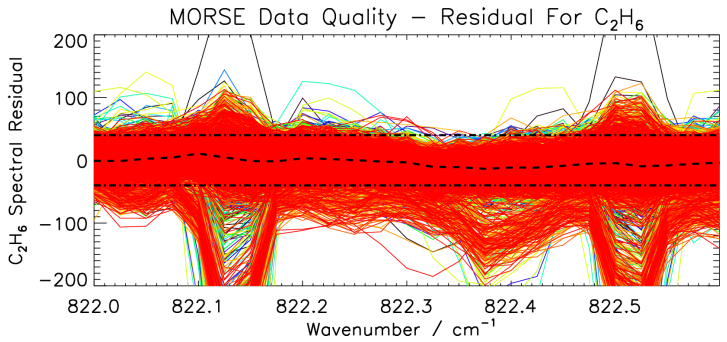

(a) CI > 1.8

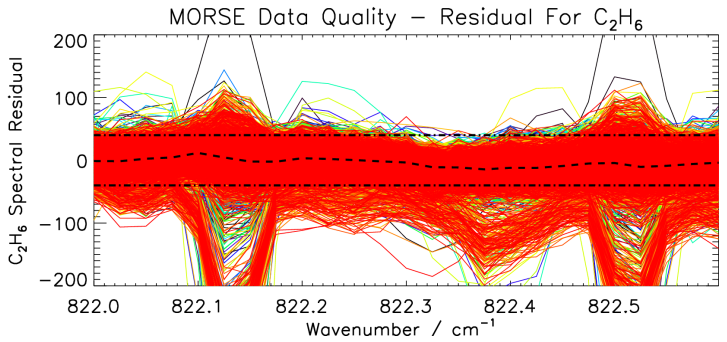

(b) CI > 4

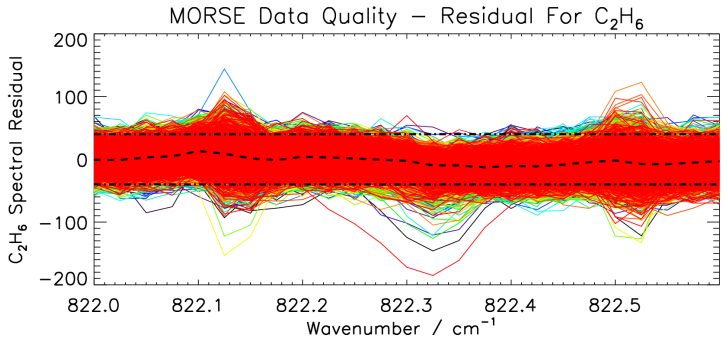

(c) CI > 4 and CHISQ < 10

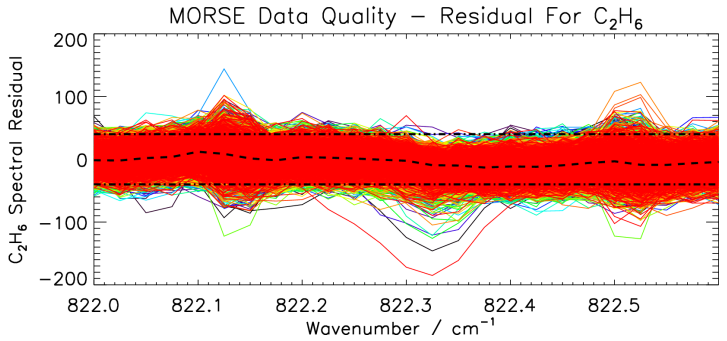

(d) CI > 4, CHISQ < 10 and PCHISQ < 10

FIGURE 5.34. Residuals for the C_2H_6 retrieval under the different filtering scenarios. Even under the strictest filtering (Fig. 5.34(d)) the retrieval still struggles to fit a small number of spectra to the C_2H_6 peak located at 822.3 cm^{-1}. The interfering O_3 lines are also not always correctly fitted although the filtering does greatly improve this.

5.8 Comparison Between Detection And Retrieval Of C_2H_6

Having shown that overall the quality of the C_2H_6 is good, Figure 5.35 compares the retrieval results (Fig. 5.35(a)) to the detection results (Fig. 5.35(b)).

Overall there is a strong similarity between the two techniques with both capturing the general distribution as well as the shape of the strong enhancement observed over north-western South America and Central America. Although the enhancement over the Asian monsoon anticyclone is present in both, in the retrieval results the distribution is dominated by the enhancement over Central America.

Care must be taken when interpreting the C_2H_6 results as whilst the C_2H_2 detected peak radiance can be as high as almost 300 nW/cm^2·sr·cm^{-1}, the C_2H_6 signature is much weaker with a maximum of just 150 nW/cm^2·sr·cm^{-1} but typical values below 100 nW/cm^2·sr·cm^{-1}. When considering that the MIPAS noise can be as high as 40 nW/cm^2·sr·cm^{-1}, that means that it is considerably harder to distinguish the C_2H_6 spectral signature from both the noise and other interfering species.

This issue is highlighted when examining the correlation between the detection and retrieval results discussed above (Fig. 5.35(c)). Although the qualitative comparison performed above did show a strong similarity between the results, when correlating the two datasets the correlation is much poorer than might be expected. Although there is still a recognisable correlation between the two techniques (with a value of 0.58), the effect of the noise is considerably enhanced due to the fact that C_2H_6 has a much smaller spectral signature but at the same time has a greater variability in VMR (up to 1000 pptv) compared to the variability of the C_2H_2 (up to 300 pptv).

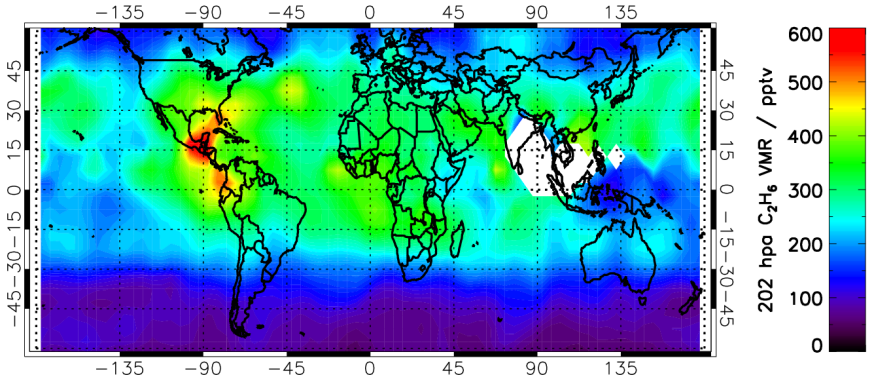

(a) MORSE Retrieved C_2H_6

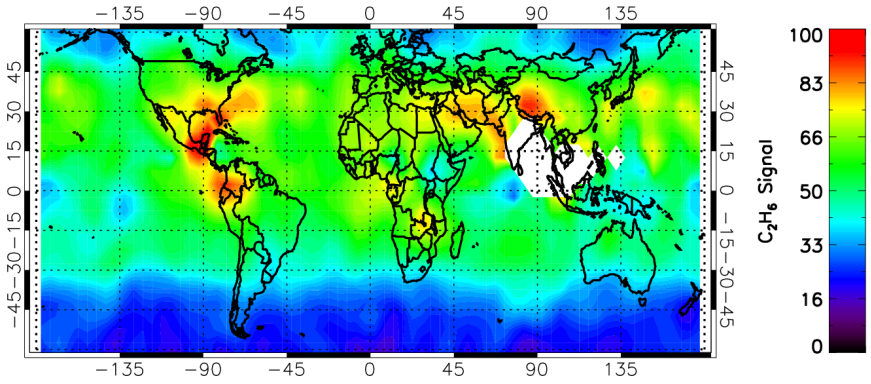

(b) Detected C_2H_6 Peak Radiance

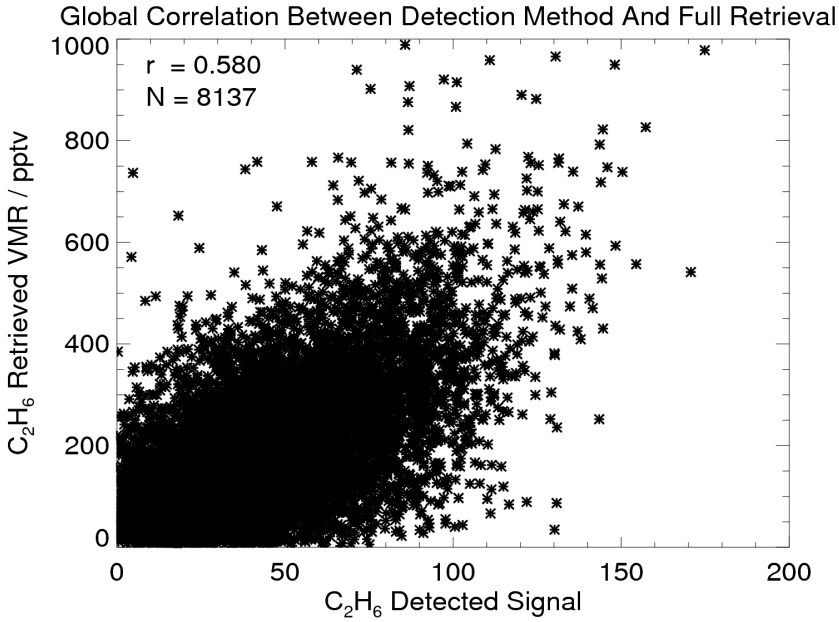

(c) Correlation

FIGURE 5.35. Global distribution of C_2H_6 for August 2003 from the retrieval (Fig. 5.35(b)) and detection (Fig. 5.35(b)) schemes showing a reasonable agreement, especially for the enhancement over Central America. The correlation between the two techniques is considerably poorer than for C_2H_2 due to the much weaker spectral signature of C_2H_6 and is hence more affected by the noise.

5.9 Summary

This section discussed the results from the MORSE retrieval algorithm for the retrieval of C_2H_2 for August 2003.

The error analysis discussed the various contributors to both the random and systematic errors for the retrieval of C_2H_2 (Fig. 5.2) and found the total error estimate at 200 hpa to be 16 % with the random retrieval error dominating this with a value of 14 % compared to 7 % for the contribution from the systematic errors. Out of the various contributors to the systematic error, the C_2H_2 spectroscopy and line-shape effects as well as the uncertainty in the pressure and temperature were found to be the major sources of systematic error.

In addition to the error analysis, a discussion of the data quality issues was undertaken in Section 5.3. The averaging kernels for the retrieval show that the 9 km and 12 km nominal MIPAS altitudes (300 hpa and 200 hpa respectively) have a low dependence on the a priori whereas the retrieval at higher altitudes has more dependence on the a priori. The cloud index threshold of 4.0 was found to be preferable to a lower threshold of 1.8 as it allowed the effects of partially cloudy scenes to be removed from the retrieval.

The quality filtering of the final C_2H_2 dataset was discussed in detail with reference to the use of the cloud index and the CHISQ parameter obtained from the retrieval as methods of filtering the final data. The CHISQ value as well as the DOFS and the final spectral residual were all used as indicators of the quality of the retrieval and the effect of the various stages of filtering were applied to each of these in order to justify the full filtering technique. It was found that by filtering with a cloud index threshold of 4.0, a C_2H_2 CHISQ value less than or equal to 2.0 and a pressure CHISQ value less than or equal to 10.0 all of the various indicators of the quality of the data suggest a high quality retrieval. In particular, the fact that the spectral residual is within the conservative noise level of MIPAS of 40 $nW/cm^2 \cdot sr \cdot cm^{-1}$ suggests that the retrieval is fitting the C_2H_2 peak as well as possible.

Once the quality of the C_2H_2 retrieval was confirmed, the data was analysed and the global distribution of C_2H_2 showed a large enhancement over the Asian monsoon anticyclone region. Strong C_2H_2 enhancements are also observed over the African biomass burning region as well as in the eastward transport from Asia into the Northern Pacific Ocean.

The C_2H_2 retrieval results were compared to the results from the detection algorithm discussed in Chapter 4 and a strong agreement was found between the two different techniques. This agreement was found to hold on both the global scale as well as on more regional scales. The correlation between the two techniques was found to be poorest when there was not sufficient variability, for example when over a low ocean background with no significant source region. Overall, the strong correlation between the two techniques is expected to allow the far less

computationally expensive detection algorithm to act as a useful "first look" when analysing the large amounts of data being considered.

In order to confirm that the detection technique is valid for more than just when the Asian monsoon anticyclone is present, a similar analysis was undertaken for January 2003. Again it was found that the detection and retrieval techniques produced a high level of agreement, not only in the general distribution but down to the level of specific regional enhancements. This provided further confidence that is it valid to apply the detection algorithm to any month of the year (as was done in Chapter 4) as a means of examining where interesting features may be present and which require analysis from a full retrieval.

In addition to the retrieval of C_2H_2, C_2H_6 for August was also retrieved and through a similar analysis of the various data quality indicators it was found that overall the retrieval quality of the C_2H_6 data was reasonable with both a low CHISQ value and a good spectral fit between the measurement and forward model simulation. A poor fit of the spectral residual was observed for a small number of scans and was mainly related to the fitting of the interfering ozone within the C_2H_6 microwindow.

However, when compared to the detection results, whilst overall showing a reasonable level of similarity, the results here were poorer than those for C_2H_2. This was mainly due to the increased difficulty of separating the smaller spectral signature of C_2H_6 from both the noise and other interfering species in both the detection and retrieval. Despite this, it is expected that the detection technique when applied to C_2H_6 will be capable of highlighting regions of interest although further work may be required in optimising the retrieval to remove the effects of interfering species such as ozone.

Chapter 6

Analysis Of C_2H_2 And C_2H_6 Distributions and Comparisons To MOPITT CO

This chapter compares the C_2H_2 and C_2H_6 to CO data from the MOPITT instrument in order to examine how the species remain correlated through various dynamical processes and hence photochemical age of air information can be obtained due to the different photochemical lifetimes involved.

The distribution of C_2H_2 is examined in more detail by both zonal and meridional plots taken across the various regions of interest. The strong chemical isolation inside the Asian monsoon anticyclone is again demonstrated with the deep convection over South-East Asia identified as the source of the C_2H_2. Potential evidence of tropopause penetration is also presented.

Finally the relationship between C_2H_2 and c_2H_6 is used to differentiate between biomass/biofuel burning sources and natural gas production.

6.1 Using Retrieved C_2H_2 And C_2H_6 With MOPITT Global CO Data

Due to their similar sources and sinks, the VMR of carbon monoxide is expected to be heavily correlated to that of C_2H_2 [Wang et al., 2004] with the ratio between the two acting as an indicator for the relative age of an air mass and the extent of atmospheric processing it has undergone [Xiao et al., 2007; Smyth et al., 1996, 1999]. C_2H_6 can also has similar sources and sinks to CO as well as having a longer lifetime than C_2H_2 and hence should provide additional information on the photochemical ageing. This however is complicated by the fact that the primary source of C_2H_6 is natural gas production, with biomass burning being a lesser source.

To analyse these relationships, the 200 hpa MORSE retrieved C_2H_2 and C_2H_6 VMRs were averaged into 5° by 5° boxes (Fig.6.1(a) and Fig.6.1(b) respectively)

using a weighted distance mean method (see 4.2.2). These retrievals were then compared to the corresponding 150 hpa MOPITT CO (Measurement Of Pollution In The Troposphere) data averaged over the whole of August 2003 (Fig.6.1(c)). Some care must be taken in interpreting these correlations as whilst MIPAS is observing at a 12 km nominal altitude with an approximate 3 km field of view and a mean pressure of 200 hpa, MOPITT is a nadir-sounding instrument with the retrieved vertical levels a result of its broad averaging kernels in the troposphere.

In order to test this effect, simulated CO profiles were smoothed with MOPITT averaging kernels. The tests indicated that the maximum effect was likely to be a systematic underestimation of the ratio with CO of approximately 10%. A strong correlation between the two datasets would still be expected.

The strong African biomass burning signature is clearly observed in all data sets, indicating that both C_2H_2 and C_2H_6 enhancements due to biomass burning are present. In addition, there are strong CO, C_2H_2 and C_2H_6 enhancements observed over Asia, particularly the Asian outflow into the Northern Pacific Ocean. Although the data in the South-East Asia region is sparser due to the cloud associated with the Asian monsoon, enhancements are observed over this region where data is present.

It is the strong enhancement of these species in the Middle East region which is of particular interest. Rather than local production, the cause of this feature is long-range transport of the enhancement observed over South-East Asia via the Easterly Jet associated with the Asian monsoon anticyclone into the Middle East region [Li et al., 2001].

6.1.1 MOPITT Global CO Data At Each Level

This section uses the analysis of MOPITT CO data in order to determine that the enhancements of C_2H_2 and C_2H_6 observed over the Middle Eastern region are not due to the production in the region from local biomass burning but are instead transported into the area by the circulation of the Asian monsoon anticyclone.

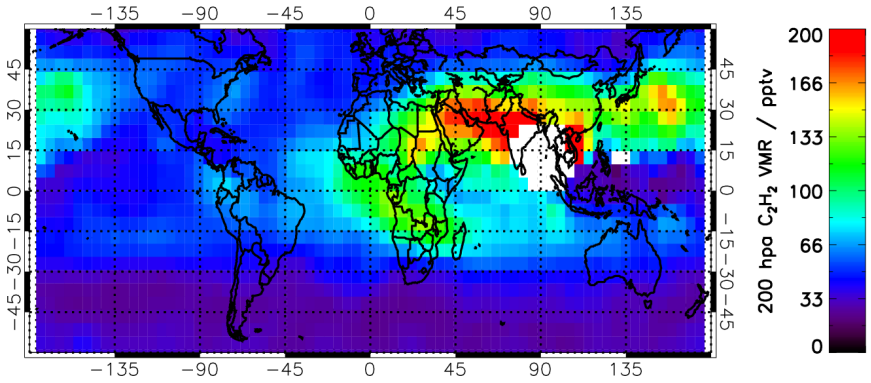

(a) MORSE C_2H_2

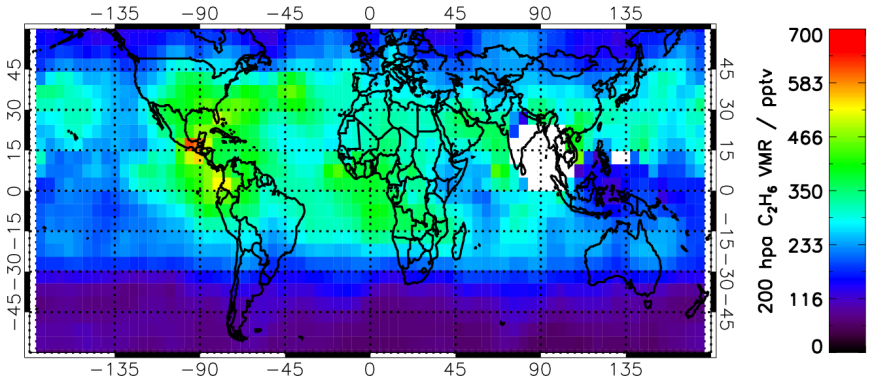

(b) MORSE C_2H_6

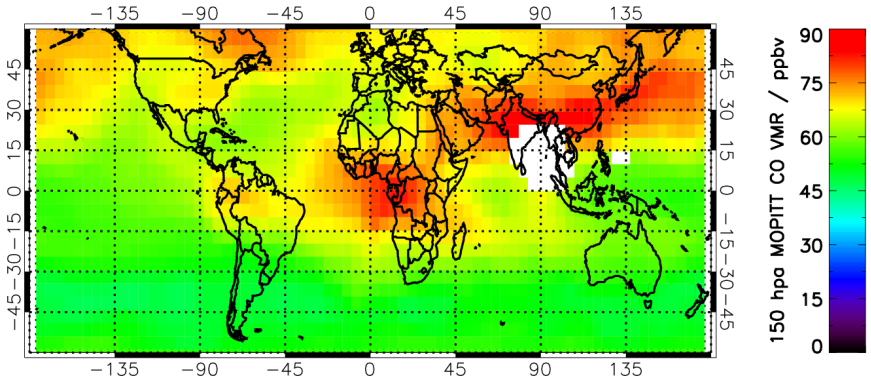

(c) MOPITT CO

FIGURE 6.1. 5° gridded 200 hpa MORSE retrieved C_2H_2 VMRs, 200 hpa MORSE retrieved C_2H_6 VMRs and 150 hpa MOPITT CO VMRs For August 2003. Enhancements in all species are observed over the monsoon anticyclone region in the Middle East. Enhancements are also observed over Asia and Africa including the subsequent outflow from these regions. The C_2H_6 results show further enhancements over North America which are not observed in the C_2H_2.

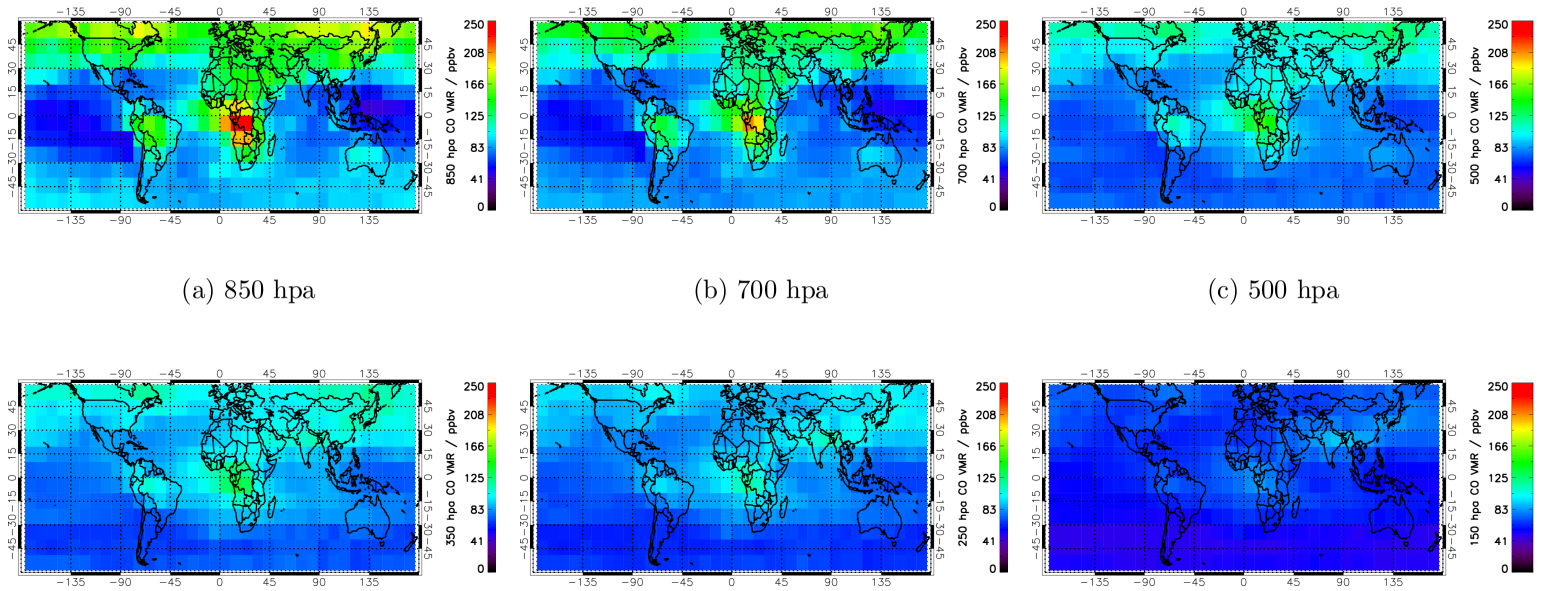

(a) 850 hpa (b) 700 hpa (c) 500 hpa

(d) 350 hpa (e) 250 hpa (f) 150 hpa

FIGURE 6.2. Averaged MOPITT CO data for August 2003 for each of the MOPITT pressure levels (850 hpa, 700 hpa, 500 hpa, 350 hpa, 250 hpa and 150 hpa) showing the enhanced signature of CO corresponding to the African biomass burning with no apparent single source over the Asian monsoon anticyclone region.

Figure 6.2 shows the MOPITT CO data for each of the 6 MOPITT pressure levels from 850 hpa to 150 hpa gridded into 10° boxes for the whole of August 2003. The hemispheric gradient of CO is clear in the lower altitude data with a much stronger average CO value in the Northern Hemisphere compared to the Southern Hemisphere. This gradient becomes less distinct with altitude as the CO becomes more well mixed.

The dominant feature at the 850 hpa level is the large biomass burning signature over Africa. The effects of the enhancement can be seen in each of the MOPITT levels up to the troposphere. In addition to the African biomass burning signal, there is a similar albeit weaker biomass burning present over the Amazon region of South America. What is important to note is that there does not appear to be any significant CO enhancement or biomass burning signal over the monsoon anticyclone region where the previous C_2H_2 and C_2H_6 enhancements are observed, again suggesting it is transport into this region via the anticyclone system rather than local production which is the dominating factor.

This fact becomes even more apparent when just comparing the 150 hpa MOPITT CO data to the 850 hpa data as shown in Figure 6.3. In these plots the colour scales have been optimised independently to show the features for each level separately. Whilst the 850 hpa level (Fig. 6.3(a)) only shows signs of biomass burning over Africa and South America, the 150 hpa level (Fig. 6.3(b)) not only shows the same enhancements over Africa and South America but there are significant indications of transport with the Asian transport eastwards towards North America being clearly evident. More importantly however, there is a large CO enhancement at the 150 hpa over the monsoon anticyclone region which does not appear to have a local source when examining the 850 hpa level.

It is not only biomass burning but also domestic biofuel burning which acts as a major source of C_2H_2, an analysis of the distribution of fires during the period being analysed also adds further weight to these conclusions. Figure 6.4 shows the AATSR Fire product for August 2003. The large biomass burning features observed in the CO, C_2H_2 and C_2H_6 over Africa and South America are clearly the result of the large fires detected over these regions. In contrast, there is no single large fire source over the Asian monsoon anticyclone region which is able to account for the large CO and C_2H_2 observed which further suggests that it is transport into these regions becoming isolated inside the anticyclone which is being observed.

6.1.2 MOPITT CO Day-Night As Indicator Of Sources

Due to the difference in the MOPITT averaging kernel between the day-time and night-time measurements, it is possible to use the difference between the two to gain extra sensitivity to the CO surface conditions. This technique is discussed in far greater detail in Richards [2004]. Figure 6.5 shows the difference between the day and night MOPITT CO measurements at the 850 hpa pressure level averaged for August 2003. Positive values indicate potential surface sources of CO and as can be seen, these largely agree with the sources already discussed over Africa and

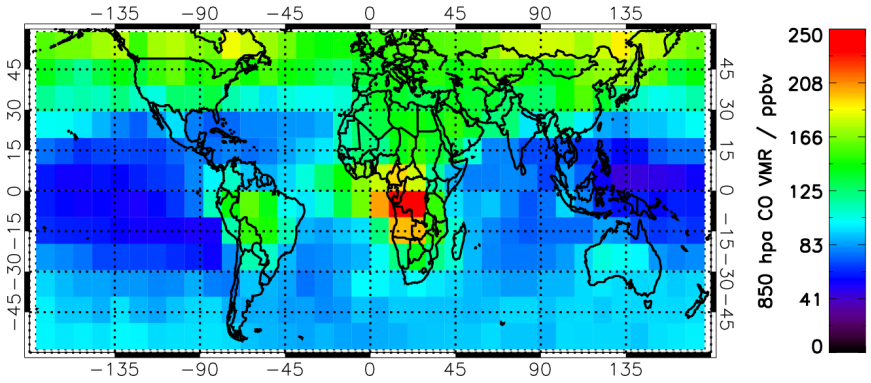

(a) 850 hpa

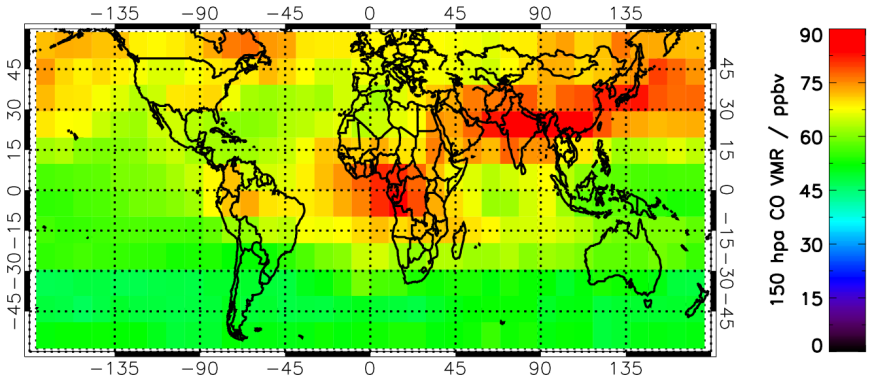

(b) 150 hpa

FIGURE 6.3. Averaged MOPITT CO data for August 2003 for the 850 hpa and 150 hpa showing that although there is no significant single source of CO over the monsoon anticyclone, there is a considerably large signal at 150 hpa due to the chemical isolation inside the anticyclone.

South America. This analysis suggests that there are no significant surface sources of CO over the Asian monsoon anticyclone region and instead it is the transport into this region which is being observed. It should however be noted that this is a null test and the lack of a large day-night difference may be attributed to insufficient thermal contrast. Hence this does not categorically show that no CO sources are present, instead it should only be used to show where they are present.

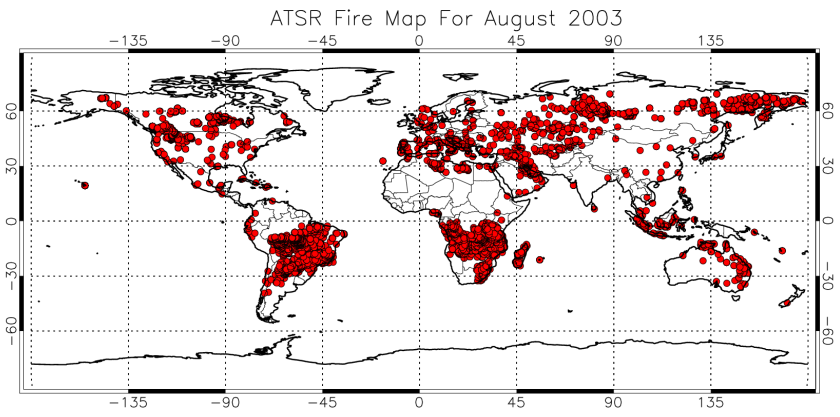

(a) 150 hpa

FIGURE 6.4. AATSR fire map for August 2003 showing large biomass burning regions in Africa and South America along with additional burning in Europe, Siberia, North America and South-East Asia.

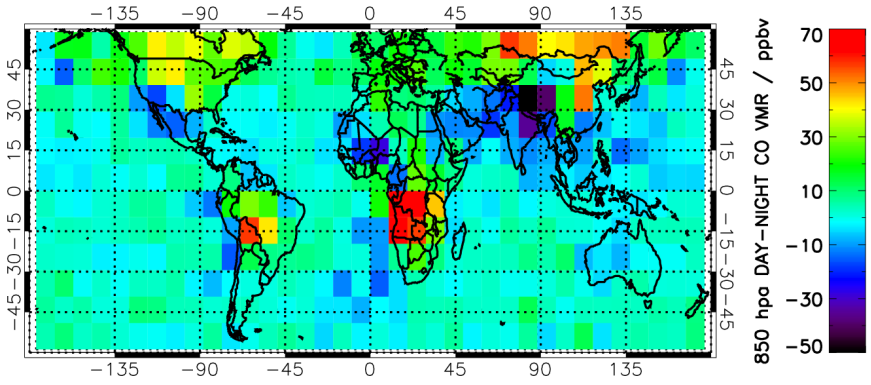

FIGURE 6.5. The day-night difference between MOPITT CO measurements at the 850 hpa pressure level averaged for August 2003. Previous work has shown that this technique is capable of highlighting source regions of CO and such regions are observed over Africa and South America but not over the Asian monsoon anticyclone region.

6.2 Correlations Between C_2H_2, C_2H_6 And MOPITT CO

As discussed above, it is expected that C_2H_2 is highly correlated to CO and the C_2H_2/CO ratio can provide important information relating to the age of the biomass plume and the amount of atmospheric processing it has undergone [Xiao et al., 2007]. As C_2H_6 has a longer lifetime, whilst it should also be correlated to both C_2H_2 and CO, the correlation may prove weaker due to increased mixing and transport over the lifetime of the gas. In addition, the fact that biomass burning is not the predominant source of C_2H_6 (fossil fuel production, see Chapter 1) is expected to weaken any correlation globally but it may still prove useful on a regional scale.

6.2.1 Global Comparison

Correlations on a global scale between these species were performed. The 200 hpa MORSE C_2H_2 VMRs (Fig. 6.1(a)) were correlated against the 150 hpa MOPITT CO VMRs (Fig. 6.1(c)) for the globally averaged monthly data and the result is shown in Figure 6.6. The red points indicate the mean values of the data in 2 ppbv bins (10 pptv bins in the case of the C_2H_2-C_2H_6 correlations) with the lines indicating the standard deviation in each bin. This figure clearly shows a strong correlation between the two VMRs (with r=0.76) but at the same time, there appear to be two distinct domains within this correlation with distinctly different gradients.

The correlation between the 200 hpa MORSE C_2H_6 VMRs and the 150 hpa MOPITT CO VMRs was found to be weaker than the correlation between the C_2H_2 and CO as expected. It is apparent from looking at the global C_2H_6 distribution (Fig. 6.7) that the reason for this poor correlation is mainly related to the large C_2H_6 enhancement observed over Central and North America where neither significant enhancements of C_2H_2 nor CO are observed. The attribution of this C_2H_6 enhancement to fossil fuel production will be discussed in more detail in Section 6.6.1.

The effect of this C_2H_6 enhancement is also seen in the correlation between C_2H_2 and C_2H_6 as shown in Figure 6.8. A reasonably strong correlation would exist but the correlation becomes forked with the high C_2H_6 values over America distorting the correlation between the two species. This C_2H_6 enhancement was also observed in the detection of C_2H_6 discussed in Chapter 4 and will be discussed in more detail later.

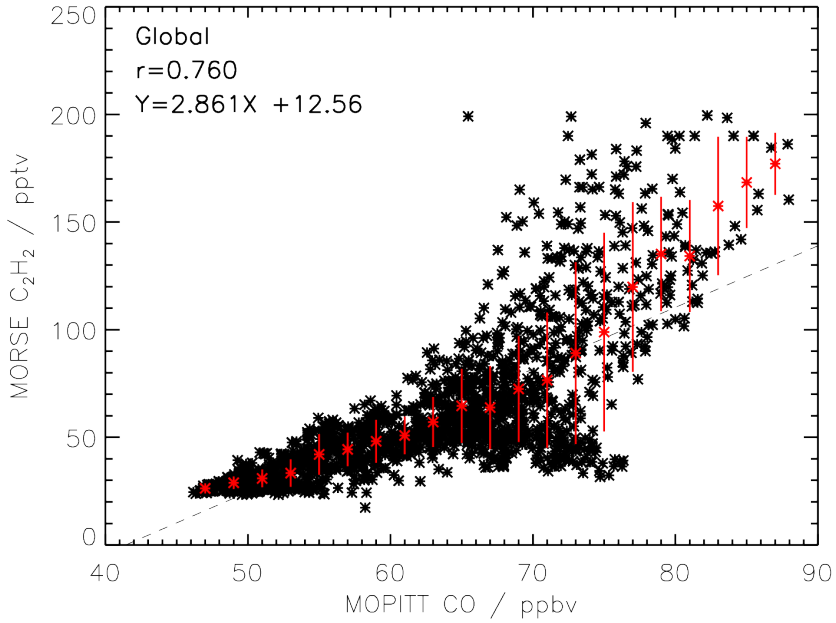

FIGURE 6.6. Correlation of the 200 hpa MORSE C_2H_2 VMRs against 150 hpa MOPITT CO VMRs averaged for August 2003. The two distinct domains observed in the Global correlation are due to the differences in sources and transport for the Northern Hemisphere and Southern Hemisphere.

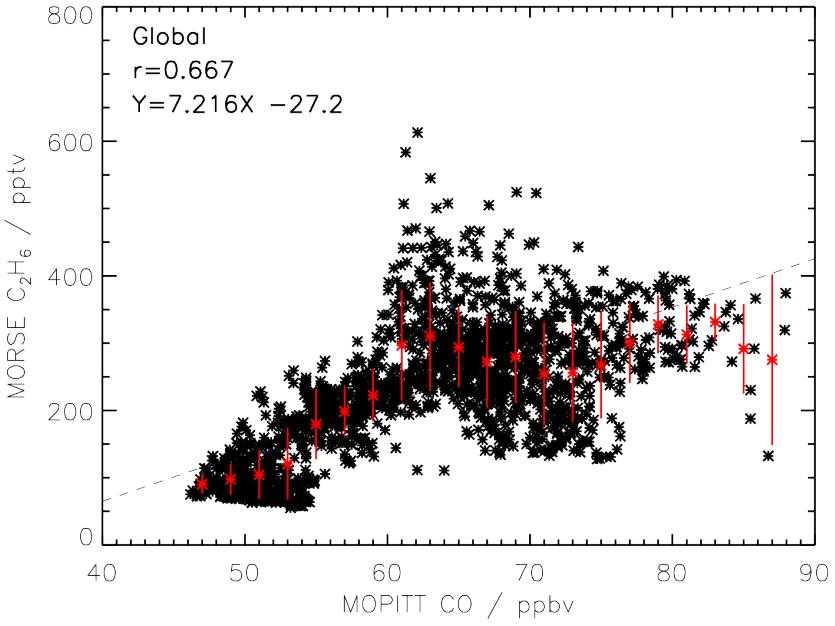

FIGURE 6.7. Correlation of the 200 hpa MORSE C_2H_6 VMRs against 150 hpa MOPITT CO VMRs averaged for August 2003.

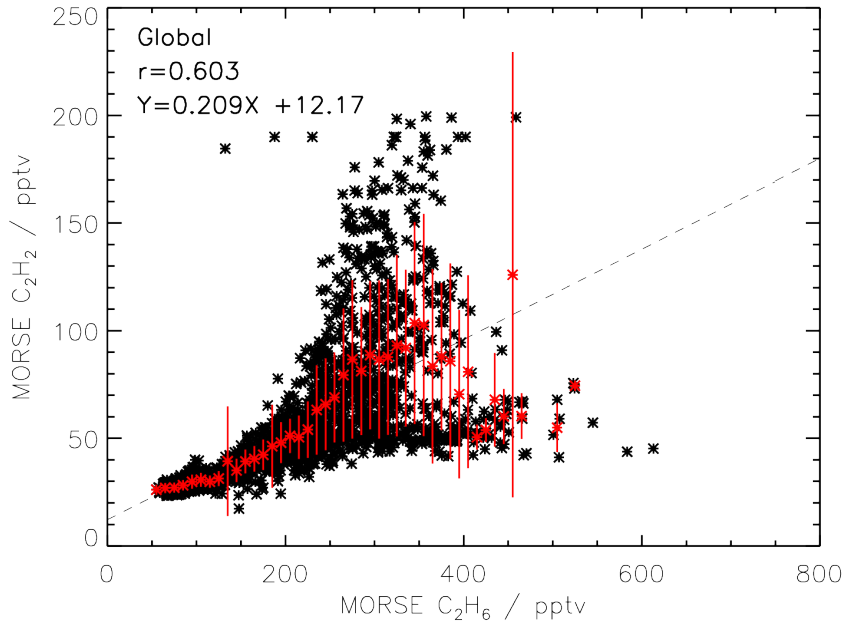

FIGURE 6.8. Correlation of the 200 hpa MORSE C_2H_2 VMRs against 200 hpa MORSE C_2H_6 VMRs showing a distinct split in the distribution relating to the enhanced C_2H_6 values observed over America where no enhanced C_2H_2 was observed.

To examine these relationships further, the correlations were performed separately for the Northern Hemisphere (Fig. 6.9(a)) and the Southern Hemisphere (Fig. 6.9(b)). From the C_2H_2-CO correlations it becomes apparent that the two domains seen in the global correlation are due to the difference in C_2H_2 sources and transport between the two hemispheres. The strong correlation of 0.92 for the Southern Hemisphere is due to the lack of significant sources of C_2H_2 or long-range transport south of the equator whereas not only does the Northern Hemisphere contain the strong Asian C_2H_2 sources but there is a considerably higher background of CO in the Northern Hemisphere when compared to the Southern Hemisphere resulting in a lower correlation of 0.67.

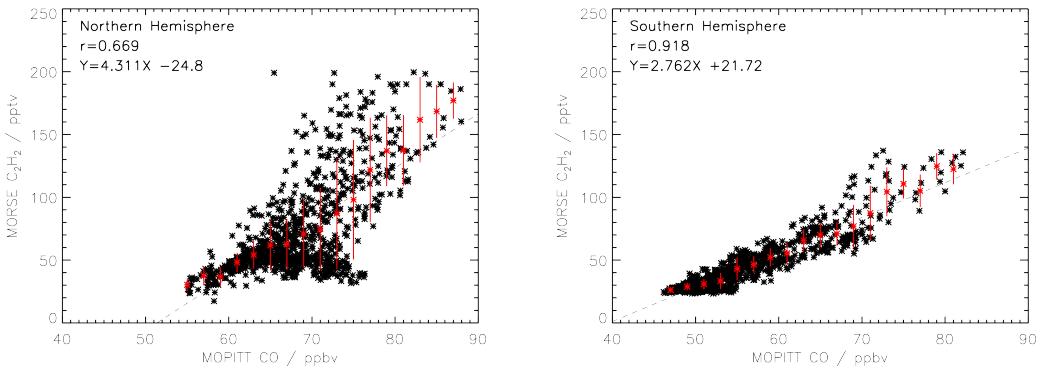

(a) Northern Hemisphere

(b) Southern Hemisphere

FIGURE 6.9. Correlation of the 200 hpa MORSE C_2H_2 VMRs against 150 hpa MOPITT CO VMRs averaged for August 2003 for Northern Hemisphere and Southern Hemisphere.

Similarly the correlation between C_2H_6 and CO is strong for the Southern Hemisphere (Fig. 6.10(b)) with a value of 0.88 but the Northern Hemisphere correlation is dominated by the high C_2H_6 over America resulting in no correlation between the two species.

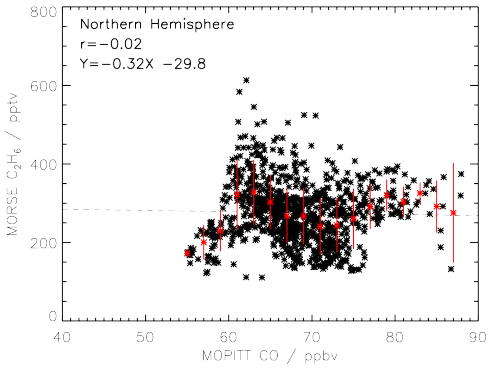

(a) Northern Hemisphere

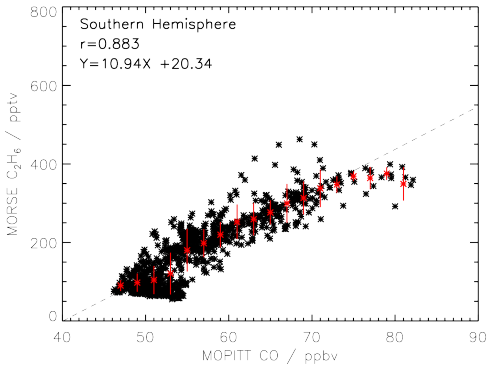

(b) Southern Hemisphere

FIGURE 6.10. Correlation of the 200 hpa MORSE C_2H_6 VMRs against 150 hpa MOPITT CO VMRs averaged for August 2003 for Northern Hemisphere and Southern Hemisphere.

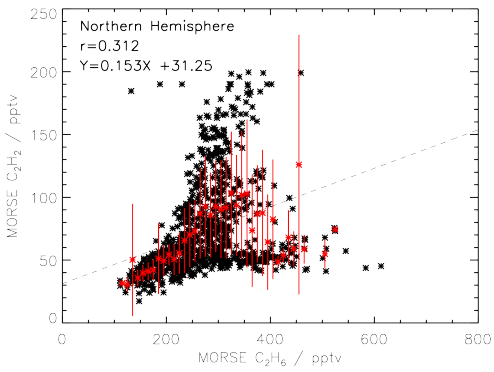

(a) Northern Hemisphere

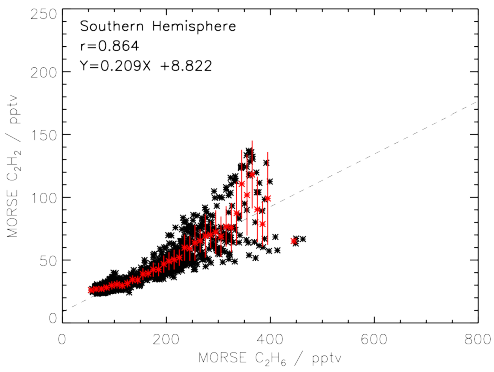

(b) Southern Hemisphere

FIGURE 6.11. Correlation of the 200 hpa MORSE C_2H_2 VMRs against 200 hpa MORSE C_2H_6 VMRs for August 2003 for Northern Hemisphere and Southern Hemisphere.

6.3 Regional Comparison

In order to examine the relationships between the C_2H_2 and C_2H_6 retrieved via MORSE and the MOPITT CO more fully, several regions of interest are defined that represent different scenarios (Fig. 6.12). As well as considering the relationship on both a global scale as well as a hemispherical scale, the regional scenarios consist of large source regions with substantial transport and fire activity (Africa), long range transport (Asian outflow), a large source with minimal transport (South America) and the unique case of the chemical isolation caused by the monsoon anticyclone (Monsoon region). These are the same regions of interest as were used in Chapter 5 to compare the retrieved C_2H_2 to the fast detection technique.

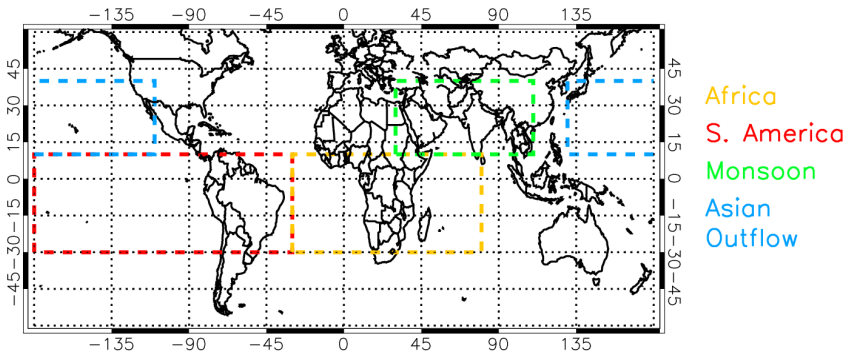

FIGURE 6.12. Map showing the various regions of interest selected for the correlation - Africa, South America, Asian Monsoon Anticyclone and Asian Outflow.

6.3.0.1 Africa

The first region to be considered is the African region. This region is defined as 30°S to 10°N and 30°W to 80°E and covers the southern half of the African continent as well as Madagascar and sections of the Indian Ocean and the South Atlantic Ocean. The centre of the large CO source observed from MOPITT (Fig. 6.13(c)) is located over the Congo basin and the surrounding area which is in strong agreement with both the location of fires in the region identified from the AATSR fire map for August 2003 (Fig. 6.4) as well as the location of the surface sources as identified by the MOPITT day/night comparison (Fig. 6.5).

Qualitatively, the source region and spatial distribution of the retrieved C_2H_2 VMRs for the African region (Fig. 6.13(b)) appears to agree strongly with the CO data. All three datasets, the C_2H_2, C_2H_6 and CO, exhibit similar spatial patterns with clear transport from the source region both north-west into the Atlantic Ocean and eastwards over Madagascar into the Indian Ocean. However, the C_2H_6 does

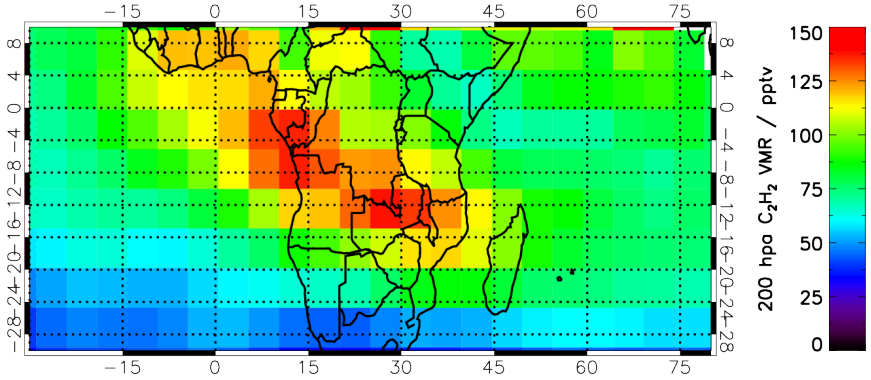

(a) MORSE C_2H_2

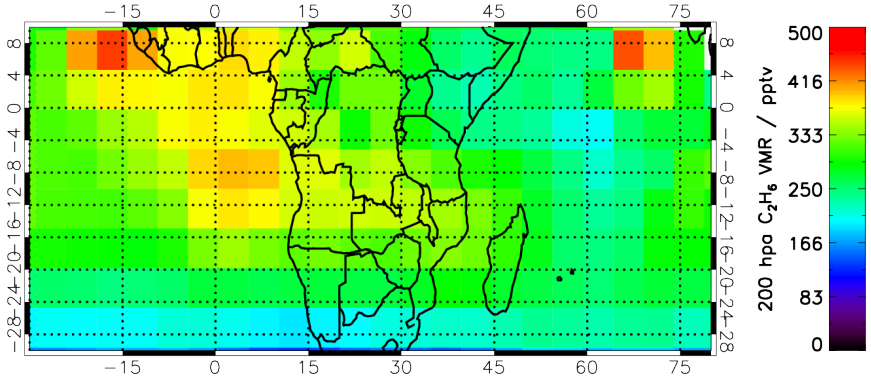

(b) MORSE C_2H_6

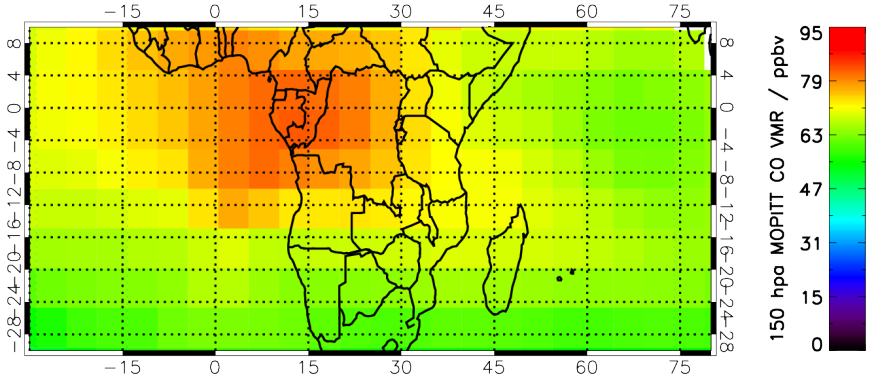

(c) MOPITT CO

FIGURE 6.13. 200 hpa MORSE C_2H_2 VMRs, 200 hpa MORSE C_2H_6 VMRs and 150 hpa MOPITT CO VMRs averaged for August 2003 for: Africa [30°S to 10°N, 30°W to 80°E]

show a stronger enhancement over western Africa, either as a result of its extended lifetime or due to further differences in the source regions.

The correlation between the C_2H_2 and CO datasets is shown in Figure 6.14(a). The strong correlation is confirmed with a correlation coefficient of 0.813 indicating that C_2H_2 and CO in this region are likely to both have common sources and to remain correlated throughout the transport. The gradient of 3.167 here is higher than the gradient calculated for the correlation for the entire Southern Hemisphere.

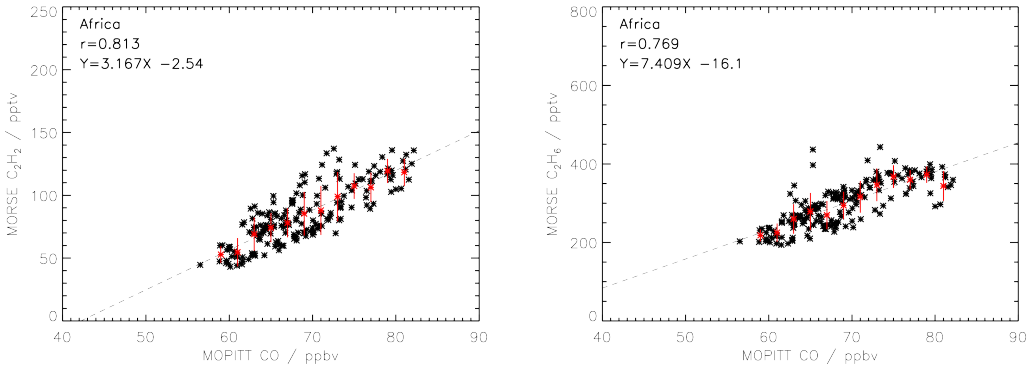

(a) MORSE C_2H_2 vs CO

(b) MORSE C_2H_6 vs CO

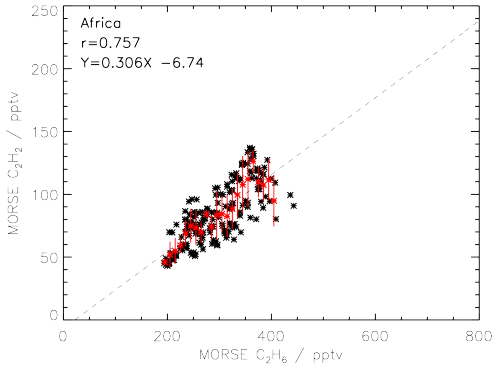

(c) MORSE C_2H_6 vs C_2H_2

FIGURE 6.14. 200 hpa MORSE C_2H_2 VMRs against 150 hpa MOPITT CO VMRs averaged for August 2003 for: Africa [30°S to 10°N, 30°W to 80°E]

The C_2H_6 and CO plot (Fig. 6.14(b) for the African region shows a similar high correlation of 0.769 suggesting that all three species share at least to some degree the similar source of biomass burning in this region.

The correlation between C_2H_2 and C_2H_6 is shown in Figure 6.14(c) and has a value of 0.757 and confirms the relationship between C_2H_2 and C_2H_6 from biomass burning in the African region.

One has to be a little careful about the strength of the correlations. Due to the

fact that the chosen area was defined as to contain not only over a large source region but also a low ocean background there is substantial variability in the dataset. The MOPITT CO values ranges from 55 ppbv to 85 ppbv, whilst the retrieved C_2H_2 VMRs range from 50 pptv to 150 pptv and the C_2H_6 VMRs range from 200 pptv to 450 pptv. This variability allows an adequate range of values to be compared to sufficiently sample the relationship between the three species and provide strong correlations. This demonstrates the importance of selecting the regions to be correlated correctly as without enough variability the points to be correlated may cluster together (e.g. all be low values) and even though there may exist a strong qualitative correlation between the values it will result in a poor correlation coefficient. This issue is further amplified by the fact that it is necessary to average the data into large grid boxes on a monthly scale, removing some of the variability in the data and substantially reducing the number of points to be correlated.

6.3.0.2 South America

The next region to be considered is the Souther American region defined as 30 °S to 10 °N and 180 °W to 30 °. This large region covers the Amazon region of South America where biomass burning would be expected but also extends considerably over the Southern Pacific Ocean which is expected to act as a clean background region.

Figure 6.15(c) shows the 150 hpa MOPITT CO VMRs over this region. In contrast to the African region, although the AATSR fire map (Fig. 6.4) suggests that there is considerable biomass burning occurring in this region and the MOPITT day-night difference (Fig. 6.5) does indicate an apparent source of CO in this region, the CO observed from MOPITT at 150 hpa is considerably lower than in the African region. When examining the 850 hpa MOPITT CO (Fig. 6.2(a)) it is also apparent that there is significantly lower CO in the lower troposphere than over the African region at this level, suggesting a less intense biomass burning source. In addition to this weaker biomass burning signal, there is also no sign of any CO enhancement being transported out over the Pacific Ocean.

The retrieved C_2H_2 VMRs over this region are shown in Figure 6.15(a) but it should be noted that due to the lack of a significant enhancement in C_2H_2, the scale has been adjusted to have a maximum value of 80 pptv as opposed to the value of 200 pptv typically used throughout the rest of this section. In this case the qualitative agreement between the C_2H_2 and CO is not as convincing as it was for the African region. This is mainly related to the fact that there are very few grid boxes that seems to contain a significant C_2H_2 enhancement of 80 pptv with more having a value between 50 and 70 pptv which although it is above the background level of approximately 40 pptv is still relatively weak. One explanation for this lack of enhanced C_2H_2 values is due to the fact that as the coverage due to cloud over the Amazon region is already poor and when averaging a month of data into a grid box this reduces the impact of the few enhanced values that are observed as they

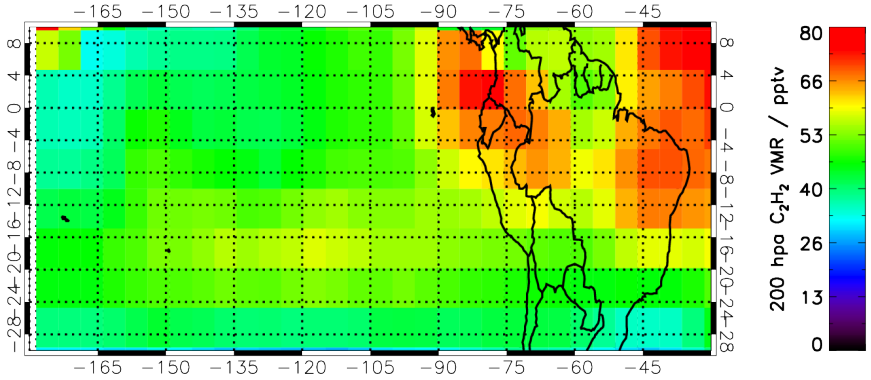

(a) MORSE C_2H_2

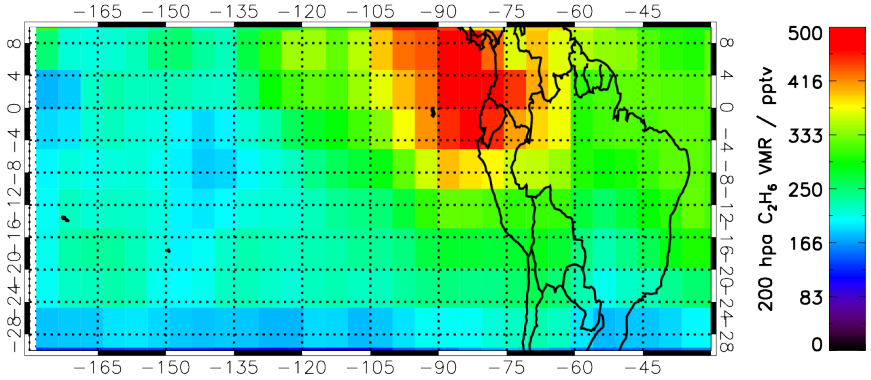

(b) MORSE C_2H_6

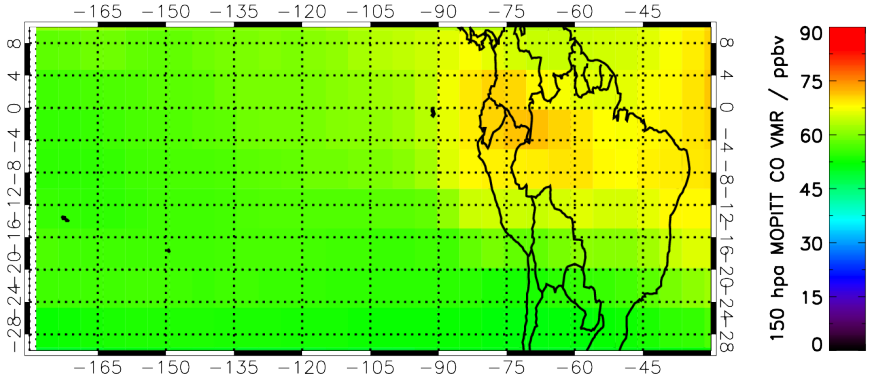

(c) MOPITT CO

FIGURE 6.15. 200 hpa MORSE C_2H_2 VMRs, 200 hpa MORSE C_2H_6 VMRs and 150 hpa MOPITT CO VMRs averaged for August 2003 for: South America [30°S to 10°N, 180°W to 30°W]

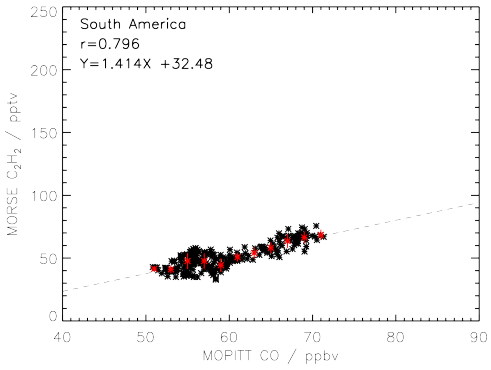

(a) MORSE C_2H_2 vs CO

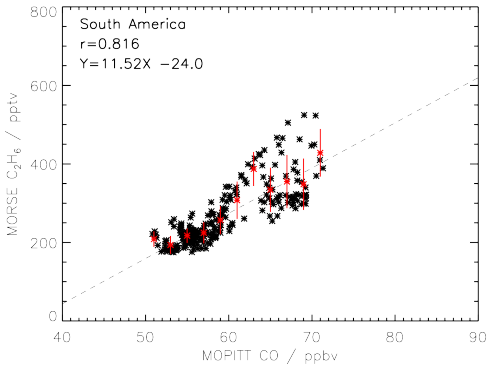

(b) MORSE C_2H_6 vs CO

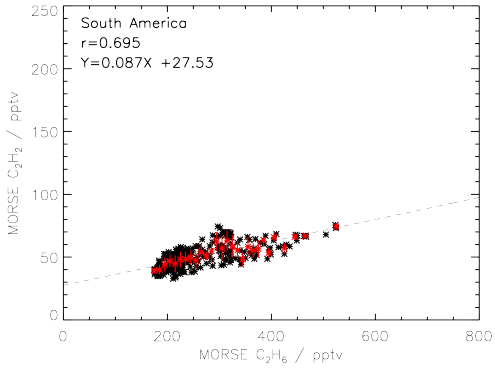

(c) MORSE C_2H_6 vs C_2H_2

FIGURE 6.16. 200 hpa MORSE C_2H_2 VMRs against 150 hpa MOPITT CO VMRs averaged for August 2003 for South America South America [30°S to 10°N, 180°W to 30°W]

become dominated by the larger number of lower values. This is confirmed to be the case when the original dataset before gridding is examined. It becomes apparent that there are a small number of measurements with retrieved values between 100 pptv and 150 pptv over this region but that there are also a considerable number of much lower values. This is one of the issues which must be taken account of when considering species with relatively short lifetimes and analysing them on monthly time-scales. If there is a consistently strong source as observed over the African region the magnitude of this effect is quite small but when the source is weaker and not as persistent as it appears to be over the South American region then more care must be taken in interpreting the results.

The C_2H_2 (Fig. 6.15(a)) and the C_2H_6 results (Fig. 6.15(b)) do show more of an enhancement in this region which may be related to the deep convection of biomass burning emissions. The source of this enhancement seems to be located over the Colombian region. A similar enhancement is seen in the CO data (Fig.

6.15(c)), again suggesting common sources for these species.

In comparison to the African region where the CO values ranged from 55 ppbv to 85 ppbv, here they range from 50 ppbv to 75 ppbv. Although containing approximately the same amount of variability with a range of 25 ppbv, this reduction in the absolute value is in agreement with the relatively weaker source region and the lower background values which were expected due to the cleaner Pacific Ocean background. The C_2H_2 values also show a similar result. For the African region, the lowest C_2H_2 background values were around 50 pptv with the maximum C_2H_2 enhancement values being 150 pptv. In this region, the clean Pacific Ocean leads to background values as low as 35 pptv with the majority of values below 70 pptv, even over the Amazon region.

Despite the above issues, the correlation between C_2H_2 and CO for this region (Fig. 6.16(a)) is still strong with a value of 0.796 and fits a straight line with a gradient of 1.414. This lower gradient is indicative of both a weaker source region for CO and C_2H_2 as well as significantly less transport.

The correlation between C_2H_6 and CO (Fig. 6.16(b)) is even stronger with a value of 0.816. Finally the correlation between C_2H_2 and C_2H_6 (Fig. 6.16(c)) has a value of 0.695.

6.3.0.3 Asian Outflow

The third region examined differs from the previous two as not only does it not include any significant source regions, it is also almost exclusively over the ocean and extends from 10 °N to 40 °N and 130 °E to 110 °W. The purpose of selecting this region was to examine the long-range transport from the large Asian source region over the Pacific Ocean towards North America.

As seen in Figure 6.1(c), MOPITT observes a substantial amount of CO being transported from the Asia into the Pacific Ocean. When examining this more closely in Figure 6.17(c), a strong longitudinal gradient in CO is apparent as the high concentration released from the strong Asian source region diminishes as it crosses the Pacific and is affected by atmospheric processing and mixing.

The retrieved C_2H_2 for this region is shown in Figure 6.17(a). Qualitatively the same spatial distribution is apparent for the C_2H_2 as for the CO with a longitudinal gradient extending from the Asian region across the Pacific Ocean. Although this gradient still exists, the data does contain more variability in the C_2H_2 due to the sampling and data coverage issues discussed previously. The fact that both plots show the enhancement confined above 20 °N with a sharp boundary below this further suggests that the two species are being detected in the same transport plume from Asia. In addition to the overall similarity in distribution between the C_2H_2 and CO, the C_2H_2 results also show more localised enhancements both over Japan and also over the Pacific Ocean between 150°E and 165°E which is not apparent in the CO. The C_2H_6 retrieval results also show a similar general

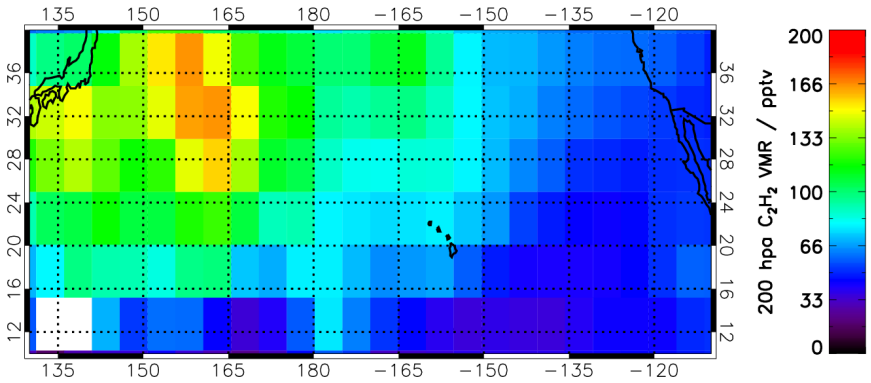

(a) MORSE C_2H_2

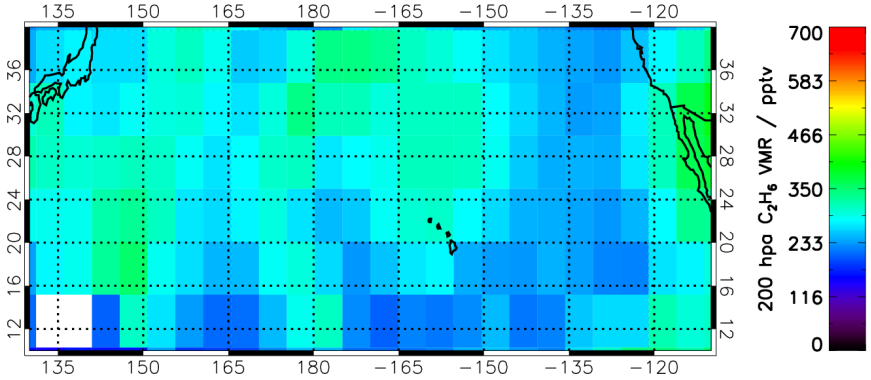

(b) MORSE C_2H_6

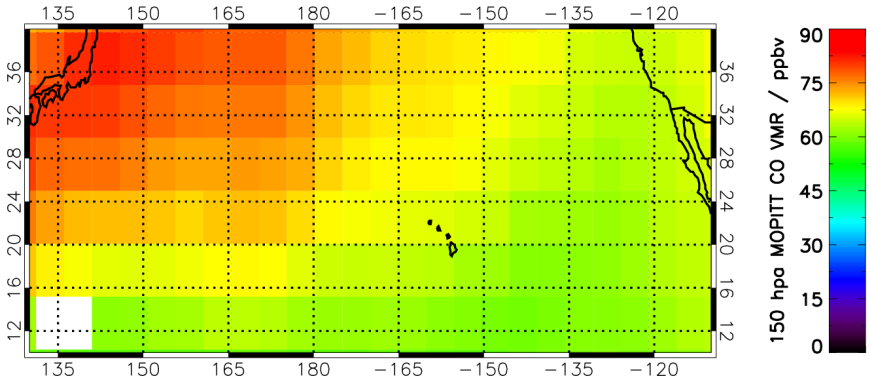

(c) MOPITT CO

FIGURE 6.17. 200 hpa MORSE C_2H_2 VMRs, 200 hpa MORSE C_2H_6 VMRs and 150 hpa MOPITT CO VMRs averaged for August 2003 for: Asian Outflow [10°N to 40°N, 130°E to 110°W]

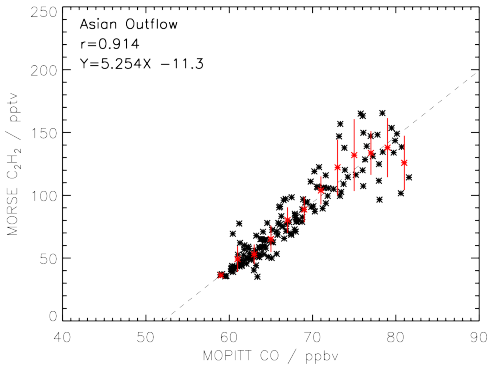

(a) MORSE C_2H_2 vs CO

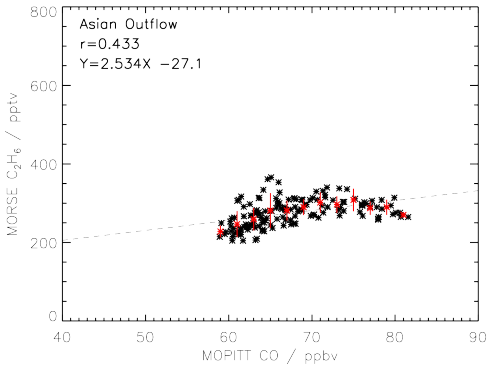

(b) MORSE C_2H_6 vs CO

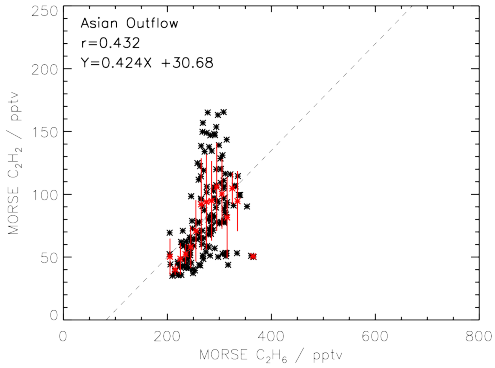

(c) MORSE C_2H_6 vs C_2H_2

FIGURE 6.18. 200 hpa MORSE C_2H_2 VMRs against 150 hpa MOPITT CO VMRs averaged for August 2003 for Asian Pacific Outflow [10°N to 40°N, 130°E to 110°W]

distribution indicating transport from Asia towards North America although with a generally weaker signal.

The C_2H_2-CO correlation for this region is extremely strong with a correlation coefficient of 0.914 and a strong gradient of 5.254. Similar to the African region, the CO varies between 60 ppbv and 85 ppbv. The variability in the C_2H_2 is slightly more and varies between 40 pptv and 180 pptv demonstrating that this region contains both clean background regions as well as very enhanced C_2H_2 values. The fact that such high amounts of C_2H_2 are being observed away from any possible source region and hence that there is such a high gradient suggests that the transport in this region is happening on a relatively quick time scale so that the C_2H_2 with a typical life-time of 2 weeks is not being largely affected by atmospheric processing or mixing.

The correlation between C_2H_6 and CO for this region is shown in Figure 6.18(b) and is considerably poorer than the previous correlations with a value of just 0.433.

Although the points lie close to a straight line, a large number of the C_2H_6 retrievals have low values and the C_2H_6 VMR is not enhanced sufficiently to provide a strong correlation. This effect is also seen in the correlation between the C_2H_2 and C_2H_6 shown in Figure 6.18(c) where a correlation coefficient of 0.432 again shows how the C_2H_6 values are not sufficiently enhanced.

6.3.0.4 Monsoon Anticyclone

The final region examined was the region covered by the Asian monsoon anticyclone and extends from 10 °N to 40 °N and 30 °E to 110 °E. This range means that this region covers the Middle East, India and Asia which in contrast to the other regions contains no ocean background at all.

Due to the fact that this region contains no clear ocean background region some care must be taken in interpreting the spatial distribution of C_2H_2, C_2H_6 and CO as shown in Figure 6.19. This entire regions appears to contain enhanced CO as observed from MOPITT which can be explained by the persistence of the monsoon anticyclone in this region and the resulting chemical isolation as discussed in Chapter 5. The shorter lifetime of C_2H_2 allows slightly more variability than the longer-lived CO which accounts for the small qualitative differences between the two as well as the sharp gradient which the C_2H_2 has at the anticyclone boundary. The C_2H_6 shows a similar distribution, although does not present as strong a gradient at the monsoon boundary as its lifetime is closer to that of CO rather than C_2H_2. The C_2H_6 shows one more major difference to the other species and that is that there appears to be a region of low C_2H_6 on the edge of the convective monsoon region over India which may be accounted for by the effect of cloud in this region.

As this region is entirely over land, the lowest values of the C_2H_2, C_2H_6 and CO are much higher than in the previous regions. For the previous regions, the low values of CO have been around 50 ppbv - 60 ppbv but in this case the lowest value of CO is over 70 ppbv. Similarly, whilst previously the C_2H_2 values have ranged from a low of between 35 pptv to 50 pptv up to a maximum of between 100 pptv - 150 pptv, in the case of this region the lowest C_2H_2 values are in excess of 100 pptv with the maximum values reaching 210 pptv. These extreme enhancements of C_2H_2 compared to the other regions are due to the chemical isolation experienced inside the monsoon anticyclone. As discussed previously (Sec. 1.4.1), domestic biofuel burning, particularly from Asia, is a major source of C_2H_2. Whilst this may not have significantly affected the other regions, the combination of this large source of C_2H_2 along with the chemical isolation caused by the monsoon anticyclone leads to the large amounts of C_2H_2 which are continually maintained by the Asian emissions and persistence of the anticyclone during the summer months.

The correlation between C_2H_2 and CO for the Asian monsoon anticyclone region has a value of 0.59 (Fig. 6.20(a)). As this region is entirely over land, the background values of both the C_2H_2 and CO are much higher than in the previous regions. The correlation of 0.59 results from the fact that the anticyclone bound-

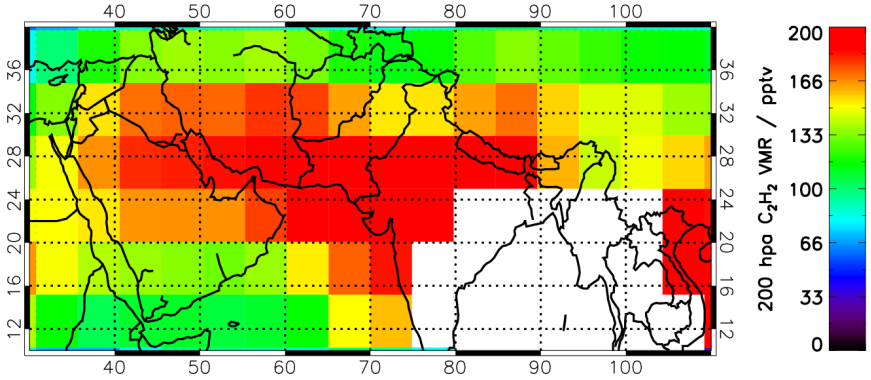

(a) MORSE C_2H_2

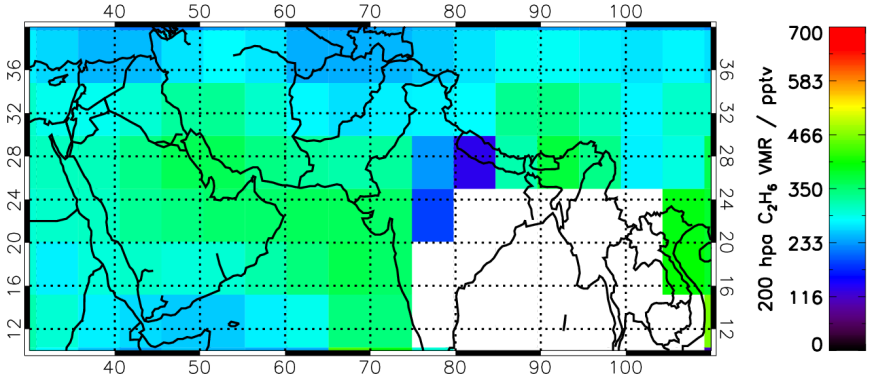

(b) MORSE C_2H_6

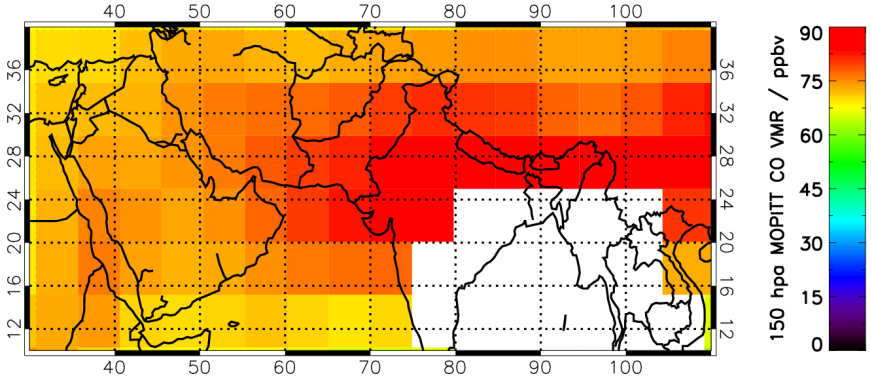

(c) MOPITT CO

FIGURE 6.19. 200 hpa MORSE C_2H_2 VMRs, 200 hpa MORSE C_2H_6 VMRs and 150 hpa MOPITT CO VMRs averaged for August 2003 for: Monsoon anticyclone region [10°N to 40°N, 30°E to 110°E]

ary has a much stronger effect on the C_2H_2 which has a sharp gradient across the anticyclone compared to the CO.

Due to the differences between C_2H_6 and CO mentioned above, as expected the correlation over the monsoon region between C_2H_6 and CO is poor (Fig. 6.20(b)). The correlation between C_2H_2 and C_2H_6 is also poor ((Fig. 6.20(c)) despite a reasonable qualitative agreement but this can be seen to be due to the three low C_2H_6 values observed on the edge of the cloudy convective region. If these three points are removed, the correlation coefficient would increase from 0.472 to 0.75 showing similar C_2H_6 isolation to that of C_2H_2.

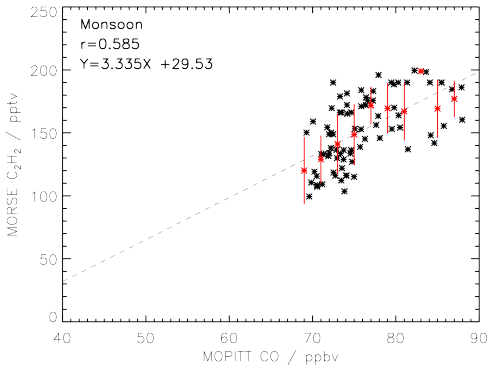

(a) MORSE C_2H_2 vs CO

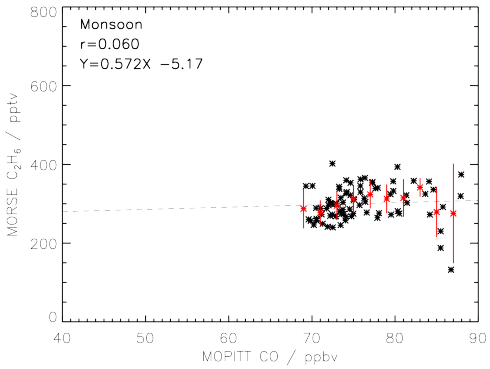

(b) MORSE C_2H_6 vs CO

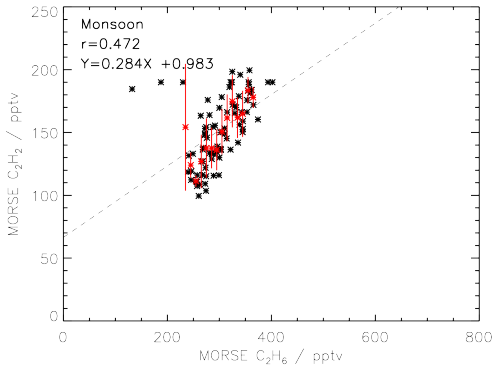

(c) MORSE C_2H_6 vs C_2H_2

FIGURE 6.20. 200 hpa MORSE C_2H_2 VMRs against 150 hpa MOPITT CO VMRs averaged for August 2003 for monsoon anticyclone region [10°N to 40°N, 30°E to 110°E]

6.4 C_2H_2 and C_2H_6 Vertical Information

In contrast to the detection results, the full optimal estimation retrieval allows the entire profile of C_2H_2 to be retrieved which can provide important information on the uplift and transport of C_2H_2 from the various source regions. The following section examines the vertical distribution of C_2H_2 and C_2H_6 for August 2003 over different retrieval levels as well as discussing the zonal and meridional distributions as a function of altitude.

6.4.1 C_2H_2 Vertical Information

Figure 6.21 shows the C_2H_2 retrieval results for the 9 km, 12 km, 15 km and 18 km MIPAS nominal altitudes which have corresponding average pressures of 313 hpa, 200 hpa, 120 hpa and 72 hpa respectively. Several interesting features become apparent when examining the C_2H_2 retrieval results on multiple levels. Firstly the strong enhancement of C_2H_2 located over Asia and the Middle East associated with the isolation caused by the Asian monsoon anticyclone is present at other levels. Some care must be taken when considering the 72 hpa and 120 hpa levels as the averaging kernels for these level examined in Chapter 5 only have a value of 0.5, suggesting that a significant part of the information is coming from not only the a priori but also the levels below. The 313 hpa and 200 hpa levels both have much strong distinct averaging kernels giving more confidence in the results at these levels. When examining the 313 hpa level the isolation caused by the monsoon is not as apparent and instead enhancements centre over the source regions of Northern India and South-East Asia. This suggests that this level is sampling the convective uplift of C_2H_2 before it expands out inside the anticyclone to cover a much larger region at the upper levels.

The second interesting feature when examining the different altitudes is that the Asian outflow towards North America is much more pronounced in the 313 hpa layer than the 200 hpa one. In order to understand this, Figure 6.22 shows the NCEP average tropopause pressure for August 2003. The tropopause in the region where the enhanced Asian outflow is observed in Figure 6.21(a) is actually apparently at or above 200 hpa, meaning that in this region (Figure 6.21(b)) the 200 hpa level could be above the tropopause which is acting as a barrier to vertical transport from the Asian outflow and hence the enhanced values observed at 313 hpa.

Finally the third interesting feature observed is that the African biomass burning feature is drastically enhanced at the 313 hpa level compared to at 200 hpa, suggesting that the concentrations drops away relatively quickly before reaching the tropopause and instead spreading out horizontally both into the Atlantic and Indian Oceans.

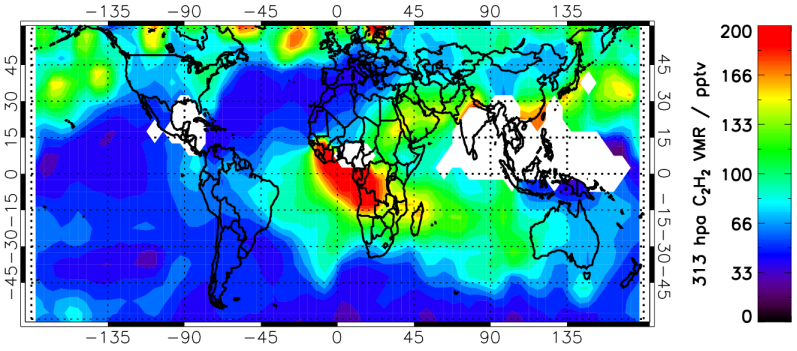

(a) 313 hpa (9 km nominal altitude)

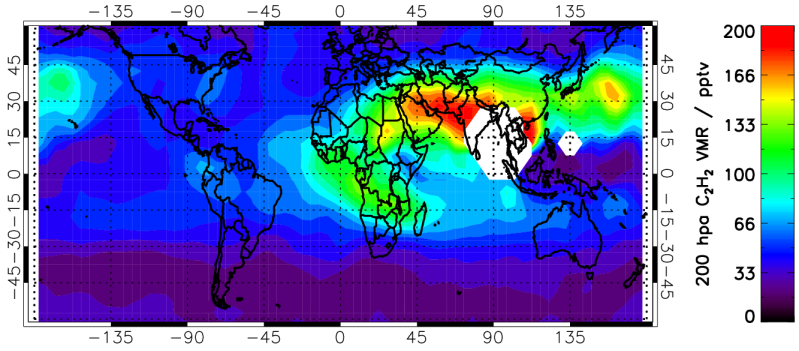

(b) 200 hpa (12 km nominal altitude)

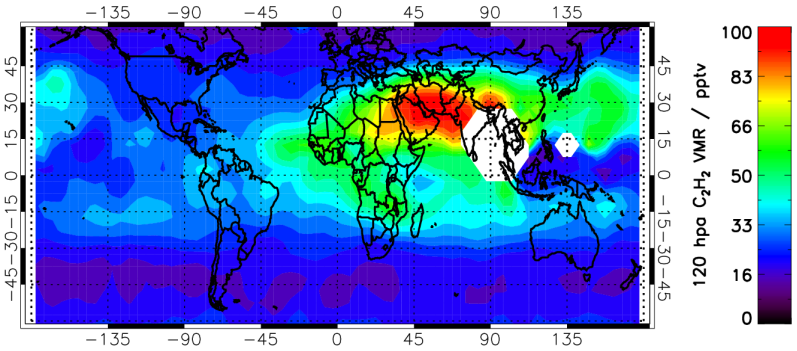

(c) 120 hpa (15 km nominal altitude)

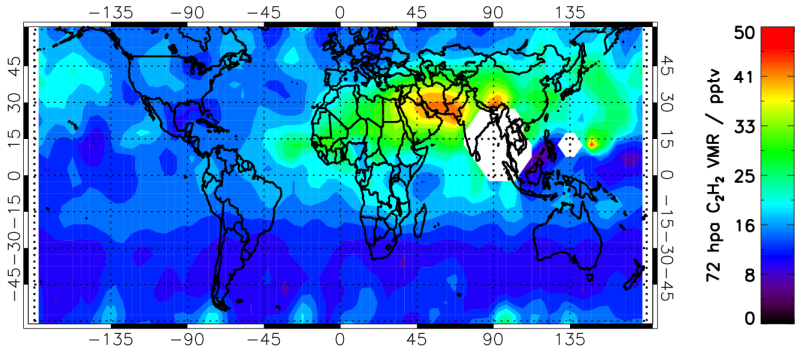

(d) 72 hpa (18 km nominal altitude)

FIGURE 6.21. The MORSE retrieved C_2H_2 distributions for August 2003 for the 9 km, 12 km, 15 km and 18 km nominal MIPAS tangent altitudes. The strong Asian monsoon anticyclone isolation is clearly evident as well as significant transport from Asia towards North America, particulary at lower altitudes.

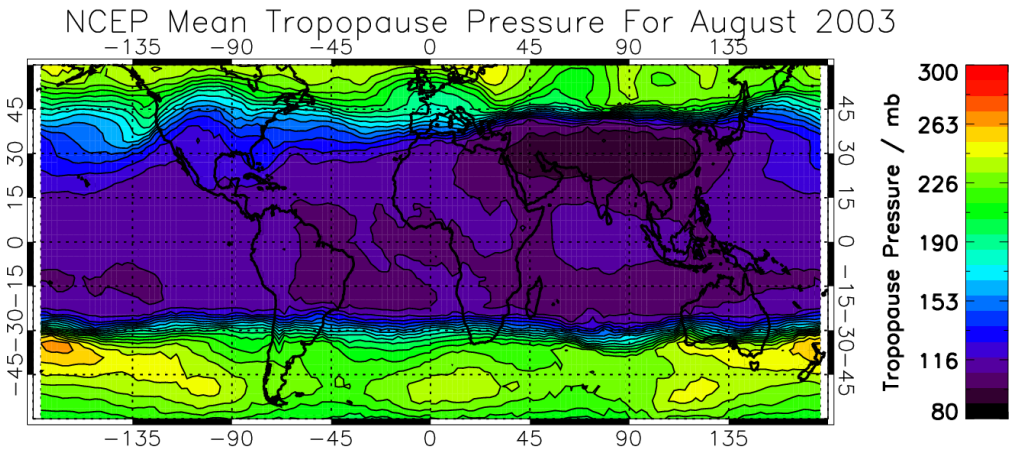

FIGURE 6.22. NCEP Tropopause Pressure for August 2003 showing the average pressure of the tropopause. This can be used to explain some of the features observed in the C_2H_2 distributions as it can act as an indicator as to whether a region is in the troposphere or stratosphere at a particular pressure.

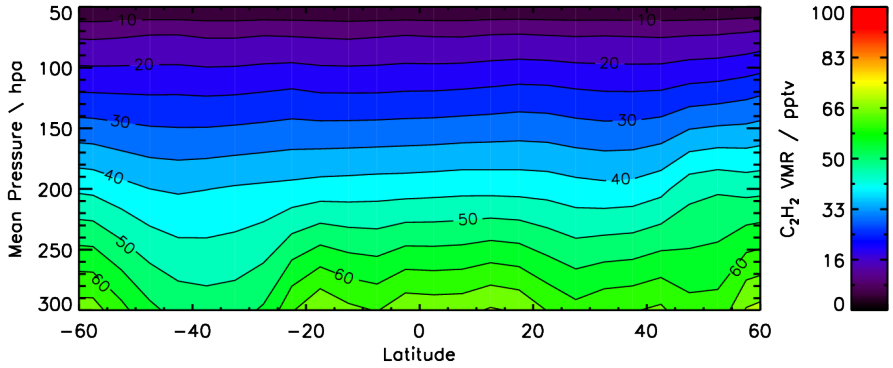

FIGURE 6.23. Zonal Mean C_2H_2 plot showing the strong enhancements between 20°S and 20°N relating to tropical biomass burning.

Figure 6.23 shows the zonal mean for the August C_2H_2 retrieval. This plot shows a strong enhancement up to 250 hpa between 20°S and 20°N relating to the biomass burning in the tropics, specifically over Africa. In addition to this, there is actually a decrease in the zonal mean between 20°N and 50°N as the isolation related to the Asian monsoon anticyclone confines the distribution to a relatively small region.

The meridional mean is also calculated and shown in Figure 6.24. The distribution at higher altitudes shows an increase over the anticyclone region between 0°E and 120°E. At lower altitudes, strong enhancements are observed over both African biomass burning longitudes as well as inside the anticyclone region.

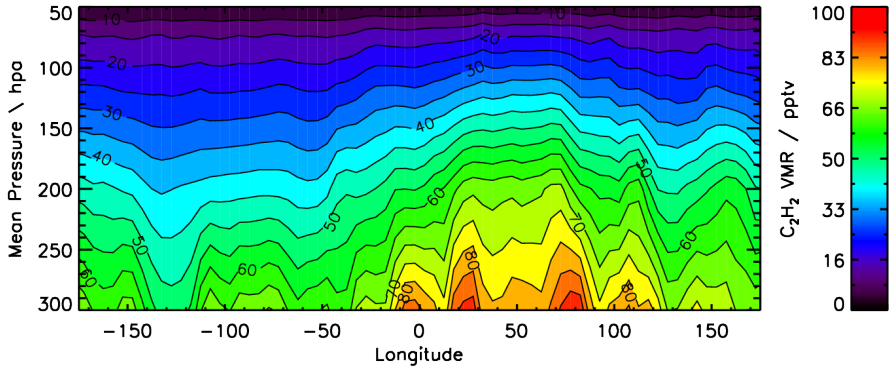

FIGURE 6.24. Meridional Mean C_2H_2 plot showing the strong enhancements due to both the Asian monsoon anticyclone as well as African biomass burning.

In order to examine some of these features in more detail, cross-sections were taken for both the meridional and zonal distributions to show the behaviour through different regions. The NCEP mean tropopause pressure for August 2003 is plotted as a red dashed line in order to give some indication of the location of the tropopause and to allow some preliminary discussion on whether any tropopause penetration into the stratosphere is observed.

6.4.2 Zonal Cross-Sections

The C_2H_2 distribution for August 2003 was sampled in the zonal direction along latitudes lines at 15°N, 20°N, 25°N and 30°N. These zonal cross-sections are shown in Figure 6.25. These figures provide perhaps one of the most interesting result as they show cross-sections taken through the core of the monsoon anticyclone region.

Figure 6.25(a) shows the zonal cross-section taken along 30°N with the NCEP tropopause pressure indicated by the red dashed line. The extent of the anticyclone is clearly identified over multiple levels between 40°E and 130°E with the strong C_2H_2 enhancement being confined to the convective region at lower altitudes before spreading out to cover the entire region as it reaches the tropopause. In addition to the anticyclone enhancement, the transport of C_2H_2 from Asia into the Pacific is observed with an enhancement at 170°E between 200 hpa and 250 hpa.

Figure 6.25(b) shows a similar distribution when a cross-section is taken at 25°N. However, we are now closer to the area of deep convection between 70°E and 110°E identified from the OLR plot in Chapter 4 (Fig. 4.41). As a result, data over the area of deep convection is contaminated by clouds but interestingly enhanced C_2H_2 is observed on both sides of the convective region, again suggesting that it is from this region where the C_2H_2 is being uplifted from the surface. Figure 6.25(c) is taken across 20°N passing directly through the deep convection zone and shows the same result. At this latitude, although there is no cloud-free data between 70°E

and 110°E, the data that is available on the edge of the convection zone clearly shows enhanced C_2H_2 emerging from the cloud-convection region.

Finally Figure 6.25(d) is taken at 15°N which passes just below the Southern edge of the anticyclone region and does not show as large an enhancement as its on the edge of the anticyclone's influence. This helps to confirm that it is the deep convection over Northern India, China and South-East Asia which is the source of the C_2H_2 enhancement inside the anticyclone. Whilst the strongest enhancements (over 100 pptv) in all of these figures are contained within the troposphere, there is some suggestion that above the Asian monsoon anticyclone, there is potentially some enhancement of C_2H_2 compared to the stratospheric background values. As all of these plots deal with the distribution in a mean sense, we will explore this possibility in more detail on a point-by-point basis in Section 6.4.4.

In addition to analysing the Asian monsoon anticyclone region, the African biomass burning region was also analysed by taking cross-sections along the equator as well as at 5°S, 10°S and 5°N. These are shown in Figure 6.26. All of these figures clearly show the enhanced C_2H_2 being uplifted from the surface over the African biomass burning region between 0°E and 30°E and demonstrate the large area over which this burning and uplift takes place.

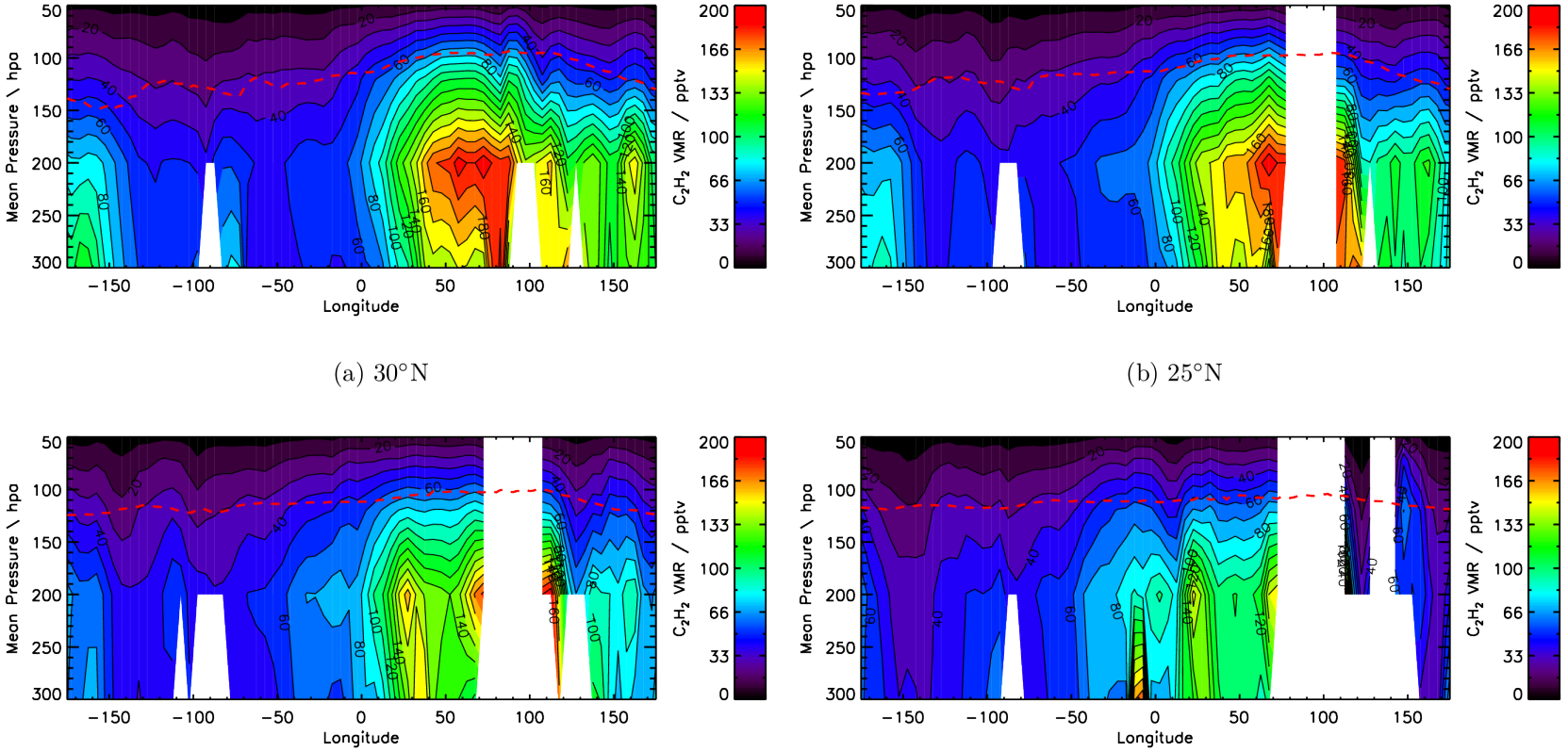

(a) 30°N

(b) 25°N

(c) 20°N

(d) 15°N

FIGURE 6.25. Zonal cross-sections of the retrieved C_2H_2 distributions along the 15°N, 20°N, 25°N and 30°N latitude lines passing horizontally through the strong Asian monsoon anticyclone isolation.

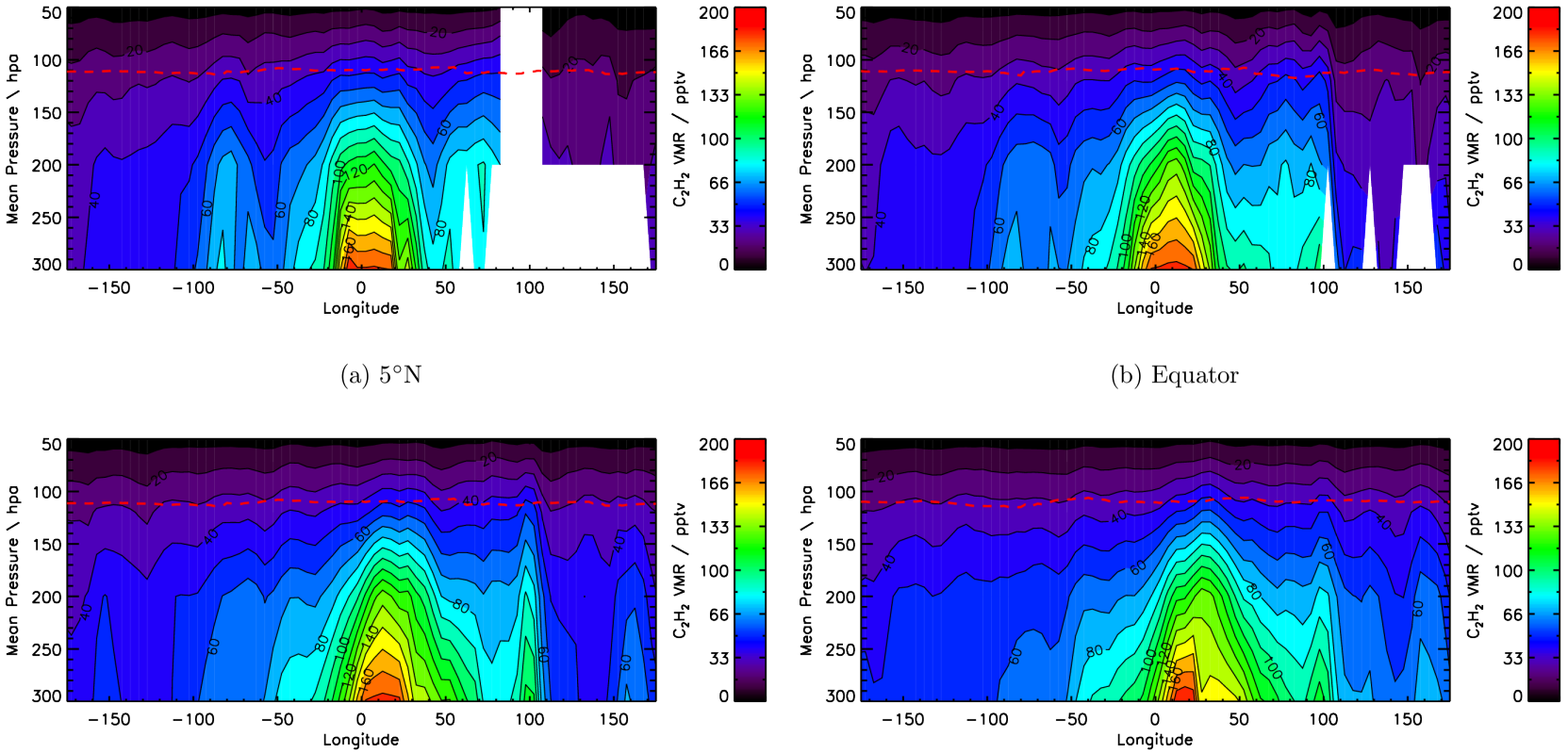

(a) 5°N

(b) Equator

(c) 5°S

(d) 10°S

FIGURE 6.26. Zonal cross-sections of the retrieved C_2H_2 distributions along the 5°N, 0°N, 5°S and 10°S latitude lines passing horizontally through the African biomass burning feature.

6.4.3 Meridional Cross-Sections

In addition to examining zonal cross-sections, meridional cross-sections were also taken along lines of latitude to examine both the monsoon and African features at 20°E, 40°E and 75°E as well as the Asian outflow at 135°E, 160°E and 170°W. Again, all of these figures include the NCEP mean tropopause pressure indicated by the red dashed line.

The meridional cross-sections for 20°E, 40°E and 75°E are shown in Figure 6.27. At 20°E (Fig. 6.27(a), the cross-section only encounters the edge of the monsoon anticyclone between 15°N and 30°N but the transport of the air northwards as it continues to be uplifted inside the anticyclone is still observable. The strong African biomass burning feature between 5°N and 20°S is also clearly visible although the two features are somewhat merged at this longitude as the influence from each of them becomes partially mixed over Northern African. The confinement of the enhanced C_2H_2 by the tropopause is evident as well as some indication of the Hadley Cell circulation which uplifts at the equator and transports towards the mid-latitudes.

Figure 6.27(b) shows the cross-section taken at 40°E which passes through the section of the anticyclone edge with the strongest northward winds (see Fig. 4.39). At this longitude the signal relating to the anticyclone and African eastward outflow features are well separated. The northward transport of C_2H_2 within the monsoon anticyclone is again apparent where significant enhancements are transported from 20°N to 30°N. Finally Figure 6.27(c) shows the cross-section taken at 75°E through the centre of the anticyclone as well as encountering the eastward outflow from Africa. Whilst a small signal is seen for the African outflow, the strong enhancement within the monsoon anticyclone region is clearly observed and again is shown to originate from the region of deep convection between 5°N to 20°N. In this region, it appears that again the enhanced C_2H_2 within the Asian monsoon anticyclone may penetrate the tropopause into the stratosphere.

Meridional cross-sections were also taken at 135°E, 160°E and 170°W in order to sample the Asian outflow into the Pacific and towards North America. Figure 6.28(a) show the cross-section taken at 135°E which passes through the western edge of the convective area over South-East Asia and samples the eastward transport from Asia into the Pacific. A strong enhancement is observed between 20°N and 40°N related to the outflow as well as possibly from local emissions over Japan. Figure 6.28(b) shows the cross-section at 160°E which dissects the long-range transport over the ocean and indicates a broadening of the transport plume between 20°N and 50°N. Finally Figure 6.28(c) shows the cross-section taken at 170°W, showing that the plume moves further northwards as it crosses the Pacific Ocean and extends from 25°N and 60°N although by this time the C_2H_2 VMR has decreased due its relatively short lifetime.

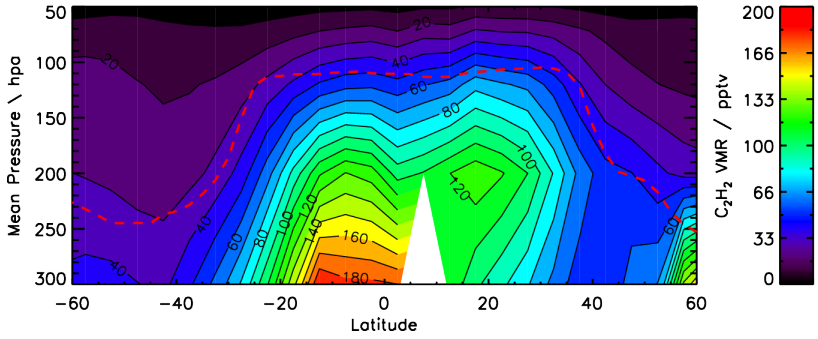

(a) 20°E

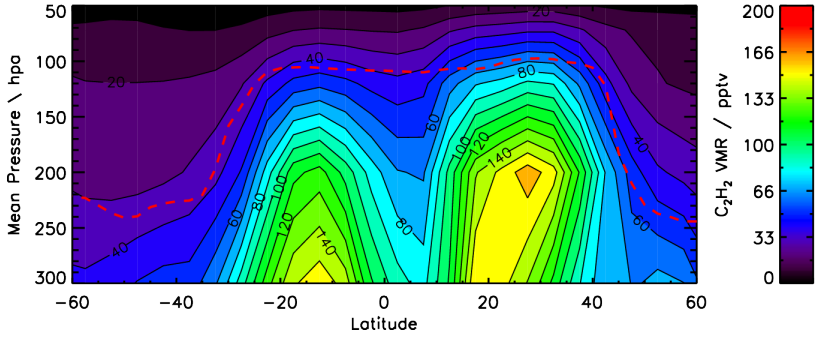

(b) 40°E

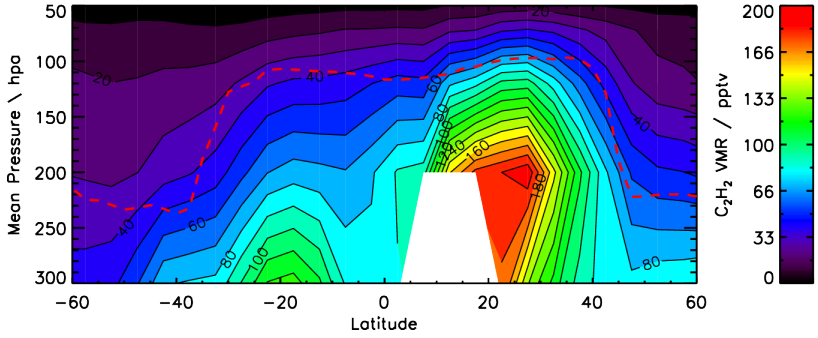

(c) 75°E

FIGURE 6.27. Meridional cross-sections of the retrieved C_2H_2 distribution along the 20°E, 40°E and 75°E longitude lines cutting vertically through the strong Asian monsoon anticyclone isolation.

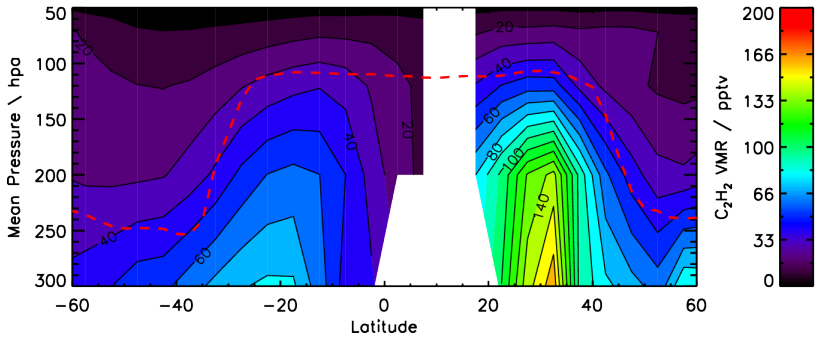

(a) 135°E

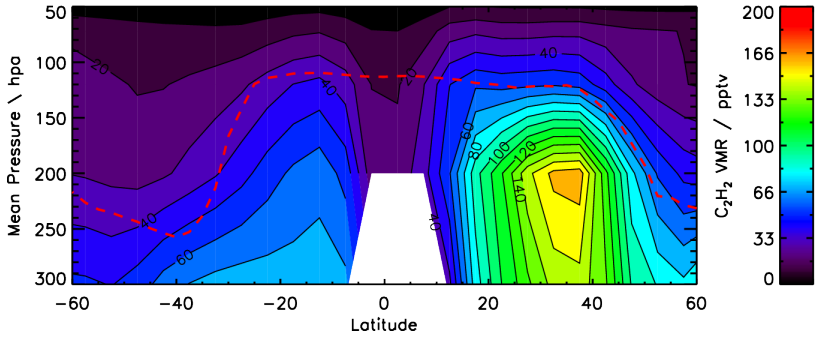

(b) 160°E

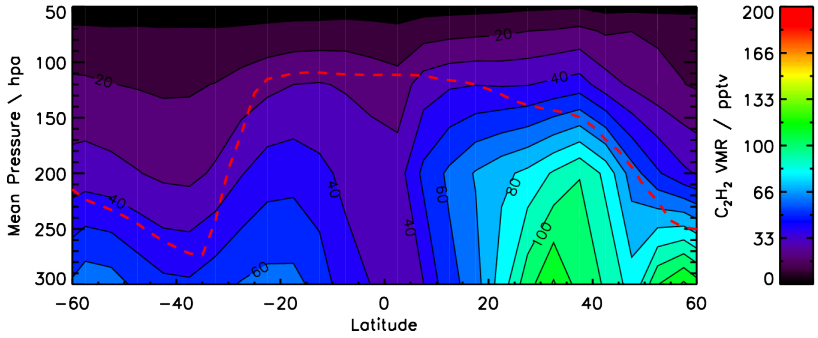

(c) 170°W

FIGURE 6.28. Meridional cross-sections of the retrieved C_2H_2 distribution along the 135°E, 160°E and 170°W longitude lines cutting vertically through the eastwards Asian outflow into the Pacific Ocean.

6.4.4 Evidence For Tropopause Penetration

The above section has briefly discussed the possibility of observing tropopause penetration from the C_2H_2 retrieval and found potential evidence. It is not surprising that such tropopause penetration is not clear as we are hoping to observe individual events by using a monthly average of the C_2H_2 distribution. It may be more appropriate to examine the individual retrieval values with no averaging applied.

Figure 6.29 shows the C_2H_2 vertical distribution taken for all of the data in the 15°N to 45°N latitude band for August 2003. This latitude range was taken so as to cover the Asian monsoon anticyclone region where we would expect strong convective activity and hence possibly tropopause overshooting, especially in South-East Asia. C_2H_2 is observed chemically isolated within the Asian monsoon anticyclone where it is lofted up to 100 hpa with possible enhancements of 80-90 pptv observed above the tropopause around 70-80 hpa. This result may tentatively suggest that we are observing some tropopause overshooting into the stratosphere.

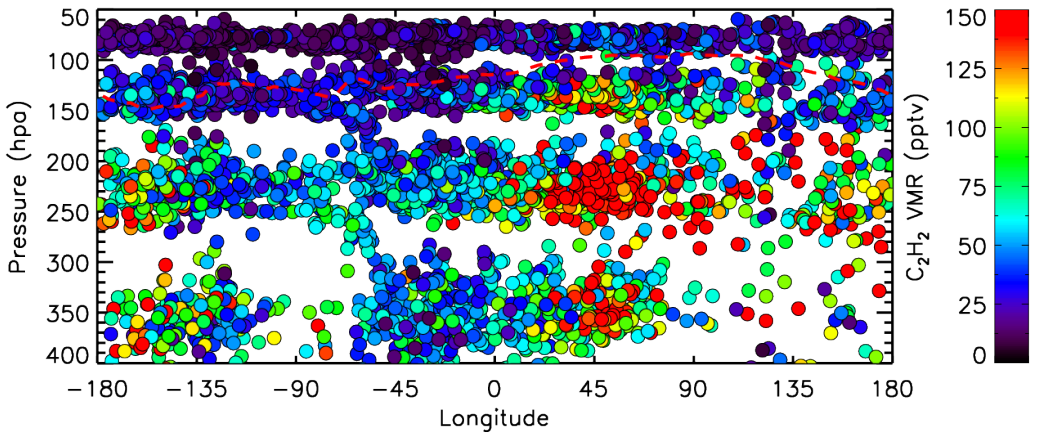

FIGURE 6.29. C_2H_2 vertical distribution for August 2003 in latitude band between 15°N and 45°N

In order to investigate this more full, Figure 6.29 is repeated below but only including measurements at pressure above the 150 hpa level (Fig. 6.30) and using a logarithmic scale. From this plot it is clearer than values do appear enhanced compared to the stratospheric background. These background values are typically below 25 pptv whilst values above the monsoon are typically closer to 50 pptv with a few values exceeding 80 pptv.

A similar plot for the biomass burning region in southern Africa is produced by taking the values between 30°S and 15°N where we might expect to see strong convection 6.48. Here, although the strong enhancement is observed up to 150 hpa, no obvious enhancement is observed in the stratosphere as it was for the anticyclone region. However, a few anomalous points do suggest an enhancement over the

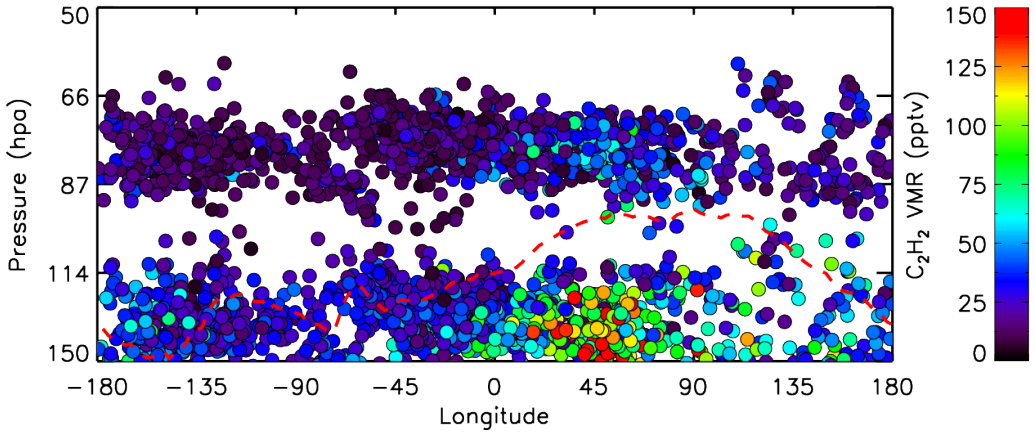

FIGURE 6.30. C_2H_2 vertical distribution for August 2003 in latitude band between 15°N and 45°N, with a logarithmic pressure scale highlighting the upper troposhere/lower stratosphere and showing only altitudes above 150 hpa.

tropopause 6.32 but as these are so limited in number it is more likely that they are related to poor retrievals of either the C_2H_2 or the pressure. Further investigation would be required to draw any conclusions from these few points.

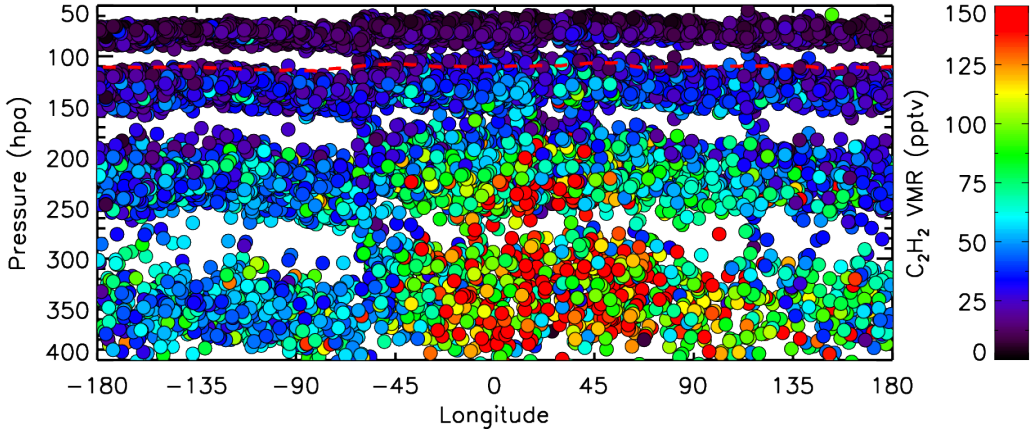

FIGURE 6.31. C_2H_2 vertical distribution for August 2003 in latitude band between 30°S and 15°N

This section has shown potential evidence for tropopause overshooting of C_2H_2 into the stratosphere above the Asian monsoon anticyclone. However, care must be take to ensure that these results are not an artifact of the retrieval and as

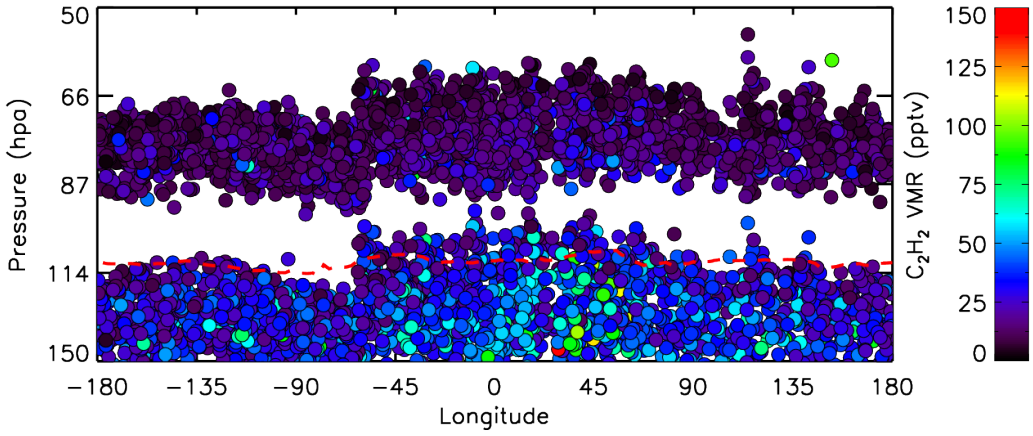

FIGURE 6.32. C_2H_2 vertical distribution for August 2003 in latitude band between 30°S and 15°N, with a logarithmic pressure scale highlighting the upper troposhere/lower stratosphere and showing only altitudes above 150 hpa.

such further investigation beyond the scope of this thesis is required. Ideally, in-situ aircraft measurements would be used to confirm that such an overshooting is present.

6.4.5 The Asian Monsoon Anticyclone

In order to further analyse the Asian monsoon anticyclone and the resulting chemical isolation of C_2H_2, the HYSPLIT trajectory model [Draxler and Rolph, 2003] was used to calculate a 10-day forward trajectory (Fig. 6.33). It can be seen that not only do the C_2H_2 VMRs in Figure 5.13 capture the general location of the anticyclone but the north/west boundaries of the monsoon anticyclone region are clearly defined by a sharp gradient in C_2H_2 VMR and the features are captured in considerable detail. The northern edge which is bounded by the Himalayas is captured well, as is the section that extends into Northern Africa.

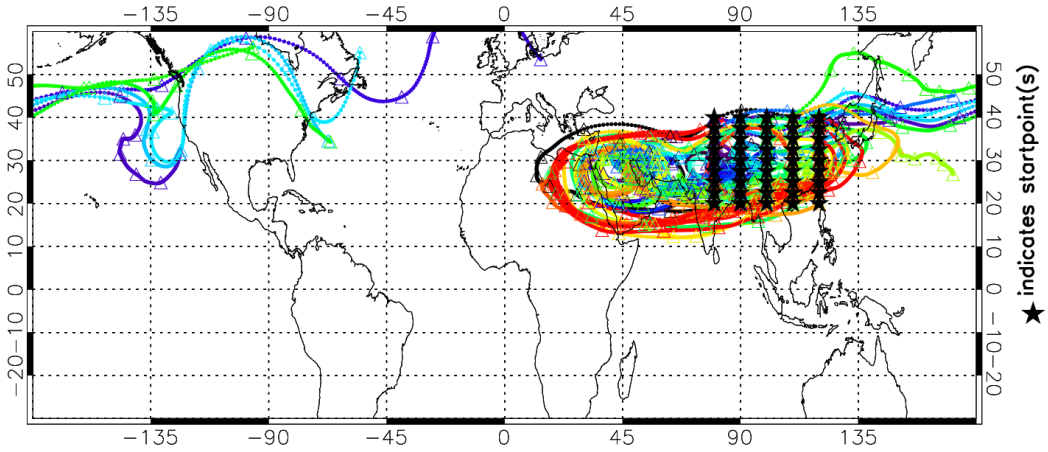

FIGURE 6.33. 10-day forward trajectory originating from Asia using the HYSPLIT model. The trajectory clearly shows the well-defined monsoon boundary, with the majority of trajectory paths isolated to within the anticyclone and the remainder identifying the Asian transport towards North America.

The ability to capture the monsoon boundary so well in satellite data provides valuable information on the extent of its influence. To examine this boundary further, Figure 6.34 shows C_2H_2 profiles taken across the western boundary of the monsoon at 32°N. The dramatic change in the C_2H_2 profiles across the monsoon boundary shows the strength of the chemical isolation inside the monsoon as previously identified by Park et al. [2008] but with much higher spatial and temporal resolution.

The vertical distribution of C_2H_2 was examined over the various regions of interest. It was found that the chemical isolation relating to the Asian monsoon anticyclone was captured extremely well by the C_2H_2 distribution and vertical profiles of the region show the sharp gradient in C_2H_2 which exists across the anticyclone boundary.

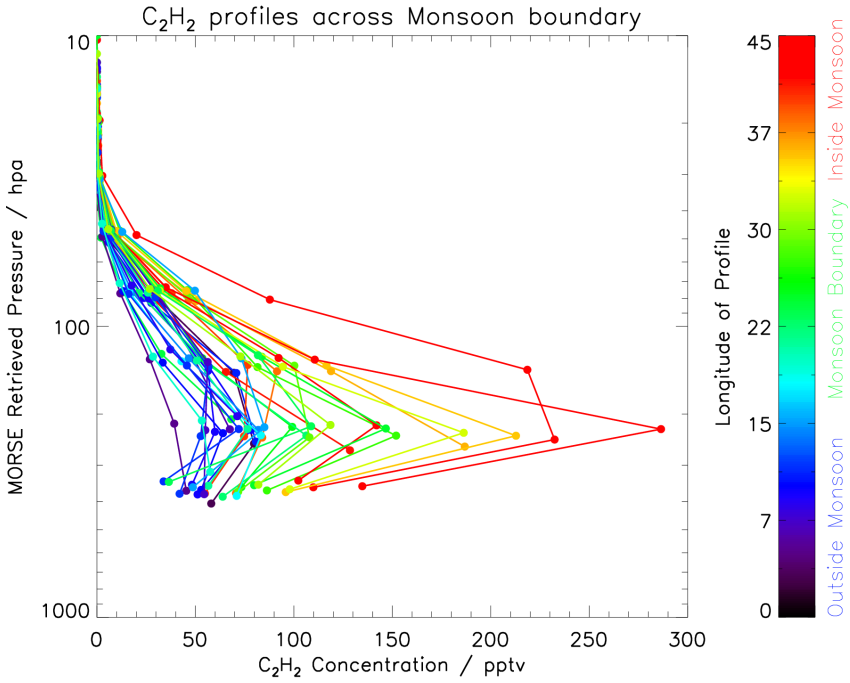

FIGURE 6.34. C_2H_2 retrieved profiles across the western monsoon boundary over Northern Africa at 32°N. Colours denote the longitude position of profile measurements, with red indicating profiles within the monsoon anticyclone, green on the monsoon boundary and blue outside of the monsoon. A sharp gradient in the C_2H_2 VMR across the monsoon anticyclone boundary is shown.

6.4.6 C_2H_6 Vertical Information

Although as discussed above, the C_2H_6 retrievals may require further work in order to improve their quality, Figure 6.35 shows the C_2H_6 distributions on the 9 km, 12 km, 15 km and 18 km MIPAS nominal tangent altitudes. The 9 km level (Fig. 6.35(a)), with a mean pressure of 311 hpa, shows a significant enhancement of C_2H_6 over the Siberian region which is located in the same area as intense biomass burning observed from AATSR. An enhancement was observed for C_2H_2 in this region although with a considerably lower intensity. These enhancements are not observed at higher altitudes due to the low height of the tropopause at these latitudes. In addition to this Siberian enhancement, other signatures of biomass burning are observed both over Africa and Central America. At higher altitudes (Fig. 6.35(b)) it is this Central American enhancement which appears stronger, with enhancements observed both over the Mexico City region as well as the north-western area of South America which we attribute to fossil fuel (natural gas) production in the region.

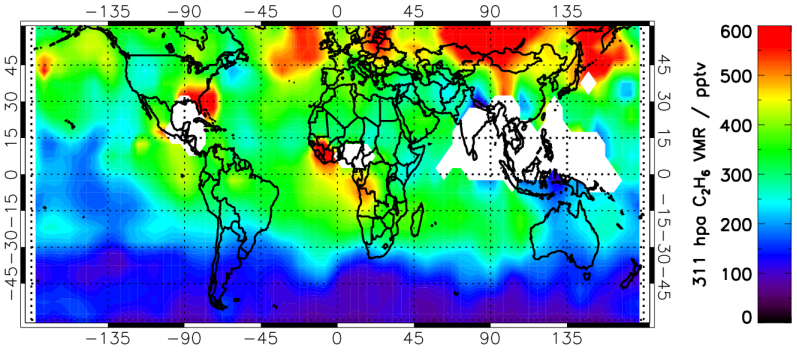

(a) 311 hpa (9 km nominal altitude)

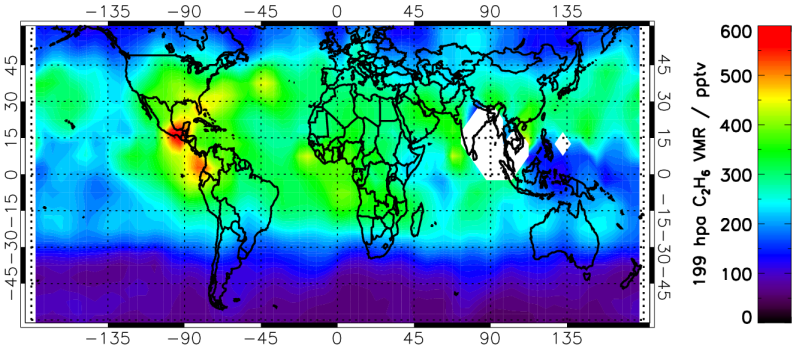

(b) 199 hpa (12 km nominal altitude)

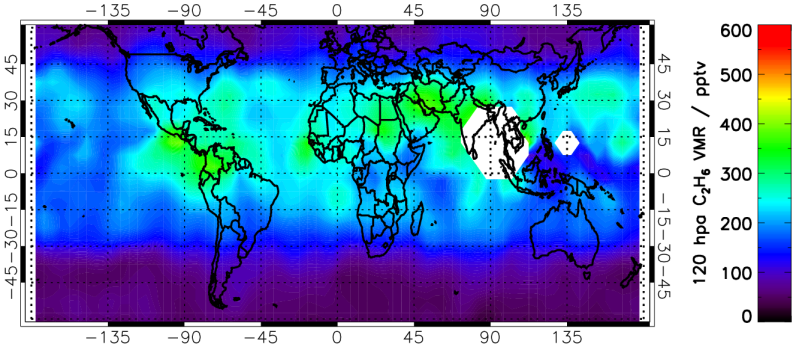

(c) 120 hpa (15 km nominal altitude)

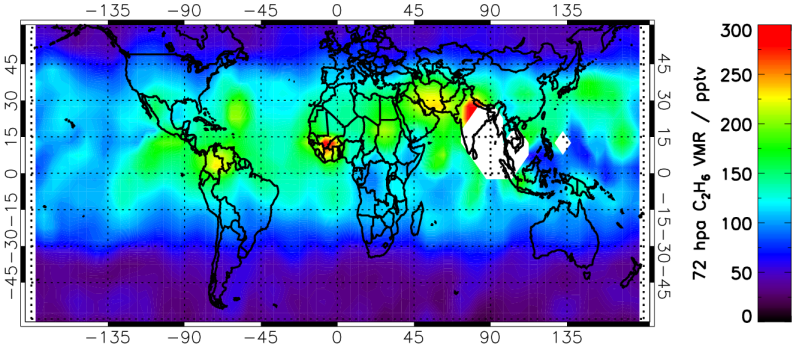

(d) 72 hpa (18 km nominal altitude)

FIGURE 6.35. The MORSE retrieved C_2H_6 distributions for August 2003 for the 9 km, 12 km, 15 km and 18 km nominal MIPAS tangent altitudes.

In order to investigate this further, the C_2H_6 cross-sections are compares to the corresponding cross-sections for C_2H_2. Figure 6.36 compared the cross-sections taken along the equator for both C_2H_6 (Fig. 6.36(a)) and C_2H_2 (Fig. 6.36(b)). It is immediately obvious that whilst both distributions contain the signature of the large African biomass burning, the C_2H_6 distribution also shows the large fossil fuel signature at 95°W which is not present in the C_2H_2 distribution. It can further be seen that this leads to a general enhancement of C_2H_6 over the Atlantic Ocean due to the longer lifetime and multiple sources of C_2H_6.

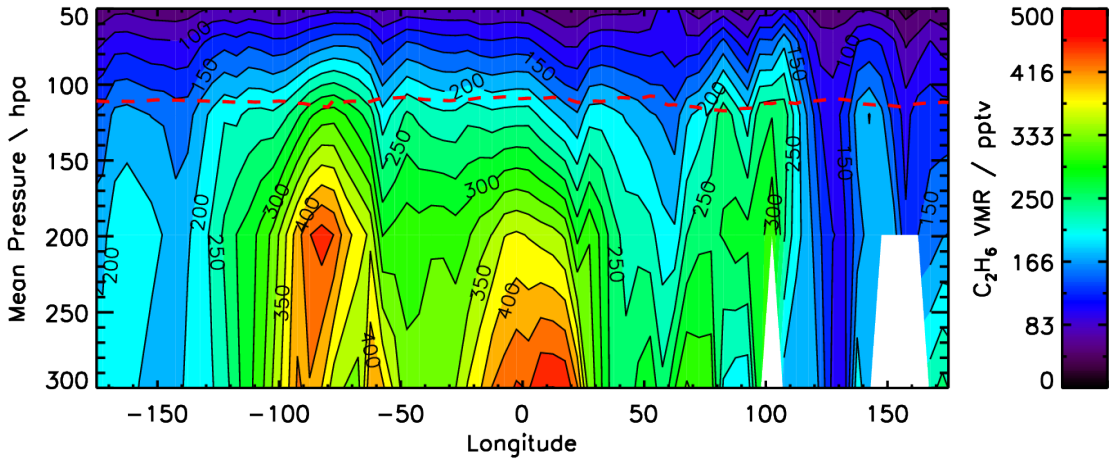

(a)

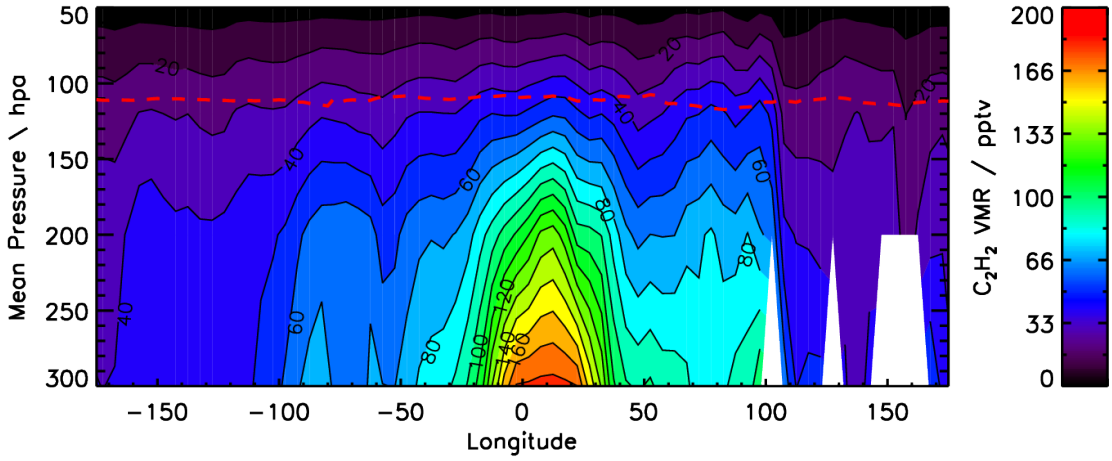

(b)

FIGURE 6.36. Cross-sections of C_2H_6 and C_2H_2 along the Equator showing both the similarity in biomass burning signatures between the two species over Africa as well as the distinctly different behaviour when sampling the C_2H_6 fossil fuel production over Central America.

By performing a similar comparison, but this time further south along 30°S (Fig. 6.37), the Central American fossil fuel enhancement is now largely excluded and very similar distributions exist for the biomass burning transport from Southern Africa towards Australia.

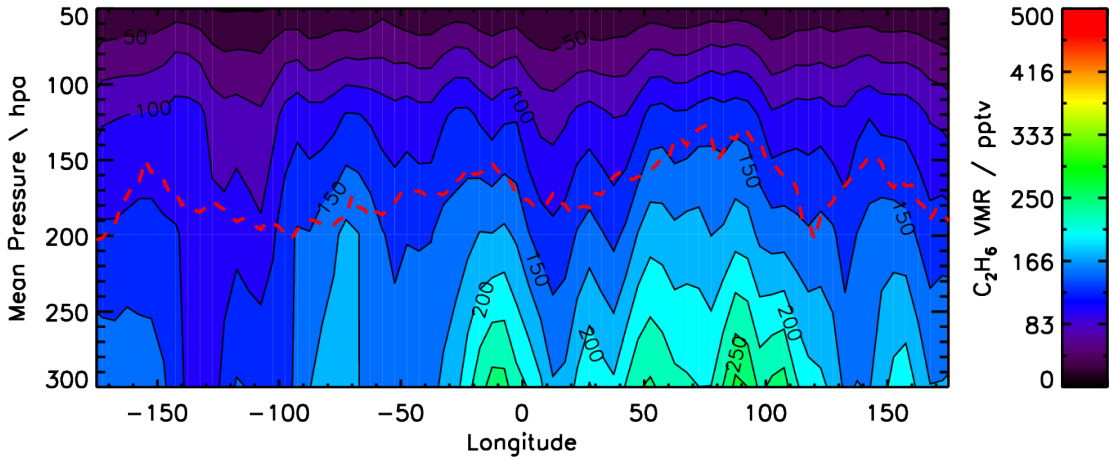

(a)

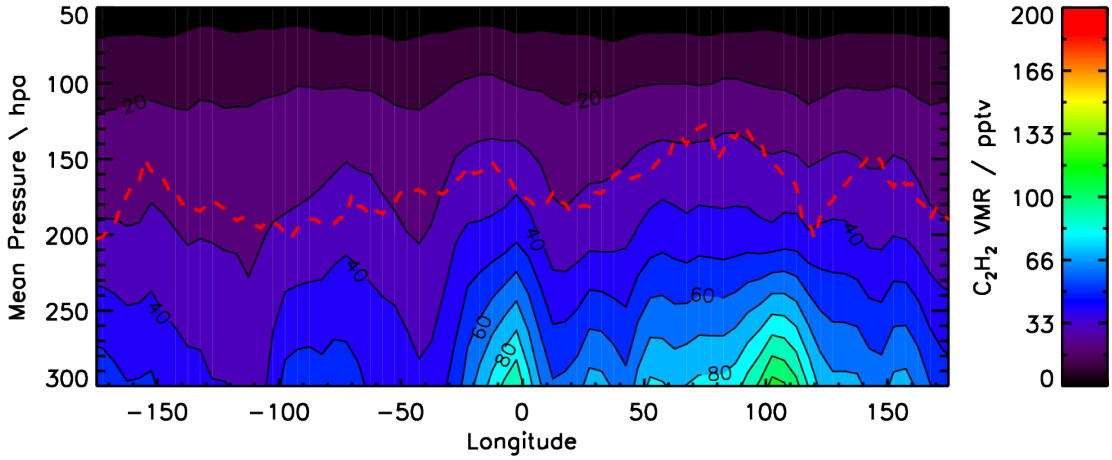

(b)

FIGURE 6.37. Cross-sections of C_2H_6 and C_2H_2 along 30°S showing the similarity in biomass burning signatures between the two species where the fossil fuel component of the C_2H_6 is not present.

Finally, by comparing the cross-sections taken meridionally down 20°W (Fig. 6.38) we can examine the latitudinal distribution of the gases off the western coast of Africa. Here we see qualitatively similar distributions with both an enhancement at northern latitudes as well as the Southern African biomass burning being transported northwards towards the equator. It is worth noting that in the C_2H_6

distribution the Hadley Cell circulation appears evident. The fact that it is not as clear for the C_2H_2 may be attributed to the much short lifetime of C_2H_2. Additionally, the C_2H_6 signature is relatively much more enhanced compared to the C_2H_2 which possibly suggests that we are observing a fairly aged plume where the C_2H_2 has had sufficient time to undergo photochemical reactions with its significantly shorter lifetime when compared to C_2H_6. A further explanation which needs exploring is that, as seen for Central America, natural gas production in the area is contributing as a significant source of C_2H_6 as explored in Section 6.6.1.

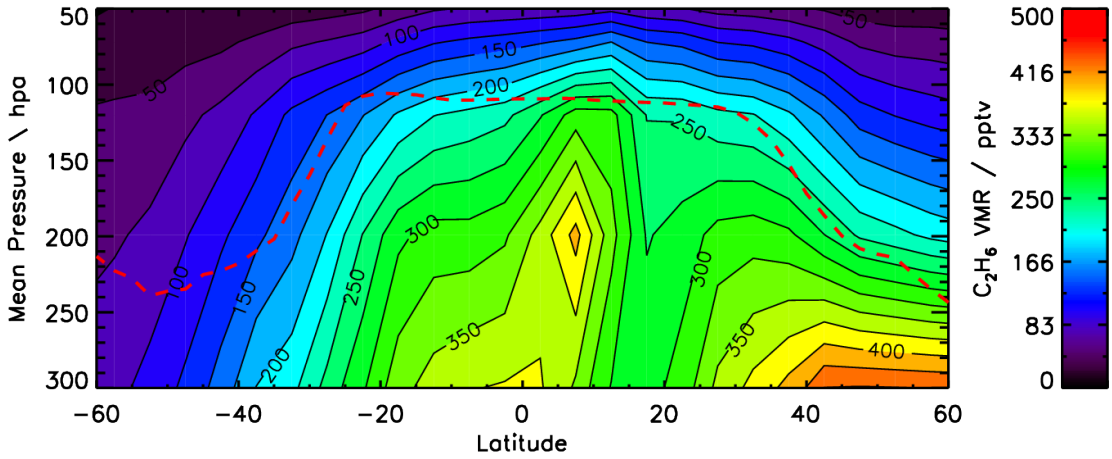

(a) C_2H_6 distribution

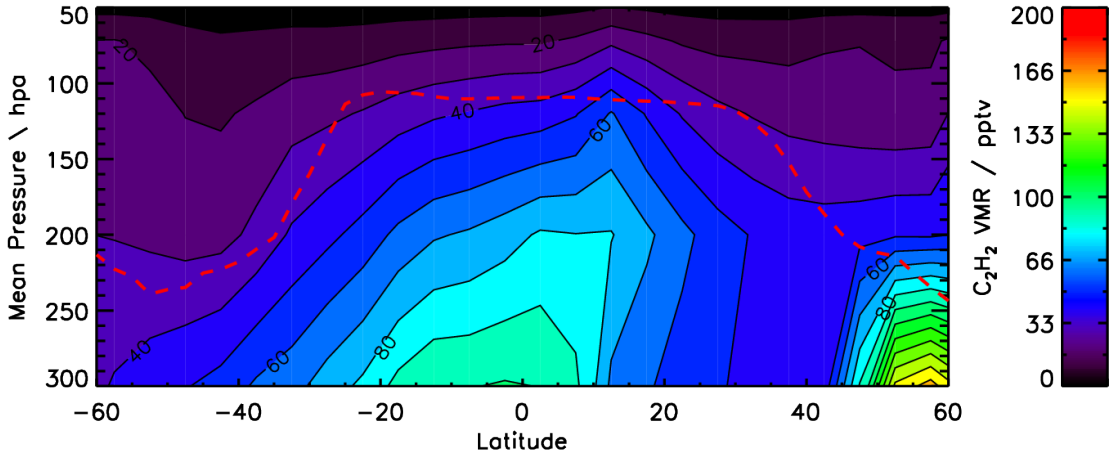

(b) C_2H_2 distribution

FIGURE 6.38. Meridional cross-sections of C_2H_6 and C_2H_2 along 20°W showing the relatively enhanced C_2H_6 as well as the large scale circulation of the Hadley Cell.

6.5 C_2H_2 - CO Ratio As Indicator Of Source Regions and Photochemical Age Of Air/Transport

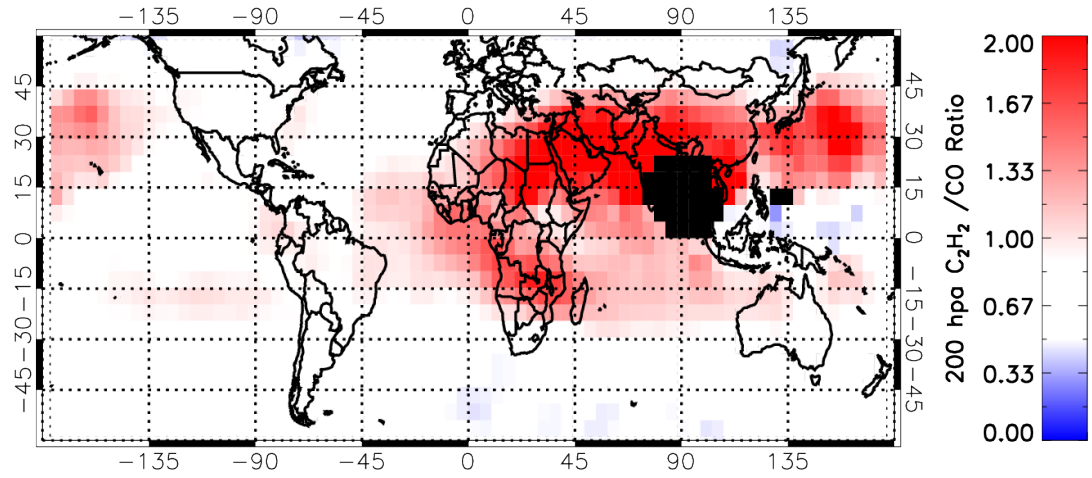

FIGURE 6.39. 200 hpa MORSE C_2H_2 / 150 hpa MOPITT CO ratio calculated from the 5°N globally gridded data (in units of $1x10^{-3}$). This ratio acts as an indicator of biomass burning sources and photochemical ageing of plumes and hence providing information on the relative speed of transport mechanisms. Features of note include the transport from African biomass into the Atlantic, transport from Asia into the Pacific and the isolation of the monsoon anticyclone. Note on this colour scale, regions where there is no data due to cloud coverage are indicated in black.

Having shown that the C_2H_2 and CO relationship maintains a strong correlation and remains preserved through the processes of convection and mixing as suggested by Smyth et al. [1996], the C_2H_2/CO ratio can be used to further analyse the transport dynamics from the combustion source regions. The gridded C_2H_2 and CO values (as shown in Figures 6.1) are used to calculate the C_2H_2/CO ratio (Fig. 6.39). The ratio is expected to be highest over source regions where C_2H_2 and CO are both produced from the combustion process and diminish with time as the age of air increases with atmospheric processing. Due to the difference in lifetimes of C_2H_2 (approximately 2 weeks) and CO (approximately 2 months) [Xiao et al., 2007], for a high C_2H_2/CO ratio to exist, the C_2H_2 must be relatively young. Hence, if a high C_2H_2/CO ratio is observed (i.e. greater than $2x10^{-3}$) then either the observation is over a region where combustion is taking place or the observed plume has been transported from such a source region in a relatively short space of time.

It is therefore possible to identify two clear transport mechanisms from the C_2H_2/CO ratio in Figure 6.39. The high ratio located over Southern Africa can be

seen to decrease as the plume travels north-west out into the Atlantic Ocean. This would suggest a relatively slow transport mechanism where the plume has had time to undergo a significant amount of atmospheric processing. In contrast, the second obvious pathway is from Asia out into the Pacific Ocean is related to the tongue of the Asian Monsoon anticyclone that extends out over the Pacific (as discussed in Section 4.2.4). This process is known to transport air relatively quickly and this is confirmed by the fact that a high C_2H_2/CO ratio is maintained out over the ocean where there are no source regions present.

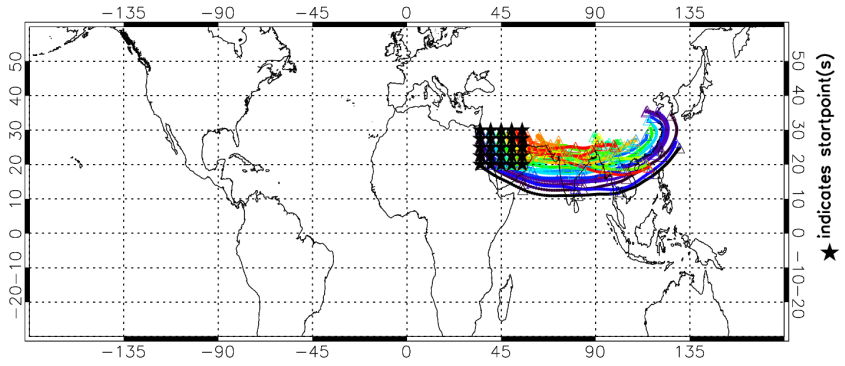

FIGURE 6.40. HYSPLIT 5-day back-trajectory showing the Easterly Jet transport from Asia into the Middle East. This fast transport of C_2H_2 and CO is observed in the C_2H_2/CO in Figure 6.39.

The fact that the C_2H_2/CO ratio agrees so closely with the known transport mechanisms in these regions provides substantial confidence in the approach taken. Furthermore, it allows the Easterly Jet transport from Asia into the Middle East to be discussed in the context of the C_2H_2/CO ratio. The high C_2H_2/CO ratio extends over the whole of the region between Asia and the Middle East and again clearly shows the strong chemical isolation of the monsoon. As this region is entirely over land some care must be taken to distinguish between a maintained high ratio due to fast transport or the alternative that the ratio remains high due to there being various combustion sources distributed over the whole region. There is no CO enhancement in the MOPITT surface data in this region. Along with this, the fact that a clear gradient exists in the distribution of the high C_2H_2 and CO values (Fig.6.1) between the Middle East and Northern Africa provides confidence that it is the Easterly Jet transport that is being observed. The anticyclone continues to transport newly formed C_2H_2 and CO into the region from its biomass and biofuel sources in Asia, leaving no time for substantial photochemical processing to occur before it is circulated back towards the source region. It is this circulation due to the monsoon anticyclone which causes the persistence of the high C_2H_2/CO which is observed. In order to verify this further and show that the source of the observed high VMR of C_2H_2 was from South-East Asia, a 5-day back-trajectory calculation using the HYSPLIT model was performed. Figure 6.40 shows the calculated back-

trajectory and agrees that the transport into the Middle-East was from South-East Asia, passing over Northern India as deduced from the C_2H_2/CO ratio.

In order to analyse the C_2H_2, C_2H_6 and CO relationships in more detail, in particular the C_2H_2/CO ratio, in the follow section we have identified three regions of long-range transport as well as a further two regions of interest over which the relationships will be examined.

The pathways are shown below in Figure 6.41, overlaid on top of the 200 hpa C_2H_2 distribution from Figure 6.1(a).

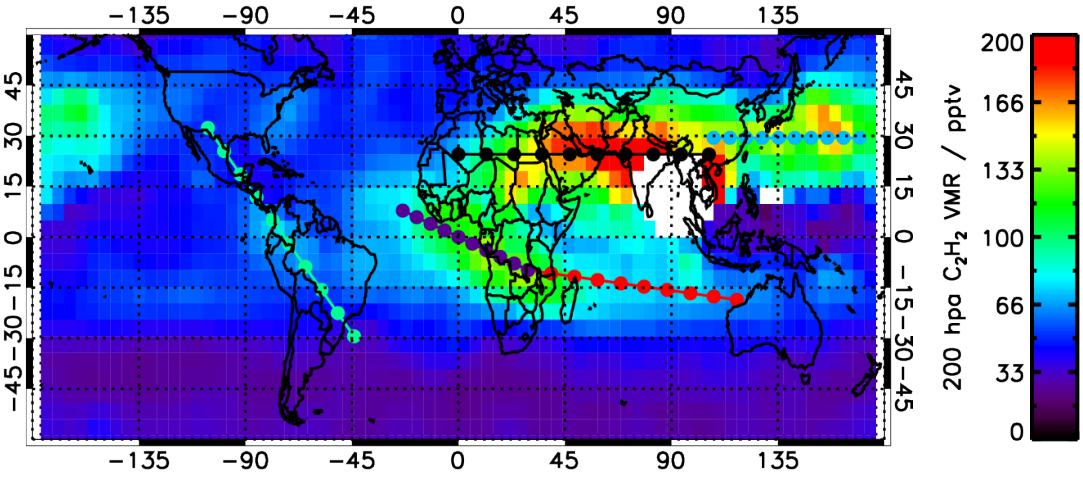

FIGURE 6.41. Selected pathways overlaid onto the C_2H_2 distribution from Figure 6.1(a) showing the various regions of interest and observed transport pathways which will be analysed in the following section.

The pathways over which this analysis is performed are:

- Transport Pathway Between Southern Africa and Australia (red)
- Transport Pathway Between Southern Africa and Atlantic Ocean (purple)
- Transport Pathway Between Asia and North America (blue)
- Region of Interest Over Mexico (green)
- Region of Interest Over Asian Monsoon Anticyclone (black)

6.5.1 Transport Pathway Between Southern Africa And Australia

The first pathway considered is that from Southern Africa, eastwards towards Australia. The C_2H_2 and C_2H_6 show similar patterns for this path as they both decrease

quickly as the path reaches the ocean and remain relatively constant throughout the remainder of the path. Interestingly we see a small increase in the C_2H_6 to the south of the deep convective region in the Indian Ocean, suggesting some transport from that region. The CO remains relatively constant all along the pathway, indicative of its longer lifetime.

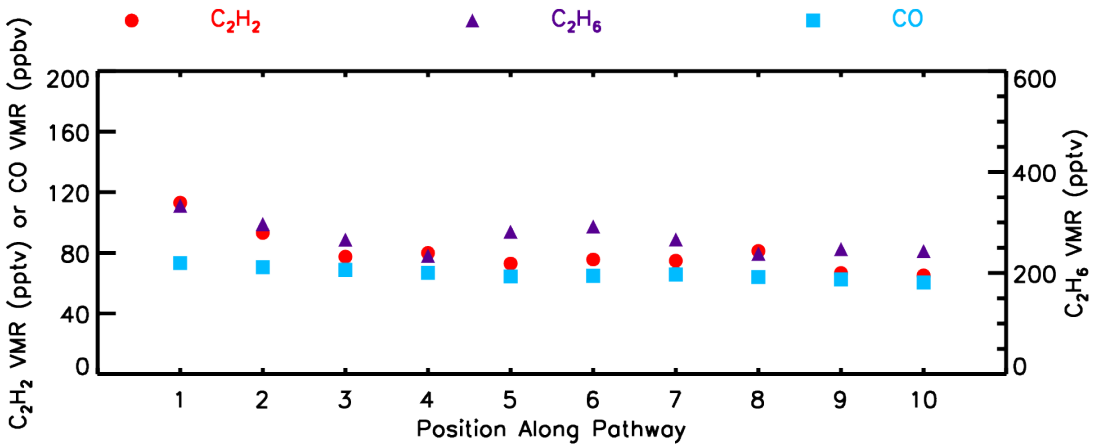

(a)

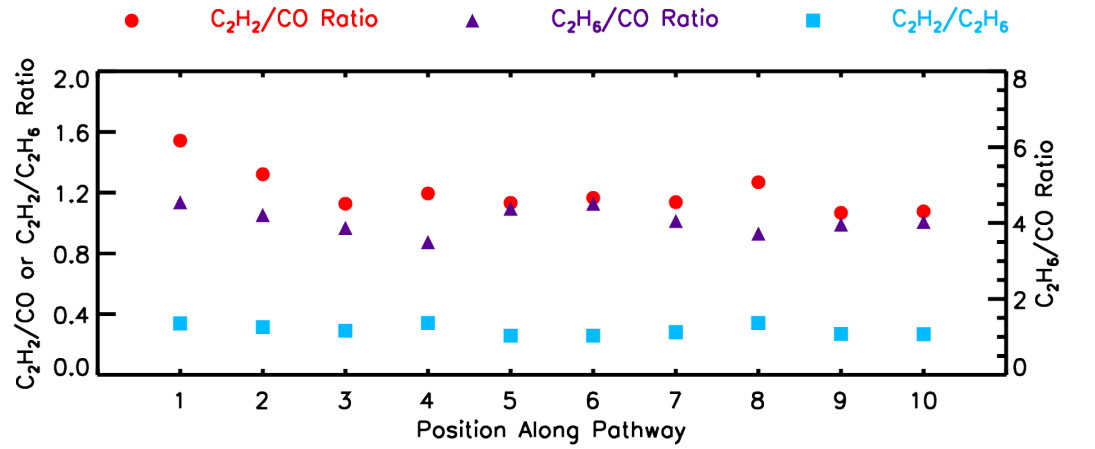

(b)

FIGURE 6.42. Pathway from Southern Africa, eastwards towards Australia.

When considering the ratio between the species, in this case as the CO is relatively constant, the ratio of both C_2H_2 and C_2H_6 to CO exhibit similar behaviour. The C_2H_2/CO ratio decreases steadily from 1.6 over Africa down to 1.2 by the time the air mass had reached Australia, suggesting that we are seeing the effect of air mass ageing, although this should only be considered as a qualitative indication [Xiao et al., 2007]. In order to quantify these effects, further work would include

the use of simulations with chemical transport models. Also note that C_2H_2 and C_2H_6 are in units of pptv whilst CO is in units of ppbv and hence that there is a factor of 1E-3 in the ratios which has been omitted for simplicity.

Finally the C_2H_2/C_2H_6 ratio remains relatively flat, as would be expected due to both species behaving similarly apart from the discrepancy over the Indian Ocean due to enhanced C_2H_6.

6.5.2 Transport Pathway Between South Africa And Atlantic Ocean

The second pathway considered is from Southern Africa but this time moving westwards into the Atlantic Ocean (Fig. 6.43. Again the C_2H_2 and C_2H_6 show very similar behaviour until near the end of the pathway (position 9) located off the west coast of Africa where the C_2H_6 becomes relatively more enhanced.

Again, the C_2H_2/CO ratio begins over Africa with a value of 1.6 and decreases to 1.2 although this time rather than the steady decrease, we see the ratio maintain a relatively high value of around 1.6 for the majority of the pathway before dropping off rapidly down to 1.2 as the measurements take place over the ocean. This suggests that either the plume is moving relatively quickly whilst over land and slows down as it reaches the ocean or that the C_2H_2 is being maintained by various smaller biomass burning sources until it reaches the ocean where no sources are then present. The C_2H_2/CO and C_2H_6/CO behave similarly up until this point when the C_2H_6 becomes more enhanced, potentially due to non-biomass burning sources such as natural gas production.

6.5.3 Transport Pathway Between Asia And North America

The final obvious transport pathway is that from Asia eastwards towards North America (Fig. 6.44). Again, very similar behaviour is observed in the C_2H_2 and C_2H_6 for the majority of the pathway until positions 7-9 where this time the C_2H_2 becomes enhanced. As discussed earlier, this enhancement observed over the Pacific is related to the tongue of the Asian monsoon anticyclone which extends out over the Pacific. This results in the C_2H_2/CO ratio again starting ar around 1.6 but this time increasing to 2.3 as it reaches the boundary of the Asian monsoon anticyclone where it then quickly decreases down to 1.5 once outside the anticyclone circulation. Both the C_2H_6 and CO show a much flatter distribution as neither exhibit as strong a chemical isolation within the anticyclone.

6.5.4 Region of Interest Over Mexico

Rather than an obvious transport path, the next region analysed is the one passing over Central America where a strong enhancement of C_2H_6 is observed (Fig. 6.45).

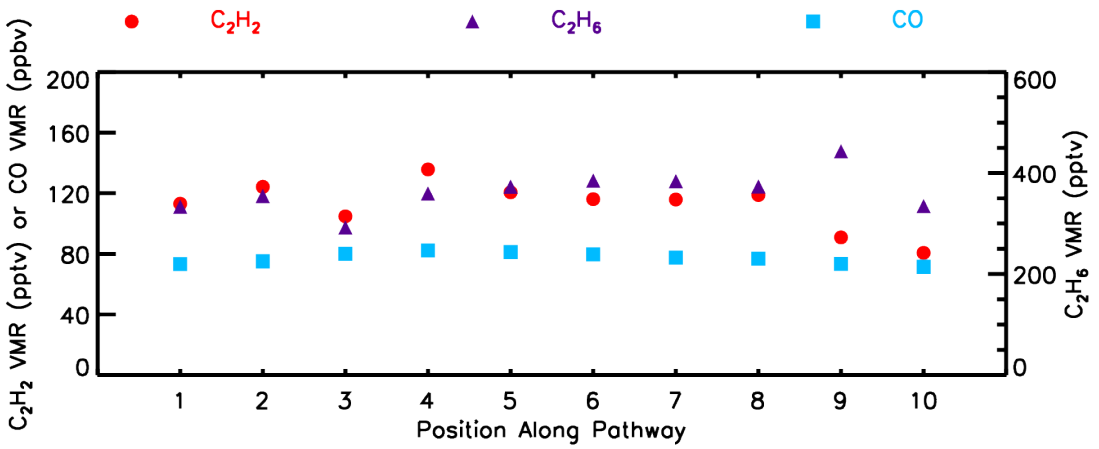

(a)

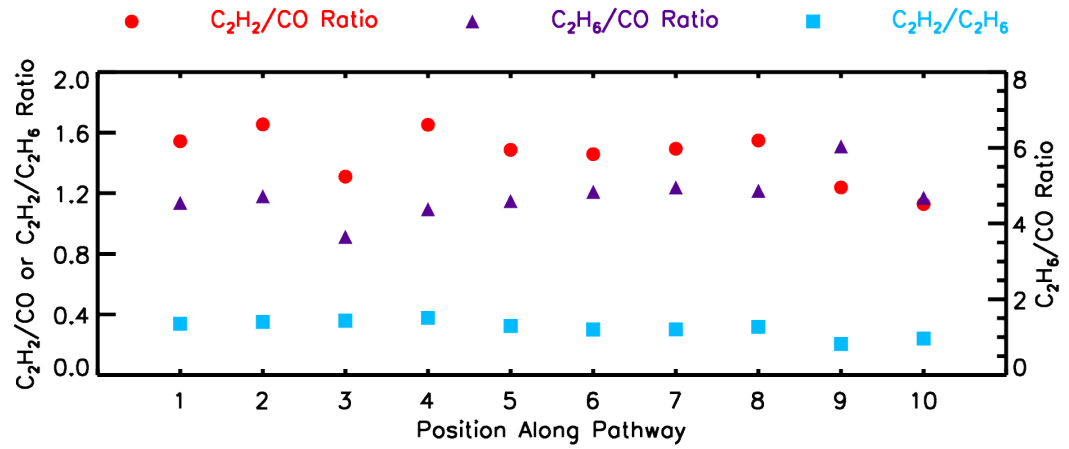

(b)

FIGURE 6.43. Pathway from Southern Africa, westwards into Atlantic Ocean.

Whilst the C_2H_2 and CO show similar behaviour, increasing as it reaches Mexico and then decreasing again, the C_2H_6 shows two distinct peaks reaching 500 pptv associated with the enhancements over Colombia and Mexico, much higher than observed elsewhere.

In contrast to the previous regions, the C_2H_2/CO begins at around 0.6 and only reaches a maximum of 1 before decreasing back to 0.6, suggesting that no significant biomass burning sources are sampled through this region. Therefore, as the C_2H_6 is extremely enhanced here, the C_2H_2/C_2H_6 ratio becomes lower, acting as an indicator for C_2H_6 emissions from fossil fuel production as opposed to biomass burning.

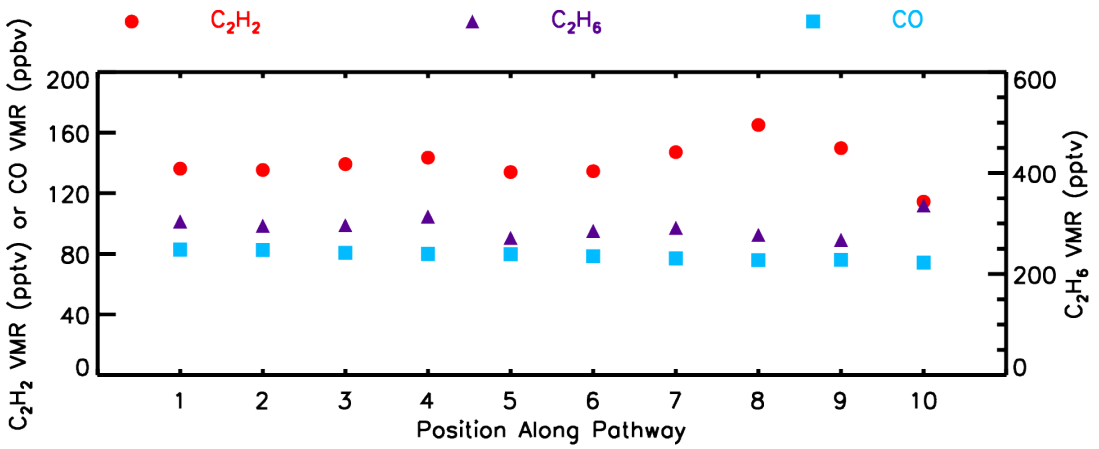

(a)

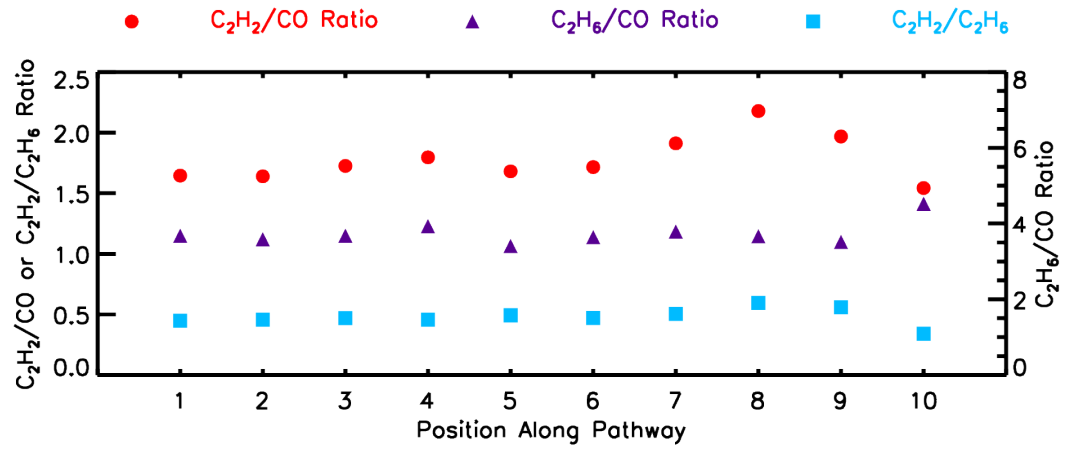

(b)

FIGURE 6.44. Pathway from Asia, eastwards towards North America.

6.5.5 Region of Interest Over Asian Monsoon Anticyclone

Finally, we examine the behaviour over the Asian monsoon anticyclone region (Fig. 6.46). Whilst the C_2H_6 and CO are moderately enhanced over this region, the C_2H_2 shows a much larger increase, indicative of the chemical isolation observed above. This is reflected in the C_2H_2/CO ratio which is enhanced to 2.5 over this region, much higher than previously observed elsewhere. Similarly the C_2H_2/C_2H_6 ratio is much more enhanced over this region with a value peaking at over 0.7, suggesting that it is the strong biomass burning in South-East Asia which maintains the high concentration of C_2H_2 within the anticyclone.

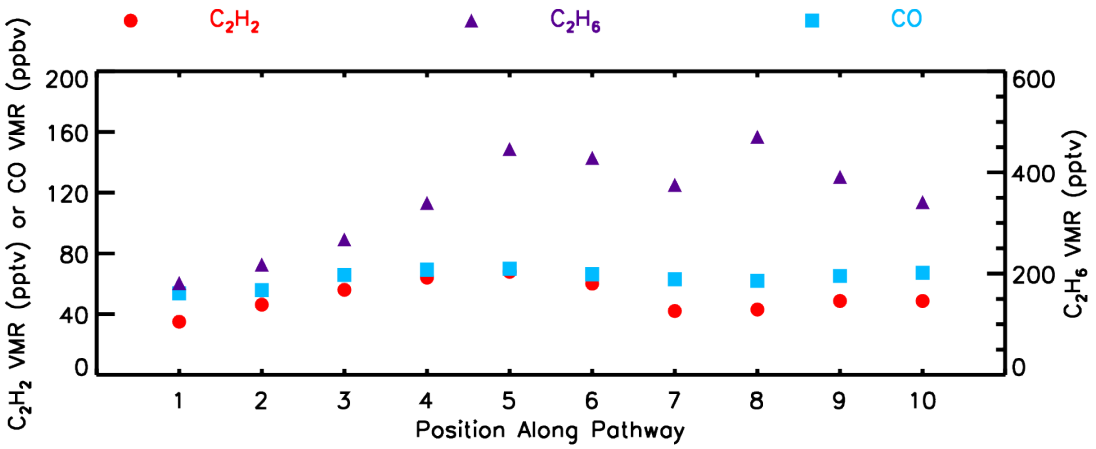

(a)

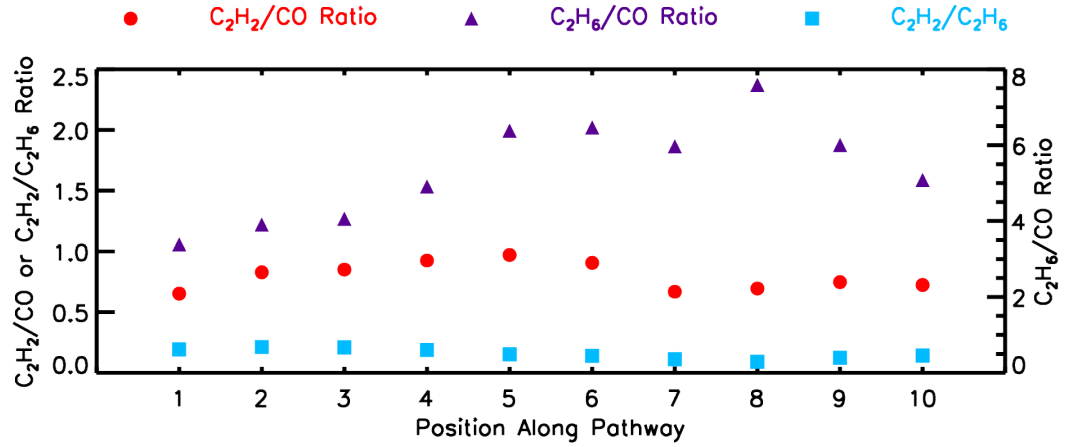

(b)

FIGURE 6.45. Pathway from South America to North America, passing over Mexico.

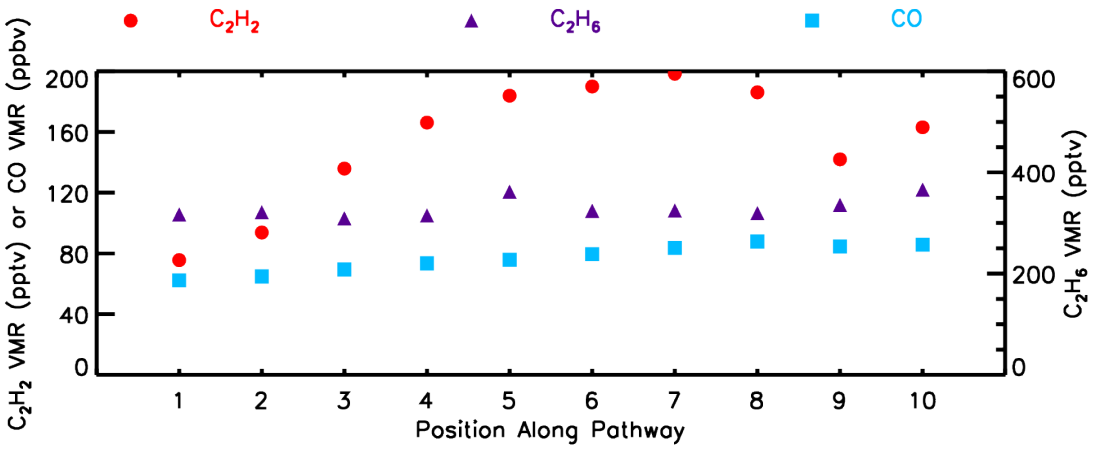

(a)

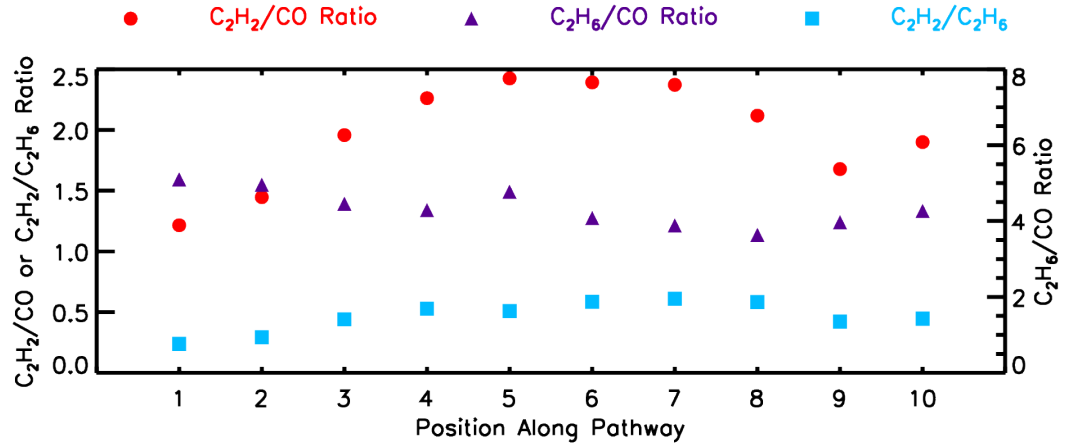

(b)

FIGURE 6.46. Pathway passing eastwards through the Asian Monsoon Anticyclone

6.6 C_2H_2/C_2H_6 Ratio To Differentiate Fossil Fuel And Biomass Burning Sources

Despite being used above as an indicator for biomass burning activity, the largest source of C_2H_6 is still related to fossil fuels, specifically the production of natural gas Xiao et al. [2008]. Using the same approach as described above, the C_2H_6/CO ratio was calculated for August 2003 (Fig. 6.47). Rather than highlighting the biomass burning enhancements as the C_2H_2/CO ratio did, in this case there is a large signature located over Central America and which we attribute to natural gas production (see Chapter 1 for a discussion of C_2H_6 emissions from fossil fuel production).

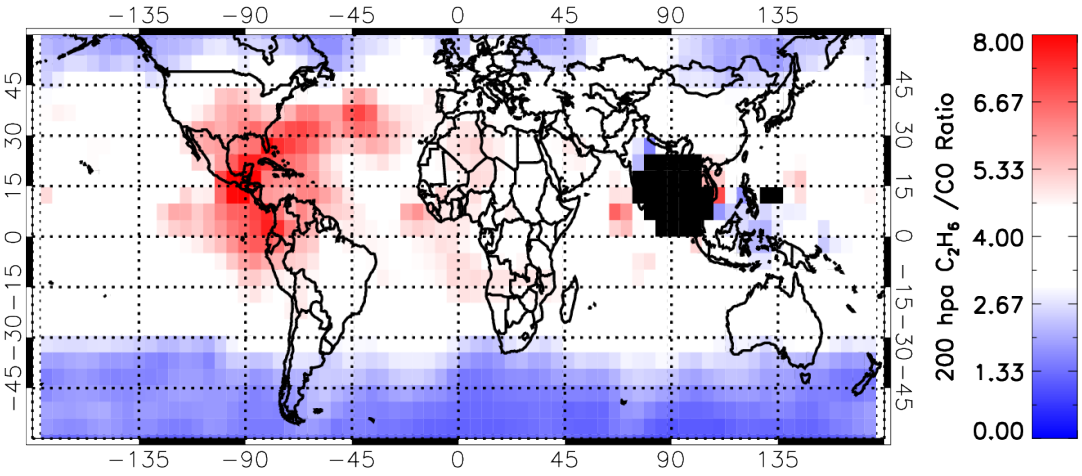

FIGURE 6.47. 200 hpa MORSE C_2H_6 / 150 hpa MOPITT CO ratio calculated from the 5°N globally gridded data (in units of $1x10^{-3}$).

As the C_2H_6 signature is predominantly related to natural gas production Xiao et al. [2008] (albeit with a component from biomass burning) and C_2H_2 is largely an indicator of biomass burning, it is expected that the ratio between the two could potentially be used to differentiate between fossil fuel and biomass burning sources. Figure 6.48 shows the ratio between the 200 hpa MORSE C_2H_2 / 200 hpa MORSE C_2H_6. The high ratio (red) is indicative of considerably higher C_2H_2 than C_2H_6, suggesting a signature of fresh biomass burning. A low ratio (blue) indicates that C_2H_6 is present without C_2H_2 and hence suggests that an observed source is not biomass burning related but rather is a signature of natural gas production.

The enhancement of C_2H_6 from fossil fuel production is consistent with recent work by Glatthor et al. [2009] who note a similar enhancement in their own C_2H_6 retrievals for October 2003.

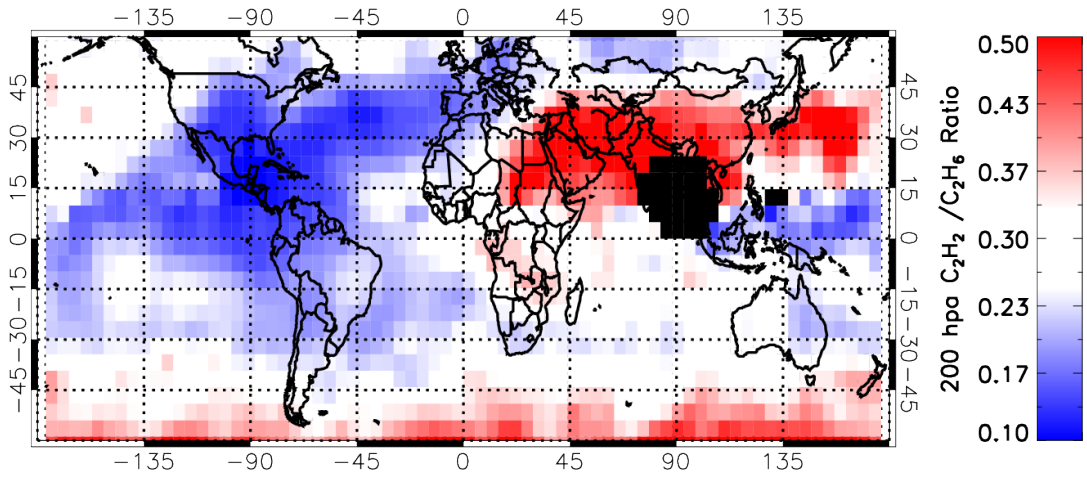

FIGURE 6.48. 200 hpa MORSE C_2H_2 / 200 hpa MORSE C_2H_6 ratio calculated from the 5°N globally gridded data). High values of this ratio (red) indicate that the source is likely related to biomass burning, whilst low values (blue) indicate that substantially more C_2H_6 than C_2H_2 is present. This means that either the source is likely related to the major primary source of C_2H_6, natural gas production or that the air is relatively photochemically aged and hence contains less C_2H_2.

6.6.1 C_2H_6 Fossil Fuel Enhancement In Central America

Whilst the above has shown the potential of using a C_2H_2/C_2H_6 ratio to differentiate between biomass burning and fossil fuel production, an attempt to verify that this large signature observed over Central America is indeed related to natural gas production would provide some confidence in the technique.

Figure 6.49 shows the retrieved 200 hpa C_2H_6 distribution over Central America with a particularly large enhancement observed over Southern Mexico as well as a smaller enhancement off the coast of Colombia.

In order to determine whether such natural gas production is occurring in this region we obtained information on the natural gas infrastructure in Mexico taken from the The Baker Institute Energy Forum (Fig. 6.50). This figure shows the location of the natural gas processing centres as being on the Mexican coast, in the same location as where we observe both enhanced C_2H_6 as well as convective activity to allow the vertical transport giving encouragement that it is indeed the C_2H_6 signature from industrial natural gas production that we are observing.

By examining the vertical structure of this enhancement over Central America we can further explore the likely source region. Figure 6.51 shows a cross-section taken along 15°N which passes through the enhancement. Here we can see that the enhancement is present at each altitude between 300 hpa and 100 hpa and is isolated

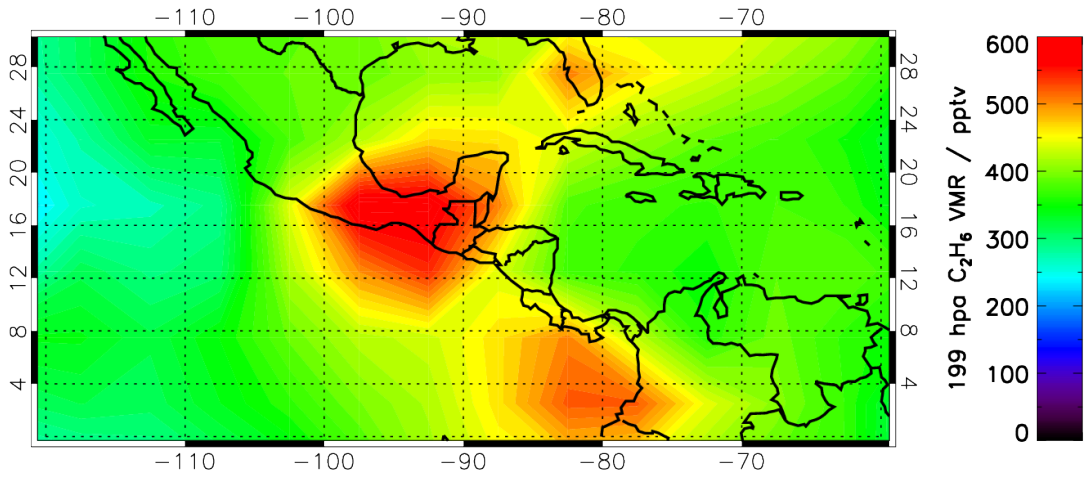

FIGURE 6.49. MORSE 200 hpa C_2H_6 over Central America

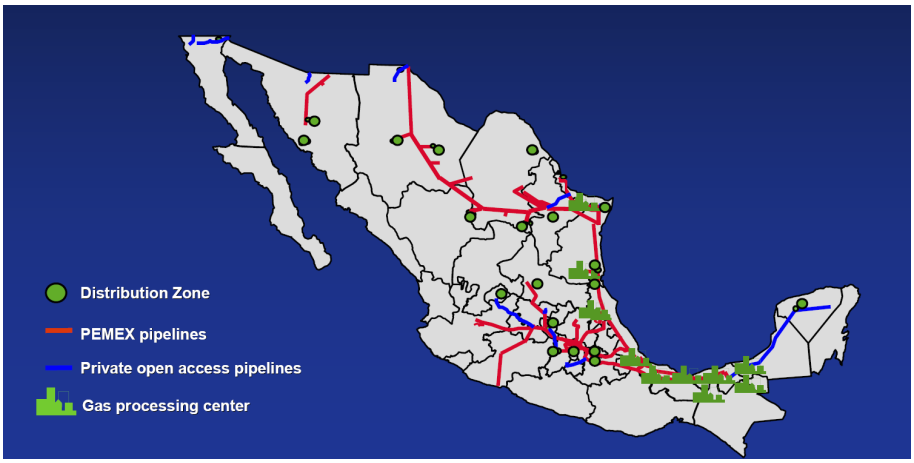

FIGURE 6.50. Natural Gas Infrastructure in Mexico taken from The Baker Institute Energy Forum - "Natural Gas in Mexico Current trends and alternate scenarios". Source http://www.rice.edu/energy/

to a relatively confined location at about 95°W and appears to be associated with a convective region (hence the lack of data due to clouds).

Examining a cross-section taken along the 95°W direction (Fig. 6.52), we see that the enhancement again appears to be directly over a convective region. In order to investigate this further, the OLR (Fig. 6.53) is again used to indicate regions of convection.

When compared to the OLR data for August 2003, we see that this is considerably convection in this region, suggesting that any industrial natural gas production

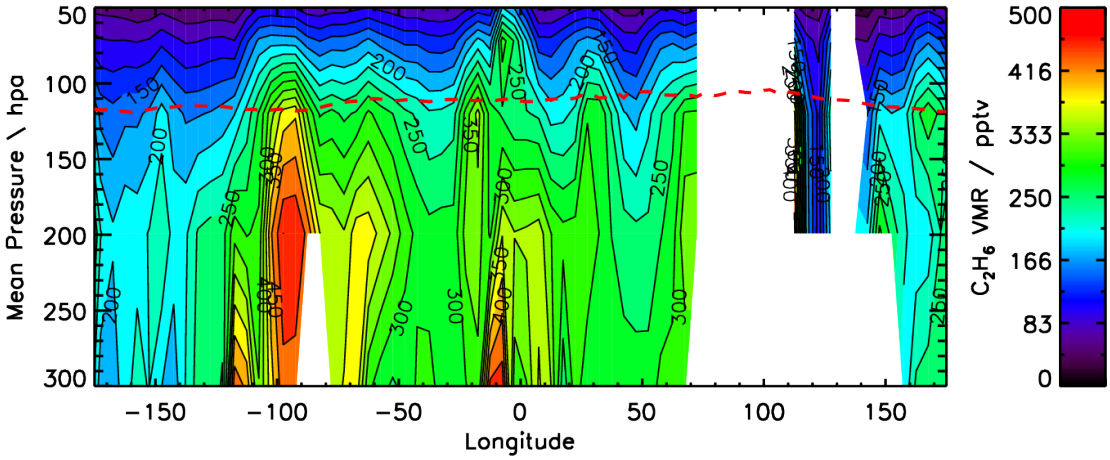

FIGURE 6.51. Cross-section along 15°N passing through the enhanced C_2H_6 observed over Central America showing the vertical extent of the C_2H_6 enhancement observed at around 95°W.

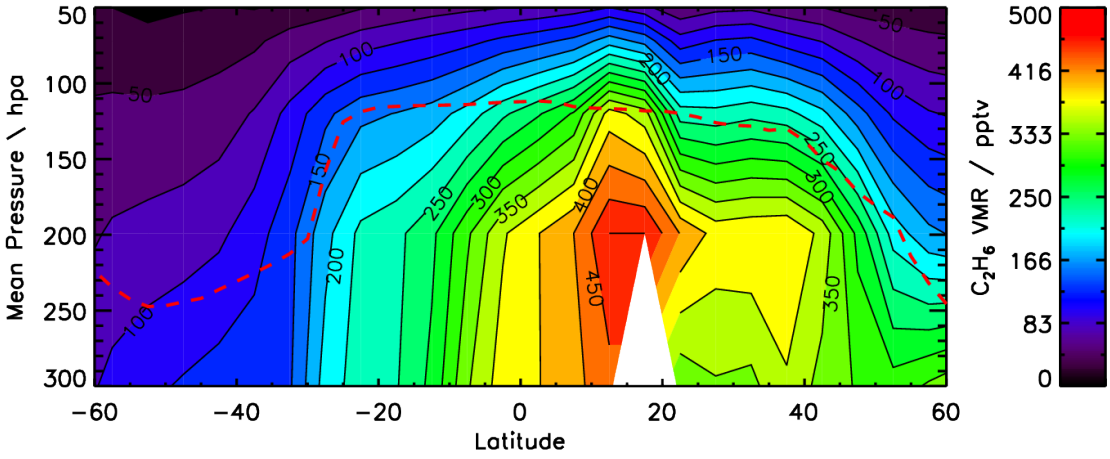

FIGURE 6.52. Cross-section along 95°W passing through the enhanced C_2H_6 observed over Central America.

at the surface would have a mechanism to be uplifted into the MIPAS field of view at around 12 km.

This section has shown that it is possible to use the C_2H_2/C_2H_6 ratio to not only gain some information on the biomass burning source regions but also on the C_2H_6 enhancements related to natural gas production. The large C_2H_6 enhancement over Central America has been examined and appears to correspond to the large amount of natural gas processing which occurs in Mexico and whose uplift into the MIPAS

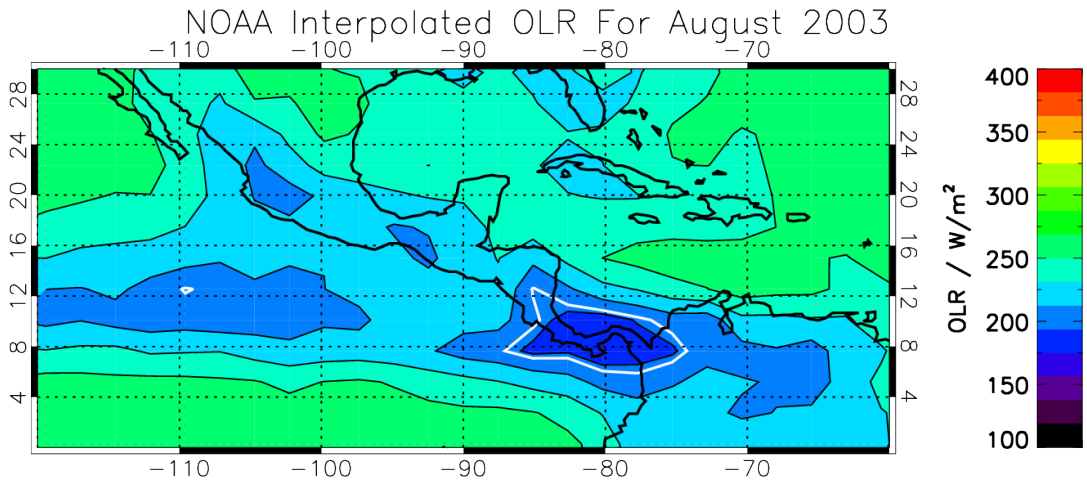

FIGURE 6.53. OLR over Central America showing that convection is present in this region and could potentially allow any C_2H_6 emitted at the surface to be uplifted into the MIPAS field of view.

field of view can be account for due to convective activity in the region.

6.7 Summary

To summarise, this chapter has examined the zonal and meridional distributions of the retrieved C_2H_2 in detail. In particular, cross-sections taken through features such as the Asian monsoon anticyclone, African biomass burning and Asian-Pacific transport have provided information relating to the vertical behaviour of the various features. Of particular note was the result from Figure 6.25 which not only showed the C_2H_2 quite clearly isolated by the monsoon anticyclone but also indicated uplift of C_2H_2 over the convective region at the edge of the anticyclone.

By examining cross-sections of the C_2H_2 distribution, the vertical structure and potential evidence for tropopause penetration of C_2H_2 was provided. Here, preliminary findings suggest that we are potentially observing an increase in C_2H_2 in the stratosphere above the Asian monsoon anticyclone but ideally verification by in-situ measurements would provide more confidence.

In addition to the above, C_2H_2 and C_2H_6 retrievals for August 2003 discussed in Chapter 5 have been analysed in conjunction with the MOPITT CO data in order to examine the relationship between the different species.

In general, strong correlations between C_2H_2 and CO were found. Once it had been shown that a strong correlation between the species was maintained through convection and mixing and hence that it was the atmospheric lifetimes which played

an important role in the differences between the distributions, it allowed the photochemical age of air to be qualitatively examined (Fig. 6.39). This photochemical age of air distribution identified the origin of the African biomass burning as well as the Asian-Pacific transport. In addition to these two transport mechanisms, the ratio between C_2H_2/CO was found to be highest over the monsoon anticyclone region, suggesting that the C_2H_2 isolated within this region is continually replenished from the deep convection near the surface. This agrees with the fact that although C_2H_2 is expected to have a lifetime of just 2 weeks, the enhancement over the monsoon anticyclone region is observed throughout the entire summer.

The C_2H_6 data produced poorer correlations but this is expected to be related not only to the longer lifetime of C_2H_6 but also to the fact that the primary source of C_2H_6 is natural gas production as opposed to biomass burning. Despite this, considerable agreement is still found with the C_2H_6 although the correlations exhibit a forked distribution where the C_2H_6 shows an enhancement over Central America. Further investigation was performed and has preliminarily attributed the C_2H_6 enhancements in this region to the large number of natural gas processing plants although a more thorough study is required which would hopefully include in-situ measurements to complement the satellite remote-sensing.

Chapter 7

Conclusions And Future Work

This final chapter summarises how the aims of this thesis were successfully achieved and provides some of the key findings. Recommendations relating to future work are also discussed.

These key findings include:

- It has been possible to develop a fast detection algorithm for both C_2H_2 and C_2H_6 which is capable of performing a "first look" at all MIPAS data for 2003
- The retrieval of C_2H_2 with MORSE provides results with a high data quality (spectral residuals, chisq, etc)
- The C_2H_2 acts as a strong indictor for biomass burning and long-range chemical transport
- The C_2H_2 can also act as a dynamical tracer for convection and chemical isolation due to the Asian monsoon anticyclone and provides potential evidence for tropopause penetration into the stratosphere
- The C_2H_6 spectroscopy has been improved by Vander Auwera et al. [2007] but still requires further work, especially at temperatures and pressures relevant to atmospheric retrievals
- The retrieval of C_2H_6 provides additional information on biomass burning but more interestingly, on the sources of natural gas production
- The sources and photochemical lifetime of biomass burning plumes can be successfully examined through a C_2H_2/CO ratio
- The differentiation of biomass burning and fossil fuel production can be achieved through a C_2H_2/C_2H_6 ratio

Finally this chapter also includes a short discussion on future satellite mission proposals and comments upon the suitability of these missions for continuation of the work in this thesis.

7.1 Fast Detection Algorithm

The aim of this thesis was primarily an investigation into the feasibility of the retrieval of C_2H_2 from the MIPAS instrument. Through the course of this work it was found that due to the large amount of data to be processed and relatively high computational expense of the optimal estimation retrieval, it was not feasible within this thesis to retrieve an entire year of C_2H_2 data. Instead, a much faster automated detection algorithm was developed (Chapter 4) which was capable of easily identifying enhancements of C_2H_2 without the need for the far slower, albeit more accurate, full retrieval scheme. Results were shown for a 12 km nominal tangent altitude.

Due to the nature of the strong C_2H_2 spectral signature and relatively simple spectral microwindow, it was found that this detection technique provided results that were highly correlated to the full retrieval and that it was more than sufficient to use this technique as a "first look" at the data before undertaking the far more computational expensive retrieval.

Although primarily intended as only a preliminary analysis of the data, several interesting results were found using this detection algorithm.

Section 4.2.3 discussed the detection results for the whole of 2003 and showed that the monthly C_2H_2 distribution could be mapped in order to highlight biomass burning sources and transport regimes. An in-depth analysis of the C_2H_2 distribution for each month included examination of the ECMWF 150 hpa wind vectors, NCEP OLR as a proxy for deep convection, AATSR fire counts and MIPAS cloud top heights. The majority of the C_2H_2 enhancements could be explained in terms of fire emissions, convection and transport giving confidence that the detection methodology is producing reasonable results and furthermore that C_2H_2 can successfully act as a useful tracer for biomass burning.

The C_2H_2 detected peak radiances clearly identified the chemical isolation of C_2H_2 due to the Asian monsoon anticyclone. Monthly plots of C_2H_2 along with the average wind vectors for those time periods (Fig. 4.37) showed that the enhancement in the C_2H_2 detected peak radiances lay within the boundary of the anticyclone. The NCEP geopotential height anomaly (Fig. 4.39) was used to further identify the location of the anticyclone and again was found to strongly agree with the location of the enhanced C_2H_2, not only in August but also in September when the core of the anticyclone had shifted as it began to dissipate.

In addition to C_2H_2, the detection algorithm was also applied to C_2H_6. The analysis of the C_2H_6 detected peak radiance proved more difficult due to the much weaker spectral signature although several interesting features were observed such as a strong enhancement in C_2H_6 observed over Central America where no corresponding C_2H_2 enhancement was found which was later attributed to the emissions from natural gas production in the region (see 6.6.1).

Correlations were also performed between the detected peak radiances for C_2H_2 and C_2H_6 and in general a strong correlation between the two species was found as

expected. However, key differences such as a "fork" in the correlation relating to the enhanced C_2H_6 over Central America were also observed, again attributed to the difference in sources between C_2H_2 and C_2H_6.

7.1.1 Future Work

Despite showing that the detection algorithm can be a useful technique in its own right as well as providing a fast method to perform a preliminary examination of a large amount of data, it is currently not an adequate replacement for the more rigourous optimal estimation retrieval. The main reason for this is that it uses no information relating to the other variables within the microwindow such as pressure, temperature or interfering gases.

In order to address these issues, future modifications to the algorithm could include using either ECMWF or MIPAS L2 data in order to obtain an estimate for the pressure and temperature in the microwindow. In addition, the use of MIPAS L2 O_3, CH_4 and HNO_3 would provide estimates of the main interfering species and allow a much more accurate calculation of the baseline and hence the C_2H_2 peak radiance.

Further future modifications to the detection algorithm could also potentially increase its usefulness. Currently it is not possible to directly extrapolate a C_2H_2 VMR from the detected peak radiance due to the fact mentioned above that the contributions from the pressure, temperature and other interfering species are not taken into account. If the alterations suggested above were made it would in theory allow the C_2H_2 VMR to be estimated for any C_2H_2 detected peak radiance once a linear fit had been calculated for a small sample of detections and retrievals.

Taking this further, increasing the complexity of the algorithm would be possible, with for example a regression or neural network approach being able to estimate the C_2H_2 VMR from the MIPAS L1B spectra. Such a change would require extensive modifications and substantial testing but would prove an interesting direction for the detection algorithm to proceed along. This would potentially lead to the detection algorithm being applicable to a variety of satellite spectra, not just MIPAS data.

However the algorithm is modified in the future, the main objectives would be to make it capable of operating on a variety of species from various data sources.

The work in this thesis has shown that even at its most basic implementation it is capable of providing a reasonable detection of C_2H_6 from MIPAS spectra and with further improvements there is no reason why the number of detectable species could not be increased further.

One of the reasons why the detection algorithm works so well for MIPAS is due to the high spectral resolution of 0.025 cm^{-1}. As discussed in Chapter 3, post-2003 MIPAS suffered a mechanical issue with one of the interferometer mirrors and is now operating at a reduced resolution of 0.06 cm^{-1}. Attempting to identify the

spectral signature of C_2H_2 in this reduced resolution MIPAS data would prove an interesting challenge for the detection algorithm as the spectral signatures would no longer be as distinct.

The option of then applying the detection algorithm to other satellite data would depend on this ability to operate the detection algorithm successfully on data at a lower spectral resolution. Whilst the Atmospheric Chemistry Experiment (ACE) satellite has a spectral resolution of 0.02 cm^{-1}, its solar occultation technique limits it to two soundings per orbit with the majority occurring at high latitudes. Hence ACE may not be suitable for sampling rapidly occurring events over short spatial and temporal scales but would prove ideal for the detection of longer lived species due to its very high signal to noise ratio.

Other instruments such as the Infrared Atmospheric Sounding Interferometer (IASI) may have the ability to provide global distributions on short timescales but are limited by the relatively low spectral resolution of around 0.5 cm^{-1} and in reality a detection algorithm may only be capable of recognising a C_2H_2 spectral signature during extremely strong enhancement episodes.

Section 7.7 at the end of this chapter discusses further potential future missions which may allow the continuation of the work in this thesis.

7.2 C_2H_2 Retrieval Results

The successful retrieval of C_2H_2 from MIPAS L1B spectra using the MORSE optimal estimation retrieval scheme and the subsequent analysis of the retrieval results have constituted a large part of this thesis. It was shown that it was possible to retrieve C_2H_2 and that its distribution could be used as a tracer for biomass burning with the identification of significant events over Africa, South America and South-Asia corresponding to regions with a high number of AATSR fire counts.

The error analysis examined both the random and systematic error components for the retrieval of C_2H_2 (Fig. 5.2) in August 2003. The total error estimate at 200 hpa was found to be 16 % with the random retrieval error dominating this with a value of 14 % compared to 7 % for the contribution from the systematic errors. The C_2H_2 spectroscopy and line-shape effects in addition to the uncertainty in the pressure and temperature were found to be the major sources of systematic error.

A detailed analysis of the data quality indictors was performed in Section 5.3. Through the examination of the averaging kernels for the C_2H_2 retrieval it was shown that the 9km and 12 km nominal MIPAS altitudes (300 hpa and 200 hpa respectively) have a low dependence on the a priori whereas the retrieval at higher altitudes has more dependence on the a priori. The cloud index threshold of 4.0 was found to be preferable to a lower threshold of 1.8 as it allowed the effects of partially cloudy scene to be removed from the retrieval.

The quality filtering of the final C_2H_2 dataset was discussed in detail with reference to the use of the cloud index and the CHISQ parameter obtained from

the retrieval as methods of filtering the final data. The CHISQ value as well as the DOFS and the final spectral residual were all used as indicators of the quality of the retrieval. The effect of the various stages of filtering were applied to each of these in order to justify the final filtering criteria. It was found that by filtering with a cloud index threshold of 4.0, a C_2H_2 CHISQ value less than or equal to 2.0 and a pressure CHISQ value less than or equal to 10.0 all of the various indicators of the quality of the data suggest a high quality retrieval. In particular, the fact that the spectral residual is within the noise level of MIPAS of 40 $nW/cm^2 \cdot sr \cdot cm^{-1}$ suggests that the retrieval is fitting the C_2H_2 peak as well as possible.

The C_2H_2 results for August 2003 were of the most interest due to the chemical isolation related to the Asian monsoon anticyclone during this time but C_2H_2 was also retrieved globally for January 2003. Through a detailed analysis of both error contributions and data quality indicators, the C_2H_2 retrieval was found to be of a high quality. Comparison with the results from the detection algorithm provided a strong agreement both for August and January, giving confidence in the ability of the detection algorithm to act as a "first look" at data in the future before performing the retrieval.

One of the most interesting results from the C_2H_2 retrieval was that not only was the location of the Asian monsoon anticyclone clearly identified by the C_2H_2 enhancement but also that the vertical distribution and source of uplift (Fig. 6.25) was shown to be located over the region of deep convection as previously suggested by Park et al. [2008].

Through the further examination of the vertical distributions of C_2H_2, potential evidence for the penetration of C_2H_2 through the tropopause into the stratosphere (see Sec. 6.4.4) was found which would prove to be an important result were it possible to verify the observation.

7.2.1 Future Work

There is considerable scope for future work now that C_2H_2 has been successfully retrieved for both August and January 2003.

The most obvious route is to complete the retrieval of C_2H_2 for the rest of 2003. Although computationally expensive, this would not only provide further information to assess how well the detection algorithm is performing over multiple months but it would allow the seasonality of C_2H_2 to be examined in detail.

Unfortunately due to MIPAS now only functioning in a reduced resolution mode, it is expected that any retrieval with post-2003 MIPAS data will be considerably poorer. The effect of retrieving with this reduced resolution mode would need to be explored in detail but if possible, the increased vertical sampling may prove beneficial in assessing the vertical transport of C_2H_2.

Perhaps more important than retrieving for an extended period of time is the need to further validate the C_2H_2 results already obtained. Ideally the C_2H_2 re-

trieved for August 2003 would be compared to in situ aircraft measurements. Unfortunately this has currently not been possible within this thesis due to lack of appropriate in situ data but is of vital importance for future work.

If no sufficient in situ measurements become available in the future, a comparison to model data would provide another means of validation. Several chemical transport models such as TOMCAT and GEOSCHEM already have C_2H_6 available and in the future it is expected that C_2H_2 may become available.

In addition to the above, once validated, the C_2H_2 itself may be assimilated into model data and provide valuable information. For example, C_2H_2 is one of the main precursors in the production of glyoxal and has implications for the production of secondary organic aerosol (SOA) as discussed recently by Volkamer et al. [2008].

7.3 C_2H_6 Spectroscopy And Retrieval Results

The uncertainty in the spectroscopic parameters are one of the largest errors in any retrieval. The C_2H_6 spectroscopy in the GEISA and HITRAN 2004 spectroscopic databases were shown to disagree considerably with each other. An update to the C_2H_6 spectroscopy proposed for inclusion into HITRAN by Vander Auwera et al. [2007] was shown to again differ from both previous datasets.

In order to assess the quality of this C_2H_6 spectroscopy, preliminary C_2H_6 spectroscopic measurements were performed at the NERC-sponsored Molecular Spectroscopy Facility at the Rutherford Appleton Laboratory. These measurements were recorded at a variety of pressures and temperatures representative of the real atmosphere.

Simulations using the improved C_2H_6 spectroscopy were performed and it was found that even though the spectroscopy of C_2H_6 has been significantly improved, the difference between the improved spectroscopy and our laboratory measurements is equivalent to as much as a 15% reduction in the amount of ethane. It follows therefore that any retrieval using the current ethane spectroscopy may be underestimating the amount of ethane responsible for a measured spectral signature. This obviously has implications for any accurate retrieval of ethane and requires future work to perform improved measurements of the ethane spectroscopy, particularly for scenarios of pressure and temperature relevant to upper tropospheric measurements.

C_2H_6 was retrieved for August 2003 using the same pre-retrieved values for pressure, temperature, O_3, H_2O and HNO_3 as for the C_2H_2 retrieval. As for C_2H_2, a detailed analysis of the various retrieval quality indictors was performed and it was found that overall the retrieval quality of the C_2H_6 data was reasonable with both a low CHISQ value and a good spectral fit between the measurement and forward model simulation. A poor fit to of the spectral residual was observed for a small number of scans and was mainly related to the fitting of the interfering ozone within the C_2H_6 microwindow.

When compared to the C_2H_6 detection results, whilst overall showing a reasonable level of similarity, the results here were poorer than those for C_2H_2. This was mainly due to the increased difficulty of separating the smaller spectral signature of C_2H_6 from both the noise and other interfering species in both the detection and retrieval. Despite this, it is expected that the detection technique when applied to C_2H_6 will be capable of highlighting regions of interest although further work may be required in optimising the retrieval to remove the effects of interfering species such as ozone.

7.3.1 Future Work

The work in this thesis has shown that whilst the improved C_2H_6 spectral parameters measured by Vander Auwera et al. [2007] appear to be considerably closer to our own measurements than previous values, there is still additional work required to obtain accurate C_2H_6 spectra at a variety of atmospherically relevant pressures and temperatures. In addition, a full analysis will be required to characterise the spectral parameters as opposed to the simple approach taken by the comparison in this thesis. It is expected that this improved spectroscopy would considerably improve the retrieval of C_2H_6 from MIPAS.

7.4 Photochemical Lifetime Of Plumes

Correlations between C_2H_2 and MOPITT CO were performed over a variety of regions and scales. Global and hemispheric correlations showed in general a strong correlation between C_2H_2 and CO. Regional correlations showed a greater variability but still maintained a strong correlation.

Once it has been shown that a strong correlation between the species was maintained through convection and mixing and hence that it was the atmospheric lifetimes which played an important role in the differences between the distributions, it allowed the photochemical age of air to be qualitatively shown (Fig. 6.39). This photochemical age of air distribution identified the origin of the African biomass burning as well as the Asian-Pacific transport. In addition to these two transport mechanisms, the ratio between C_2H_2/CO was found to be highest over the monsoon anticyclone region, suggesting that the C_2H_2 isolated within this region is continually replenished from the deep convection near the surface. This agrees with the fact that although C_2H_2 is expected to have a lifetime of just 2 weeks, the enhancement over the monsoon anticyclone region is observed throughout the entire summer.

Further analysis was performed by taking specified pathways from obvious source regions or over regions of interest and examining the behaviour of the relationships between C_2H_2, C_2H_6 and CO. These results further verified that the C_2H_2/CO ratio is a useful indicator for examining the relative photochemical ageing of plumes and their source distribution from biomass burning.

This work has therefore shown that it is possible to use the C_2H_2/CO ratio as an indication of photochemical ageing and that it allows various atmospheric transport mechanisms to be identified. In addition, although only in its preliminary stages with further work required, the C_2H_6 retrieval data was also used to provide additional information on this ageing.

7.4.1 Future Work

Ideally it would be possible to obtain a whole suite of gases which could be used to examine biomass burning and transport. Potential candidates in addition to C_2H_2 and C_2H_6 would include C_2H_4 as well as unique tracers of biomass burning such as HCN and CH_3CN. The potential for the retrieval of the two latter species from MIPAS using MORSE is already being examined within our group.

One of the only issues with the C_2H_2/CO ratio itself is that the two species are retrieved from different instruments. Whilst we have shown that it is possible to use the CO from MOPITT, the possibility of using CO from additional sources should be examined. For example, CO data is available from the Microwave Limb Sounder which would provide greater vertical resolution.

Ideally, future work would use the CO retrieved from MIPAS itself and although some work has already been performed on this retrieval, a mature CO product was not available for MIPAS during this thesis but may well be in the near future [Funke et al., 2009]. If this were the case it would considerably reduce any uncertainties in the C_2H_2/CO ratio as both species would be available for each MIPAS measurement without the need to consider average monthly data as has been the case in this thesis.

7.5 Fossil Fuel And Biomass Burning Source Differentiation

As C_2H_6 has its primary source from fossil fuel production whilst C_2H_2 is primarily from biomass/biofuel burning, the ratio between the two has been used to differentiate between biomass burning sources and fossil fuel production (Fig. 6.47). The results from this clearly indicated a large signature over Central America which through further investigation in Section 6.6.1 has been attributed to the large number of natural gas processing plants in Mexico.

The vertical information suggests that the C_2H_6 is being uplifted by deep convection into the MIPAS field of view at an average 12 km tangent altitude and is even potentially penetrating into the stratosphere. As was the case for C_2H_2, validation from aircraft in-situ measurements is vital in order to verify the MIPAS observations.

7.5.1 Future Work

Future work in this area would include performing a similar analysis for different months to examine the seasonality of the fossil fuel production. Ideally, as discussed above, additional species such as HCN could be used which act as unique tracers for biomass burning and would allow further differentiation both in terms of sources and lifetimes. Additional data pertaining to the activity of these natural gas processing centres would also prove useful in order to verify any findings.

7.6 Future Missions

In addition to the planned launch of the 2nd and 3rd nadir-sounding infrared IASI missions onboard future MetOp satellites in 2012 and 2016, there are currently several mission proposals relevant to the continuation of the work in this thesis.

The PREMIER (PRocess Exploration through Measurements of Infrared and millimetre-wave Emitted Radiation) mission is a proposed ESA Earth Explorer mission regarded as a follow-on to MIPAS with a launch planned for 2016 if the proposal is successful. It is intended that this instrument will build upon the heritage of previous infrared limb emission sounding instruments over the past three decades such as LRIR (Nimbus-6, 1975), LIMS and SAMS (Nimbus-7, 1978), CLAES and ISAMS (UARS, 1991), CRISTA (Space Shuttle, 1994), SABER (TIMED, 2001), MIPAS (Envisat, 2001), HIRDLS and TES (Aura, 2004).

The aim of PREMIER is stated as being "to observe atmospheric composition for a better understanding of chemistry-climate interactions".

The mission objectives are stated as being:

- to quantify relationships between atmospheric composition and climate
- to quantify atmospheric transport processes important to climate and air quality
- to quantify relationships between atmospheric dynamics and climate

In order to achieve these objectives, PREMIER will be able to produce tomographic measurements of the atmosphere through the use of an IR detector array capable of simultaneously measuring between 5 km and 50 km with a high vertical resolution. The mission requirements for PREMIER state a spectral resolution of less than 0.2 cm^{-1}, along with cross-track sampling of 25 km and along-track sampling of 100 km.

It is also expected that there will be substantial synergy between PREMIER to both the future planned IASI missions onboard MetOp in order to quantify surface emissions and pollution as well as to the Post-EPS/MetOp missions.

The EUMETSAT Post-EPS plans include the High-Resolution Infrared Sounding (IRS) mission as a high priority.

The primary objective of the IRS is to support Numerical Weather Prediction at regional and global scales building upon the success of IASI. In order to achieve this objective it is expected that IRS will be capable of providing 90% global coverage within 12 hours and 100% within 24 hours with the spatial sampling at nadir as high as 10 km allowing IRS to be capable of providing:

- Atmospheric temperature and water-vapour profiles at high vertical resolution in clear and partly cloudy air
- Surface temperature over sea, ice and land
- Cloud parameters
- Various atmospheric trace gases

The secondary objective is to provide support for:

- Pollution monitoring and air quality forecasting at global and regional scales
- Trace gas measurements and the assessment of composition-climate interaction

As can be seen, both of the proposed missions above show the importance placed by the international scientific community on continuing to monitor atmospheric composition and dynamics through the use of infrared sounding instruments. However, when examining the proposals in more detail, although both list C_2H_6 as a target species (with PREMIER placing it as one of its trace gas priorities along with CO, PAN, HNO_3 and "additional nitrogen and organic compounds") the proposed spectral resolution will make retrieval more difficult. Although work with IASI has shown that it is possible to perform such retrievals at a lower spectral resolution when there are significant enhancements, these situations are generally exceptions.

As far as we are aware there are currently no proposals for a high-spectral resolution (greater than 0.02 cm^{-1}) instrument which would be capable of performing such measurements. Ideally such an instrument would be a follow-on to ACE, capable of achieving a high SNR with a high spectral resolution. As discussed in Chapter 1, the drawback of ACE's relatively poor spatial sampling would need to be addressed, possibly by a series of instruments in different orbits providing complementary occultation measurements or by an alteration to the current orbit.

7.7 Closing Remarks

The work undertaken in this thesis has demonstrated that it is possible to explore the upper-tropospheric distributions of key hydrocarbon species, specifically C_2H_2 and C_2H_6, with a much higher temporal and spatial resolution than has previously been possible. In addition, it has shown that these species can act as tracers for not only investigating dynamical effects such as transport and convection but also for differentiating between source types and for identifying photochemically aged plumes. With the ACE and IASI instruments currently in orbit, as well as the proposed future missions such as PREMIER, there is a wealth of satellite infrared measurements probing the troposphere which must continue to be utilised to the fullest in order to provide the best description of the sources, transport and subsequent impact of these important species.

ACKNOWLEDGEMENTS FOR PROVISION OF DATA AND FUNDING

This work was funded by a Natural Environment Research Council studentship at the University of Leicester, UK.

- I would like to thank Anu Dudhia at The University of Oxford for providing us with the Oxford Reference Forward Model (RFM) and the MIPAS Orbital Retrieval using Sequential Estimation (MORSE) codes used in this study.
- I also gratefully acknowledge the NOAH Air Resources Laboratory (ARC) for the provision of the HYSPLIT transport and dispersion model used in this publication.
- MIPAS data was provided by the European Space Agency under CUTLSOM (AO–357).
- MOPITT data was obtained from the NASA Langley Research Center Atmospheric Science Data Center.
- AATSR World Fire Atlas data from the Data User Element of the European Space Agency.
- NCEP data was provided by the NOAA-ESRL Physical Sciences Division, Boulder Colorado from their Web site at http://www.cdc.noaa.gov/
- ECMWF Operational Analysis data wind data was provided by the European Centre for Medium-Range Weather Forecasts through the British Atmospheric Data Centre at http://badc.nerc.ac.uk/data/ecmwf-op/

Bibliography

Barret, B., Ricaud, P., Mari, C., Atti, J.-L., Bousserez, N., Josse, B., Le Flochmon, E., Livesey, N. J., Massart, S., Peuch, V.-H., Piacentini, A., Sauvage, B., Thouret, V. and Cammas, J.-P. [2008], 'Transport pathways of CO in the African upper troposphere during the monsoon season: a study based upon the assimilation of spaceborne observations', *Atmospheric Chemistry and Physics* **8**(12), 3231–3246.

Bernath, P. F., McElroy, C. T., Abrams, M. C., Boone, C. D., Butler, M., Camy-Peyret, C., Carleer, M., Clerbaux, C., Coheur, P., Colin, R., DeCola, P., DeMazire, M., Drummond, J. R., Dufour, D., Evans, W. F. J., Fast, H., Fussen, D., Gilbert, K., Jennings, D. E., Llewellyn, E. J., Lowe, R. P., Mahieu, E., McConnell, J. C., McHugh, M., McLeod, S. D., Michaud, R., Midwinter, C., Nassar, R., Nichitiu, F., Nowlan, C., Rinsland, C. P., Rochon, Y. J., Rowlands, N., Semeniuk, K., Simon, P., Skelton, R., Sloan, J. J., Soucy, M., Strong, K., Tremblay, P., Turnbull, D., Walker, K. A., Walkty, I., Wardle, D. A., Wehrle, V., Zander, R. and Zou, J. [2005], 'Atmospheric chemistry experiment (ACE): Mission overview', *Geophysical Research Letters* **32**(15).

Bertschi, I. T., Yokelson, R. J., Ward, D. E., Christian, T. J. and Hao, W. M. [2003], 'Trace gas emissions from the production and use of domestic biofuels in Zambia measured by open-path Fourier transform infrared spectroscopy', *Journal of Geophysical Research D: Atmospheres* **108**(13).

Bey, I., Jacob, D. J., Logan, J. A. and Yantosca, R. M. [2001], 'Asian chemical outflow to the Pacific in spring: Origins, pathways, and budgets', *Journal of Geophysical Research D: Atmospheres* **106**(D19), 23097–23113.

Blake, N. J., Blake, D. R., Sive, B. C., Chen, T. Y., Rowland, F. S., Collins Jr, J. E., Sachse, G. W. and Anderson, B. E. [1996], 'Biomass burning emissions and vertical distribution of atmospheric methyl halides and other reduced carbon gases in the South Atlantic region', *Journal of Geophysical Research D: Atmospheres* **101**(19), 24151–24164.

Bloss, W. J., Evans, M. J., Lee, J. D., Sommariva, R., Heard, D. E. and Pilling, M. J. [2005], 'The oxidative capacity of the troposphere: Coupling of field measurements of oh and a global chemistry transport model', *Faraday discussions* **130**, 425–436.

Brown, J. M. [1998], *Molecular Spectroscopy*, Oxford Science Publications.

Burgess, A. B., Graiger, R. G. and Dudhia, A. [2006], 'Zonal mean atmospheric distribution of sulphur hexaflouride (SF_6)', *Geophysical Research Letters* **33**(7).

Burgess, A. B., Grainger, R. G. and Dudhia, A. [2005], Progress in the retrieval of sulphur species from MIPAS, pp. 1065–1072.

Carlotti, M., Brizzi, G., Papandrea, E., Prevedelli, M., Ridolfi, M., Dinelli, B. M. and Magnani, L. [2006], 'GMTR: Two-dimensional geo-fit multitarget retrieval model for michelson interferometer for passive atmospheric sounding/environmental satellite observations', *Applied Optics* **45**(4), 716–727.

Chung, E., Sohn, B. and Schmetz, J. [2008], 'CloudSat shedding new light on high-reaching tropical deep convection observed with Meteosat', *Geophysical Research Letters* **35**(2).

Cooper, J. R. and Moazzen-Ahmadi, N. [2006], 'Global fit analysis including the $\nu 9$ + $\nu 4$ - $\nu 4$ hot band of ethane: Evidence of an interaction with the $\nu 12$ fundamental', *Journal of Molecular Spectroscopy* **239**(1), 51–58.

Cortesi, U., Lambert, J. C., De Clercq, C., Bianchini, G., Blumenstock, T., Bracher, A., Castelli, E., Catoire, V., Chance, K. V., De Mazire, M., Demoulin, P., Godin-Beekmann, S., Jones, N., Jucks, K., Keim, C., Kerzenmacher, T., Kuellmann, H., Kuttippurath, J., Iarlori, M., Liu, G. Y., Liu, Y., McDermid, I. S., Meijer, Y. J., Mencaraglia, F., Mikuteit, S., Oelhaf, H., Piccolo, C., Pirre, M., Raspollini, P., Ravegnani, F., Reburn, W. J., Redaelli, G., Remedios, J. J., Sembhi, H., Smale, D., Steck, T., Taddei, A., Varotsos, C., Vigouroux, C., Waterfall, A., Wetzel, G. and Wood, S. [2007], 'Geophysical validation of MIPAS-ENVISAT operational ozone data', *Atmospheric Chemistry and Physics* **7**(18), 4807–4867.

Crutzen, P. J. [1974], 'Photochemical reaction initiated by and influencing ozone in unpolluted tropospheric air', *Tellus* **26**, 45 – 55.

Crutzen, P. J. and Andreae, M. O. [1990], 'Biomass burning in the tropics: Impact on atmospheric chemistry and biogeochemical cycles', *Science* **250**(4988), 1669–1678.

Damoah, R., Spichtinger, N., Servranckx, R., Fromm, M., Eloranta, E. W., Razenkov, I. A., James, P., Shulski, M., Forster, C. and Stohl, A. [2006], 'A case study of pyro-convection using transport model and remote sensing data', *Atmospheric Chemistry and Physics* **6**(1), 173–185.

Draxler, R. and Rolph, G. [2003], 'HYSPLIT (HYbrid Single-Particle Lagrangian Integrated Trajectory) Model access via NOAA ARL READY Website (http://www.arl.noaa.gov/ready/hysplit4.html). NOAA Air Resources Laboratory, Silver Spring, MD.'.

Dudhia, A. [2004], 'Report on The Optimisation Of The AMIPAS Spectral Resolution'.

Dudhia, A. [2005], 'The Oxford Reference Forward Model, see website http://www.atm.ox.ac.uk/RFM/'.

Duncan, B. N., Martin, R. V., Staudt, A. C., Yevich, R. and Logan, J. A. [2003], 'Interannual and seasonal variability of biomass burning emissions constrained by satellite observations', *Journal of Geophysical Research D: Atmospheres* **108**(2), ACH 1–1 ACH 1–22.

Edwards, D. P. [1992], 'GENLN2: A general line-by-line atmospheric transmittance and radiance model. Version 3.0: Description and users guide', *Report NCAR /TN-367 +STR, National Center for Atmospheric Research, Boulder, Col.* .

ESA [2007], 'MIPAS Handbook', http://envisat.esa.int/handbooks/mipas/CNTR2-8-2.htm.

Fischer, H., Birk, M., Blom, C., Carli, B., Carlotti, M., Von Clarmann, T., Delbouille, L., Dudhia, A., Ehhalt, D., Endemann, M., Flaud, J. M., Gessner, R., Kleinert, A., Koopman, R., Langen, J., Lopez-Puertas, M., Mosner, P., Nett, H., Oelhaf, H., Perron, G., Remedios, J., Ridolfi, M., Stiller, G. and Zander, R. [2008], 'MIPAS: An instrument for atmospheric and climate research', *Atmospheric Chemistry and Physics* **8**(8), 2151–2188.

Freitas, S. R., Longo, K. M., Chatfield, R., Latham, D., Silva Dias, M. A. F., Andreae, M. O., Prins, E., Santos, J. C., Gielow, R. and Carvalho Jr., J. A. [2007], 'Including the sub-grid scale plume rise of vegetation fires in low resolution atmospheric transport models', *Atmospheric Chemistry and Physics* **7**(13), 3385–3398.

Freitas, S. R., Longo, K. M., Silva Dias, M. A. F., Silva Dias, P. L., Chatfield, R., Prins, E., Artaxo, P., Grell, G. A. and Recuero, F. S. [2005], 'Monitoring the transport of biomass burning emissions in South America', *Environmental Fluid Mechanics* **5**(1-2), 135–167.

Funke, B., Lopez-Puertas, M., Garca-Comas, M., Stiller, G. P., von Clarmann, T., Hpfner, M., Glatthor, N., Grabowski, U., Kellmann, S. and Linden, A. [2009], 'Carbon monoxide distributions from the upper troposphere to the mesosphere inferred from 4.7 μm non-local thermal equilibrium emissions measured by MIPAS on Envisat', *Atmospheric Chemistry and Physics* **9**(7), 2387–2411.

Glatthor, N., Von Clarmann, T., Fischer, H., Funke, B., Grabowski, U., Hopfner, M., Kellmann, S., Linden, A., Milz, M., Steck, T. and Stiller, G. P. [2007], 'Global peroxyacetyl nitrate (PAN) retrieval in the upper troposphere from limb emission spectra of the Michelson Interferometer for Passive Atmospheric Sounding (MIPAS)', *Atmospheric Chemistry and Physics* **7**(11), 2775–2787.

Glatthor, N., von Clarmann, T., Stiller, G. P., Funke, B., Koukouli, M. E., Fischer, H., Grabowski, U., Hpfner, M., Kellmann, S. and Linden, A. [2009], 'Source classification of upper tropospheric pollution by MIPAS HCN and C_2H_6 global distributions', *Atmospheric Chemistry and Physics Discussions* **9**(4), 16197–16232.

Guan, H., Chatfield, R. B., Freitas, S. R., Bergstrom, R. W. and Longo, K. M. [2007], 'Modeling the effect of plume-rise on the transport of carbon monoxide over Africa and its exports with NCAR CAM', *Atmospheric Chemistry and Physics Discussions* **7**(6), 18145–18177.

Hahn, J., Steinbrecber, R. and Sloemr, J. [1992], 'Study of the emission of low molecular weight organic compounds of various plants', *Eurotrac Annual Report* **4**, 180–185.

Hall, D. O. [1991], 'Biomass energy', *Energy Policy* **19**(8), 711–737.

Hegg, D. A., Radke, L. F., Hobbs, P. V., Rasmussen, R. A. and Riggan, P. J. [1990], 'Emissions of some trace gases from biomass fires', *Journal of Geophysical Research* **95**(D5), 5669–5675.

Henne, S., Furger, M., Nyeki, S., Steinbacher, M., Neininger, B., de Wekker, S. F. J., Dommen, J., Spichtinger, N., Stohl, A. and Prvt, A. S. H. [2004], 'Quantification of topographic venting of boundary layer air to the free troposphere', *Atmospheric Chemistry and Physics* **4**(2), 497–509.

Hoffmann, L., Spang, R., Kaufmann, M. and Riese, M. [2005], 'Retrieval of CFC-11 and CFC-12 from Envisat MIPAS observations by means of rapid radiative transfer calculations', *Advances in Space Research* **36**(5), 915–921.

Houghton, Taylor and Rodgers [1984], *Remote Sounding Of Atmospheres*, Cambridge University Press.

Jacquemart, D., Mandin, J. Y., Dana, V., Claveau, C., Vander Auwera, J., Herman, M., Rothman, L., Regalia-Jarlot, L. and Barbe, A. [2003], 'The IR acetylene spectrum in HITRAN: update and new results', *Journal of Quantitative Spectroscopy and Radiative Transfer* **82**(1-4), 363–382.

Jacquinet-Husson, N., Scott, N. A., Chdin, A., Garceran, K., Armante, R., Chursin, A. A., Barbe, A., Birk, M., Brown, L. R., Camy-Peyret, C., Claveau, C., Clerbaux, C., Coheur, P. F., Dana, V., Daumont, L., Debacker-Barilly, M. R., Flaud, J. M., Goldman, A., Hamdouni, A., Hess, M., Jacquemart, D., Kpke, P., Mandin, J. Y., Massie, S., Mikhailenko, S., Nemtchinov, V., Nikitin, A., Newnham, D., Perrin, A., Perevalov, V. I., Rgalia-Jarlot, L., Rublev, A., Schreier, F., Schult, I., Smith, K. M., Tashkun, S. A., Teffo, J. L., Toth, R. A., Tyuterev, V. G., Vander Auwera, J., Varanasi, P. and Wagner, G. [2005], 'The 2003 edition of the GEISA/IASI spectroscopic database', *Journal of Quantitative Spectroscopy and Radiative Transfer* **95**(4), 429–467.

Kar, J., Drummond, J. R., Jones, D. B. A., Liu, J., Nichitiu, F., Zou, J., Gille, J. C., Edwards, D. P. and Deeter, M. N. [2006], 'Carbon monoxide (CO) maximum over the Zagros mountains in the Middle East: Signature of mountain venting?', *Geophysical Research Letters* **33**(15).

Kiefer, M., von Clarmann, T., Grabowski, U., De Laurentis, M., Mantovani, R., Milz, M. and Ridolfi, M. [2007], 'Characterization of MIPAS elevation pointing', *Atmospheric Chemistry and Physics* **7**(6), 1615–1628.

Kleinert, A., Aubertin, G., Perron, G., Birk, M., Wagner, G., Hase, F., Nett, H. and Poulin, R. [2007], 'MIPAS Level 1B algorithms overview: Operational processing and characterization', *Atmospheric Chemistry and Physics* **7**(5), 1395–1406.

Koppmann, R., von Czapiewski, K. and Reid, J. S. [2005], 'A review of biomass burning emissions, part i: gaseous emissions of carbon monoxide, methane, volatile organic compounds, and nitrogen containing compounds', *Atmospheric Chemistry and Physics Discussions* **5**(5), 10455–10516.

Lelieveld, J., Berresheim, H., Borrmann, S., Crutzen, P. J., Dentener, F. J., Fischer, H., Feichter, J., Flatau, P. J., Heland, J., Holzinger, R., Korrmann, R., Lawrence, M. G., Levin, Z., Markowicz, K. M., N., M., Minikin, A., Ramanathan, V., De Reus, M., Roelofs, G. J., Scheeren, H. A., Sciare, J., Schlager, H., Schultz, M., Siegmund, P., Steil, B., Stephanou, E. G., Stier, P., Traub, M., Warneke, C., Williams, J. and Ziereis, H. [2002], 'Global air pollution crossroads over the Mediterranean', *Science* **298**(5594), 794–799.

Lelieveld, J. and Crutzen, P. [1993], Methane emissions into the atmosphere: An over-view, *in* A. van Amstel, ed., 'Methane and nitrous oxide: methods in national emissi-ons inventories and options for control', IPCC/RIVM, pp. 17–25.

Li, Q., Jacob, D. J., Logan, J. A., Bey, I., Yantosca, R. M., Liu, H., Martin, R. V., Fiore, A. M., Field, B. D., Duncan, B. N. and Thouret, V. [2001], 'A tropospheric ozone maximum over the Middle East', *Geophysical Research Letters* **28**(17), 3235–3238.

Liang, Q., Jaegl, L., Hudman, R. C., Turquety, S., Jacob, D. J., Avery, M. A., Browell, E. V., Sachse, G. W., Blake, D. R., Brune, W., Ren, X., Cohen, R. C., Dibb, J. E., Fried, A., Fuelberg, H. E., Porter, M. J., Heikes, B. G., Huey, G., Singh, H. B. and Wennberg, P. O. [2007], 'Summertime influence of Asian pollution in the free troposphere over North America', *Journal of Geophysical Research D: Atmospheres* **112**(12).

Liou, K. [1980], *An Introduction to Atmospheric Radiation*, Academic Press.

Liou, K. [1992], *Radiation and Cloud Processes in the Atmosphere*, Oxford University Press.

McKeen, S. A. and Liu, S. C. [1993], 'Hydrocarbon ratios and photochemical history of air masses', *Geophysical Research Letters* **20**(21), 2363–2366.

MIPAS ACP Special Issue [2006], 'MIPAS (Michelson Interferometer for Passive Atmosphere Sounding) Potential of the experiment, data processing and validation of results', *Atmospheric Chemistry and Physics* .

Moore, D. P. and Remedios, J. J. [2008], 'Growth rates of stratospheric HCFC-22', *Atmospheric Chemistry and Physics* **8**(1), 73–82.

Park, M., Randel, W. J., Emmons, L. K., Bernath, P. F., Walker, K. A. and Boone, C. D. [2008], 'Chemical isolation in the Asian monsoon anticyclone observed in Atmospheric Chemistry Experiment (ACE-FTS) data', *Atmospheric Chemistry and Physics* **8**(3), 757–764.

Park, M., Randel, W. J., Gettelman, A., Massie, S. T. and Jiang, J. H. [2007], 'Transport above the Asian summer monsoon anticyclone inferred from Aura Microwave Limb Sounder tracers', *Journal of Geophysical Research Atmospheres* **112**(16).

Parrish, D. D. [1992], 'Indications of photochemical histories of Pacific air masses from measurements of atmospheric trace species at Point Arena, California', *Journal of Geophysical Research* **97**(D14), 15,883–15,901.

Plass-Dulmer, C., Koppmann, R., Ratte, M. and Rudolph, J. [1995], 'Light non-methane hydrocarbons in seawater an overview', *J.Global Biogeochem.Cycles* **9**, 83–100.

Poisson, N., Kanakidou, M. and Crutzen, P. J. [2000], 'Impact of non-methane hydrocarbons on tropospheric chemistry and the oxidizing power of the global troposphere: 3-Dimensional modelling results', *Journal of Atmospheric Chemistry* **36**(2), 157–230.

Raspollini, P., Belotti, C., Burgess, A., Carli, B., Carlotti, M., Ceccherini, S., Dinelli, B. M., Dudhia, A., Flaud, J.-M., Funke, B., Hpfner, M., Lpez-Puertas, M., Payne, V., Piccolo, C., Remedios, J. J., Ridolfi, M. and Spang, R. [2006], 'MIPAS level 2 operational analysis', *Atmospheric Chemistry and Physics* **6**(12), 5605–5630.

Ratte, M., Plass-Dulmer, C., Koppmann, R. and Rudolph, J. [1995], 'Horizontal and vertical profiles of light hydrocarbons in sea water related to biological, chemical and physical parameters', *Tellus, Series B* **47 B**(5), 607–623.

Remedios, J. J., Allen, G., Waterfall, A. M., Oelhaf, H., Kleinert, A. and Moore, D. P. [2007], 'Detection of organic compound signatures in infra-red, limb emission spectra observed by the MIPAS-B2 balloon instrument', *Atmospheric Chemistry and Physics* **7**(6), 1599–1613.

Richards, N. [2004], 'PhD Thesis - Characteristics of Tropospheric Carbon Monoxide Profiles Retrieved from MOPITT Measurements.'.

Rinsland, C. P., Dufour, G., Boone, C. D., Bernath, P. F. and Chiou, L. [2005], 'Atmospheric Chemistry Experiment (ACE) measurements of elevated Southern Hemisphere upper tropospheric CO, C_2H_6, HCN, and C_2H_2 mixing ratios from biomass burning emissions and long-range transport', *Geophysical Research Letters* **32**(20), 1–4.

Rinsland, C. P., Dufour, G., Boone, C. D., Bernath, P. F., Chiou, L., Coheur, P. F., Turquety, S. and Clerbaux, C. [2007], 'Satellite boreal measurements over Alaska and Canada during June-July 2004: Simultaneous measurements of upper tropospheric CO, C_2H_6, HCN, CH_3Cl, CH_4, C_2H_2, CH_3OH, HCOOH, OCS, and SF_6 mixing ratios', *Global Biogeochemical Cycles* **21**(3).

Rinsland, C. P., Gunson, M. R., Wang, P. H., Arduini, R. F., Baum, B. A., Minnis, P., Goldman, A., Abrams, M. C., Zander, R., Mahieu, E., Salawitch, R. J., Michelsen, H. A., Irion, F. W. and Newchurch, M. J. [1998], 'ATMOS/ATLAS 3 infrared profile measurements of trace gases in the November 1994 tropical and subtropical upper troposphere', *Journal of Quantitative Spectroscopy and Radiative Transfer* **60**(5), 891–901.

Rodgers, C. [2000], 'Inverse methods for atmospheric sounding: theory and practice'.

Rothman, L. S., Jacquemart, D., Barbe, A., Benner, D. C., Birk, M., Brown, L. R., Carleer, M. R., Chackerian Jr., C., Chance, K., Coudert, L. H., Dana, V., Devi, V. M., Flaud, J. ., Gamache, R. R., Goldman, A., Hartmann, J. ., Jucks, K. W., Maki, A. G., Mandin, J. ., Massie, S. T., Orphal, J., Perrin, A., Rinsland, C. P., Smith, M. A. H., Tennyson, J., Tolchenov, R. N., Toth, R. A., Vander Auwera, J., Varanasi, P. and Wagner, G. [2005], 'The HITRAN 2004 molecular spectroscopic database', *Journal of Quantitative Spectroscopy and Radiative Transfer* **96**(2 SPEC. ISS.), 139–204.

Rudolph, J. [1995], 'The tropospheric distribution and budget of ethane', *Journal of Geophysical Research* **100**(D6), 11,369–11,381.

Smyth, S. B., Sandholm, S. T., Bradshaw, J. D., Talbot, R. W., Blake, D. R., Blake, N. J., Rowland, F. S., Singh, H. B., Gregory, G. L., Anderson, B. E., Sachse, G. W., Collins, J. E. and Bachmeier, A. S. [1996], 'Factors influencing the upper free tropospheric distribution of reactive nitrogen over the South Atlantic during the TRACE A experiment', *Journal of Geophysical Research D: Atmospheres* **101**(19), 24165–24186.

Smyth, S., Sandholm, S., Shumaker, B., Mitch, W., Kanvinde, A., Bradshaw, J., Liu, S., McKeen, S., Gregory, G., Anderson, B., Talbot, R., Blake, D., Rowland, S., Browell, E., Fenn, M., Merrill, J., Bachmeier, S., Sachse, G. and Collins, J. [1999], 'Characterization of the chemical signatures of air masses observed during the PEM experiments over the western Pacific', *Journal of Geophysical Research D: Atmospheres* **104**(D13), 16243–16254.

Spang, R., Remedios, J. J. and Barkley, M. P. [2004], 'Colour indices for the detection and differentiation of cloud types in infra-red limb emission spectra', *Advances in Space Research* **33**(7), 1041–1047.

Stephen, G. L. [1994], *Remote Sensing of the Lower Atmosphere: An Introduction*, Oxford University Press.

Streets, D. G., Bond, T. C., Carmichael, G. R., Fernandes, S. D., Fu, Q., He, D., Klimont, Z., Nelson, S. M., Tsai, N. Y., Wang, M. Q., Woo, J. H. and Yarber, K. F. [2003], 'An inventory of gaseous and primary aerosol emissions in Asia in the year 2000', *Journal of Geophysical Research D: Atmospheres* **108**(21).

Talbot, R., Dibb, J., Scheuer, E., Seid, G., Russo, R., Sandholm, S., Tan, D., Singh, H., Blake, D., Blake, N., Atlas, E., Sachse, G., Jordan, C. and Avery, M. [2003], 'Reactive nitrogen in Asian continental outflow over the western Pacific: Results from the NASA Transport and Chemical Evolution over the Pacific (TRACE-P) airborne mission', *Journal of Geophysical Research D: Atmospheres* **108**(20).

Tikhonov, A. [1963], 'On the solution of incorrectly stated problems and method of regularization', *Dokl. Akad. Nauk. SSSR* **153(3)**, 501–504.

US-EPA [1995], 'US Environmental Protection Agency - The Determination of Acute Toxicity Exposure Levels for Airborne Toxicants'.

Vander Auwera, J., Moazzen-Ahmadi, N. and Flaud, J. . [2007], 'Toward an accurate database for the 12 μm region of the ethane spectrum', *Astrophysical Journal* **662**(1 I), 750–757.

Volkamer, R., Ziemann, P. J. and Molina, M. J. [2008], 'Secondary organic aerosol formation from acetylene (C_2H_2): Seed effect on SOA yields due to organic photochemistry in the aerosol aqueous phase', *Atmospheric Chemistry and Physics Discussions* **8**(4), 14841–14892.

von Clarmann, T., Ceccherini, S., Doicu, A., Dudhia, A., Funke, B., Grabowski, U., Hilgers, S., Jay, V., Linden, A., Lopez-Puertas, M., Martin-Torres, F., Payne, V., Reburn, J., Ridolfi, M., Schreier, F., Schwarz, G., Siddans, R. and Steck, T. [2003], 'A blind test retrieval experiment for infrared limb emission spectrometry', *Journal of Geophysical Research D: Atmospheres* **108**(23).

von Clarmann, T., Glatthor, N., Stiller, G. P., Grabowski, U., Hopfner, M., Kellmann, S., Linden, A., Milz, M., Steck, T., Fischer, H., Funke, B. and Koukouli, M. E. [2007], 'MIPAS measurements of upper tropospheric C_2H_6 and O_3 during the Southern hemispheric biomass burning season in 2003', *Atmospheric Chemistry and Physics Discussions* **7**(4), 12067–12095.

Wang, D. Y., Hpfner, M., Blom, C. E., Ward, W. E., Fischer, H., Blumenstock, T., Hase, F., Keim, C., Liu, G. Y., Mikuteit, S., Oelhaf, H., Wetzel, G., Cortesi, U., Mencaraglia, F., Bianchini, G., Redaelli, G., Pirre, M., Catoire, V., Huret, N., Vigouroux, C., De Mazire, M., Mahieu, E., Demoulin, P., Wood, S., Smale, D., Jones, N., Nakajima, H., Sugita, T., Urban, J., Murtagh, D., Boone, C. D., Bernath, P. F., Walker, K. A., Kuttippurath, J., Kleinbhl, A., Toon, G. and Piccolo, C. [2007], 'Validation of MIPAS HNO_3 operational data', *Atmospheric Chemistry and Physics* **7**(18), 4905–4934.

Wang, T., Wong, C. H., Cheung, T. F., Blake, D. R., Arimoto, R., Baumann, K., Tang, J., Ding, G. A., Yu, X. M., Li, Y. S., Streets, D. G. and Simpson,

I. J. [2004], 'Relationships of trace gases and aerosols and the emission characteristics at Lin'an, a rural site in eastern China, during spring 2001', *Journal of Geophysical Research D: Atmospheres* **109**(19).

Wayne, C. and Wayne, R. [1996], *Photochemistry*, Oxford University Press.

Wetzel, G., Bracher, A., Funke, B., Goutail, F., Hendrick, F., Lambert, J.-C., Mikuteit, S., Piccolo, C., Pirre, M., Bazureau, A., Belotti, C., Blumenstock, T., De Mazire, M., Fischer, H., Huret, N., Ionov, D., Lpez-Puertas, M., Maucher, G., Oelhaf, H., Pommereau, J.-P., Ruhnke, R., Sinnhuber, M., Stiller, G., Van Roozendael, M. and Zhang, G. [2007], 'Validation of MIPAS-ENVISAT NO_2 operational data', *Atmospheric Chemistry and Physics* **7**(12), 3261–3284.

Whitby, R. A. and Altwicker, E. R. [1978], 'Acetylene in the atmosphere: sources, representative ambient concentrations and ratios to other hydrocarbons', *Atmospheric Environment* **12**(6-7), 1289–1296.

Xiao, Y., Jacob, D. J. and Turquety, S. [2007], 'Atmospheric acetylene and its relationship with CO as an indicator of air mass age', *Journal of Geophysical Research D: Atmospheres* **112**(12).

Xiao, Y., Logan, J. A., Jacob, D. J., Hudman, R. C., Yantosca, R. and Blake, D. R. [2008], 'Global budget of ethane and regional constraints on U.S. sources', *Journal of Geophysical Research D: Atmospheres* **113**(21).